## ABSTRACT

## FOAMING OF AMORPHOUS DRUG DELIVERY SYSTEMS PREPARED BY HOT MELT MIXING AND EXTRUSION

**by**
**Graciela Terife**

Currently there is considerable interest from both academe and pharmaceutical industry in exploring foaming processes and their products in drug delivery applications. However, there is still little knowledge of the impact of the morphology of the foamed structures on the performance of drug products in spite of some publications in this area. Therefore, the main objective of this dissertation is to gain a fundamental understanding of the correlation between foam morphology and performance of amorphous drug delivery systems, which are comprised of an Active Pharmaceutical Ingredient (API) and Polymer excipient.

The Hot Melt Extrusion (HME) process is used to compound the following API / polymer binary systems: Indomethacin (INM) with Soluplus® (PVCap-PVAc-PEG); Carbamazepine (CBZ) with PVCap-PVAc-PEG; and INM with Eudragit® EPO. Comprehensive characterization of these binary systems carried out by combining Differential Scanning Calorimetry, Fourier Transform Infrared spectroscopy, X-Ray Diffraction, and Scanning Electron Microscopy, shows that in all HME-prepared and foamed samples the APIs are amorphous and dissolved in the polymer excipients.

The most important contributions of this dissertation can be grouped into three areas: (a) an understanding of the mechanisms by which foamed dosage forms can lead to faster API release, as well as the key morphological aspects of the cellular structures to achieve this, (b) an understanding of the correlation between the mechanism controlling the release of an API from an amorphous dosage and the enhancement in its release rate upon foaming, and (c) an understanding of the impact of the morphology of the cellular

structures in the milling efficiency of HME products and the dissolution performance of the particles produced.

In the first area, foamed amorphous solid solutions with three different morphologies are produced through the batch foaming process. A strong correlation between foam morphology and the enhancement in API release rate is observed. A significant increase in API release rate is achieved by fast *disintegration*. Through a very broad distribution of wall thicknesses, internal stresses are generated due to different *local* swelling rates in the sample. In this sense, such foam morphologies act as *disintegrant-less disintegrants*, speeding up API release and release rates.

In the second area, the release controlling mechanisms of INM and CBZ from the amorphous systems are identified by using the Power Law model. Three distinct mechanisms are observed: relaxation controlled, anomalous transport, and diffusion controlled. In all cases, the release rates of the APIs are increased upon foaming. However, in cases where the API release is relaxation-controlled, the foamed structures show to have the strongest impact at the initial stages of its *in vitro* release.

Finally, the Foam Hot Melt Extrusion process is used to produce foamed amorphous solid solutions with two different morphologies. Their performance in terms of milling efficiency and *in vitro* dissolution behavior is compared to that of the un-foamed extrudates of the same composition. The milling efficiency is increased appreciably through foamed extrudates, and smaller particles with narrower particle size distributions are obtained compared to un-foamed extrudates. Additionally, it is found that the enhancement of the release rate exhibited by milled foamed extrudates is the most significant for the particles produced by milling the lower density foam extrudates.

# FOAMING OF AMORPHOUS DRUG DELIVERY SYSTEMS PREPARED BY HOT MELT MIXING AND EXTRUSION

**by**
**Graciela Terife**

**A Dissertation**
**Submitted to the Faculty of**
**New Jersey Institute of Technology**
**in Partial Fulfillment of the Requirements for the Degree of**
**Doctor of Philosophy in Materials Science and Engineering**

**Interdisciplinary Program in Materials Science and Engineering**

**May 2013**

.

**APPROVAL PAGE**

**FOAMING OF AMORPHOUS DRUG DELIVERY SYSTEMS PREPARED BY HOT MELT MIXING AND EXTRUSION**

**Graciela Terife**

---

Dr. Costas G. Gogos, Dissertation Co-Advisor — Date
Distinguished Research Professor of Chemical Engineering, NJIT

---

Dr. Marino Xanthos, Dissertation Co-Advisor — Date
Professor of Chemical Engineering, NJIT

---

Dr. Laurent Simon, Committee Member — Date
Associate Professor of Chemical Engineering, NJIT

---

Dr. Piero Armenante, Committee Member — Date
Distinguished Professor of Chemical Engineering, NJIT

---

Dr. Niloufar Faridi, Committee Member — Date
Research Consulting Engineer, Polymer Processing Institute, Newark, NJ

## BIOGRAPHICAL SKETCH

**Author:** Graciela Terife

**Degree:** Doctor of Philosophy

**Date:** May 2013

### Undergraduate and Graduate Education:

- Doctor of Philosophy in Materials Science and Engineering,
  New Jersey Institute of Technology, Newark, NJ, 2013
- Master of Science in Plastic Engineering,
  Universitat Politècnica de Catalunya, Barcelona, Spain, 2006
- Bachelor of Science in Materials Engineering specialized in Polymer Engineering,
  Universidad Simón Bolívar, Caracas, Venezuela, 2004

**Major:** Materials Science and Engineering

### Publications:

Terife, G., N. Faridi, P. Wang and C. G. Gogos (2012). "Polymeric Foams for Oral Drug Delivery - A Review." Polymer Engineering **68**: 32-39.

Terife, G., P. Wang, N. Faridi and C. G. Gogos (2012). "Hot Melt mixing and Foaming of Soluplus® and Indomethacin." Polymer Engineering & Science **52**(8): 1629-1639.

Terife, G. and K. A. Narh (2011). "Properties of carbon nanotube reinforced linear low density polyethylene nanocomposites fabricated by cryogenic ball-milling." Polymer Composites **32**(12): 2101-2109.

### Peer Reviewed Conference Papers:

Terife, G., N. Faridi and C. G. Gogos (2012). "Increasing Drug Release Rate Through Foamed Structures". ANTEC 2012. Society of Plastic Engineers. Orlando, FL. (Oral presentation)

Terife, G., N. Faridi, P. Wang and C. G. Gogos (2011). "Polymeric Foams for Oral Drug Delivery. A Review". Foams 2011. Society of Plastic Engineers. Iselin, NJ. (Oral presentation and poster)

Terife, G., P. Wang and C. G. Gogos (2011). "Hot Melt Mixing of Indomethacin and Solupus® for Oral Drug Delivery". ANTEC 2011. Society of Plastic Engineers**:** 1253-1258. Boston, MA. (Oral presentation)

G. Terife and K. A. Narh (2010). "Characterization of Carbon Nanotube-reinforced Polyethylene Nanocomposite Produced by Cryogenic Ball-milling Process". NanoTech Proceedings: 909-912.

G. Terife and K. A. Narh (2010). "Improving the Mechanical Properties of Polyethylene by Cryogenic Mixing with Multi-Walled Carbon Nanotubes". ANTEC 2010. Society of Plastic Engineers: 107-111, Orlando, FL. (Oral presentation)

G. Terife and K. A. Narh (2009). "Creating Polymer-Carbon Nanotubes Nanocomposites by Cryomilling". ANTEC 2009. Society of Plastic Engineers: 349-353, Chicago, IL. (Oral presentation)

M. Candal, A. Gordillo, G. Terife and O. Santana (2007). "Effect of the Process Conditions over the Adhesion between two Overmolded Polymers". ANTEC 2007. Society of Plastic Engineers: 620-624, Cincinnati, OH. (Poster)

**Oral presentations:**

"Cellular plastics in Drug Delivery" Invited speaker at Leistritz's Pharmaceutical Extrusion Seminar (Somerville, NJ – June 2012).

"Manufacturing Oral Drug Delivery Systems By Hot Melt Mixing/Hot Melt Extrusion". Invited speaker at Society of Plastics Engineers – Palisades-NJ section (Iselin, NJ - June 2011)

**Conference posters:**

G. Terife, N. Faridi, P. Wang and C. G. Gogos (2011), "Increasing the Dissolution rate of Soluplus® and release rate of Indomethacin by Foamed Structures" PSWC 2011. American Association of Pharmaceutical Scientists, Washington, DC (Poster)

G. Terife, C. G. Gogos and P. Wang (2010), "Preparing a solid solution of Indomethacin and Soluplus® through Hot Melt Mixing" PSWC 2010. American Association of Pharmaceutical Scientists, New Orleans, LA. (Poster)

**Recognition:**

Best poster award for Foams 2011 poster from Society of Plastic Engineers (SPE), September 2011.

Recipient of the Mel Gerson Scholarship from the Palisades-NJ section of the Society of Plastic Engineers (SPE), July 2010.

For Antonio
and
my dear family (José Antonio, Elena, Ele, Carmen, Ana, and Sofi)

## ACKNOWLEDGMENTS

First of all I would like to express my deepest gratitude to my advisors Professor Costas G. Gogos and Professor Marino Xanthos. It has been a great honor to work closely with both them. Professor Costas G. Gogos has provided me with guidance and support not only professionally but he has also given me continuous encouragement and life lessons. I will always be deeply grateful to him for opening the doors to the Polymer Processing Institute (PPI) and with it a professional environment with the opportunity to interact with professionals from the polymer and pharmaceutical industries. Professor Marino Xanthos has given me frequent advice and guidance even before I became an NJIT student. I greatly value his directness and attention to detail. The support from both of them has been invaluable for this research and for my professional development

I would like to thank all the committee members Professor Piero Armenante, Professor Laurent Simon, Dr. Niloufar Faridi, and the late Professor Peng Wang for their time and guidance. Specially, Dr. Niloufar Faridi, who has patiently taught me about polymer foaming technology and has guided and supported me throughout the thesis work. Her contribution has been instrumental to completion of my research.

This dissertation was partially supported by the US Department of the Army, DAAE30-03-D1015 Advanced Cluster Energetics (ACE$^{TM}$) Program at New Jersey Institute of Technology (NJIT). Additionally, it was partially funded by the National Science Foundation (NSF) under Grant CMMI-0927142. During my PhD program I also received financial support from the Materials Science and Engineering program through the Teaching Assistantship program, Newark College of Engineering, and NSF under Grants CMMI-0802947 and EEC-0552587.

I would also like to express my gratitude to all PPI's staff for their assistance and for making it a wonderful work environment. I would like to specially thank Mr. Michael Zawisa, whose technical support in the processing lab was vital for this dissertation, as well as Ms. Mariann Pappagallo, Dr. Fei Shen, Dr. Lu Chunmeng, Dr. John Suwardie, Dr. Linjie Zhu, and Dr. Ming-Wan Young.

I would also like thank BASF and Evonik for their generous donations of the polymer excipients and one of the active ingredients used in this work.

I am very grateful to Leistritz, and specially Mr. Charlie Martin and Mr. Augue Machado for making it possible to perform the foam extrusion experiments in their facility in Somerville, NJ.

I would like to thank Dr. Qian Zheng, Dr. Nikolaos Ioannidis, Dr. Huiju Liu, Dr. Jin Uk Ha, Dr. Min Yang and Mr. Nonjaros Chomcharn for their discussions and friendship during my studies at NJIT.

Finally, I'm deeply grateful to my father and mother in-law, Aldo Cossutta and Patricia Cossutta, for their financial support, as well as to my husband Antonio Rodriguez and my parents, Jose Antonio Terife and Elena Gil de Terife, for their unconditional support and encouragement.

## TABLE OF CONTENTS

**Chapter** **Page**

**TABLE OF CONTENTS**
**(Continued)**

**Chapter** **Page**

**TABLE OF CONTENTS**
**(Continued)**

**Chapter** **Page**

**TABLE OF CONTENTS**
**(Continued)**

**Chapter** **Page**

**TABLE OF CONTENTS**
**(Continued)**

**Chapter** **Page**

## LIST OF TABLES

**Table** **Page**

## LIST OF TABLES
## (Continued)

**Table** **Page**

## LIST OF TABLES
## (Continued)

**Table** **Page**

## LIST OF FIGURES

## LIST OF FIGURES
## (Continued)

## LIST OF FIGURES
## (Continued)

**Figure** **Page**

## LIST OF FIGURES
## (Continued)

**Figure** **Page**

## LIST OF FIGURES
## (Continued)

**Figure** **Page**

## LIST OF FIGURES
## (Continued)

**Figure** **Page**

## LIST OF FIGURES
## (Continued)

**Figure** **Page**

## LIST OF FIGURES
## (Continued)

**Figure** **Page**

## LIST OF FIGURES
## (Continued)

**Figure** **Page**

## LIST OF SYMBOLS

| | |
|---|---|
| $\alpha_i$ | Thermal expansion coefficient of material "i" |
| $Co$ | Equilibrium penetrant concentration |
| $C_1$ | Initially concentration of API in a polymer slab |
| $C_s$ | Concentration of API at the surface of the sample |
| $CO_2$ | Carbon dioxide |
| $D$ | Diffusion coefficient |
| $\Delta H$ | Enthalpy change |
| $E_s$ | Heat of solution for a gas in a polymer |
| $f_1$ | Difference factor |
| $f_2$ | Similarity factor |
| $k$ | Power Law constant |
| $K$ | System specific constant (Gordon-Taylor model) |
| $k_a$ | Acid dissociation constant |
| $k_o$ | Relaxation constant |
| $k_p$ | Henry's law constant |
| $k_{po}$ | Temperature independent Henry's Law constant |
| L | Characteristic length of the sample |
| $m$ | Number of time points |
| $\dot{m}$ | Mass flow rate |
| $M_\infty$ | Mass of released API at infinite time |
| $M_t$ | Mass of released API at a given time “t” |
| MW | Molecular weight |

| | |
|---|---|
| $n$ | Release exponent |
| $P_{CO_2}$ | Pressure of $CO_2$ |
| $Q$ | Volumetric flow |
| $\rho$ | Density |
| $R$ | Universal gas constant |
| $R_t$ | Percentage of API released from reference sample at time "t" |
| $S$ | Volume of gas dissolved at STP per unit weight of polymer |
| STP | Standard temperature and pressure |
| T | Temperature |
| $t$ | Time |
| $T_g$ | Glass transition temperature |
| $T_m$ | Melting temperature |
| $T_t$ | Percentage of API released from post change sample at time "t" |
| $v$ | Void fraction in a foamed sample |
| $w_i$ | Weight fraction of component "i" |

## LIST OF ACRONYMS

| | |
|---|---|
| API | Active Pharmaceutical Ingredient |
| CBZ | Carbamazepine |
| CBA | Chemical Blowing Agent |
| DSC | Differential Scanning Calorimetry |
| EPO | Eudragit® EPO, poly(butyl methacrylate-co-(2-dimethylaminoethyl) methacrylate-co-methyl methacrylate) (1:2:1) |
| EPO30INM | Eudragit® EPO loaded with 30 wt% Indomethacin |
| FDA | Food and Drug Administration |
| f-EPO30INM | Foamed Eudragit® EPO loaded with 30 wt% Indomethacin |
| f-S15CBZ | Foamed Soluplus® loaded with 15 wt% Carbamazepine |
| f-S30INM | Foamed Soluplus® loaded with 30 wt% Indomethacin |
| FT-IR | Fourier Transformed Infrared Spectroscopy |
| HD-fHME | High Density foamed extrudate |
| HME | Hot Melt Extrusion |
| HMM | Hot Melt Mixing |
| HPMC | Hydroxypropyl Methylcellulose |
| INM | Indomethacin |
| LD-fHME | Low Density foamed extrudate |
| MTDSC | Modulated Temperature Differential Scanning Calorimetry |
| PAT | Process Analytical Technology |
| PBA | Physical Blowing Agent |

| | |
|---|---|
| PEG | Polyethylene Glycol |
| PM | Physical Mixture |
| POM | Polarized Optical Microscopy |
| PSD | Particle Size Distribution |
| PVAc | Polyvinyl acetate |
| PVCap | Polyvinyl caprolactam |
| PVCap-PVAc-PEG | Soluplus® a polyvinyl caprolactam-polyvinyl acetate-polyethylene glycol graft copolymer (57:30:13) |
| PVDF | Polyvinylidene fluoride |
| RH | Relative Humidity |
| S10INM | Soluplus® loaded with 10 wt% Indomethacin |
| S15CBZ | Soluplus® loaded with 15 wt% Carbamazepine |
| S30INM | Soluplus® loaded with 30 wt% Indomethacin |
| S50INM | Soluplus® loaded with 50 wt% Indomethacin |
| S75INM | Soluplus® loaded with 75 wt% Indomethacin |
| $ScCO_2$ | Supercritical Carbon Dioxide |
| SEM | Scanning Electron Microscopy |
| STP | Standard temperature and pressure |
| TGA | Thermogravimetric Analysis |
| USP | United States Pharmacopeia |
| XRD | X-Ray diffraction |

# CHAPTER 1

# INTRODUCTION

Pharmaceutical Hot Melt Extrusion (HME) has and is being incorporated into the units of operation used to manufacture of drug delivery systems. This has been driven by the Process Analytical Technology (PAT) initiative of the Food and Drug Administration (FDA). The PAT initiative promotes the used of continuous manufacturing process with in-line quality control (FDA 2004), which can be easily accomplished through the extrusion process. HME is a continuous, solvent-free manufacturing process that allows to uniformly distribute an Active Pharmaceutical Ingredient (API) in a polymeric excipient or carrier; additionally, other intergranular excipients can be incorporated in a single process. The API may exist in its native crystalline state or it may be dissolved in an amorphous polymer excipient in order to produce single phase amorphous systems. The latter case is of great value for solubilization of APIs with poor aqueous solubility. Since amorphous systems make it possible to increase the release and apparent solubility of an API, then, potentially its bioavailability can be enhanced.

In spite of extensive research conducted in the HME area since the 1980's, there still exist challenges associated to this process, specifically in view of the conservative nature of the pharmaceutical industry. First, many APIs are susceptible to thermal degradation during processing. Similarly, the majority of the polymer excipients used in the manufacture of orally delivered dosage forms are not well suited (or were not originally developed) to be melt processed. In other words, many of the polymer

excipients used have high melt viscosities and very narrow processing windows which makes them very difficult to be processed without plasticizers.

Other challenges associated with the HME process are related to the nature of the extrudates produced after compounding. On the one hand, extrudates tend to be very tough, and, thus, difficult to mill into suitable particle sizes with narrow distributions to be used for tableting, to fill into capsules or to be used in liquid suspension. Additionally, extrudates tend to be non-porous and, as result, their dissolution rates are hindered by slow fluid absorption by the HME products.

In order to overcome the aforementioned challenges associated with HME, foaming processes widely used in the polymer industry, such as foam extrusion and foam injection molding, have been explored in the last decade. Physical blowing agents have been used as "fugitive" plasticizers, foamed extrudates have shown to facilitate milling operation, and cellular structures have been evaluated as a means to enhance API release rate. Detailed literature review of these and other uses of foaming processes and foamed products in pharmaceutics are presented in section 2.3 of Chapter 2.

Currently there is a lot of interest from both academe and pharmaceutical industry in exploring foaming processes and their products in drug delivery applications. However, there is still little knowledge of the impact of the morphology of the foamed structures on the performance of drug products in spite of some publications in this area. Therefore, the main objective of this dissertation is to gain a fundamental understanding of the correlation between foam morphology and performance of amorphous drug delivery systems using foam extrusion and batch foaming processes. Additionally, the effect of the foaming processes on the state of the API is studied.

In the first part of this dissertation the HME process is used to compound the binary system comprising of Indomethacin (INM) as model API and Soluplus® (PVCap-PVAc-PEG). Since this is the binary systems used for the majority of the foaming studies, its general properties (i.e. solubility of INM is the excipient, *in vitro* dissolution and $CO_2$ solubility in the binary system) are studied in detail.

Since batch foaming is carried with supercritical carbon dioxide ($ScCO_2$) as the blowing agent, its effect on crystallization of INM from its amorphous state is investigated. Amorphous samples of INM are subjected to different batch foaming conditions, and their morphological changes are evaluated through Fourier Transform Infrared Spectroscopy (FT-IR).

The Foam Hot Melt Extrusion process is used to produce foamed extrudates of the INM / PVCap-PVAc-PEG binary system. The objective of the foam extrusion study been to understand the effect of the morphology of the cellular structure on the milling efficiency of extrudates and the *in vitro* dissolution performance of the particles produced. In this study by varying the foam extrusion conditions two foam morphologies were produced and their performance is compared to that of the un-foamed extrudate of the same composition.

The batch foaming process is used perform two different studies. The main objective of first batch foaming study is to understand the correlation between the mechanisms controlling the release of an API from an amorphous dosage form and the enhancement in its release rate upon foaming. The Power law model is used to identify the API release mechanism from four amorphous systems: 30:70 INM / PVCap-PVAc-PEG, 15: 75 Carbamazepine / PVCap-PVAc-PEG, and 30:70 INM / Eudragit® EPO in

two aqueous buffer solutions with pHs 1.2 and 7.4. In addition, the effect of the batch foaming process with $ScCO_2$ as blowing agent in the physical state of the APIs is studied combining Scanning Electron Microscopy (SEM), FT-IR, and X-ray diffraction (XRD).

The main objective of the second study performed through batch foaming, is to gain an understanding of the mechanisms by which foamed dosage forms can lead to faster API release as well as the key morphological aspects of the cellular structure needed to achieve this. A secondary goal if this study is to evaluate the impact of the cellular structure in the long term physical stability of an amorphous solid solution. The 30:70 INM / PVCap-PVAc-PEG binary system is used for this section of the dissertation. Foamed samples with three distinct morphologies are produced by varying the batch foaming conditions, and compared to the performance of compression molded (non-porous) samples of same weight and composition.

# CHAPTER 2

# LITERATURE REVIEW

## 2.1 Pharmaceutical Hot Melt Extrusion / Hot Melt Mixing

Pharmaceutical Hot Melt Extrusion (HME) has been an area of great interest in academe and pharmaceutical industry since the 1980's (Crowley et al. 2007), with many and extensive investigations, as well as numerous patents and research papers published since then. Briefly, HME is a polymer melt compounding process, adapted from the polymer processing industry, where one or more active pharmaceutical ingredients (APIs) are fed in an extruder with at least one polymeric excipient. The processed stream undergoes melting of the polymer excipient, mixing and / or dissolution of the API, and is then shaped into a continuous extrudate by pumping it through a die followed by cooling. The typical applications of pharmaceutical HME include: sustained release delivery systems, drug solubilization, target release and prevention of substance abuse. Some of these applications can be seen in the list of drug products shown in Table 2.1, where a summary of their commercial status and the purpose of the HME process are listed.

As can be seen in Table 2.1, a significant number of the drug delivery systems currently manufactured by HME in the market are implants. In order words, these products are drug delivery systems or medical devices that provide sustained API release, where the HME process is used to produce an homogenous blend of the API – in either its crystalline or amorphous form – with a polymer excipient or carrier and to provide the desired shape of the device (Ghebre-Sellassie and Martin 2007). It should be pointed out that manufacturing sustained release systems by HME is not limited to devices.

Controlled release oral dosages have been also be manufactured by this process (Follonier et al. 1995; Repka et al. 2007). The release of the API is delayed or modulated by the carrier, which can be either insoluble or slow dissolving in body fluids (Follonier et al. 1995).

Given that one of the prerequisites for absorption of an orally administered API is that it must dissolve along the gastrointestinal tract (GI) (Amidon et al. 1995; Dahan and Miller 2012), solubilization of APIs with poor aqueous solubility through HME is another area where significant research efforts and interest lay. A significant portion of the new discovered APIs have poor aqueous solubility (Crowley et al. 2007; Dahan and Miller 2012); it has been estimated that more than 30 % of the APIs in the market have poor solubility in an aqueous medium. Furthermore and more significantly, 70 % out of all new molecule entities are expected to show poor aqueous solubility (Benet et al. 2006).

Through HME and Hot Melt Mixing (HMM), a batch melt compounding process that can be used to perform feasibility assessment for HME, it is possible to dissolve an API in a molten polymer excipient, and, thus increase its release rate and apparent solubility (Breitenbach 2002; Crowley et al. 2007; Ghebre-Sellassie and Martin 2007; Repka et al. 2007; Liu 2010). It is important though to bear in mind that this does not necessarily result in enhanced bioavailability, since permeability of the API through the GI track also plays a significant role in its absorption (Amidon et al. 1995; Dahan and Miller 2012). However, rendering a poorly soluble API soluble is the starting point for rendering poorly soluble APIs bioavailable. The dissolution mechanisms of the API in the molten polymer are described in more detail below.

**Table 2.1** Examples of Drug Products Manufactured by the HME Process

| Name | API | Polymer Excipient* | Delivery Form | Indication | Status [b, c] | HME Purpose |
|---|---|---|---|---|---|---|
| Dapivirine-Maraviroc | Dapivirine + Maraviroc [a] | EVA[a] | Implant | Anti-Viral (HIV) | UD[a] | Shape |
| Lacrisert® | None | HPMC | Implant | Dry eye syndrome | M | Shape |
| NuvaRing | Etonogestrel + Ethinyl Estradiol | EVA[a] | Implant | Contraceptive | M | Shape |
| Zoladex | Goserelin acetate | PLGA | Implant | Prostate cancer | M | Shape |
| Implanon | Etonogestrel | EVA | Implant | Contraceptive | M | Shape |
| Ozurdex® | Dexamethasone | PLGA | Implant | Macular Edema | M | Shape |
| Kaletra® | Lopinavir + Ritonavir | PVP-VA | Tablet | Anti-Viral (HIV) | M | Amorphous solution |
| Norvir® | Ritonavir | PVP-VA | Tablet | Anti-Viral (HIV) | M | Amorphous solution |
| Eucreas® | Vildagliptin + Metformin hydrochloric | HPMC | Tablet | Diabetes | M | Melt granulation |
| Zithromax® | Azithromycin | HPMC | Tablet | Antibiotic | M | Taste Masking |
| Gris-PEG® | Griseofulvin | PEG | Tablet | anti-fungal | M | Crystalline dispersion |
| Rezulin® | Troglitazone | PVP | Tablet | Diabetes | W | Amorphous solution |
| Palladone™ | Hydrophone | EC + ERS | Tablet | Pain | W | Controlled release |
| Posaconazole | Posaconazole | - | - | Anti-fungal | UD | Amorphous solution |
| Anacetrapib | Anacetrapib | - | - | Cardiovascular disease | UD | Amorphous solution |

*EVA: Ethyl Vinyl Acetate, HPMC: Hydroxypropyl methylcellulose, PLGA: Poly(lactic-co-glycolic acid), PVP-VA: Polyvinyl pyrrolidone co-vinyl acetate, PEG: Polyethylene glycol, PVP: Polyvinyl pyrrolidone, EC: Ethyl cellulose, ERS: Eudragit® RS.
Source: [a] (Loxley 2010) [b] (DiNunzio 2011). [c] UD: Under development, M: Marketed product, and W: Withdrawn from the market

Besides sustained release and API solubilization, HME allows to target the release of an API to a specific section of the GI tract. This is accomplished by embedding the API (either in its crystalline or amorphous form) in a polymer excipient that only dissolves in a specific pH range (Doelker 1993; Follonier et al. 1995; Andrews et al. 2008) or through specific API / excipient interactions (Sriwongjanya and Bodmeier 1998; Lele and Hoffman 2000). This is also of great interest for taste-masking applications.

Finally, HME allows the manufacturing of dosage forms that aid the prevention of substance abuse (Oshlack et al. 2001; Arkenau-Maric and Bartholomaus 2008). Many APIs have habit-forming side effects that may lead to addiction and substance abuse. For example, in order to obtain a fast-acting and high dosage of such types of APIs, abusers crush the dosage forms into fine powders, which then can be consumed nasally or can be dissolved to be administered intravenously (Arkenau-Maric and Bartholomaus 2008). Therefore, HME is used to manufacture very tough dosage forms – with breakage strengths exceeding 500N (Arkenau-Maric and Bartholomaus 2008) – which makes it very difficult to break and grind them.

### 2.1.1 Description of the HME Process and Mechanisms

The pharmaceutical HME process is carried out at temperatures 50° to 100 °C above the glass transition temperature ($T_g$) of the polymer (or above its melting point in the case of semi-crystalline polymer excipients) and generally below the melting point of the API, though it can also be carried out above the melting point of the API if thermal degradation is not an issue.

From a general perspective, the HME process can be described by the following elementary steps: solids conveying, melting, mixing, API's dissolution in the excipient (if

the system is miscible), devolatilization and pumping (Tadmor and Gogos 2006; Gogos 2012).

In more detail, the API and the polymer are fed as solids particulates, either independently or as a dry blend. These solids are then conveyed by the screws, thereafter the materials are heated and the polymer melts primarily by heat generated volume-wise through frictional and plastic energy dissipation created by the action of kneading blocks deforming fully-filled stream regions (Tadmor and Gogos 2006). Once the polymer is melted, and if the system is miscible, the API can be progressively dissolved in the polymer, by distributive laminar mixing flows.

Figure 2.1 shows the dissolution mechanism of API in a molten polymer of a miscible system when compounding is carried out below the melting point of the active ingredient. This schematic representation shows first the dry blend of the API and the excipient, representing the feed, and once the polymer is melted the crystalline particles are suspended in the melt. Then, dissolution of the API in the polymer commences by the formation of a boundary layer along the surface of the crystalline particles, followed by distributive and dispersing mixing, until the API is completely dissolved in the polymer.

After melting and mixing, devolatilization or venting is necessary to remove trapped air and steam in the melt (Todd 1998). Lastly, pressure is generated by the rotating screws in order to pump the melt stream through the die. Finally, this API / Polymer single phase mixture is cooled to room temperature and solidifies. As a result the dissolved API is immobilized by the matrix in an amorphous state. Two factors prevent recrystallization of the API; one is the greatly reduced mobility of the API in the

glassy polymer matrix aided by choosing an API / Polymer system with a $T_g$ considerably above the storage temperature, and the other and most important, is the existence of specific and strong interactions between the API and the polymer, such as hydrogen bonding and ionic bonding (Breitenbach 2002; Bhugra and Pikal 2008).

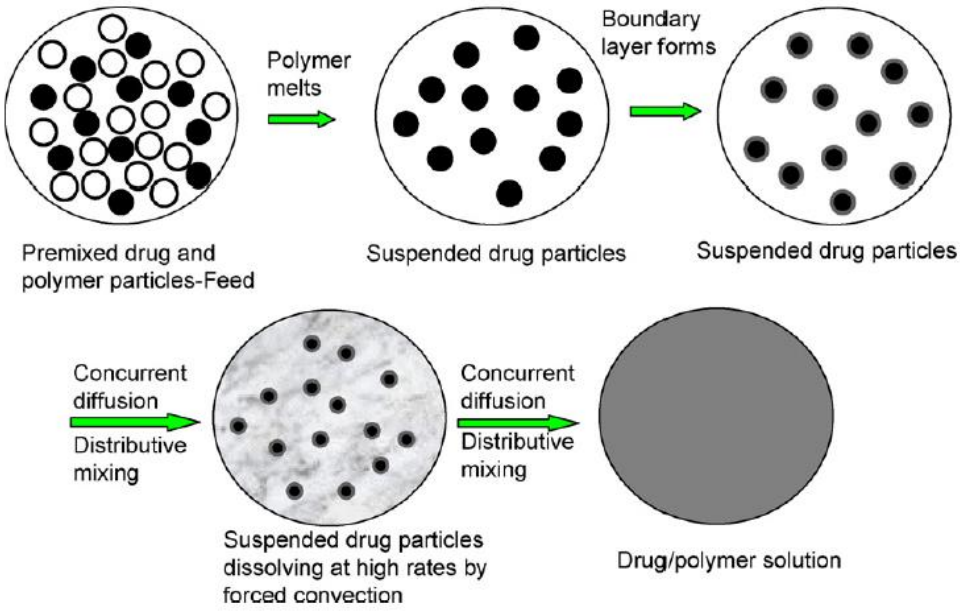


**Figure 2.1** Schematic representation of the dissolution mechanism of an API during the HME process carried out at a temperature above the melting point of the API. Source: (Liu et al. 2010)

## 2.2 Foams, Foaming Processes, and Mechanisms

The terms "foams" and "cellular structures" refer to solid porous structures, which can be visualized as, and often is a honeycomb structure, in the case of closed cells foams shown in Figure 2.2 (a), or as a rigid sponge, for the case of open cell foams, Figure 2.2 (b). Foams are widely used in both food and plastic industries, and for the last decade the applications of foamed products and foaming processes have grown dramatically, as the need for thermal and sound insulation, as well as for light-weight vehicle components

have grown. They have been also recently explored by the pharmaceutical industry to investigate novel drug delivery methods.

Some examples of foams in the food industry include: bread, cakes and puffed cereals and snacks. Some of the typical applications of foamed products in the plastic industry include: insulation (thermal, acoustic and electrical), floating devices, shock mitigation, packaging and cushioning among others. The end use, as well as the performance and properties of polymeric foams strongly depend on their physical characteristics. For example open cell foams, where all the cells are interconnected, are used for applications that require high permeability to gasses and higher capacity to absorb fluids and moisture (Shutov 1991; Mills 2007). On the other hand, closed-cell foams – where each cell is isolated from the rest – are preferred for thermal, noise and electrical insulation over open-cell foams. (Mills 2007).

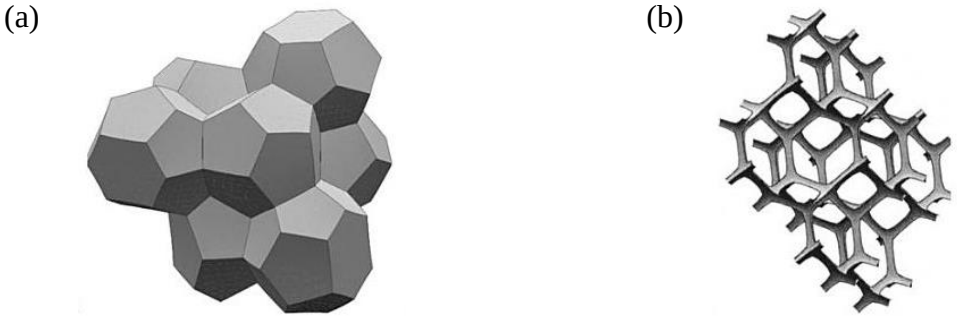


**Figure 2.2** Schematic representation of: (a) a closed cell foam, and (b) an open cell foam. Source: (Mills 2007).

### 2.2.1 Foaming Processes and Mechanism

Cellular structures can be commercially created through continuous processes, such as foam extrusion, or through batch or semi-continuous processes, such as injection molding. From a general perspective, the foaming process involves the following elementary steps: (1) dissolution of a gas in a polymer based formulation, (2) cell

nucleation, (3) bubble growth, and (4) stabilization of the cellular structure (Zhang and Xanthos 2004), these are depicted schematically in Figure 2.3.

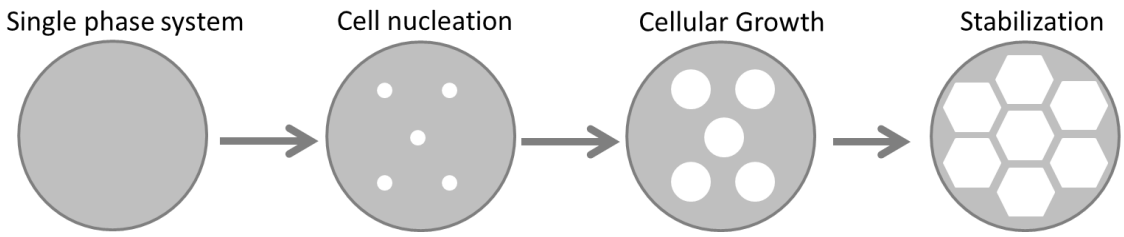


**Figure 2.3** Schematic representation of the foaming elementary steps.

Independently of the method used for producing the foam structure, first the polymer is saturated with a gas, and then a thermodynamic instability is induced by a rapid increase in temperature or drop in pressure. As a result, the system becomes oversaturated and cell nucleation and growth takes place. From a physical perspective, as depicted in Figure 2.3, the first isolated spherical bubbles are formed by nucleation, which then start to grow. Once these gas bubbles start to touch each other, their spherical shapes start becoming hexagonal and the facets become planar, and, depending on the strength of the material, the walls could either remain intact (i.e. forming a closed-cell structure) or may break generating an open cell structure (Saunders 1991; Mills 2007).

Cell nucleation can be homogeneous, heterogeneous or of a mixed mode (Colton and Suh 1987; Ramesh 2004). Homogenous nucleation occurs when the dissolved gas coalesces forming a second phase. During the formation of this second phase the free energy of the system changes according to expression 2.1 below, where the first term on the right side of the equation corresponds to a reduction in free energy as the gas molecules are incorporated into the bubble. The second term on the right side of the

equation corresponds to an increase on free energy due to the formation of a new surface and it is associated interfacial energy (Colton and Suh 1987).

$$\Delta G_{hom} = -V_b \Delta P + A_{bp}\gamma_{bp} \tag{2.1}$$

Where $\Delta G_{hom}$ is the change of free energy during homogenous nucleation, $V_b$ is the nucleus volume, $\Delta P = P_{sat} - P_s$ is the difference between saturation pressure ($P_{sat}$) and atmospheric pressure ($P_s$), $A_{bp}$ is the surface area of the nucleus, and $\gamma_{bp}$ is the surface energy of the polymer-bubble interface (Colton and Suh 1987; Kumar and Suh 1990; Goel and Beckman 1994a; Ramesh 2004).

As can be seen in Figure 2.4 (a), at the beginning of the nucleation process the interfacial energy plays a dominant role, but once a critical nucleus size is reached ($r^*$) the energy barrier for nucleation is overcome and the bubble growth process is favored. By assuming a spherical nucleus with radius $r$ – since this is the geometry that will give the minimum excess in energy (Colton and Suh 1987; Ramesh 2004) – then, from the expression 2.1 the critical radius (r*) and the nucleation activation energy ($\Delta G^*_{hom}$) can be obtained as defined by the following expressions:

$$r^* = \frac{2\gamma_{bp}}{\Delta P} \tag{2.2}$$

$$\Delta G^*_{hom} = -\frac{16\pi}{3}\frac{\gamma^3_{bp}}{\Delta P^2} \tag{2.3}$$

Another important parameter that defines the cellular structure is the nucleation rate, which in the case of homogenous nucleation is given by equation 2.4.

$$J_{hom} = f_0 C_0 exp\left(\frac{-\Delta G^*_{hom}}{\kappa T}\right) \tag{2.4}$$

Where $J_{hom}$ is the homogenous nucleation rate, $f_o$ is frequency of formation of stable nuclei, $C_o$ is the gas concentration, $\kappa$ is the Boltzmann constant and $T$ the absolute temperature (Colton and Suh 1987).

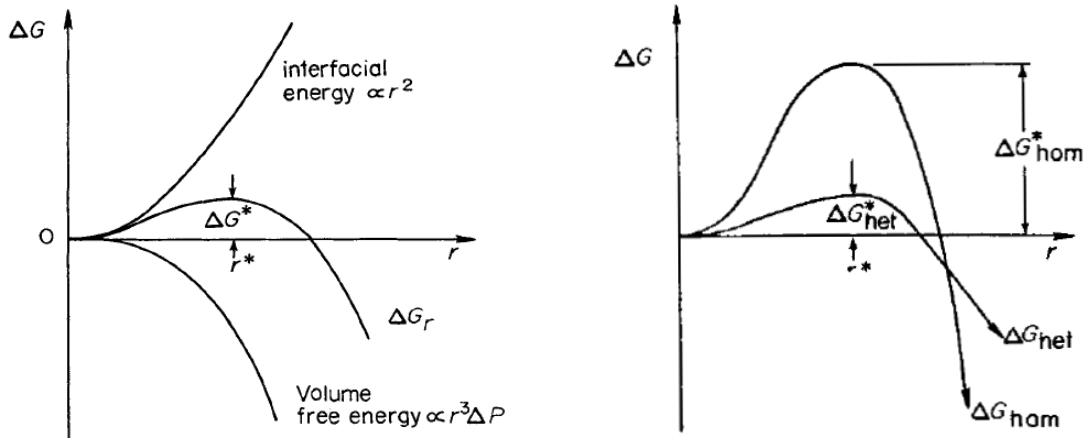


**Figure 2.4** Change in free energy as a function of radius (r) of the nucleus. (a) Change in interfacial energy, volume free energy, and net free energy associated with homogeneous nucleation process as a function of the radius of the nucleus. (b) Comparison between homogenous and heterogeneous free energies of nucleation as a function of the radius of the nucleus. Source: (Colton and Suh 1987).

By understanding the homogenous nucleation theory it is easy then to identify the variables that affect the cellular morphology in a given process. From expressions 2.2 through 2.4 it is evident that by increasing the saturation pressure and/or reducing the surface energy, both the $r^*$ and the activation energy are reduced, and hence the nucleation rate can be significantly increased. From expression 2.4 it is also clear that other parameters that can be utilized to affect the nucleation kinetics are the gas

concentration and temperature, where an increase in either one results in faster nucleation rate.

Finally, through heterogeneous nucleation, it is also possible to accelerate nucleation, as shown schematically in Figure 2.4 (b). Nucleation agents are used to reduce the nucleation activation energy by providing lower surface energy sites, or by lowering the polymer surface tension (Saunders 1991; Ramesh 2004). Based on the above, crystalline API particles suspended in the melt, whether insoluble or only partially soluble in the polymer, may act as nucleating agents during foaming operations.

In general, by increasing the nucleation rate it is possible to produce foams with smaller cells and lower densities.

Once critical size nuclei are formed, gas dissolved in the polymer diffuses into in the gas bubbles, and as a result, the pressure inside the bubbles increases subjecting the polymer to bi-axial tension and deformation. The rate of cell growth will depend on the gas diffusion rate, heat transfer affecting melt temperature, and polymer strength (i.e. melt strength and polymer-gas rheological and viscoelastic properties) (Holl et al. 1999; Tadmor and Gogos 2006).

**2.2.1.1 Types of Foaming Agents.** The sources of the gases that provide expansion during foaming of the material are called “Foaming or Blowing Agents”. These are divided into two categories: chemical blowing agents (CBAs) and physical blowing agents (PBAs). CBAs are compounds added to a given formulation that, upon heating and at CBA-specific temperature ranges decompose releasing a gas, such as nitrogen, water, and carbon dioxide ($CO_2$) (Throne 2004; Ahuja et al. 2007). An example of a CBA that could be used in pharmaceutical applications and that is commonly used in

food industry is sodium bicarbonate. In general, CBAs result in high density foams (Han et al. 1976; Throne 2004).

In contrast to chemical foaming agents, PBAs do not undergo any chemical reaction to produce a blowing gas. PBAs can be grouped into two categories: permanent gases and volatile organic compounds (Throne 2004). Table 2.2 shows a summary of the properties of PBAs that are used in the polymer industry and have direct applications in the manufacture of pharmaceutical products. It should be noted that both water vapor and $CO_2$ are commonly used in the food industry to manufacture puffed snacks and cereals through the foam "extrusion cooking" process (Moraru and Kokini 2003; Cho and Rizvi 2010).

**Table 2.2** Properties of Commonly Used Physical Blowing Agents

| PBA | Density at 23°C [g/cm$^3$] | Boiling Point [°C] | Critical Temperature [°C] | Critical Pressure [MPa] |
|---|---|---|---|---|
| Nitrogen | 1.146 | - | -147 | 3.40 |
| Carbon dioxide | 1.811 | -78.5 | 31 | 7.39 |
| Water vapor | 1.000 | 100 | 374.1 | 22.1 |

Source: (Throne 2004)

**2.2.1.2 Batch Foaming.** During the batch foaming process with PBAs the polymeric sample is saturated with a gas at high pressure, then a thermodynamic instability is introduced to the process to initiate cell nucleation In general two approaches are used: (1) a low temperature gas saturation method, and (2) a high temperature gas saturation method or sometimes called the pressure quenching method.

When the low temperature approach is used, the sample is saturated with gas at a temperature below the system's $T_g$. Then the gas-saturated sample is immersed in a high

temperature bath to raise its temperature above the $T_g$ of the polymer-gas system. As a result the system becomes oversaturated with gas and, due to the increased molecular mobility, the nucleation process is triggered (Colton and Suh 1987; Kumar and Suh 1990; Ramesh et al. 1991; Goel and Beckman 1994a). Afterwards, the cellular structure is stabilized by quench-cooling the foamed sample (Goel and Beckman 1994b).

On the other hand, through the pressure quenching method the polymeric sample is saturated with gas at a temperature above its $T_g$ and at a high pressure. The driving force for nucleation in this case is a sudden depressurization of the system which makes the system oversaturated with gas. Therefore, very fast and extensive nucleation can be promoted and, thus, foams with very small cells can be produced (Goel and Beckman 1994a; Arora et al. 1998; Sun et al. 2002). It should be mentioned that the depressurization step takes place at a constant temperature, even though the temperature of gases tends to decrease, due to expansion following the Joule-Thomson effect (Burnett 1923). The overall temperature change can be considered negligible. Goal and Beckman (Goel and Beckman 1994b) reported only 2° to 3 °C drop in temperature during the pressure quenching batch foaming process with supercritical carbon dioxide ($ScCO_2$).

Figure 2.5 shows a summary of the variables that affect the properties of foams produced by batch foaming. As in any other process, these are grouped in terms of process, material and design variables. However, these groups of variables are not independent of each other, in the sense that even the independent process variables are chosen based on the properties of the material been foamed.

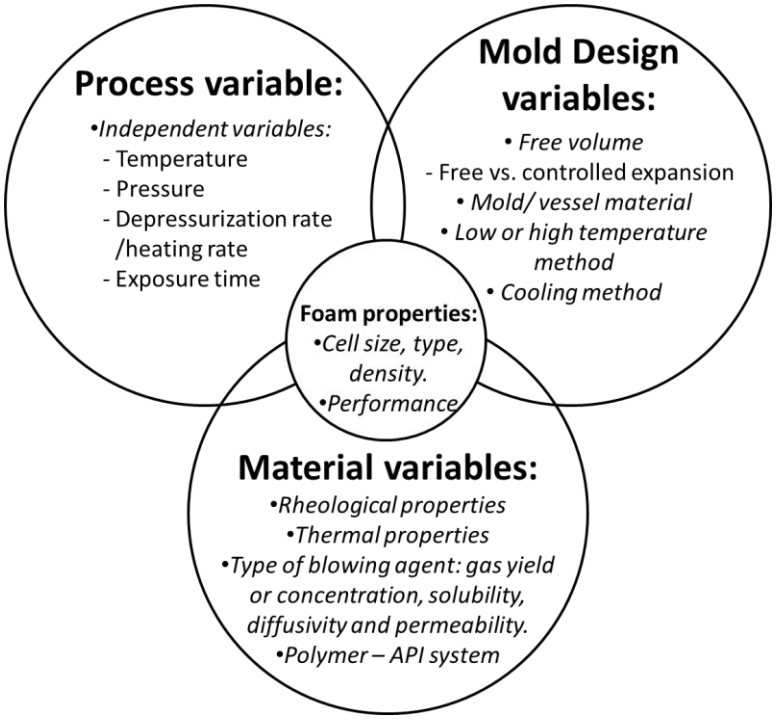


**Figure 2.5** Summary of the variables that affect the properties of foams produced by the batch foaming process.

**2.2.1.3 Foam Extrusion.** In contrast to the batch foaming process, where the sample is exposed to the PBA at a temperature close to its $T_g$, during foam extrusion the gas is dissolved in the molten polymer inside an extruder. Figure 2.6 shows schematically the elementary steps during the foam extrusion process in the presence of an API, which is miscible with the excipient. Prior to gas injection, the foam extrusion process is equivalent to the conventional HME process described above. However, a melt seal must be created upstream, that is before the gas injection in order to prevent gas back flow and, thus, gas loss thought the hopper. Such melt seal is achieved by having a fully-filled screw section, which is generated in a co-rotating twin screw extruder through reversing self-wiping screw elements. Subsequently, downstream of the gas injection site, the gas must be dissolved in the melt and this "solution" has to be cooled in order to increase the melt viscosity and melt elasticity and provide the necessary melt strength to sustain the

cellular structure without collapsing. Finally, foaming occurs along the die as the pressure is rapidly dropped to atmospheric conditions. (Lee 2000; Zhang and Xanthos 2004)

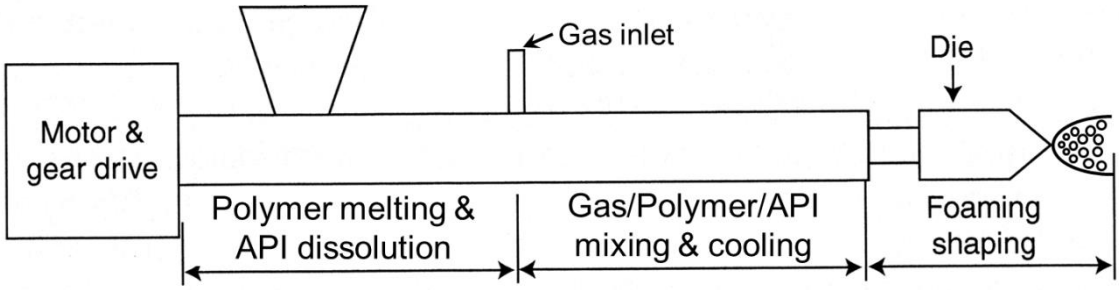


**Figure 2.6** Schematic representation of the foam extrusion process. Extruder sketch modified from: (Lee and Scholz 2009)

Figure 2.7 shows schematically a summary of the process, design and material variables that affect the morphology of the cellular structure. It is important to have in mind that all these variables are not fully independent, as mentioned above. As an example, the amount of PBA dissolved is dependent not only on the material variables, such as the miscibility and viscosity of the melt, but it also depends on processing variables such as pressure, temperature, and screw speed, and design variables such as screw configuration (Zhang and Xanthos 2004). Among the design variables, die geometry is one of the most important design variables, since it defines the depressurization rate and it has a very strong influence on the magnitude of the pressure drop.

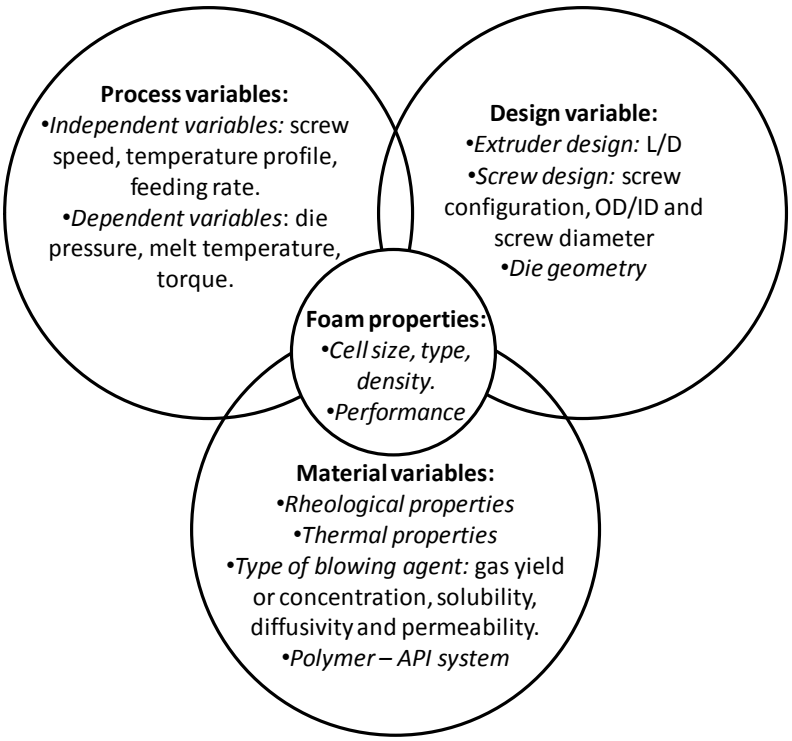


**Figure 2.7** Summary of the variables that affect the properties of foams produced by the foam extrusion process.

### 2.3 Use of Foaming Technology in the Manufacture of Drug Products

Even though for the last decade research work has been conducted and published related to foams and foaming processes in drug delivery products, results are very scarce and further studies must be conducted in order to gain fundamental understanding of the impact of foaming on the performance of HME products.

The application of polymeric foams in drug delivery can be grouped in four categories: (1) the use of PBAs as "fugitive" plasticizers (Verreck et al. 2005; Verreck et al. 2006a; Verreck et al. 2006b; Lyons et al. 2007; Verreck et al. 2007; Nikitine et al. 2010; Nagy et al. 2012), (2) floating oral dosages (Nakamichi et al. 2001; Streubel et al. 2003; Fukuda et al. 2006), (3) foams as intermediate products (Hsu et al. 1996; Hsu et al. 1997; Verreck et al. 2005; Verreck et al. 2006b; Verreck et al. 2007; Nagy et al. 2012),

and (4) foams to increase release rate of amorphous systems (Breitenbach and Baumgartl 2000; Clarke 2005; Lyons et al. 2007; Andrews et al. 2010; McKelvey et al. 2010).

### 2.3.1 Physical Blowing Agents as "Fugitive" Plasticizers

Many APIs are susceptible to thermal degradation under HME processing conditions. Thus, they may become inactive or lose their functionality (Verreck et al. 2007). Similarly, many polymeric excipients in the market have very narrow processing windows and high viscosity which makes them very difficult to be processed without plasticizers.

However, adding permanent plasticizers may be unfavorable to the formulation for several reasons: (1) they add "dead weight" to the dosage, which could become unacceptably high (Verreck et al. 2006b). (2) Plasticizer volatilization during storage may result in unexpected changes in product performance during the shelf life of the dosage (Crowley et al. 2007). (3) Finally, plasticizers permanently increase the overall mobility of the system; thus, it may be detrimental to the stability of the system, reducing the shelf life of the product. Therefore the use of "fugitive" plasticizer during HME process is of great interest for the pharmaceutical industry, because the processing temperature can be decreased without affecting the long term stability of the product. Since it is well known that, once a PBA is dissolved in a polymer can act as a plasticizer, these are great candidates as "fugitive" plasticizers. For example Elkovitch and Tomasko (Elkovitch and Tomasko 2000) observed a maximum decrease in viscosity for poly(methyl methacrylate) and polystyrene of 80 and 70 %, respectively in the presence of $CO_2$.

Verreck et al. (Verreck et al. 2005; Verreck et al. 2006b; Verreck et al. 2007) evaluated the effect of $CO_2$ as plasticizer during the HME process in a 18 mm twin screw

extruder by determining the minimal temperature at which the maximum torque of the extruder was reached with and without injecting $CO_2$. In studies performed with pure polymer excipients (placebos) a decrease in minimum temperature for PVP-VA, Eudragit® E100 (EPO) and EC of 30°, 15° and 65 °C, respectively (Verreck et al. 2006b) was observed. The same study was performed using two binary systems: Itraconazole / EC (Verreck et al. 2007) and Itraconazole / PVP-VA (Verreck et al. 2005). In the former case the minimum processing temperature was decreased by 30° and 65°C and in the latter case by 5° and 10 °C, depending on API loading.

Verreck et al. (Verreck et al. 2006a) used $CO_2$ as a fugitive plasticizer during compounding of p-Amino salicylic acid – which is highly sensitive to thermal degradation – with EC in an 18 mm twin screw extruder. The authors observed that through a conventional HME process, 17 % of the API decomposed during compounding, but by using $CO_2$ as fugitive plasticizer the processing temperatures were reduced and the amount of decomposed API was reduced to 5 %.

Other evidence of the plasticizing effect of $CO_2$ in pharmaceutical materials can be found in the literature. Nikitine et al. (Nikitine et al. 2010) observed a 27 – 43 % reduction in torque by injecting $CO_2$ when extruding EPO in a 30 mm single screw extruder. Nagy et al. (Nagy et al. 2012) also observed a decrease in torque of 7 to 20 % by using $CO_2$ as PBA during compounding of the binary system of Carvedilol and EPO in a 30 mm single screw extruder. Lyons et al. (Lyons et al. 2007) also observed a decrease in toque and die pressure upon $CO_2$ injection in a 16 mm co-rotating twin screw extruder.

### 2.3.2 Floating Oral Dosage Forms

Gastroretentive drug delivery systems, with up to 6 h of sustained release, are required for some orally administered APIs. Some drugs must be absorbed in the stomach or upper section of the intestine due to either therapeutic reasons or to instabilities of the API at higher pH values (Nakamichi et al. 2001; Streubel et al. 2003; Fukuda et al. 2006). Floating dosages, using polymeric foams have been studied for this application.

Fukuda et al. (Fukuda et al. 2006) produced floating oral dosages by foam extrusion in a single screw extruder, using 5 - 10 wt% of sodium bicarbonate as CBA. The polymeric matrix used for the study was Eudragit® RS, an ionic acrylic based co-polymer which is highly hygroscopic but does not dissolve in aqueous solution or body fluid, but only swells. Two model APIs were used in order to evaluate two different oral dosage systems: (1) a miscible system using chlorpheniramine maleate (CMP), and (2) an immiscible system using acetohydroxamic acid (AHA). The foamed extrudates produced had average cell size of ~200 μm and densities in the range 0.8 - 0.6 g/cm$^3$. These foamed dosages maintained their buoyancy for 24 h in an acid aqueous solution. API release profiles obtained for all samples (foamed and un-foamed) showed sustained API release in a 24 h period. Nonetheless, the miscible system showed an increase in release rate upon foaming (approximately 80 % of CMP was released from the foamed sample in 24 h whereas only approximately 40 % from the un-foamed sample). In contrast, no appreciable variation was observed for the immiscible system. The influences of cell size and foam density on API's release profiles were not explored.

Nakamichi et al. (Nakamichi et al. 2001) used foam extrusion with water as PBA to produce floating dosages of Hydroxypropyl methylcellulose acetate succinate

(HPMCAS), an enteric polymer (i.e. soluble only in aqueous solution with pH 5 or higher), containing nicardipine hydrochloride (NH) as the model drug. Compounding and foaming was conducted in a co-rotating twin screw extruder. In addition, Calcium phosphate dehydrate (CP) was added to the formulation as nucleating agent. Closed-cell foams were produced with cell size in the range 1-350 μm and porosities ranging from 5 % up to 72 %. The porosity as well as the average cell size increased as the CP concentration increased. Buoyancy and dissolution tests were conducted in aqueous solution with pH 1.2. An increase in initial buoyancy was observed as the porosity increased; however, for high CP loading the dosage form disintegrates due to CP's dissolution and its buoyancy was lost. Cell size showed negligible effect over the release profile of the API.

Streubel et al. (Streubel et al. 2003) developed a floating oral dosage by incorporating into the formulation foamed Polypropylene (PP) powder. Tablets were produced by direct compression of HPMC, the API, foamed PP particles and other excipients. The tablets showed good floating behavior for 8 hours, but it was lost afterwards due to dissolution of the HPMC phase.

### 2.3.3 Foams as Intermediate Products

While for gastroretentive applications the foamed samples is the final product, in some other cases the foamed material is just an intermediate product during the manufacture of the final dosage form. Two approaches can be found in the literature for foamed intermediate products: milling of HME products and API infusion. Since the former is of greater interest to the pharmaceutical industry, milling of foamed extrudates will be discussed in more detail.

After HME compounding, the extrudates are often milled. The final dosage form is produced by pressing the ground material into tablets, filling capsules with it or using the particles in suspension for liquid formulations. However, extrudates tend to be very difficult to mill into suitable particle sizes with narrow distribution (Verreck et al. 2005; Verreck et al. 2006b; McKelvey et al. 2010; Brown et al. 2011).

Verreck et al. (Verreck et al. 2005; Verreck et al. 2006b; Verreck et al. 2007) used foamed extrudates to improve the milling efficiency of HME products. The studies were carried out using a pure polymer excipient (i.e. placebos) (Verreck et al. 2006b), and two polymer-API pairs (Verreck et al. 2005; Verreck et al. 2007). Compounding and foaming was carried out in an 18 mm co-rotating TSE, employing $CO_2$ as PBA. The milling efficiency was determined by grinding 25 g of each extrudate for 30 s with a Bamix blender; the resulting particle size distributions were determined through a vibrating sieve method. In all cases, the particles produced by grinding foamed extrudates had smaller measured average particles size, higher porosity and bigger specific surface area than the particles produced from un-foamed extrudates, thus, improving the milling efficiency of drug products.

In the cases of the polymers alone (Verreck et al. 2006b) and the Itraconazole / EC binary system (Verreck et al. 2007), API release rates of milled foams were faster than that of the ground un-foamed extrudates. Faster API release rates were a consequence of smaller particle size with higher surface area and porosity.

Surprisingly, for the system Itraconazole / PVP-VA Verreck et al. (Verreck et al. 2005) observed that API release from particles obtained by milling the foamed extrudates had much slower release rate than the ones obtained from milled un-foamed extrudates.

Since water absorption was very fast for the milled foams, particle agglomeration took place slowing the API release rate.

On the other hand, Nagy et al. (Nagy et al. 2012) observed only a slight faster API release for ground foams compared to the particles produced by milling un-foamed extrudates. The small enhancement in the *in vitro* performance was attributed to higher surface area in the case of the milled foams.

In summary, it has been shown in the literature that the milling process of foamed extrudates is more efficient than that of un-foamed extrudates, and as expected, it yields smaller particles with higher surface area and porosity. However, a direct relationship between particle size distribution and cell size distribution has not been established. Neither a target nor optimal cell size and density have been defined.

Another application of polymeric foams as intermediate product was explored by Hsu et al. (Hsu et al. 1996; Hsu et al. 1997). Lyophilization (i.e. freeze-drying technology) was used to produce low density open cell foams of PLGA. Then the API (Isoniazid, INH) was incorporated by immersing the foam in an INH aqueous solution. Following drying, the drug impregnated foam was compression molded into the dosage form.

### 2.3.4 Foams to Increase API Release Rate

One of the challenges of the HME process, which is inherent to the process, is that the extrudates have very low porosity. This may slow down penetration of body fluids into the sample and, thus, hinder API release (Andrews et al. 2010). Thus, foaming could be used to introduce porosity into the matrix and facilitate dissolution.

Andrews et al. (Andrews et al. 2010) observed that the release rate of Celecoxib (CX) from PVP, a water soluble polymer, was significantly increased upon foaming; the time for 100% release was reduced in half . Compounding was carried out in the conical twin screw extruder MiniLab. Foams were produced through a batch foaming process of the extrudates employing $ScCO_2$ as PBA. The authors did not provide information regarding average cell size or foam densities.

Verreck et al. (Verreck et al. 2007) also observed an increase in release rate for the Itraconazole / EC system upon foaming. By the end of the dissolution test the amount of API released from the foamed samples was approximately 11-fold higher than that from un-foamed samples.

Lyons et al. (Lyons et al. 2007) also observed an increase in API release rate by using foamed samples. HME and foam extrusion of a ternary system comprising Carvedilol, Polyethylene oxide (PEO) and EPO was carried out in a 16 mm co-rotating twin screw extruder, with $CO_2$ as the PBA. However, the morphologies of the cellular structures produced were not shown or analyzed.

Since API's release rate can be increased by foaming, then this process could be used in the manufacture of orally disintegrating dosages (ODT). These types of dosages must disintegrate within 30 s in the buccal cavity (FDA 2008) and are of great interest in pediatrics or for adults when swallowing is difficult (Clarke 2005; Banbury and MacGregor 2011). Commercially used ODT manufacturing techniques based on freeze-drying technology include: Zydis®, Lyoc®, Quicksolv™ and Pharmafreeze (McLaughlin et al. 2009; Badgujar and Mundada 2011; Banbury and MacGregor 2011). Freeze-drying technology results in highly porous open cell structures with extremely fast disintegration

times; in the case of dosages manufactured by Zydis® technology this has been reported to be between 0 and 2 s (McLaughlin et al. 2009). However, this technology has some limitations in terms of drug loading and friability of the dosage form (McKelvey et al. 2010; Badgujar and Mundada 2011).

McKelvey et al. (McKelvey et al. 2010), explored the used of foam injection molding to produce fast dissolving dosage forms for pediatric applications. The *in vitro* dissolution performance of the foamed dosage forms was compared to conventionally compressed tablet. The authors found that through foam injection molding it was possible to attain the same dissolution performance as compressed tablets, but with a 40 % smaller dosage. However, the release times were not in the 30 s requirement for ODT applications.

Clarke also proposed the use of foam injection molding to produce these "flash-dissolving" dosage forms (Clarke 2005). Similarly, the patent by Breitenbach and Baumgartl (Breitenbach and Baumgartl 2000) proposes the use of foam extrusion process to produce "flash-dissolving" foamed dosages. As an example the authors reported that API release was 30-fold faster upon foaming. The model API used was Ibuprofen and the carrier in a mixture of PVP and PVAc (Polyvinyl acetate); $ScCO_2$ was used as the PBA.

## 2.4 Brief Overview on the Applications of Supercritical Fluids in the Pharmaceutics

Since many of the foaming processes described here use $ScCO_2$ as the PBA it is of interest to briefly review the applications of supercritical fluids in pharmaceutical applications. Some of its applications include: gas anti-solvent crystallization (GAS or SAS) and particle manufacture.

The use of $ScCO_2$ for the GAS process is shown schematically in Figure 2.8. Through this technology the API is first dissolved in a good solvent, then the supercritical fluid is injected enabling API crystallization and as a result it precipitates; then, the system is drained and the crystals are dried (Moribe et al. 2008; Brittain 2009). Other anti-solvent approaches include: SEDS, solution-enhanced dispersion by supercritical fluids; and ASES, aerosol solvent extraction system (Moribe et al. 2008). These anti-solvent processes have been used to produce specific API polymorphs and particles composed of an API and a polymeric excipient (Sethia and Squillante 2004; Davies et al. 2008; Moribe et al. 2008).

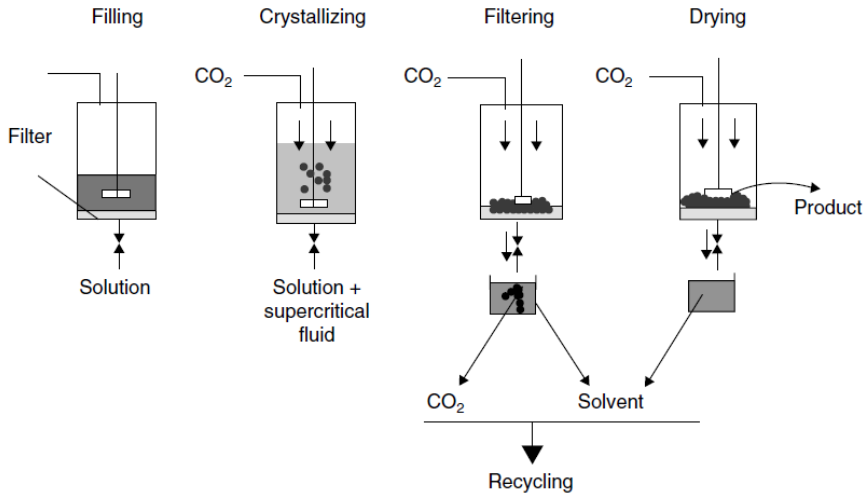


**Figure 2.8** Schematics describing gas anti-solvent crystallization (GAS) process. Source: (Brittain 2009)

Other processes that use supercritical fluids are rapid expansion of supercritical fluid (RESS) and particles from gas-saturated solutions (PGSS). In both cases the API is dissolved in the supercritical fluid followed by depressurization as the fluid is sprayed through a nozzle producing drug particles. These techniques are used as a means to reduce API particle size, manufacture of nanoparticles and induce API polymorphic changes (Davies et al. 2008; Moribe et al. 2008).

# CHAPTER 3

# EXPERIMENTAL

## 3.1 Materials

### 3.1.1 Active Pharmaceutical Ingredients (APIs)

Two model Active Pharmaceutical Ingredients (APIs), Indomethacin (INM) and Carbamazepine (CBZ) were evaluated. Their chemical structures are presented in Figure 3.1 and a summary of their properties in Table 3.1.

(a) (b)

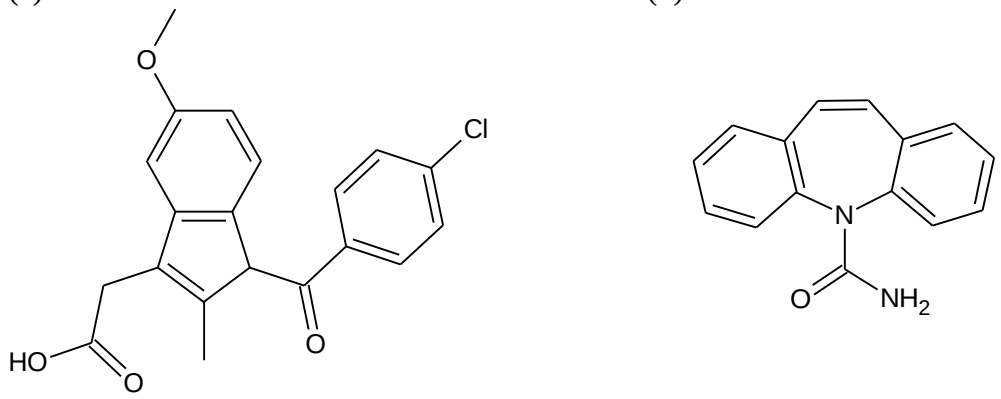


**Figure 3.1** Chemical structures of: (a) INM and (b) CBZ.

INM, purchased from Spectrum Chemical and Laboratory Products (Gardena, CA), is an acidic nonsteroidal anti-inflammatory drug (NSAID), with pKa value of 4.5 (Yazdanian et al. 2004). The carboxylic group gives INM the capacity to form hydrogen bonds with itself and with other molecules. Due to the ionizable character of carboxylic group its solubility in aqueous solution is pH-dependent, being extremely low (1 mg/L) at a pH 1.2 and higher at neutral or slightly basic pH (1300 mg/L at pH 7.4) (Yazdanian et al. 2004).

**Table 3.1** Summary of Some of the Properties of INM and CBZ

| Property | INM | CBZ |
|---|---|---|
| Melting temperature [°C] | Polymorph dependent | Polymorph dependent |
| Glass transition temperature [°C] | 46.3±0.1 | 53[c]-56[d] |
| MW [g/mol] | 357.79 | 239 |
| Solubility parameter [$MPa^{1/2}$] | 22.1[a] | 26.2 |
| LogP | 3.4[b] | 2.3[b] |

Source: [a](Forster et al. 2001), [b](Wishart et al. 2012), [c](Patterson et al. 2005), [d](Li et al. 2000)

INM can exist in either of two crystalline polymorphic forms (namely γ-form and α-form) or in the amorphous state. γ-INM is the most stable form, while α-form and amorphous INM are metastable; the latter being the less stable state. However, crystallization of INM from its amorphous state into either γ or α forms is very slow and temperature dependent; furthermore, it may exist as a glass by itself for several days (Andronis and Zografi 2000). Table 3.2 summarizes the properties of its two crystalline forms; the differences in density and melting behavior result from the differences in molecular packing within their unit cells. In the case of γ-INM two molecules are packed in the unit cell by forming cyclic dimmers through hydrogen bonds between carboxylic groups. On the other hand, three molecules are packed into each unit cell in α- INM (Taylor and Zografi 1997; Andronis and Zografi 2000). Since molecular interactions are weaker due to looser packing in the latter case; thus α-INM has lower melting point and melting enthalpy.

**Table 3.2** Main Properties of the Two Crystalline Forms of INM

| Property | γ- INM | α- INM |
|---|---|---|
| Melting temperature [°C] | 161* | 155 |
| Melting Enthalpy [J/g] | 116* | 91 |
| Density [g/cm$^3$] | 1.37 | 1.43 |
| Crystal system | triclinic | monoclinic |

Source: (Andronis and Zografi 2000). *Experimentally determined values in this dissertation

Carbamazepine (CBZ), kindly donated by BASF, was also used as model API. This drug substance is used as anticonvulsant to treat epilepsy and trigeminal neuralgia (Matsuda et al. 1994; Rustichelli et al. 2000; Brittain 2009). CBZ has been reported to have several polymorphs: triclinic, trigonal, and two monoclinic forms (Otsuka et al. 1999; Rustichelli et al. 2000; Ugaonkar et al. 2007; Brittain 2009), their differences are summarized in Table 3.3. Solid-solid transitions between polymorphs can occur upon heating (Lowes et al. 1987; Rustichelli et al. 2000; Brittain 2009). Among all forms, monoclinic CBZ with four molecules per unit cell is the most stable form at room temperature (Brittain 2009); it also provides the highest bioavailability (Kipouros et al. 2006).

**Table 3.3** Summary of CBZ Polymorphs and their Properties

| Property | Crystal System | | | |
|---|---|---|---|---|
| | Triclinic | Trigonal | p-Monoclinic | c-Monoclinic |
| $T_m$ [°C] | 192 | 183 | 176 | Not reported |
| Molecules in unit cell | 4 | 18 | 4 | 8 |
| Density [g/cm$^3$] | Not reported | 1.235 | 1.35 | 1.31 |

Source: (Brittain 2009)

CBZ is considered a BSC Class II API (i.e. a low solubility, high permeability compound) (Sethia and Squillante 2004). Its solubility in water is limited (170 mg/L at 25°C) and is reported to have a low absorption rate when administrated orally due to its slow dissolution rate (Moneghini et al. 2001; Ugaonkar et al. 2007).

### 3.1.2 Polymer Excipients

Two polymer excipients are used in this study Soluplus® (PVCap-PVAc-PEG) and Eudragit® EPO. Their chemical structures are presented in Figure 3.2 (a) and (b), respectively, and a summary of their properties is presented in Table 3.4.

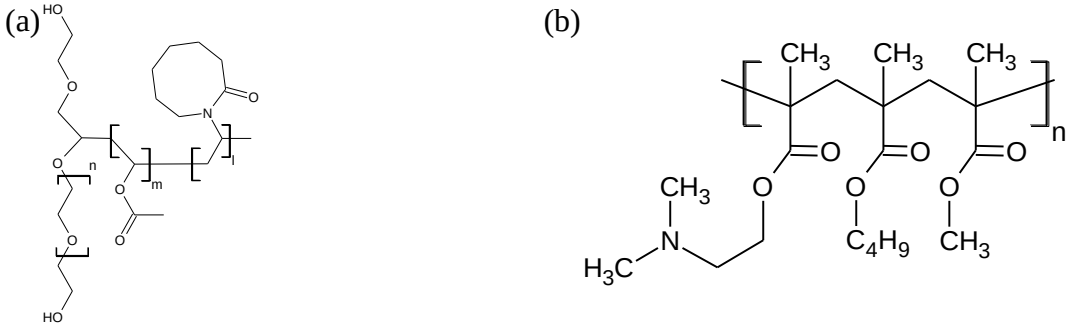


**Figure 3.2** Chemical structure of: (a) Soluplus® and (b) Eudragit® EPO.

PVCap-PVAc-PEG, donated by BASF (Tarrytown, NY), is an amorphous polyvinyl caprolactam-polyvinyl acetate-polyethylene glycol graft copolymer (molar ratio 57:30:13) (Kolter et al. 2010). Polyethylene glycol (PEG) is the backbone while polyvinyl caprolactam (PVCap) and polyvinyl acetate (PVAc) are the branches. Even though it is a graft copolymer it is reported to have a single glass transition temperature ($T_g$) at 73 ± 2°C.

This polymer was specifically developed by BASF as polymeric excipient to be used in pharmaceutical HME. It has pH independent solubility in aqueous solution, and a critical micelle concentration of 7.6 mg/L (BASF 2010). Its capability of forming

micelles at temperatures close to body temperature (37 °C) results from the PVCap branches; the lower critical solution temperature of this polymer in water can be tailored by its molecular weight (Meeussen et al. 2000). Since PVCap-PVAc-PEG is capable of acting as a surfactant (by forming micelles in aqueous solution) it can increase the apparent solubility of numerous APIs such as Carbamazepine, Griseofulvin, Cinnarizine, Clotrimazole, and Estradiol, among others (Hardung et al. 2010) and therefore prevent drug precipitation after release. In addition, it has the potential to solubilize, during HME, multiple drugs with diverse functional groups due to its dual lipophilic and hydrophilic character.

**Table 3.4** Summary of Some Important Properties of PVCap-PVAc-PEG and EPO

| Property | Material | |
|---|---|---|
| | PVCap-PVAc-PEG | EPO |
| $T_g$ [˚C] | 73±2 | 44.6±0.9 |
| $T_m$ [˚C] | - | - |
| Melting enthalpy [kJ/mol] | - | - |
| Onset degradation temperature in $N_2$ [˚C] | 300 | 276[b] |
| Onset degradation temperature in dry air [˚C] | 293 | - |
| Solubility parameter [$MPa^{1/2}$] | 19.4[a] | 18.53[b] |
| MW [g/mol] | ~118,000[a] | 47,000[b] |
| Density [$g/cm^3$] | 1.0819 | 1.09[c] |
| Bulk density [$g/cm^3$] | 0.6 | - |

Source: [a] (Kolter et al. 2010), [b](Liu 2010), [c](Ha 2011),

EPO, donated by Evonik Degussa (Piscataway, NJ), is an amorphous cationic thermoplastic poly(butyl methacrylate-co-(2-dimethylaminoethyl) methacrylate-co-

methyl methacrylate) with molar ratio 1:2:1. This polymer has pH dependent solubility in aqueous media; while soluble in acid conditions, at pH above 5.0 it only swells and is permeable but does not dissolve (Rowe et al. 2009). Therefore, this excipient is a great candidate for taste masking applications - since it will not dissolve in the buccal cavity - and for targeting API release to the stomach.

### 3.1.3 Carbon Dioxide ($CO_2$)

Supercritical $CO_2$ ($ScCO_2$) with 99% purity was purchased from GTS-Welco (Allentown, PA). The phase diagram of $CO_2$ is shown in Figure 3.3. Its critical point is 31°C and 7.37MPa (Throne 2004; Sauceau et al. 2011).

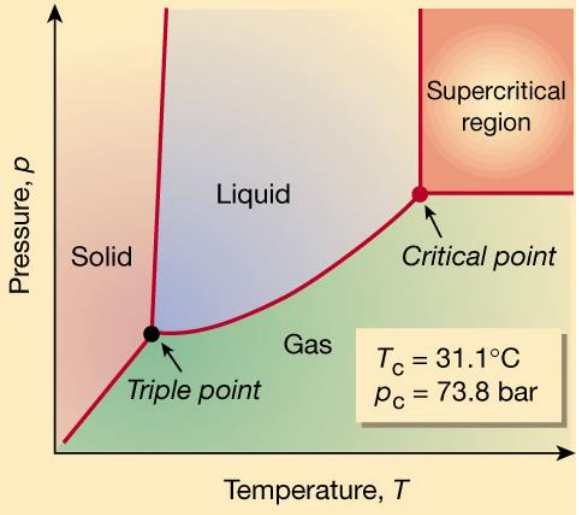


**Figure 3.3** Phase diagram of $CO_2$. Source: (Leitner 2000).

## 3.2 Sample Preparation

### 3.2.1 Hot Melt Mixing (HMM)

A particulate physical mixture (PM) of PVCap-PVAc-PEG and 30 wt% of INM was prepared using a mortar and pestle, and used as the feed material. HMM was carried out

in a batch mixer Brabender FE-2000 (C.W. Brabender Instruments Inc., South Hackensack, NJ) with counter- rotating screws operating at 50 rpm, 130 °C for 9 min. The batch mixer was electrically heated and cooled by air.

### 3.2.2 Hot Melt Extrusion (HME)

Compounding through HME of the binary mixtures described in Table 3.5 was carried out in a 16mm co-rotating twin screw extruder, the Nano16, manufactured by Leistritz (Somerville, NJ). The screws diameter was 16 mm and the length to diameter ratio (L/D) was 26. The extruder's barrel is divided into five segments as shown schematically in Figure 3.4. The feeding zone is water cooled; the remaining zones are electrically heated and cooled with air. Physical mixtures were fed as powders using a volumetric single screw feeder. The temperature settings, feeding rates, screw speeds and die size used are summarized in Table 3.6.

**Table 3.5** Composition of the Binary Systems Evaluated

| System | Polymer Excipient | API | Polymer : API ratio |
|---|---|---|---|
| S10INM | PVCap-PVAc-PEG | INM | 9:1 |
| S30INM | PVCap-PVAc-PEG | INM | 7:3 |
| S50INM | PVCap-PVAc-PEG | INM | 1:1 |
| S75INM | PVCap-PVAc-PEG | INM | 25:75 |
| S15CBZ | PVCap-PVAc-PEG | CBZ | 85:15 |
| EPO30INM | EPO | INM | 7:3 |

The screw elements of the Nano 16 have a tri-lobal design, with outer to inner diameter ratio (OD/ID) of 1.18. As shown in in Figure 3.4 the screw configuration used

consisted of only forward conveying elements with one mixing zone of 30° conveying kneading blocks located at 15 L/D.

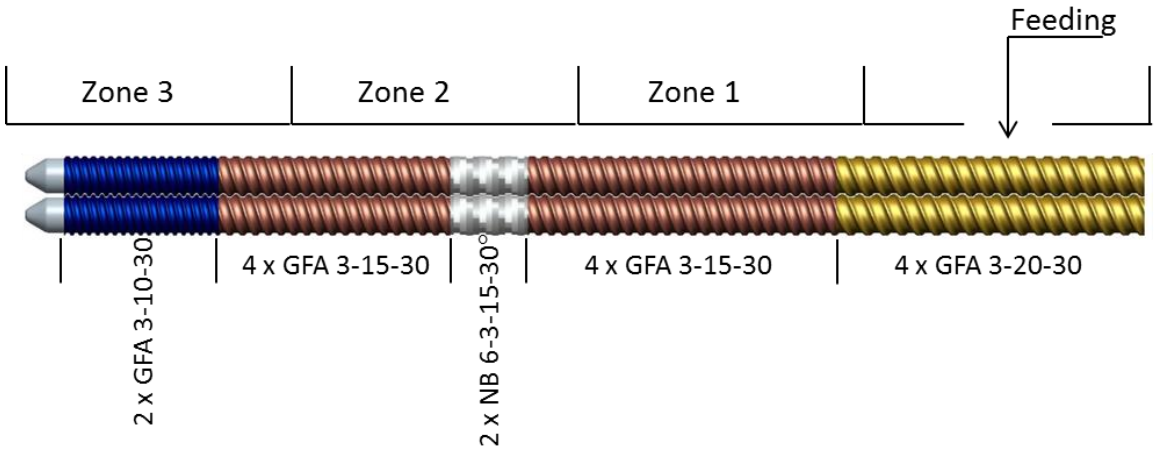


**Figure 3.4** Schematics of the screw configuration used for HME. GFA = conveying fully-intermeshing element x-yy-zz (x = number of flights, yy = pitch, zz = element length in mm). KB =kneading block x-y-zz-vv (x = number of kneading segments, y = number of flights, zz = length in mm, vv = phase angle of the individual kneading segment). See Appendix A for more details on the screw elements.

**Table 3.6** Summary of the HME Conditions Used

| System | Temperature [°C] | | | | Screw Speed | Feeding Rate | Die Diameter |
|---|---|---|---|---|---|---|---|
| | T1 | T2 | T3 | Tdie | [rpm] | [g/min] | [mm] |
| S+INM* | 120 | 130 | 130 | 138 | 200 | 4.7 | 1 |
| S15CBZ | 120 | 130 | 130 | 125 | 100 | 4.5 | 2 |
| EPO30INM | 110 | 130 | 140 | 138 | 200 | 3.3 | 2 |

*S10INM, S30INM, S50INM and S75INM

### 3.2.3 Compression Molding

After HMM and HME the processed materials were milled in a laboratory coffee grinder and molded into disks by compression molding. Four different dimensions were used through the study: 5∅ x 1 mm (HMM samples), 19∅ x 0.3 mm (release mechanism studies, HME samples), 16∅ x 1 mm (effect of foam morphology on release/dissolution rates, HME samples) and 25.4∅ x 1mm. In all cases the following molding cycle was used: 1 min at molding temperature without load, 3 min at molding temperature under load and finally 2 min cooling under load. The molding temperatures and loads used for each binary system are summarized in Table 3.7.

**Table 3.7** Compression Molding Conditions Used

| Binary system | Temperature [°C] | Load [kN] | Disk Dimensions [mm] |
|---|---|---|---|
| S30INM (HMM) | 100 | 44 | 5∅ x 1 |
| S30INM (HME) | 120 | 44 | 16∅ x 1, 19∅ x 0.3 & 25.4∅ x 1 |
| EPO30INM | 100 | 44 | 19∅ x 0.3 |
| S15CBZ | 100 | 44 | 19∅ x 0.3 |
| PVCap-PVAc-PEG | 100 | 44 | 16∅ x 1 |

### 3.2.4 Batch Foaming

Compression molded disks were foamed through a batch foaming process employing $ScCO_2$ at 10.34 MPa as the physical blowing agent (PBA). The experimental apparatus used is schematically shown in Figure 3.5. The compression molded samples were placed inside the mold cavity which was already preheated to the foaming temperature;

air in the cavity was evacuated using a vacuum pump for 4 min. Following the application of vacuum, the PBA was injected into the vessel's cavity and the system was pressurized for pre-established dwelling times to allow for the dissolution of the PBA in the polymer/API disk. Then, the pressure in the cavity was suddenly released, abruptly causing a thermodynamic instability which induces very rapid cell nucleation. Foaming temperatures and dwelling times for each of the sample sizes used are summarized in Table 3.8. It should be mentioned that the mold was not cooled during depressurization. Also due to the hygroscopic character of the polymer excipients, all the samples were dried under vacuum at 60 °C for 12 h prior to foaming.

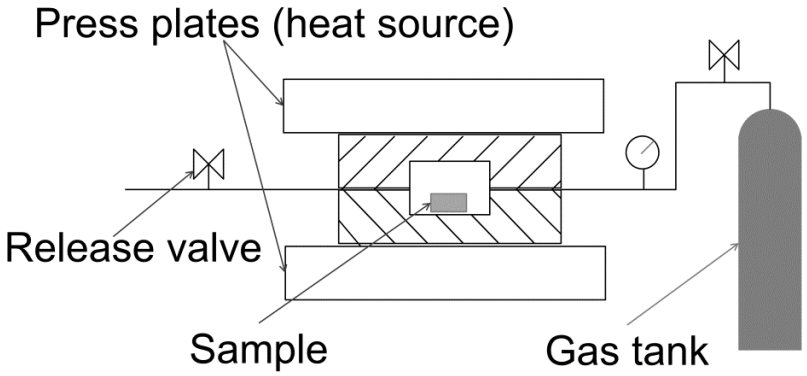


**Figure 3.5** Schematic representation of the batch foaming device.

**Table 3.8** Batch Foaming Conditions Used

| System | Disk dimensions [mm] | Foaming Temperature [°C] | Dwelling Time [min] |
|---|---|---|---|
| PVCap-PVAc-PEG | 16∅ x 1 | 90 | 15 |
| S30INM | 16∅ x 1 | 100 | 15, 30 & 60 (F15, F30 & F60) |
| S30INM | 19∅ x 0.3 | 100 | 15 |
| EPO30ONM | 19∅ x 0.3 | 95 | 15 |
| S15INM | 19∅ x 0.3 | 110 | 15 |

### 3.2.5 Foam Extrusion

Compounding and foaming was carried out in a single step through Extrusion Foaming in a co-rotating fully intermeshing twin screw extruder with screws of 18 mm in diameter and 40 L/D manufactured by Leistritz (Somerville, NJ). The barrel was equipped with a die plate having eight capillaries of 0.8 mm diameter for forming eight extrudate strands. Excipient and crystalline INM particulates were independently fed using two feeders. Their feeding rates were set so as to produce foamed extrudates containing 30 wt% of drug loading. As shown in Figure 3.6, the extruder barrel was divided in eight zones. The first one (feeding zone) was continuously cooled with water, while the remaining seven zones were electrically heated and cooled with air to control their temperature. The adapter and die were electrically heated. Carbon Dioxide ($CO_2$) was employed as the physical blowing agent, and it was injected at 5.5 - 5.8 MPa at a barrel position 18 diameters downstream from the feed, as shown in Figure 3.6. The process conditions studied are presented in Table 3.9.

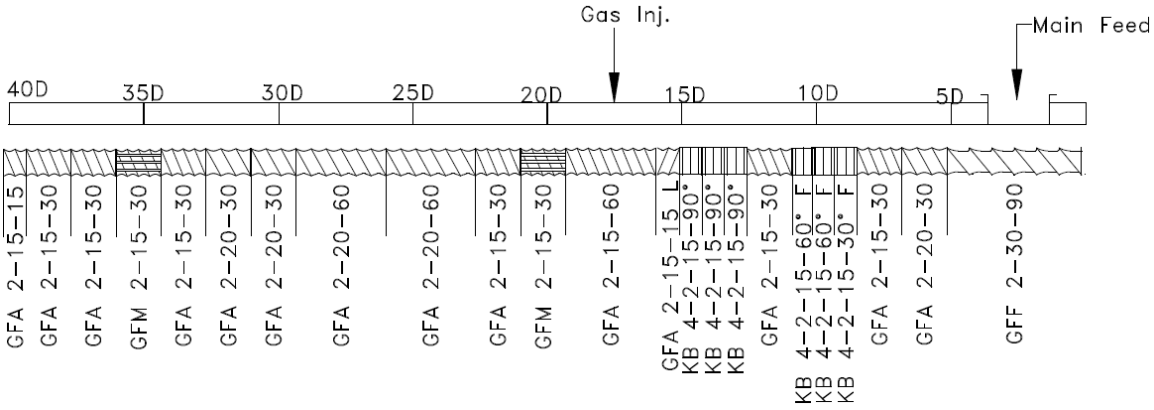


**Figure 3.6** Screw design used during foam extrusion experiments. GFF = conveying freely cut element, GFA = conveying free-meshing element, GFM = conveying mixing element x-yy-zz (x = number of flights, yy = pitch, zz = element length in mm). KB =kneading block x-y-zz-vv (x = number of kneading segments, y = number of flights, zz = length in mm, vv = phase angle of the individual kneading segment). See Appendix A for more details on the screw elements.

The 18 mm extruder screws were bilobal, and as shown in Figure 3.6 the screw configuration had one reverse conveying element prior to the gas injection site in order to create a melt hold-up, leading to a fully melt-filled section, which acts as a melt seal to prevent the pressurized gas escaping through the hopper. The extruder was also equipped with four mixing zones; the ones prior to the gas injection site were intended to complete the elementary processing steps of polymer melting, laminar mixing, and dissolution of API in the melt. The mixing zones after $CO_2$ injection were designed to promote dissolution of the gas in the melt and homogenization of the polymer-API-gas system.

**Table 3.9** Foam Extrusion Conditions Evaluated

| run | $\dot{m}$ [kg/h] | Temperature Profile [°C] | | | | | | | | | w/w % $CO_2$ |
|---|---|---|---|---|---|---|---|---|---|---|---|
| | | T1 | T2 | T3 | T4 | T5 | T6 | T7 | T8 (coupler) | T9 (die) | |
| 1 | 1 | 122 | 135 | 135 | 122 | 101 | 99 | 96 | 96 | 115 | 12 |
| 2 | 1.5 | 122 | 140 | 140 | 130 | 115 | 90 | 90 | 90 | 118 | 4 |

### 3.2.6 Milling of Extrudates

Foamed and un-foamed extrudates of the binary mixtures S30INM were milled in a laboratory coffee grinder. Batches of 20 g were ground for 25 s and collected for further analysis.

## 3.3 Characterization

### 3.3.1 Thermogravimetric Analysis (TGA)

The thermal stability of APIs and excipients was studied through TGA in a TA Instruments Q50 Thermogravimetric Analyzer (New Castle, DE). Two different studies were performed: ramp heating tests and isothermal tests. In the ramp heating studies, 5 – 10 mg of material was placed in an open aluminum pan, and heated from room temperature up to 550 ˚C at a heating rate of 10 ˚C/min, and recording the sample weight loss continuously. For the isothermal study, 5 - 10 mg of material in open aluminum pans was heated at 10 ˚C/min from room temperature to a desired-established temperature and held isothermally for 60 min, again recording sample weight loss continuously. Both ramp and isothermal TGA studies were conducted in a dry air atmosphere by purging the chamber with air at a flow rate of 40 mL/min.

### 3.3.2 Differential Scanning Calorimetry (DSC)

DSC analyses were carried out in a TA Instruments Q100 (New Castle, DE) equipment. Between 5 and 10 mg of material was placed in closed/sealed aluminum pans. Heating and cooling scans were performed at 10 °C/min between 0 and 165 °C. Samples were held isothermally for 3 min at 0 °C prior each heating scans in other to stabilize the temperature of the samples, and before the cooling scans a 3 min isothermal at 165 °C was used to erase thermal history of the material. Throughout the study, the equipment's chamber was blanketed with nitrogen ($N_2$) gas at a flow rate of 40 mL/min. Due to the hygroscopic character of the PVCap-PVAc-PEG, all samples containing this excipient were dried in a vacuum oven for 12 h at 60°C prior to DSC analysis.

First heating thermograms were used to assess the state of the APIs prior to processing and after undergoing different processing steps. Second heating thermograms were employed to evaluate the thermal properties of the materials after erasing their thermal history.

### 3.3.3 Modulated Temperature Differential Scanning Calorimetry (MTDSC)

MTDSC was carried out in a TA Instruments Q100 (New Castle, DE) equipment. Between 5 and 10mg of material was placed in closed aluminum pans. Samples were heated from 0 to 180 °C at 2 °C/min with a 60 s temperature modulation period and ± 1.25 °C amplitude. Throughout the study, the equipment's chamber was blanketed with nitrogen ($N_2$) gas at a flow rate of 40 mL/min.

### 3.3.4 Polarized Optical Microscopy (POM)

Polarized light optical microscopy was used to evaluate the presence of crystalline API after compounding. Samples drawn from the batch mixer and extrudates were observed with a Carl Zeiss microscope (Thornwood, NY) equipped with a digital camera Zeiss AxioCam MRc5 (5 MB-pixel resolution).

### 3.3.5 Fourier Transform Infrared (FT-IR) Spectroscopy

FT-IR analyzes were carried out in a PerkinElmer Spectrum One Spectrometer (Waltham, MA). Samples were analyzed in the 400 to 4000 $cm^{-1}$ wavelength region using Potassium Bromide (KBr) disks. The KBr disks were prepared by grinding together crystalline KBr and 1 wt% of sample into fine powders using a mortar and pestle, and then pressing the mixture into ~1 mm thick disks.

### 3.3.6 X-Ray Diffraction (XRD)

XRD analyzes were carried out in a Philips PW3040 X-Ray diffractometer (PANanytical Inc., Westborough, MA), using Cu Kα radiation (λ=1.54 Å) generated from a copper source operating at a power level of 40 KV and 40 mA. Samples were scanned over a 2θ range between 5 and 30°. Pure PVCap-PVAc-PEG and EPO were analyzed using disks prepared by compression molding; all other samples were analyzed while in powder form.

### 3.3.7 Scanning Electron Microscopy (SEM)

The morphology of cross-sections (or fracture surfaces) of foamed and un-foamed samples, as well as milled extrudates was examined with a LEO 1530 Field Emission Scanning Electron Microscope (Carl Zeiss SMT Inc., Peabody, MA). The fracture cross section of the samples was coated with a thin layer of carbon by sputtering to improve the conductivity and thus allow for the SEM images. The image processing software ImageJ was used to measure the cell sizes and wall thicknesses.

### 3.3.8 Particle Size Distribution (PSD)

Particle size distributions of milled samples were determined employing a laser diffraction particle size analyzer Beckman Coulter LS230 (Brea, CA). Analyses were conducted in the dry state and in triplicate.

### 3.3.9 *In Vitro* Dissolution Test

Dissolution tests were carried out in a Distek 2100A USP apparatus (North Brunswick, NJ) in triplicates. The analyses were conducted at 37.0 ± 0.5°C in 900 mL of deionized

water, pH 7.4 phosphate buffer solution, or pH 1.2 hydrochloric acid buffer solution. At pre-established time intervals 5 mL samples were withdrawn from the dissolution medium, filtered through polyvinylidene fluoride (PVDF) filters with pores size of 0.45 μm. Samples were then analyzed using a 10 mm quartz cell and an Agilent 8454 UV Spectrophotometer (Foster City, CA). The concentration of API or polymer in the solution was determined through a UV absorbance calibration curve. A summary of the in vitro dissolution test conditions used for the different samples is presented in Table 3.10.

It should be mentioned that the filters were not used during the dissolution tests of pure PVCap-PVAc-PEG; the polymer was trapped in the filter and no signal was observed during the UV analysis. In addition "sinkers" were used in the case of samples that showed tendency to float to assure full sample immersion.

**Table 3.10** Conditions Used for the *In Vitro* Dissolution Tests

| Sample description | Dosage Strength [mg] | Apparatus Type | Agitation Speed [rpm] | Dissolution Medium** | UV wavelength [nm] |
|---|---|---|---|---|---|
| PVCap-PVAc-PEG (un-foamed and foamed disks) | 240* | Paddle | 50 | Deionized water | 201 |
| PM S30INM in capsules | 24 | Basket | 100 | pHs 1.2 and 7.4 | 268 |
| HMM S30INM (un-foamed and foamed disks) | 24 | Basket | 100 | pHs 1.2 and 7.4 | 268 |
| INM in capsules | 24 | Basket | 100 | pHs 1.2 and 7.4 | 268 |
| HME S30INM (un-foamed and foamed disks) | 72 | Paddle | 50 | pH 7.4 | 319 |
| HME S30INM (un-foamed and foamed disks) | 35 | Paddle | 50 | pH 7.4 | 319 |
| INM in capsules | 25 | Paddle | 50 | pH 7.4 | 319 |
| Milled HME S30INM in capsules | 25 | Paddle | 50 | pH 7.4 | 319 |
| Milled foamed extruded S30INM | 25 | Paddle | 50 | pH 7.4 | 319 |
| HME S15CBZ (un-foamed and foamed disks) | 16 | Paddle | 50 | Deionized water | 284 |
| HME EPO30INM (un-foamed and foamed disks) | 33 | Paddle | 50 | pHs 1.2 and 7.4 | 319 |

*Reported weight corresponds to PVCap-PVAc-PEG's not to API. ** pH 1.2 corresponds to a hydrochloric acid buffer solution and pH 7.4 to a phosphate buffer solution.

### 3.3.10 Extrudate Content Uniformity

Content uniformity of the extrudates was evaluated by determining the concentration of INM in five randomly collected samples of each particular extrudate. Samples of 16 - 30 mg were placed in a 100-mL volumetric flask containing 10 mL of methanol and shaken until the extrudate was completely dissolved. Then the solution was diluted to the 100 mL volume with a pH 7.4 phosphate buffer solution. The API loading in the extrudates was calculated based in the concentration of INM in the solution. The latter was determined by UV spectroscopy at 319 nm using an absorbance calibration curve as mentioned in section 3.3.9 above.

### 3.3.11 Solubility of $CO_2$ in S30INM

Solubility measurements of $CO_2$ in S30INM were performed using HME and compression molded samples of 25.4∅ x 1mm. Two high pressure steel vessels with 45 $cm^3$ cavities, as shown in Figure 3.7, were used to saturate the samples with $CO_2$ for 24 h at different pressures and temperatures. The vessels were heated in an oven; oven temperature and pressure in each vessel were measured and recorded continuously during gas saturation. Samples were weighed and placed inside vessels preheated to the test temperature; air in the system was evacuated using a vacuum pump for 4 min. Following the application of vacuum, $CO_2$ was injected into the vessels' cavities and the system was pressurized. After 24 h of saturation, the vessels were depressurized and the samples extracted and weighed immediately. It should be mentioned that samples did not foam at any of the temperatures and pressures used, otherwise excessive gas loss would have occurred due to diffusion.

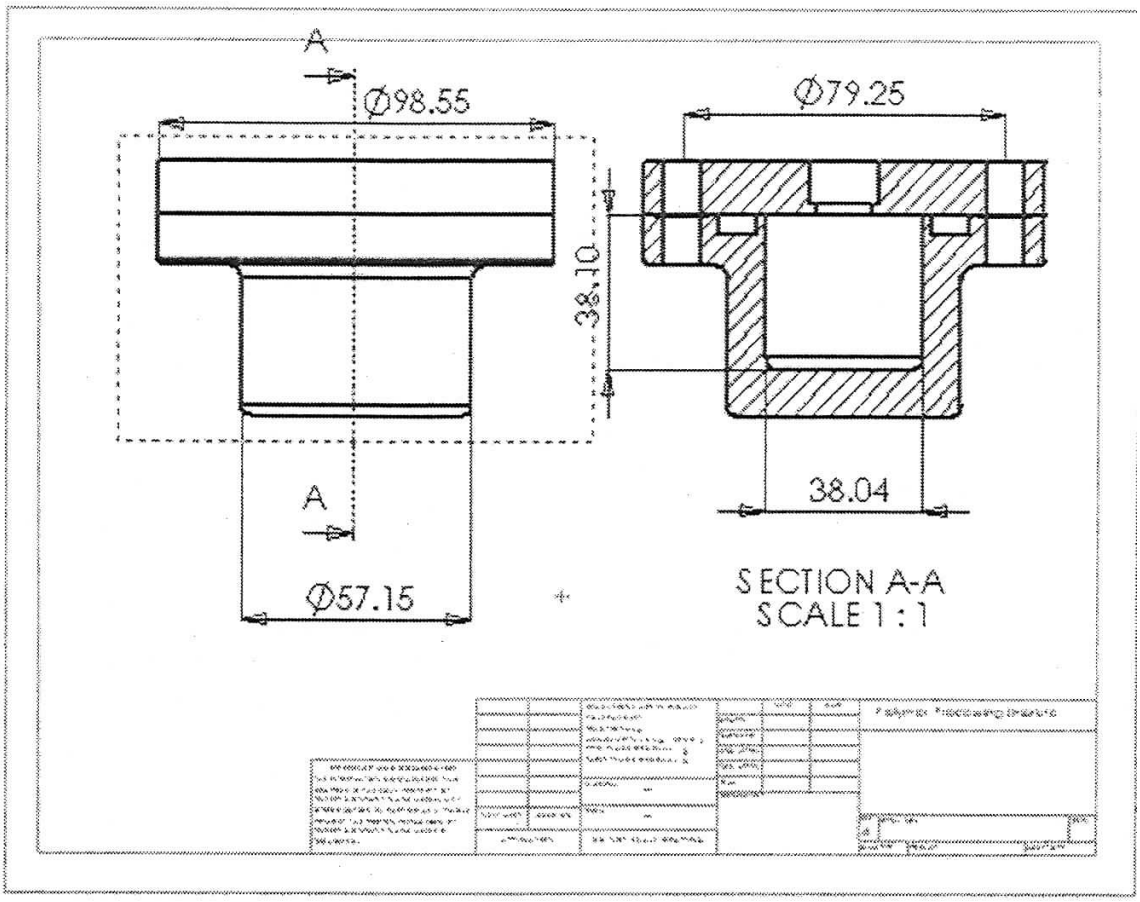


**Figure 3.7** Drawing of the high pressure vessels used for the $CO_2$ solubility measurements (Faridi and Todd 2007).

### 3.3.12 Long Term Physical Stability of the S30INM Binary System

The six month stability of the binary system S30INM was determined in open containers at 75 % RH and room temperature. Un-foamed compression molded disks of 16∅ x 1 mm and the corresponding foamed samples produced with dwelling times of 15, 30 and 60 min (F15, F30 and F60, respectively) were evaluated.

# CHAPTER 4

# RESULTS AND DISCUSSION

## 4.1 Solubility of INM in PVCap-PVAc-PEG

One of the objectives of this research is to gain fundamental understanding of the effects of the foaming process and cellular structure on the performance of amorphous solid solutions. Therefore, it is important to have a good understanding of the miscibility and solubility of the API in the polymer excipient, in order to assure that the binary system evaluated is a solid solution and not a solid dispersion.

The binary system comprising INM and PVCap-PVAc-PEG is expected to be miscible. The solubility parameter approach and criterion, although it has its limitations, suggests that this system is likely to be miscible. The difference in solubility parameters ($\Delta\delta$) between INM and PVCap-PVAc-PEG is 2.7 $MPa^{1/2}$. In general the smaller this difference the higher the probability for a given API-polymer pair to be miscible. Specifically, Greenhalgh et al. (Greenhalgh et al. 1999) proposed that miscible systems have a $\Delta\delta$ between 1.6 and 7.5 $MPa^{1/2}$, Forster et al. (Forster et al. 2001) on the other hand stated more conservatively that $\Delta\delta$ has to be less than 2.

In addition to the solubility parameter approach, by analyzing the chemical structures of INM and PVCap-PVAc-PEG [see Figures 3.1 (a) and 3.2 (b)] it is evident that these two molecules are capable of forming hydrogen bonds. The possibility of specific interactions between API and polymer could potentially facilitate drug dissolution in the polymer and furthermore provide shelf life stability to the binary blend.

INM has one proton donor (a hydrogen atom) and two proton acceptors (two oxygen atoms) in the carboxylic group. PVCap-PVAc-PEG has several proton acceptors capable of forming hydrogen bonds; oxygen atoms are available along the PEG backbone (see Figure 4.1 a) as well as along the branches of PVAc and PVCap (see Figures 4.1 b and c, respectively). Additionally, a nitrogen atom is also present on the PVCap braches but is most likely not accessible due to steric hindrance. In addition, by comparing the dipole moments of the bonds containing the proton acceptor atoms in the polymer (see Table 4.1) it is evident that the most favorable sites are the oxygen atoms forming double bonds with carbon (C=O) along the branches of PVCap and PVAc, followed by the other oxygen atoms in the PVAc branches and along the PEG backbone. A bond with larger dipole moment has a higher polarity and is thus more prone to donate or accept the positive charge or proton. This will also result in stronger hydrogen bonding. The effect of hydrogen bonding between INM and PVCap-PVAc-PEG on API release is presented in section 4.2.1.

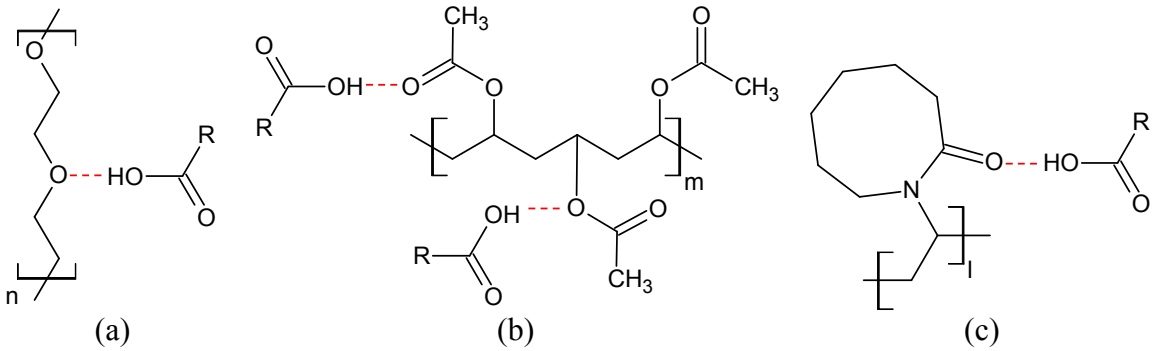


**Figure 4.1** Possible hydrogen bonds between INM and the different blocks of PVCap-PVAc-PEG terpolymer. (a) INM and PEG backbone, (b) INM and PVAc branch, and (c) INM and PVCap branch

**Table 4.1** Dipole Moments of Bonds of the Proton Donors and Acceptors in INM and PVCap-PVAc-PEG

| Bond | Bond Dipole Moment [D] |
|---|---|
| C=O | 2.4 |
| C-O | 0.86 |
| C-N | 0.22 |
| H-O | 1.53 |

Source: (Wade 1993)

The solubility of INM in PVCap-PVAc-PEG is evaluated through binary blends with drug loadings of 10, 30, 50 and 75 wt% prepared through HME and designated S10INM, S30INM, S50INM and S75INM, respectively. The morphological state of the API in the extrudates is determined by combining three characterization techniques described in the previous Chapter: POM, DSC and FT-IR. Since each technique has its own limitation and/or level of sensitivity in detecting the crystalline content, several techniques are combined in order to have a higher level of confidence regarding the morphological state of INM after HME. For example: POM is limited by the resolution of the microscope, which is diffraction-limited and thus features smaller that light's wavelength cannot be detected using this technique (Campbell et al. 2000). In the case of DSC, Leuner and Dressman (Leuner and Dressman 2000) observed the lowest detection limit for residual crystallinity is ~2 %.

POM allows detecting the presence of crystals in a sample through birefringence. Through this technique a specimen is placed between two polarizing plates oriented perpendicularly to each other resulting in no light transmission and a dark field. However, in the presence of a preferential orientation of the polymer chains, residual

stresses or two or more phases with different refractive indices, the light is scattered and bright spots or color fringes are evident (Campbell et al. 2000). Figure 4.2 shows the POM images of the extrudates containing 10, 30, 50 and 75 wt% of INM loading. Among all the samples bright particles are only visible throughout the highest API concentration sample, i.e. the S75INM. These bright particles correspond to INM crystals, suggesting that only S75INM extrudates have residual crystallinity after HME. In other words, INM was fully dissolved in PVCap-PVAc-PEG in the S10INM, S30INM and S50INM extrudates, but not in S75INM.

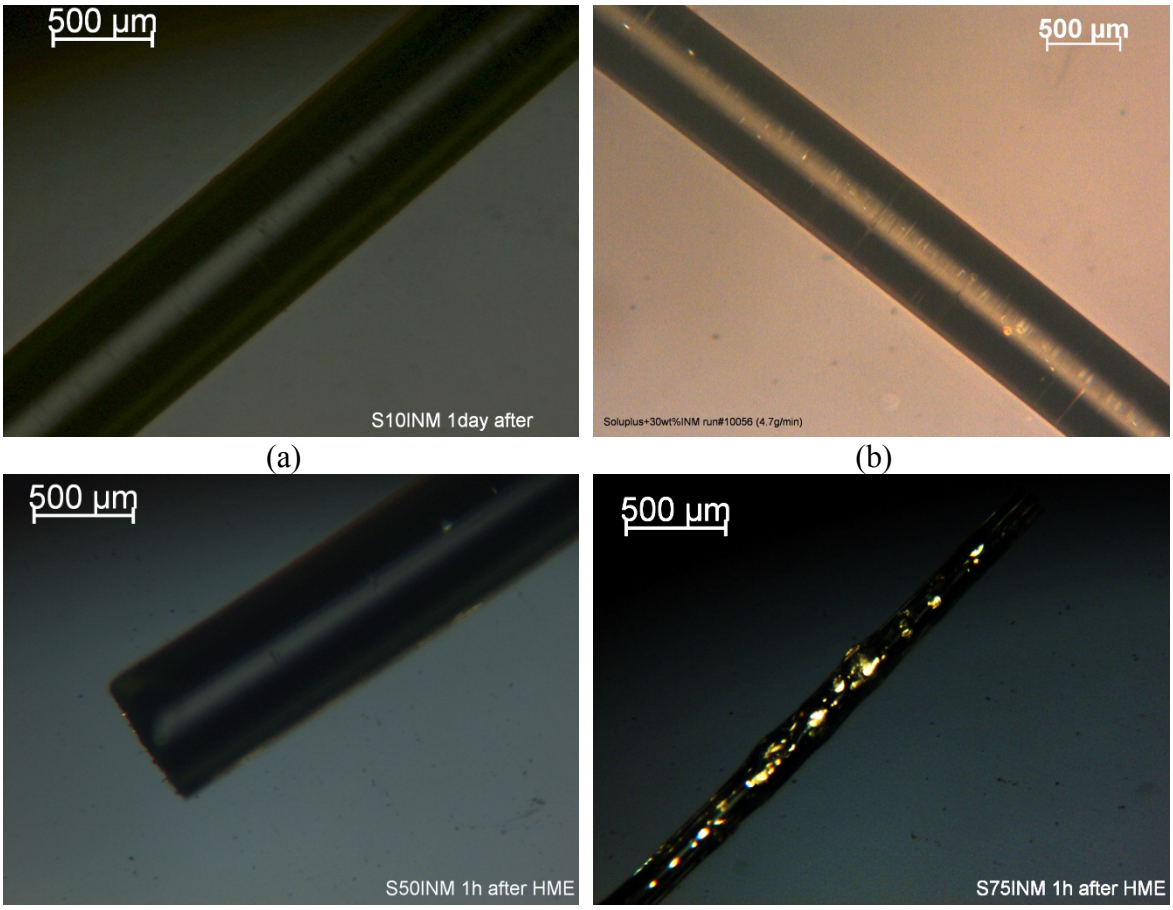


**Figure 4.2** POM images of four HME extrudates: (a) S10INM, (b) S30INM, (c) S50INM and (d) S75INM

FT-IR spectroscopy has been widely used to differentiate between drug polymorphs with high precision (Matsuda et al. 1994; Taylor and Zografi 1997; Otsuka et al. 1999; Rustichelli et al. 2000; Brittain 2009). As other spectroscopic techniques FT-IR allows the identification of different API polymorphs through shifts in the absorption frequency of specific functional group within the compound. These changes are caused by the intra-molecular coupling effect (i.e. interaction between vibrating groups) (Campbell et al. 2000). Packing or spatial arrangement of the API molecules differs among crystalline polymorphous and amorphous state, resulting in slight changes in the environment of a given functional group. Thus, the interactions between vibrating groups differ and hence the position of the absorption peak varies. In the case of INM, as summarized in Table 4.2, the locations of the absorption peaks of C=O in the carboxylic and benzoyl groups allow to clearly differentiate between amorphous, γ-INM and α-INM (Taylor and Zografi 1997).

**Table 4.2** FT-IR Positions and Assignments of INM Characteristic Absorption Peaks

| Assignment | Position of the Absorption Peaks [$cm^{-1}$] for | | |
|---|---|---|---|
| | γ-INM | α-INM | Amorphous INM |
| Asymmetric stretching of hydrogen-bonded acid C=O in a cyclic dimer | 1717 s | - | 1710 sh |
| Asymmetric stretching of hydrogen bonded hydrogen-bonded acid C=O | - | 1681 sh<br>1649 w | - |
| Stretching of non-hydrogen bonded acid C=O | - | 1735 w-m | 1735 sh |
| Stretching of benzoyl C=O | 1692 s | 1688 s | 1684 s |

s = strong, m = medium, w = weak, sh = shoulder. Source: (Taylor and Zografi 1997)

Figure 4.3 shows the FT-IR spectra of the four physical mixtures (PM) and the corresponding extrudates of S10INM, S30INM, S50INM and S75INM. By comparing the spectra of crystalline INM (γ-INM) with those of the physical mixtures [Figure 4.3 (a)], it is evident that in all cases INM is crystalline and in its γ-form. In all PMs, two sharp peaks can be clearly observed at 1692 and 1718 $cm^{-1}$. These peaks correspond to the benzoyl group stretching vibration and asymmetric stretching vibration of hydrogen-bonded acid C=O in a cycle dimer, respectively (see Table 4.2). In addition, the intensity of the peaks associated with INM increases with respect to the peaks associated with PVCap-PVAc-PEG as APIs concentration is increased. In S50INM and S75INM the absorption peaks of the polymer are no longer visible.

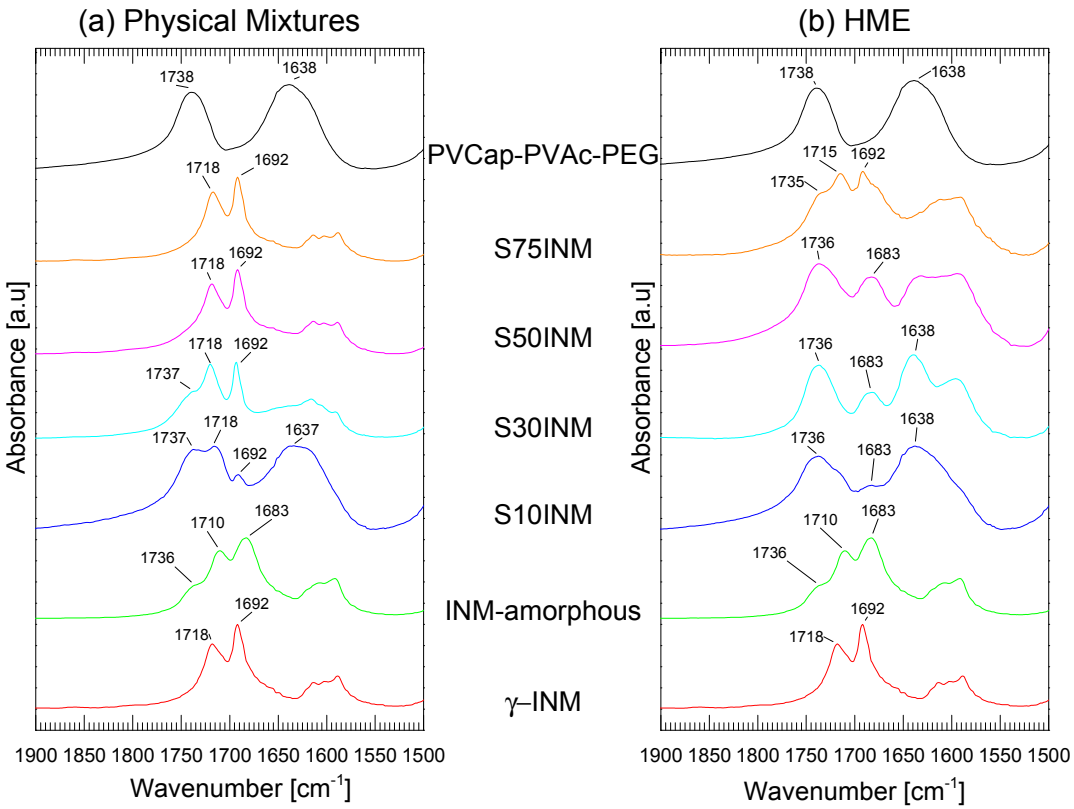


**Figure 4.3** Comparison of the FT-IR spectra of the binary systems S10INM, S30INM, S50INM and S75INM: (a) Physical mixtures and (b) HME extrudate samples. Spectra of pure PVCap-PVAc-PEG and INM (in its γ-form and amorphous state) are shown as reference.

In the case of the HME samples [see Figure 4.3 (b)], the peak at 1692 $cm^{-1}$ associated with γ-INM is no longer present in S10INM, S30INM and S50INM; but a new peak appears at 1683 $cm^{-1}$. This is a clear indication that INM is amorphous in these samples. The peak at 1683 $cm^{-1}$ can be observed in the spectrum of amorphous INM in Figure 4.3 and as indicated in Table 4.2 it corresponds to benzoyl group's stretching vibration in amorphous INM.

On the other hand, the spectrum of the S75INM extrudate shows evidence of the presence of both amorphous as well as crystalline INM. The characteristic peak of γ-INM at 1692 $cm^{-1}$ can be clearly seen. In contrast, the peak associated with asymmetric stretching vibration of hydrogen-bonded acid C=O in a cyclic dimer is observed at 1715 $cm^{-1}$, which is between the normal wavelengths of amorphous and γ-INM. This shift is due to the contribution of both forms.

Table 4.3 shows a summary of the DSC-determined thermal properties of the HME extrudates of the four binary systems. The properties of pure INM and PVCap-PVAc-PEG are also shown as reference. Figure 4.4 shows characteristic first heating thermograms of PVCap-PVAc-PEG and the HME samples S10INM, S30INM, S50INM and S75INM. In the case of INM, both first heating and second heating thermograms are shown. From the DSC analysis of the extrudates it is evident that S10INM, S30INM and S50INM have only one thermal transition during their first heating, corresponding to their glass transition temperatures. On the other hand, the S75INM extrudate showed two thermal transitions: a glass transition and endothermic peak in the high temperature region. These can be seen as an evidence of the presence of two phases, as observed through POM [see Figure 4.2 (d)].

**Table 4.3** Summary of the Thermal Transitions Determined from DSC First Heating of the Extrudates (DSC Thermal Analyses Were Performed in Triplicate).

| Sample | INM loading [wt%] | $T_g$ [°C] | $T_{edotherm,onset}$ [°C] | $T_{edotherm,peak}$ [°C] | $\Delta H_{endotherm}$ [J/g] |
|---|---|---|---|---|---|
| PVCap-PVAc-PEG | 0 | 73 ± 2 | - | - | - |
| S10INM | 10 | 68 ± 1 | - | - | - |
| S30INM | 30 | 62 ± 1 | - | - | - |
| S50INM | 50 | 61 ± 2 | - | - | - |
| S75INM | 75 | 53.0 ±0.2 | 147.4 ± 0.3 | 159 ± 1 | 6.7 ± 0.9 |
| INM | 100 | 46.33 ± 0.07* | 159.5 ± 0.2 | 161.0 ± 0.3 | 109 ± 5 |

*Value determined through DSC second heating

Besides S75INM, the only other sample that shows an endothermic peak during DSC first heating is INM (see Figure 4.4). These endothermic regions correspond to the melting of crystalline INM. In the case of pure INM [see Figure 4.4 (g)], the experimentally determined peak melt temperature is 161.0 ± 0.3 °C, which is in very good agreement with literature reported values for γ-INM (Otsuka et al. 2001). On the other hand, during INM melting in the S75INM extrudate, a depression in melting point is observed (12° and 2 °C depression in the onset and peak melting temperatures, respectively), as well as lower melting enthalpy compared to pure INM melting (see Table 4.3). Making the experimentally supported assumption that during the HME process the solubility limit of INM in the excipient was exceeded, then the depression in melting point may result from a reduction in size and or quality of the crystalline particles during HME, as a consequence of INM's partial dissolution. The lower melting enthalpy results from a smaller amount of crystalline INM in the samples. It should be noted that although enthalpy values are normalized by weight, this normalization corresponds to the total weight of the samples placed in the DSC pans, thus in the case of S75INM, out of

the total weight of the samples only 75 wt% corresponds to INM and not all of this amount is in crystalline form after the HME process; at least 66.67 % of INM was dissolved during processing (which corresponds to 50 wt% of INM loading).

In the case of S10INM, S30INM and S50INM the absence of an endothermic peak is indicative of the fact that the API was completely dissolved during the HME process. In addition, the results shown in both Figure 4.4 and Table 4.3 indicate that all HME extrudate samples have a single glass transition region with $T_g$ values between that of the polymer and the API. Lower $T_g$ of the extrudates than that of the pure polymer suggests that INM has been dissolved into the PVCap-PVAc-PEG during melt mixing, and that it acts as a plasticizer. Additionally, a single glass transition suggests one phase, thus, an amorphous solid solution.

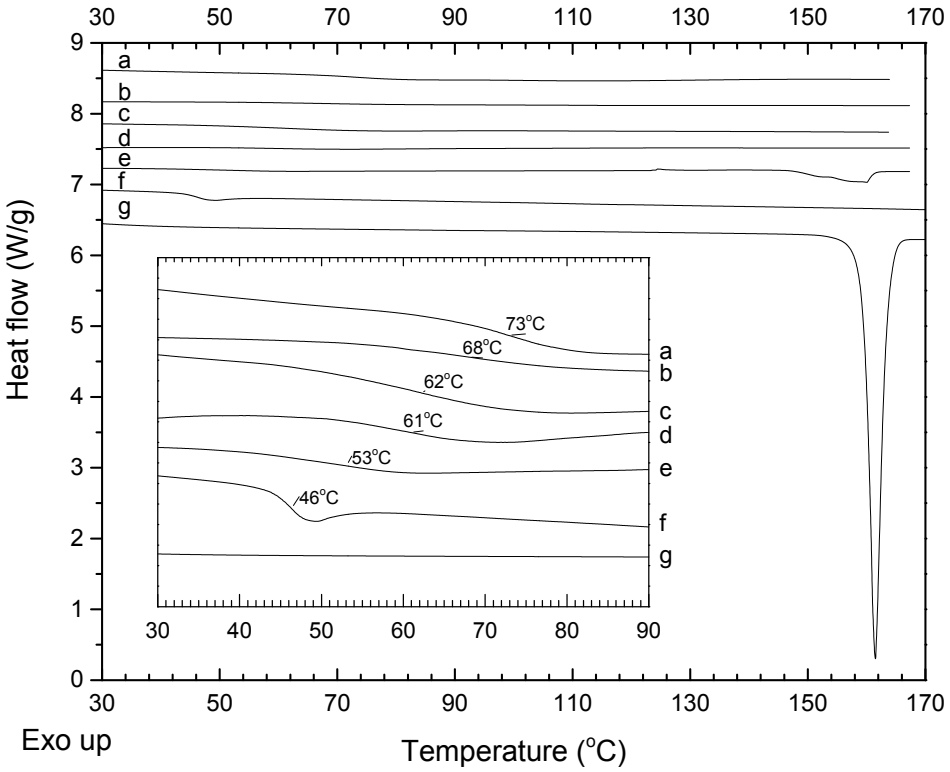


**Figure 4.4** Characteristic 1st heating thermograms (unless otherwise indicated) of: (a) PVCap-PVAc-PEG, (b) S10INM, (c) S30INM, (d) S50INM, (e) S75INM, (f) INM (2nd heating), and (g) INM.

The effects of incorporating low molecular-weight APIs on a polymer's $T_g$ have been widely studied and can be found in the literature (Chokshi et al. 2005; Chokshi et al. 2008; Guo et al. 2010; Liu 2010; Yang et al. 2011). In general, a shift in $T_g$ is expected when the API is dissolved into the polymeric excipient: on the other hand the polymer's $T_g$ will not change if the two compounds are not in one phase and the API remains crystalline. The effect of dissolved API molecules on a polymer's $T_g$ can be viewed in terms of molecular interactions or free volume. The free volume theory assumes that there is "free space" distributed between polymer molecules and that the free volume increases with molecular mobility. When a small molecule such as INM dissolves into the polymer, it increases the free volume among the polymer chains and, thus, the glass transition temperature of the system decreases (Sears and Touchette 1985; Crowley et al. 2007). From the intermolecular interaction perspective, by dissolving a low molecular-weight compound in a polymer, its inter-chain interactions are disrupted and replaced by new secondary bonds, such as the API-polymer interactions. The mobility of the systems is altered due to the change of intermolecular interactions, resulting in either an increase or depression of the $T_g$ (Chokshi et al. 2005; Zhang et al. 2005; Andrews et al. 2008). In some cases, as observed in the present case for the binary systems of INM and PVCap-PVAc-PEG, the glass transition temperatures of the mixtures are lower than that of the pure excipient (Chokshi et al. 2005; Huang et al. 2006; Chokshi et al. 2008; Qi et al. 2008) (a phenomenon often referred to as plasticization effect). In other cases (often referred to as anti-plasticization effect), the $T_g$ of the system may be higher than that of the pure excipient (Guo et al. 2010; Yang et al. 2011) or even higher than both

components in the formulation (Chokshi et al. 2005; Chokshi et al. 2008; Liu 2010). The last case may occur when the API-polymer interactions are very strong.

Since DSC results show that INM acts as a plasticizer for PVCap-PVAc-PEG, it is then expected that as a larger amount of INM is dissolved in the polymer, then the $T_g$ of the solid solution will decrease further. And as it can be seen in Table 4.3 and Figure 4.4, as INM's loading is increased, the $T_g$ of the solid solution is decreased correspondingly. It is interesting to note that even though 75 wt% of INM is not fully dissolved during HME, S75INM has a lower $T_g$ than S50INM. This suggests that the solubility limit of INM in PVCap-PVAc-PEG is between 50 and 75 wt%.

Using the Gordon-Taylor model (see equation 4.1) and $T_g$ values reported in Table 4.3, it is possible to estimate the solubility if INM in PVCap-PVAc-PEG. This model has been used to describe and predict the dependence of $T_g$ with composition of random copolymers, polymer blends (Schneider et al. 1997) and in API-polymer solid solutions (Chokshi et al. 2005; Chokshi et al. 2008; Malaj et al. 2010).

$$T_{g1,2} = \frac{w_1 T_{g1} + K w_2 T_{g2}}{w_1 + K w_2} \tag{4.1}$$

$$K = \frac{\rho_1 \Delta\alpha_2}{\rho_2 \Delta\alpha_1} \tag{4.2}$$

Where sub-indexes 1 and 2 refer to the components of the blend, $T_{gi}$ is the glass transition, $w_i$ the weight fractions of component 1 and 2, K is a system specific constant defined in equation 4.2, $\rho_i$ is the density at $T_g$, and $\Delta\alpha_i=\alpha_{melt}-\alpha_{glass}$ the increase of the thermal expansion coefficient at $T_g$.

Since the Gordon-Taylor model is based on an ideal solution behavior, and, thus, any kinds of interaction between components are neglected, deviation from the model are often seen (Schneider et al. 1997; Chokshi et al. 2005; Liu 2010; Malaj et al. 2010). Therefore the value of K for this system was determined as 1.2 by fitting the experimentally determined $T_g$s of pure materials and those of the solid solutions (S10INM, S30INM and S50INM) in equation 4.1, instead of using equation 4.2. This approach was also used by Schneider et al. (Schneider et al. 1997), to correct for the ideal solution assumption. Figure 4.5 shows the experimental data together with the Gordon-Taylor fitting. Then using equation 4.1 with K = 1.2 and $T_{g1,2}$= 53.0 – which corresponds to the experimentally determined $T_g$ for the S75INM extrudate – the amount of INM dissolved in this sample is determined to be 71 wt%.

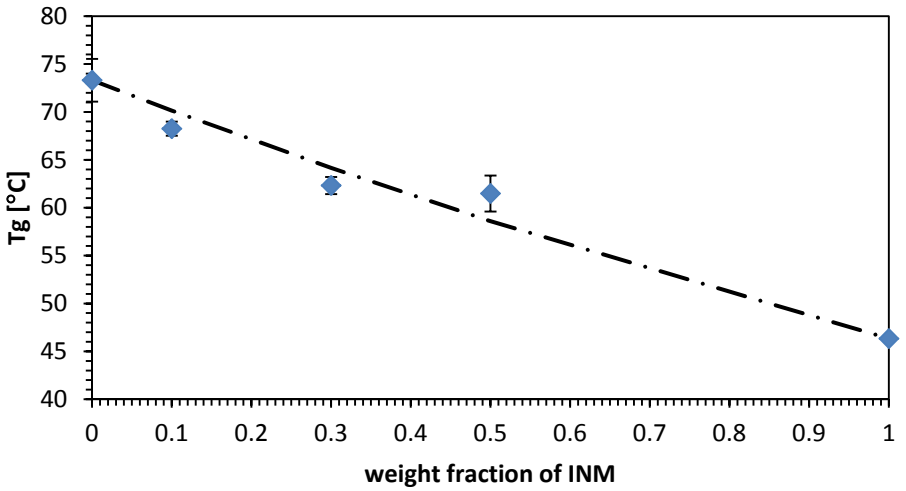


**Figure 4.5** $T_g$ vs. composition of the binary system INM/PVCap-PVAc-PEG. Points represent experimentally determined $T_g$ values and the dashed line represents the "fit" by Gordon-Taylor model with K = 1.2.

In summary, all three characterization techniques (POM, DSC and FT-IR) indicate that the solubility of INM in PVCap-PVAc-PEG is between 50 and 75 wt% (most likely 71 wt% as estimated by the Gordon-Taylor equation). In all cases INM was not fully dissolved in S75INM while in S50INM the API was fully dissolved.

## 4.2 General Properties of the Binary System S30INM

### 4.2.1 Effect of pH on INM's Release

The release profiles of INM from three different dosage forms containing an average of 24 mg of drug loading are presented in Figure 4.6. As described in Chapter 3 (Table 3.10) pure INM and the physical mixture (PM) S30INM are analyzed by filling the powder into Hydroxypropyl Methylcellulose (HPMC) capsules, while HMM S30INM samples are analyzed as compression molded disks of 5∅ x 1 mm. In addition, it is important to note that the INM loaded into the capsules is crystalline – in its γ-form. On the other hand in the HMM samples INM is amorphous, forming a solid solution with the polymer excipient. The *in vitro* dissolution tests are conducted in a pH 7.4 phosphate buffer solution and in a pH 1.2 hydrochloric acid buffer solution. The results are discussed first in terms of the pH and then in terms of the type of sample used.

It can be seen from Figure 4.6 that the release rate of INM is pH-dependent. Regardless of the type of sample, higher pH leads to faster release rate and a greater amount of INM been released. In the case of pure INM and PM, the pH-dependence is due to the ionizable character of the carboxylic group. Higher percentage of the carboxylic groups was ionized when pH increases from 1.2 to 7.4.

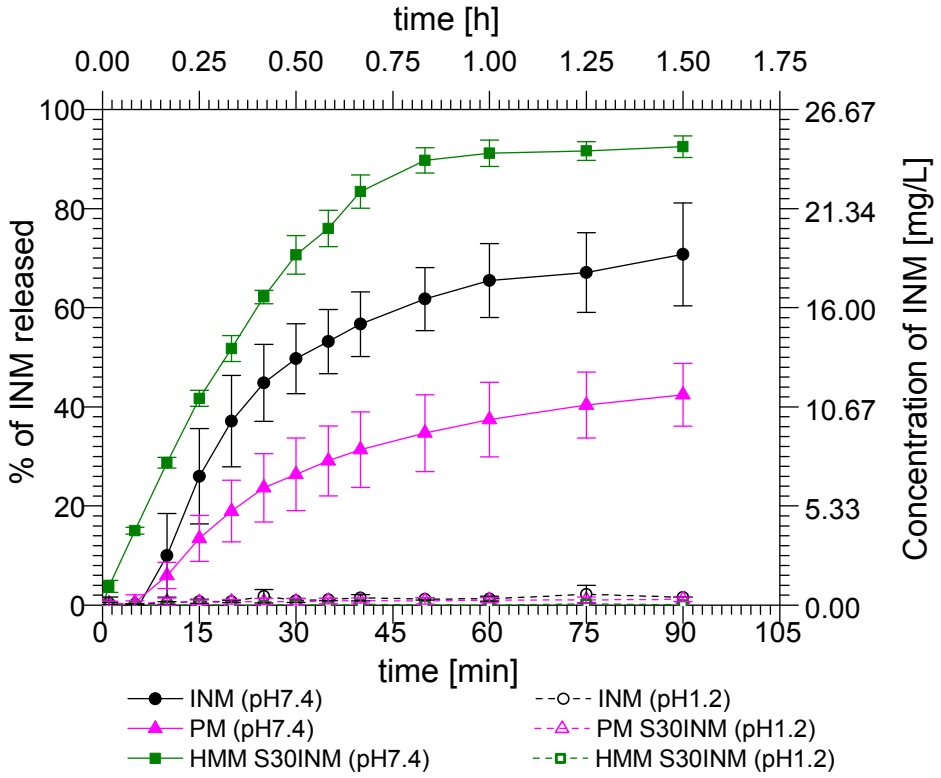


**Figure 4.6** Release profiles of pure INM in capsules (black circles), physical mixture (PM S30INM) in capsules (pink triangles), and HMM S30INM sample (green squares) at pH 7.4 (continuous lines) and at pH 1.2 (dashed lines). Dissolution tests obtained using a USP apparatus 1, and tests were performed in triplicate.

Similarly to pure INM and the physical mixture, the release profile of INM from the HMM-prepared samples also shows pH-dependency. The percentages of INM released within 1 h at pH 7.4 and 1.2 are 90 % and 0.02 %, respectively. There was no evident erosion or gel formation at pH 1.2, except for the 5 % weight increase due to water absorption, after 1.5 h in the buffer solution. It should be mentioned that pure PVCap-PVAc-PEG is soluble at both pHs. The apparent insolubility of the polymer in the HMM sample is due to hydrogen bonding between the carboxylic group in INM and the oxygen atoms in the polymer. The effect of hydrogen bonds on the polymer's solubility has been studied for mixtures comprising Polyethylene Oxide and another polymer that has carboxylic acid functional groups (such as polycarboxylic acid and

polymethacrylic acid) (Smith et al. 1959; Hemker and Frank 1990; Doseva et al. 1997; Ozeki et al. 1998; Lele and Hoffman 2000). Both polymers are individually soluble in deionized water but become insoluble due to hydrogen bonding (Smith et al. 1959; Ozeki et al. 1998; Lele and Hoffman 2000) once mixed together. However, by increasing the pH of the aqueous solution, the acid functional groups are ionized and the complex becomes unstable and the mixture becomes soluble (Smith et al. 1959; Hemker and Frank 1990; Doseva et al. 1997; Ozeki et al. 1998; Lele and Hoffman 2000).

Therefore, as reported for some polymer blends, hydrogen bonding between INM and PVCap-PVAc-PEG hinders the dissolution of the polymer at pH 1.2. However, once the pH of the solution is increased above the INM's pKa (which is 4.5 (Yazdanian et al. 2004)), as is the case at pH 7.4, the interactions between API and polymer are reduced by ionization of the INM's carboxylic groups, allowing the dissolution of the system. In more detail, by describing the ionization of INM in aqueous solution by the reaction below.

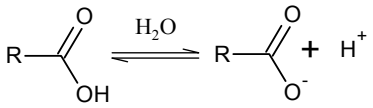


(4.3)

The acid dissociation constant ($k_a$) can be defined by equation 4.4. Rearranging equation 4.4, the relationship between pH and the concentrations of INM in various forms can be obtained according to equation 4.5.

$$k_a = \frac{[RCOO^-][H^+]}{[RCOOH]} \tag{4.4}$$

$$pH = pk_a + \log([RCOO^-]) - \log([RCOOH]) \tag{4.5}$$

Where, [$RCOO^-$] and [RCOO] are the molar concentrations of ionized INM and non-ionized INM, respectively.

Finally, since INM cannot be released from the solid solution until its carboxylic group is ionized, and thus reducing the polymer-API interaction allowing dissolution of both components, equation 4.5 is used to estimate the amount of INM that can be released from the solid solution (i.e. HMM-prepared S30INM) as a function of pH of the solution. As shown in Figure 4.7, at pH 1.2 only 0.05% of INM can be released, while at pH 7.4 99.9% INM can be released, which is in agreement with the results presented in Figure 4.6 for the melt mixed samples.

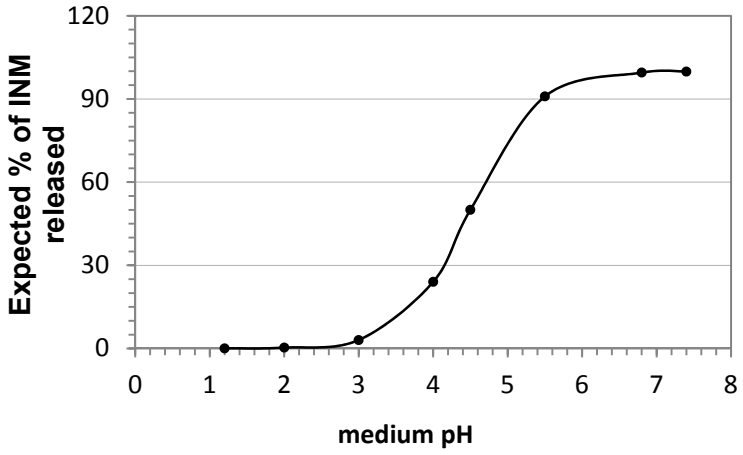


**Figure 4.7** Expected amount of INM to be released from a solid solution such as the HMM S30INM sample as a function of pH.

It should be mentioned that strong physical interactions between a drug and a polymer are in general desirable in HMM/HME products because they help to stabilize the API in the amorphous state during the shelf life of the product. However, in this case, the strong physical interactions make it difficult for the polymer to dissolve in acidic conditions, although the API has been transformed into its amorphous form.

In addition to the pH effect, Figure 4.6 also shows the impact of different oral delivery forms. At pH 7.4, the fastest release rate of INM is observed from the HMM-prepared compression molded samples, followed by γ-INM in capsules, and then the PM in capsules. The percentage of INM released in 1 h is 91 ± 3 % from the HMM sample, 65 ± 7 % for γ-INM in capsule, and 37 ± 8 % for the PM in capsule. The fastest release rate associated with the HMM sample is due to INM been in its amorphous state. Dissolution of a material in the amorphous state, compared to its crystalline counterpart, is facilitated by the lack of lattice structure. In the amorphous state the lattice energy does not have to be overcome in order to dissolve the API (Leuner and Dressman 2000). In addition, also due to the lack of lattice structure, an amorphous API has a higher free energy compared to its crystalline counterpart (Bhugra and Pikal 2008), facilitating dissolution is the former case.

It is important to mention that INM concentration determined through UV analysis most likely corresponds to only truly dissolved API, since micellar INM was probably blocked during filtration. When studying the dissolution behavior of PVCap-PVAc-PEG, no UV signal of the polymer was observed when the PVDF filters with pore size of 0.45 μm were used, even though the PVCap-PVAc-PEG is a chromophore. The dissolution profiles of pure PVCap-PVAc-PEG are presented in section 4.6.2, were obtained through UV analysis without filtration. This observation suggests that the PVCap-PVAc-PEG micelles cannot pass through the filter.

In the case of crystalline INM at pH 7.4, after 1.5 h, complete dissolution is not obtained even though the amount used is significantly below its solubility limit. The maximum amount of INM dissolved is 18 ± 3 mg/L, while its solubility has been reported

to be 1300 mg/L at pH 7.4 (Yazdanian et al. 2004). This is due to the slow dissolution rate of crystalline INM. The remaining un-dissolved INM particles precipitated to the bottom of the dissolution vessel.

Surprisingly, at pH 7.4 INM release rate from the physical mixture is slower than that of the pure crystalline INM. Because the PVCap-PVAc-PEG is a surfactant, an opposite result was expected. INM is a crystalline powder in both cases and its difference in the release rate can be attributed to the presence of the polymer. This phenomenon can be explained through a combination of two factors: polymer gelation and a low pH micro-environment. Once the physical mixture is wetted by the aqueous solution, the polymer rapidly forms a gel which encapsulates the crystalline INM particles. Because the polymer gel has a much higher viscosity than the aqueous solution, it slows down the diffusion rates of the solvent and API. In addition, the microenvironment surrounding the INM particles probably has a slightly lower pH than the bulk solution. Information appearing in PVCap-PVAc-PEG data sheet from the manufacturer states that the polymer solution has a pH of 3~5.5. It should be mentioned that other researchers have incorporated pH controlling additives into their formulations to generate a specific micro-environment around the API to control its release rate (Doherty and York 1989; Govindarajan et al. 2006). In some cases the chemical nature of the API itself is responsible for the slightly different pH of the micro-environment from that of the dissolution medium (Bruce et al. 2005). In this study, the acidic microenvironment and the gel caused by the presence of the polymer slowed down the INM's release rate. The 5 min delay in the dissolution curves of pure INM and PM corresponds to the dissolution time of the HPMC capsules.

### 4.2.2 $CO_2$ Solubility in the S30INM Binary System

The solubility of physical blowing agents in a polymer is of great importance during foaming operations. Gas solubility has also a direct impact on the rheological properties of the material, and thus the morphology and final properties of the foamed product. Various in-line and off-line methods have been used to measure the solubility of PBA in polymers. In-line gas solubility determination techniques are generally based on viscosity measurements (Todd et al. 1998; Lee et al. 1999; Choudhary et al. 2005) and optical methods (Zhang and Xanthos 2004; Faridi and Todd 2007). Pressure decay and gravimetric methods are the most commonly used off-line measurement techniques (Sato et al. 2001; Tomasko et al. 2003; Faridi and Todd 2007). These methods provide between 5-7 % accuracy in the solubility determination (Tomasko et al. 2003).

In this study a gravimetric method is used to determine the solubility of $CO_2$ in the HME-produced binary system S30INM, wherein the amount of gas dissolved is determined by weight difference of the samples before and after 24 h gas saturation at various pressures and temperatures. It is important to note that samples are weighed under ambient conditions, after removing them from the high pressure vessel, in order to avoid gas loss due to diffusion; thus bubbles are not observed at any of the conditions evaluated. This methodology has been used by other authors to successfully measure the solubility of PBAs in different polymers (Faridi and Todd 2007; Brown et al. 2011).

Figure 4.8 shows the measured $CO_2$ solubility in S30INM as a function of pressure and at three different temperatures. Two of the temperatures tested are significantly below the $T_g$ of the binary system, while the third corresponds to the measured $T_g$ value of the S30INM system (i.e. 62 ± 1 °C, as reported in Table 4.3).

However, it should be noted that the $T_g$ of the ternary system S30INM containing $CO_2$ is expected to be lower than that of the binary system S30INM, since it is known that $CO_2$ acts as a plasticizer for many polymers lowering their $T_g$ (Tomasko et al. 2003). Thus, it can be assumed that these measurements are performed at both above and below of the system's $T_g$.

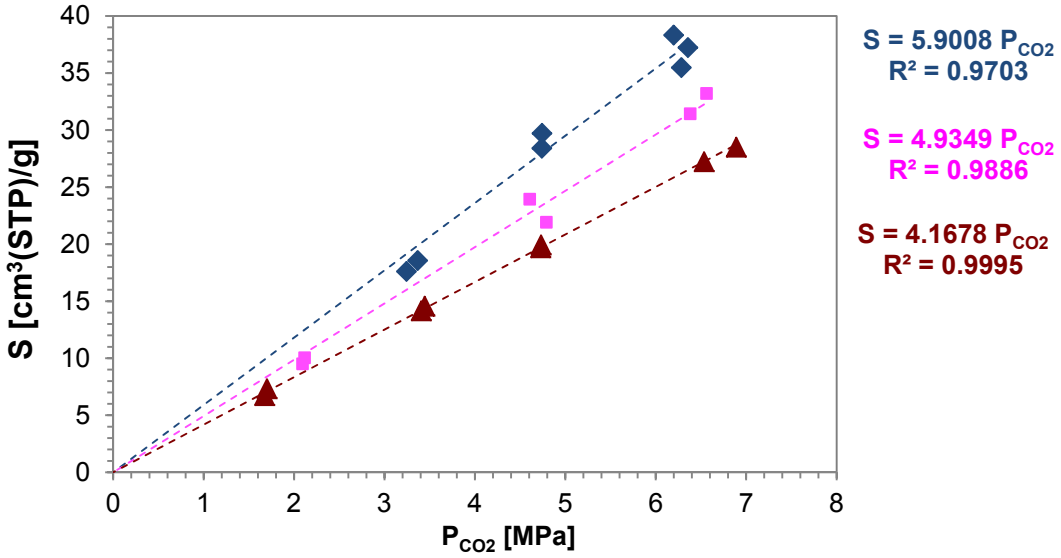


**Figure 4.8** $CO_2$ solubility (S) in S30INM as a function of $CO_2$ pressures ($P_{CO2}$) at different temperatures: ◆ 39.6 °C, ■ 52.2°C and ▲ 62.9 °C.

Results presented in Figure 4.8 indicate that the solubility increases as the pressured increases, but decreases as the temperature is increased. The latter is due to increased mobility of both the gas and solid phases, making it more difficult for the gas to remain within the solid phase. On the other hand, the pressure dependence of solubility of gases in polymers is known to follow Henry's law (Lee et al. 1999; Zhang and Xanthos 2004; Faridi and Todd 2007; Brown et al. 2011), through the following expression:

$$S = k_p P_{CO_2} \tag{4.6}$$

Where *S* is the volume of gas dissolved at STP (standard temperature and pressure – 237 K and 1 atm) conditions per unit weight of the S30INM disk [$cm^3$(STP)/g], $k_p$ is the Henry's Law constant, and $P_{CO_2}$ is the saturation pressure.

Values of Henry's law constant for the $CO_2$ - S30INM ternary system are calculated by fitting the solubility data with equation 4.6 and are reported in Table 4.4. These calculated values are of the same order of magnitude with those reported in the literature for other $CO_2$ - polymer systems not containing APIs (Faridi and Todd 2007; Brown et al. 2011).

**Table 4.4** Calculated Henry's Law Constant Values for $CO_2$ - S30INM Ternary System

| Temperature [°C] | $k_p$ [$cm^3$(STP)/g MPa] |
|---|---|
| 39.6 ± 0.9 | 5.9 ± 0.1 |
| 52.2 ± 0.5 | 4.9 ± 0.1 |
| 62.9 ± 0.3 | 4.17 ± 0.01 |

Furthermore, the temperature dependence of $k_p$ follows an Arrhenius expression as follows:

$$k_p = k_{po} exp\left(\frac{-E_s}{R\,T}\right) \tag{4.7}$$

Where $k_{po}$ is the temperature independent Henry's law constants, $E_s$ is the heat of solution, *T* is the absolute temperature and *R* is the universal gas constant.

Using equation 4.7 to fit the $k_p$ values reported in Table 4.4, it is determined that $k_{po}$ and $E_s$ for $CO_2$ - S30INM are 0.04 $cm^3$(STP)/g MPa and -128.2 L atm/mol K, respectively. Finally, by combining equations 4.6 and 4.7 the solubility of $CO_2$ in

S30INM at different temperatures and pressures relevant to foaming processing conditions can be estimated.

### 4.3 Crystallization of Amorphous INM in the Presence of $ScCO_2$

As mentioned in Chapter 2, supercritical fluids and especially supercritical $CO_2$ ($ScCO_2$) have been used to induce polymorphic transitions in APIs (Edwards et al. 2001; Moribe et al. 2008; Brittain 2009) and as processing aids during manufacture of solid solution/dispersions by different techniques (Sethia and Squillante 2004; Verreck et al. 2006a; Lyons et al. 2007; Moribe et al. 2008; Nagy et al. 2012). Given that it has already been established in the literature that $ScCO_2$ is capable of inducing polymorphic changes in an API, it is relevant to this work to study its effect on the morphology of INM. To accomplish this, the batch foaming apparatus and process are used to evaluate the crystallization of INM from its amorphous state. Samples of amorphous INM were prepared by compression molding at 165°C, and a picture of an amorphous INM sample can be seen in Figure 4.9 (a).

Amorphous INM samples were heated with and without $ScCO_2$. The samples heated without $ScCO_2$ were intended to be control samples. Figures 4.9 (a) and (b) show the effect of temperature on amorphous INM. At 25°C, the samples remain amorphous, being transparent glasses. But when heated for 15min at 100°C the sample partially crystallizes. In contrast, in the presence of $ScCO_2$ the crystallization process is accelerated as is shown in Figures 4.9 (c) and (d). Even at 25°C, temperature at which INM can remain amorphous for several weeks (Andronis and Zografi 2000) the sample became opaque, a strong indication of recrystallization.

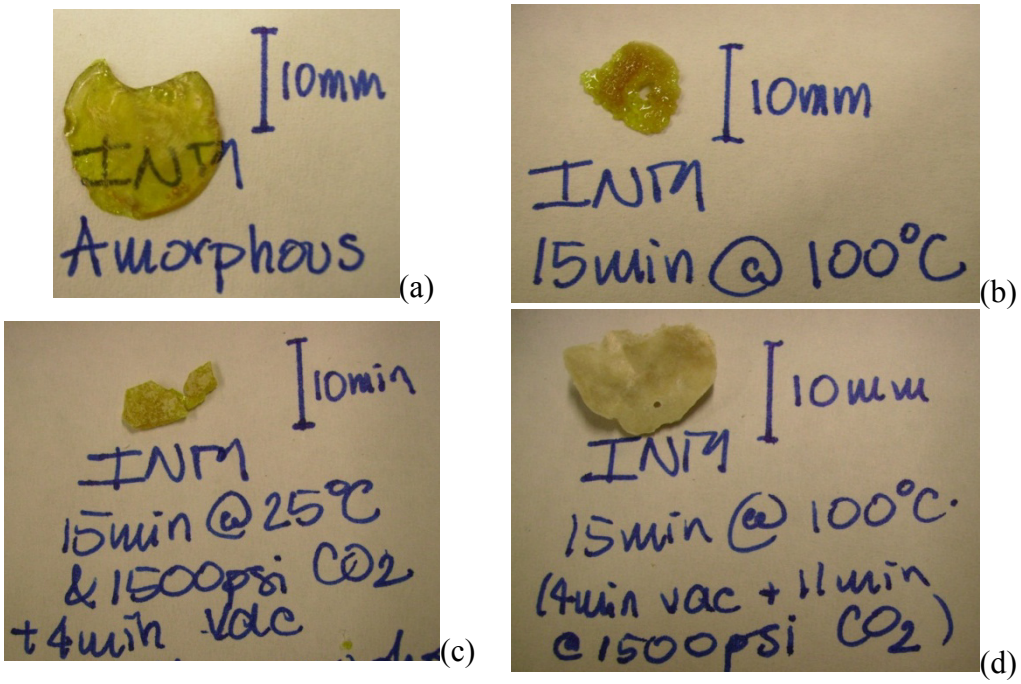


**Figure 4.9** Photographs of INM samples: (a) Initial amorphous INM sample at 25 °C, (b) sample after heating amorphous INM to 100 °C for 15 min, (c) sample after treating amorphous INM with $ScCO_2$ at 25 °C and 10.34 MPa for 15 min, and (d) sample after treating amorphous INM with $ScCO_2$ at 100° C and 10.34 MPa for 15 min.

FT-IR is used to study in more detail the state of INM on each of the samples shown in Figure 4.9. The spectra for all the samples appear in Figure 4.10. The spectrum of the sample treated with $ScCO_2$ at 25°C [Figure 4.10 (c)] is a mixture of all three forms (i.e. amorphous, α-INM and γ-INM). The shoulder observed at 1736 $cm^{-1}$ and the peak at 1692 $cm^{-1}$ belong to the amorphous and γ-INM, respectively [see Table 4.2 and Figures 4.10 (a) and (b)]. The weak band at 1650 $cm^{-1}$ is due to the asymmetric stretching of hydrogen-bonded acid C=O in α-INM. The other peaks observed correspond to coupling of two forms. For example the one at 1715 $cm^{-1}$ corresponds to the asymmetric stretching hydrogen-bonded acid C=O in a cyclic dimer

(see Table 4.2) and is observed between the normal position for the amorphous and γ-forms; the shift is due to the presence of both species in the sample.

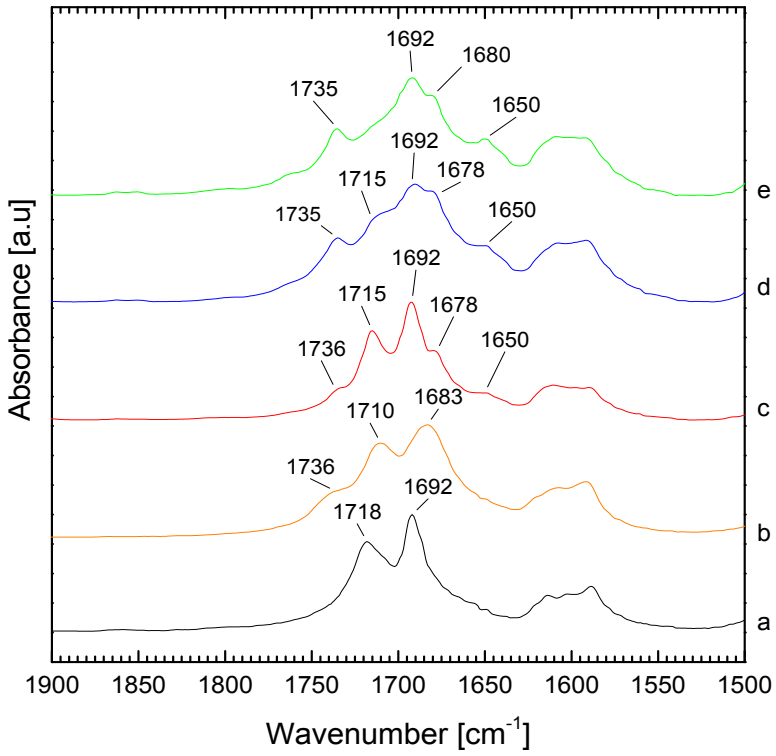


**Figure 4.10** FT-IR spectra of INM: (a) γ-INM, (b) amorphous sample prior to thermal treatment, (c) INM after treating the amorphous sample at 25 °C with $ScCO_2$ for 15 min, (d) INM after heating the amorphous sample at 100 °C for 15 min, and (e) INM after treating the amorphous sample at 100 °C with $ScCO_2$ for 15 min.

Since the sample treated at 100 °C for 15 min [see Figure 4.10 (d)] also resulted in a mixture of the three forms (amorphous, γ-INM and α-INM), its spectrum is very similar to the one of the sample treated with $ScCO_2$ at 25 °C [Figure 4.10 (c)]. However, the relative intensity of the peak is affected and the influence of α-INM becomes more dominant. For example: the shoulder at 1736 $cm^{-1}$ associated with the stretching vibration of the non-hydrogen bonded acid C=O in amorphous INM, becomes a well-defined peak at 1735 $cm^{-1}$, which corresponds to the same vibration in α-INM. Another

change observed is the reduction in intensity of the 1692 $cm^{-1}$ peak of γ-INM. The predominance of α-INM in this sample is due to the significantly faster crystal growth rate of α-INM compared to γ-INM at 100 °C (Andronis and Zografi 2000).

Finally, the sample treated for 15 min at 100 °C with $ScCO_2$ [Figure 4.10 (e)] is completely crystalline and composed of γ and α-INM. The disappearance of the peak at 1715 $cm^{-1}$ is evidence of the absence of amorphous INM and predominance of α-INM.

## 4.4 Foam Extrusion of S30INM Binary System

As mentioned in section 2.3, one of the primary interests of the pharmaceutical industry in foam extrusion technology is to facilitate the milling operation of HME products. Currently, the HME process is mainly used to produce intermediate drug products; however final dosage forms are seldom in the form of an extrudate. In general, the HME product (i.e. the extrudate) in the vast majority of the cases has to be milled and blended with other excipients to tailor the product performance and/or to improve tableting operations. Few exceptions can be found where the final drug product is an HME extrudate. Only few examples include: NuvaRing, Implanon and Lacrisert® (Zhang and DiNunzio 2010; DiNunzio 2011). However, these drug products are not oral dosages but implants or medical devices. Therefore, the objective of this section is to understand the effect of the morphology of the cellular structure on the milling efficiency of extrudates, as well as, hopefully, improve the quality of the milled products. By varying the foam extrusion conditions two foam morphologies were produced and their performance (in terms of milling efficiency and release rate) was compared to the un-foamed extrudate of the same composition.

### 4.4.1 Cellular Morphology in Foamed Samples

Prior to analyzing and discussing the cellular morphology of the foam-extruded samples it is important to bear in mind that it was not the objective of this work to perform a detailed parametric study of the effect of the processing variables on the foam morphology, which has already been studied by other researchers (Han et al. 2002; 2003; Kaewmesri et al. 2006; Nagy et al. 2012). However, it is of interest to use the already existing knowledge to produce different cellular morphologies in order to evaluate the effect of the cellular morphology on the performance of HME products.

A summary of the properties of un-foamed and foamed extrudates is presented in Table 4.5. Figures 4.11 and 4.12 show pictures of the extrudates and SEM images of their cross-sectional surfaces, respectively. The un-foamed samples are designated as HME, and were produced without injecting $CO_2$ during the HME process. On the other hand, foamed extrudates (referred to as fHME) were produced by injecting $CO_2$ as PBA into the extruder during the HME process. As can be seen in Table 4.5, by varying the concentration of $CO_2$ injected during the foam extrusion process it was possible to produce foamed extrudates with different densities, and in particular one high density foamed extrudate (HD-fHME) and a low density foamed extrudate (LD-fHME).

**Table 4.5** Summary of the Characteristics of the Un-foamed and the Foamed Extrudates (HME and fHME, Respectively)

| Sample | $CO_2$ concentration [w/w %] | Density [$g/cm^3$] | Cell Size [μm] | Wall Thickness [μm] |
|---|---|---|---|---|
| HME | 0 | 1.01 ± 0.05 | - | - |
| HD-fHME | 12 | 0.24 ± 0.05 | 774-2165 | 9.8-153.5 |
| LD-fHME | 4 | 0.071 ± 0.004 | 27-320 | 0.4-7.7 |

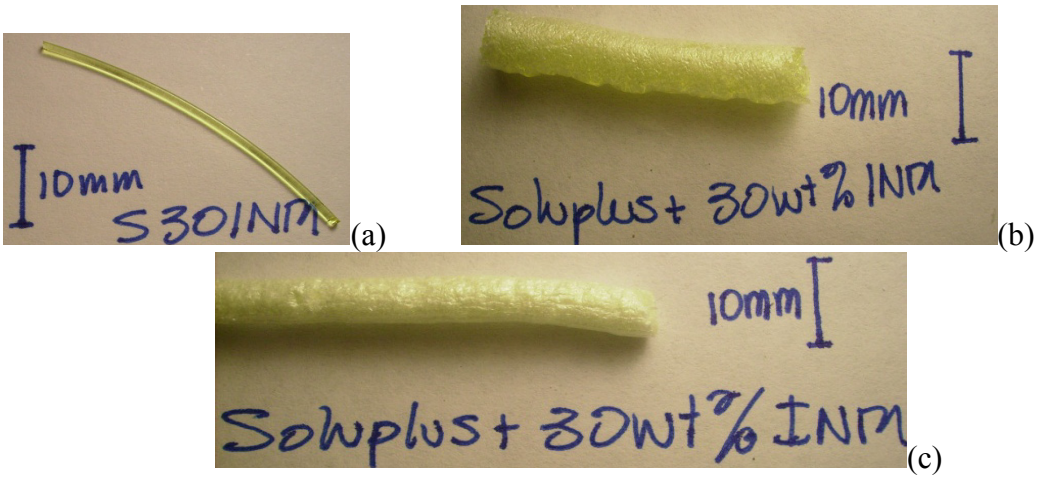


(a) (b) (c)

**Figure 4.11** Photographs of the S30INM extrudates: (a) un-foamed extrudate – HME – (b) HD-fHME extrudate, and (c) LD-fHME extrudate.

As can be seen in Figures 4.11 (a) and 4.12 (a) the un-foamed extrudates (HME sample) are non-porous. On the other hand, extrudates produced by foam extrusion (HD-fHME and LD-fHME) are porous, as seen in Figures 4.12 (b) and (c). The densities of the foamed extrudates are 4 and 14 times lower than the density of the un-foamed extrudates, which corresponds to reduction in density of 76 and 93%, respectively (see Table 4.5). These reductions in density resulted from the creation of closed cells in both HD-fHME and LD-fHME extrudates as shown in Figures 4.12 (b) and (c).

Based on the mass flow rates of polymer, API and $CO_2$ fed to the extruder it is possible to determine a theoretical or minimum density that could be achieved for the foamed samples. The values reported in Table 4.6 (see Appendix C for the detailed calculations) allow to give a semi-quantitative understanding of the morphologies of the extrudates. As can be seen in Table 4.6, in both cases the theoretical density is lower than the measured density. While in the case of the HD-fHME extrudate the theoretical density is two orders of magnitude lower than the experimental density; in the case of the LD-fHME sample the densities are within the same order of magnitude. The latter is

most likely due to small $CO_2$ losses as the melt flows through the die. In the case of the HD-fHME sample a significant amount of gas is lost due to flow instabilities as will be discussed below.

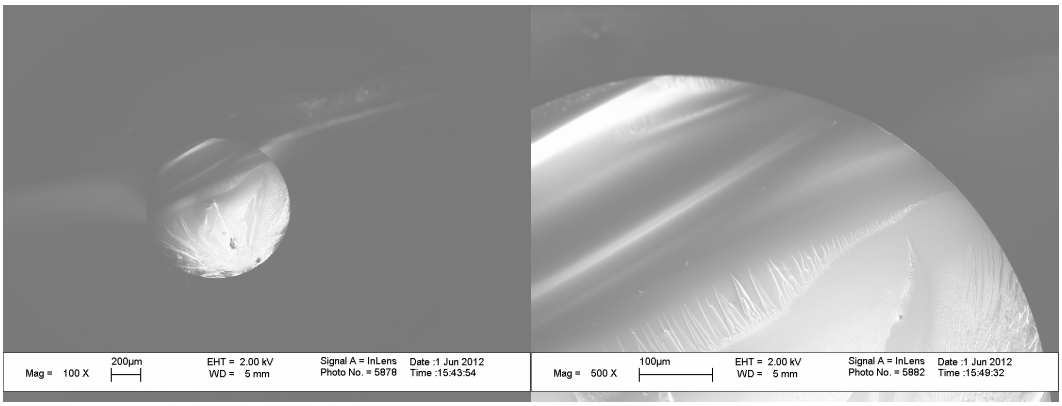


(a)

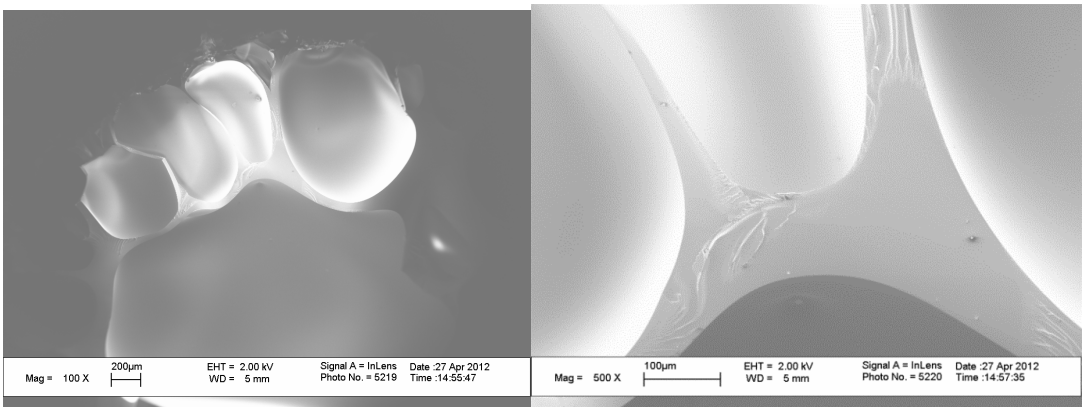


(b)

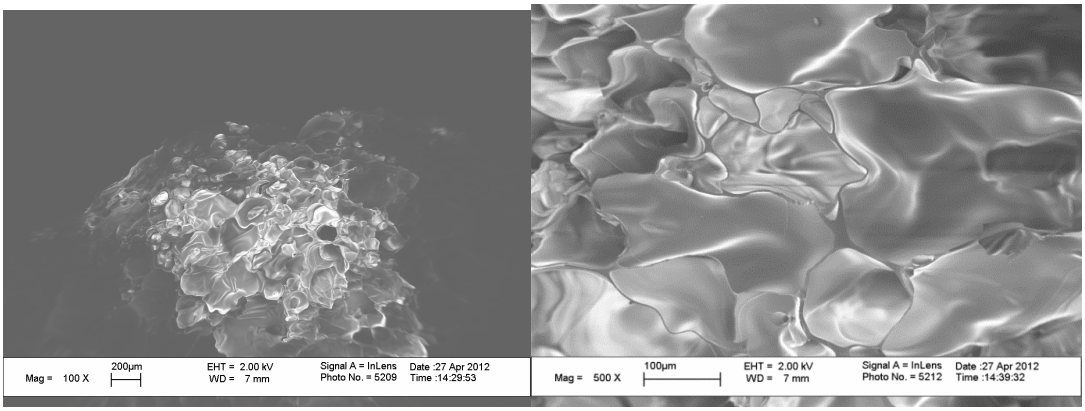


(c)

**Figure 4.12** SEM images of a cross-sectional surfaces of the S30INM extrudates (100X in the left column and 500X in the right): (a) un-foamed extrudate – HME –, (b) HD-fHME extrudate, and (c) LD-fHME extrudate.

**Table 4.6** Comparison Between the Calculated Ideal Densities and Experimentally Determined Densities for Foamed Samples

| Sample | $\dot{m}_{S30INM}$ [kg/h] | $\dot{m}_{CO2}$ [g/min] | $Q_{S30INM}$ [$cm^3/h$]* | $Q_{CO2}$ [$cm^3/h$]** | Theoretical Density [$g/cm^3$] | Experimental Density [$g/cm^3$] |
|---|---|---|---|---|---|---|
| HD-fHME | 1 | 2 | 990 | 120000 | 0.008 | 0.24 ± 0.005 |
| LD-fHME | 1.5 | 1 | 1485 | 60000 | 0.024 | 0.071 ±0.004 |

*Calculations carried out used a density of S30INM as 1.01 $g/cm^3$
**Calculations carried out using the density of $CO_2$ at measured melt temperature and 0.101MPa in both cases it is 0.001 $g/cm^3$ (NIST 2011).

The results summarized in Table 4.5 and the SEM images shown in Figure 4.12 clearly indicate that increasing the concentration of $CO_2$ from 4 to 12 w/w% resulted in a cellular structure with higher density, bigger cells and thicker cell walls. However, these results are counterintuitive, since homogenous nucleation theory predicts that higher PBA concentration leads to higher number of nuclei and therefore more and smaller cells (Colton and Suh 1987; Han et al. 2002). The opposite trend is observed in the present case because the gas concentrations utilized are above the estimated solubility limit of $CO_2$ in the S30INM system (see Table 4.7). It is important to point out that process instabilities commonly occur when gas concentrations exceed its solubility; as will be discussed in more detail below.

Figure 4.13 schematically represents the physical aspects of cell nucleation and growth during a typical foam extrusion process along a capillary die. As shown, the pressure drop between the die entrance and its exit can be approximated by a linear pressure drop along the die (Lee 2000). Ideally the gas is fully dissolved in the melt forming a single phase with the molten polymer as it enters the die. As a result of this rapid depressurization cell nucleation is triggered, by a drop in gas solubility in the melt with decreasing pressure. The onset point for nucleation occurs when a critical pressure

(Pc) is reached; at Pc the gas-polymer systems becomes oversaturated (Han et al. 2002; 2003). Then, once the nuclei reach a critical size (which has been found to be in the order of 0.3 μm in radius for polystyrene (Lee 2000)) cellular growth takes place through diffusion of the gas in the bulk toward and into the $CO_2$ bubbles. For a stable process, nucleation should occur as close as possible to the die exit.

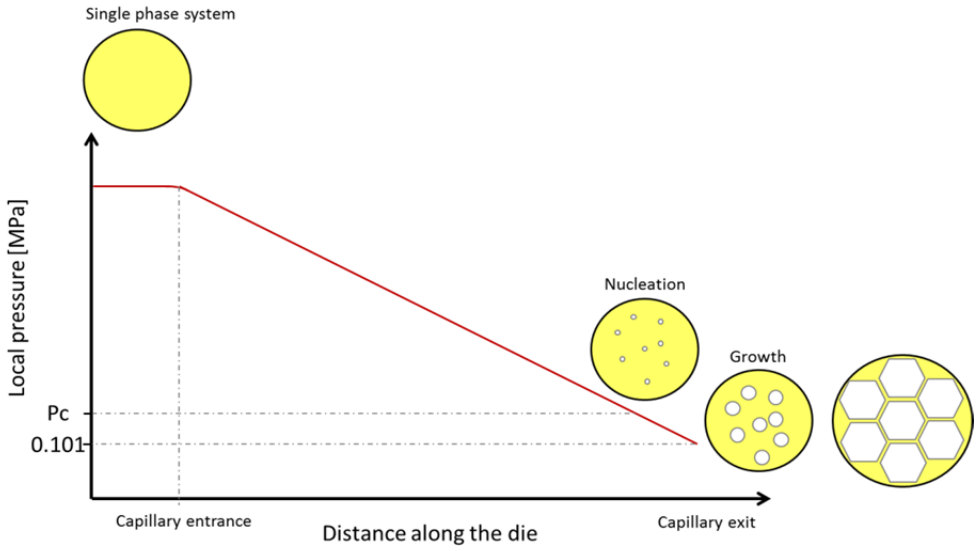


**Figure 4.13** Schematic representation of the pressure profile in a capillary die and the foaming mechanism during a foam extrusion process. Nucleation starts at a critical pressure (Pc) where the system becomes oversaturated with $CO_2$.

As mentioned above, the processing conditions used lead to gas loadings most likely above its solubility limit. The estimated solubility values of $CO_2$ in the S30INM system presented in Table 4.7 are calculated using Henry's law, with the parameters determined in section 4.2.2 for the ternary system $CO_2$ – S30INM. The temperature and pressure values used to calculate the gas solubility correspond to the experimentally measured values of melt temperature and the die pressure, which are also reported in Table 4.7. It is important to point out that this estimated solubility values may have underestimated the gas solubility at the processing conditions, due to higher free space in

the molten state compared to the "semi-solid" state at which solubility measurements were performed (at the highest measured temperature the samples were softened but did not show flow).

**Table 4.7** Calculated Solubility of $CO_2$ in the S30INM System at the Processing Conditions Used

| Sample | $CO_2$ Concentration [w/w %] | $T_{melt}$ [°C] | $P^a_{die}$ [MPa] | Estimated $CO_2$ Solubility [b] [w/w %] |
|---|---|---|---|---|
| HD-fHME | 12 | 102 | 3.65-3.72 | 1.85 - 1.88 |
| LD-fHME | 4 | 97 | 3.03-3.50 | 1.63 – 1.88 |

[a] Maximum and minimum experimental die pressures measured during foam extrusion runs.
[b] Upper and lower solubility limit were calculated using maximum and minimum die pressure values.

In the case of the HD-fHME sample, the amount of gas injected was 12 w/w%, which exceeds the estimated gas solubility in the S30INM system (1.85 – 1.88 w/w%, see Table 4.7) at the processing conditions used for this sample. In the case of the LD-fHME sample, the difference between the amount of gas injected (4 w/w%) and the estimated solubility is not as significant; the estimated solubility of $CO_2$ at the processing conditions is 1.63 – 1.88 w/w% (see Table 4.7). Therefore, before depressurization along the die (which is the driving force for cell nucleation during the foam extrusion process (Han et al. 2002; 2003)), the gas was not fully dissolved in the melt. Thus, two phases were most likely present, namely: (1) a homogenous continuous phase foamed by $CO_2$ and S30INM melt, and (2) a dispersed phase containing the $CO_2$ that was unable to dissolve. In other words, gas bubbles were already present in the melt prior depressurization. As the melt flowed through the die and the pressure drops to atmospheric conditions (~0.101 MPa) the gas bubbles that were already present in the melt expanded. Consequently, cellular growth takes place along the die without the need to go through the nucleation step.

Carrying out calculations similar to those used for the estimation of the theoretical densities of the extrudates, it is possible to roughly estimate the volume fraction occupied by un-dissolved $CO_2$. As shown schematically in Figure 4.14, in the case of HD-fHME with 12 w/w% of $CO_2$ injected, 10 w/w% remains most likely un-dissolved and, at the pressure and temperature at the capillary die entrance it occupies 64 % of the volume of the two phase stream. As the pressure decreases along the die these un-dissolved gas regions of complex morphology expand, increasing the volume fraction occupied by them. Moreover, dissolved $CO_2$ will tend to diffuse into these gas regions, due to further reduction of its solubility in the melt. For example, at a pressure of 1.8 MPa (which corresponds to approximately half-length of the die – when assuming linear pressure drop), the amount of un-dissolved $CO_2$ is estimated to be 11 w/w% which corresponds to 81 % of the volume. The presence of the expanding gas phase promotes axial acceleration of the melt / $CO_2$ two-phase stream and, because of the very large difference in viscosities between the melt and the dispersed gas phase, the morphology of the "blend" is very complex leading to flow instabilities. These favor the escape of $CO_2$ before the stream exits the die, for example, through $CO_2$ "channeling" forming a continuous streak of $CO_2$ from an upstream location of the capillary die to the exit. Such "channels" most likely appear at the die-melt stream interphase, since the number of nuclei per unit volume tends to be much higher toward the extrudate "skin" than along its core during the foam extrusion process (Lee 2000). As shown in the Optical Microscope images of HD-fHME in Figure 4.15 open cells can be seen along the edges of the cross-sectional surface and on the surface of the extrudates.

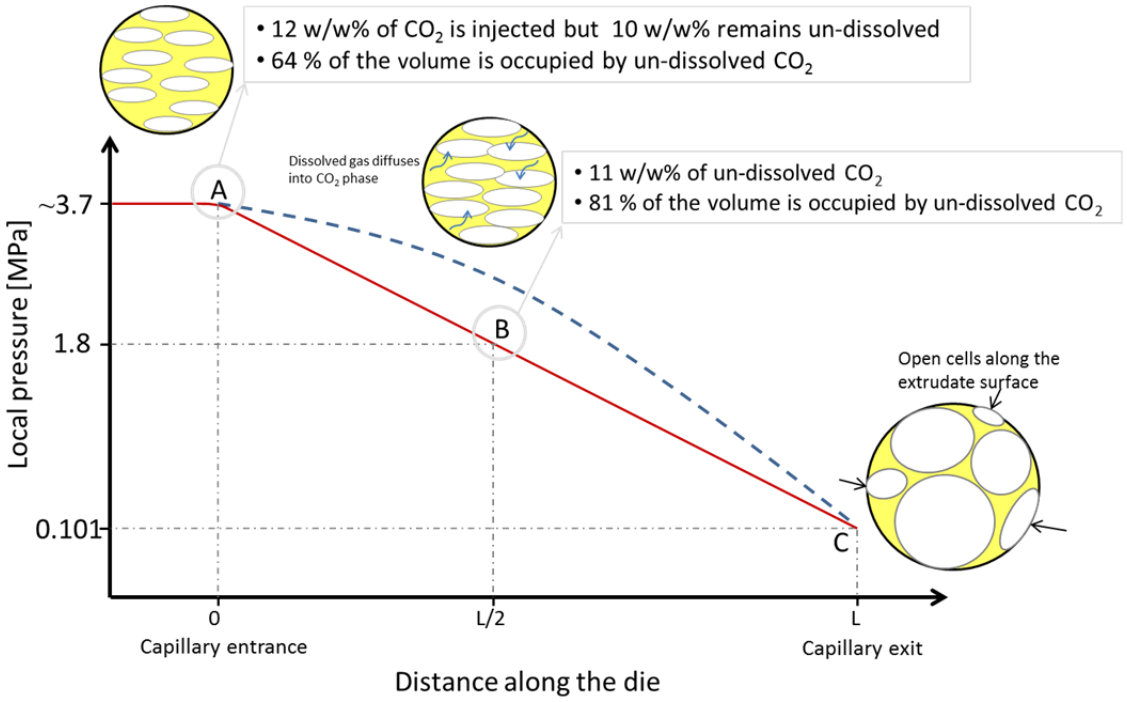


**Figure 4.14** Schematic representation of the pressure profile and two-phase melt stream morphology along the die during foam extrusion of HD-fHME sample. Point A indicates the entrance to the capillary and point C the capillary exit (or opening of the die to atmosphere).

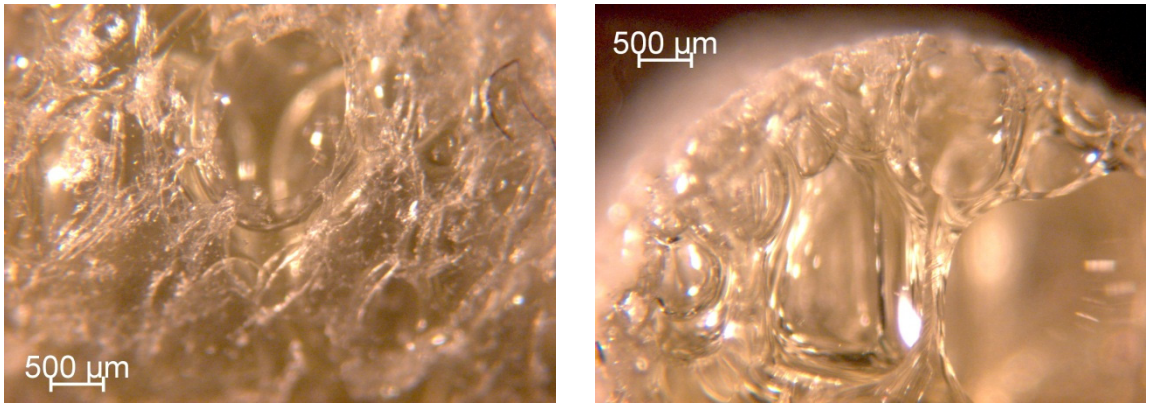


(a) (b)

**Figure 4.15** Optical Microscope images of a HD-fHME extrudate: (a) extrudate surface, and (b) cross-sectional surface.

It should be noted that although the pressure profiles along the die can be considered linear, during foam extrusion process a positive deviation, as shown by the

dashed line is Figure 4.14, may prevail. This deviation may be due to two factors: (1) increase in melt viscosity as the gas diffuses from the melt into the bubble, and (2) higher gas pressure inside the bubble compared to the melt and local pressure build up, sometimes referred to in literature as "superheat" (Lee 2000).

In the case of the LD-fHME sample, some of this flow instabilities may also occur but to a lesser degree. Performing the same calculations described above it was found that before entering the die only 2.1 w/w% $CO_2$ remains un-dissolved, and this would correspond to only 29 % of the volume of the melt stream. Again at approximately half the length of the die, the amount of un-dissolved gas is expected to be 2.3 w/w% (48 % of the volume). However, as mentioned above, local pressures along the die are most likely higher than predicted by the linear approximation; thus, the gas expansion inside the die should be less than estimated. Having this in mind and knowing that critical nuclei sizes are in the submicron level (Lee 2000), significantly lower gas losses are expected through the die due to the flow instabilities in the case of LD-fHME compared to the processing conditions used for the HD-fHME sample, as the semi-empirical analysis on the densities also suggests. In addition, open cells were not observed along the surface of the LD-fHME extrudates using both SEM and Optical Microscopy (see Figure 4.16).

Based on the discussion above then it is evident that due to the flow instabilities which most likely result in extensive gas loss along the die at the processing conditions used for HD-fHME extrusion, the foam structure resulted in the formation of few and very big cells ranging from 0.77 to 2.2 mm, as seen in Table 4.5 and Figures 4.12 (b) and 4.15 (b).

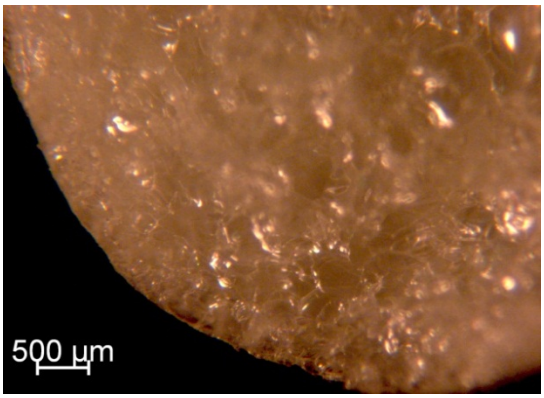


**Figure 4.16** Optical Microscope image of the cross-sectional surface of a LD-fHME extrudate.

Conversely, the processing conditions used to produce the LD-fHME sample resulted in a more stable process with minimal gas loss. Therefore, in this case significantly smaller cells were produced, with sizes in the rage between 27 – 320 µm. In addition, by comparing Figures 4.12 (c) with (b) it is evident that the LD-fHME sample has a significantly higher number of cells per unit area than the HD-fHME sample.

It should be mentioned that a foam extrusion condition where the PBA content exceeds its solubility in the melt would not be used in an industrial manufacturing setting, since it results in process and product variability. However, further optimization of the processing conditions used for the LD-fHME samples were not possible due to equipment and material limitations. On the other hand, HD-fHME samples were used – notwithstanding the limitations associated with the process – since it provided the opportunity to compare the performance of a drastically different morphology with respect to the LD-fHME extrudates, and, therefore, making it possible to observe tangible differences between the milling and dissolution performance of the two foam morphologies, as will be discussed below.

The differences in morphology observed among the extrudates are expected to affect their milling efficiency, as well as the morphology of the particles produced, and therefore the *in vitro* dissolution/release performance of the S30INM system. These aspects are discussed in detail in the next sections.

### 4.4.2 The State of INM and Content Uniformity in Foamed Extrudates

Since two independent feeders were employed during the foam extrusion process it is important to confirm that the drug loading after compounding was in fact 30 wt%. In addition, by determining the concentration of INM in randomly collected samples for each condition, it would be possible to detect variability on the drug loading as a function of time due to either feeding non-uniformities or poor axial mixing by the extruder. As can be seen in Table 4.8, the experimentally determined amount of INM in the extrudates is between 28 and 30.4 wt% (30 wt% was the intended and nominal drug loading). In addition, variability within each processing condition is less that 3.4 % in all cases. These results reflect good content uniformity and are within the requirements established in USP Monograph for the different INM's dosage forms (i.e. capsules, suppositories and oral suspensions). The monograph states that the content of INM in a dosage form can not be less than 90.0 % and no more than 110 % with respect to the theoretical amount.

**Table 4.8** Determined Drug Loading in the Extrudates Through Content Uniformity Analysis

| Sample | $CO_2$ Concentration [w/w%] | INM Concentration [wt %] |
|---|---|---|
| HME | 0 | 29 ± 1 |
| HD-fHME | 12 | 28.7 ± 0.6 |
| LD-fHME | 4 | 29.8 ± 0.6 |

In section 4.1 it was shown that solubility limit of INM in PVCap-PVAc-PEG is significantly higher than 30 wt% (with INM's estimated solubility being 71 wt%). Additionally, in the same section it was also shown that the S30INM system compounded in a twin screw extruder is an *amorphous* solid solution, that is, all of the INM has been dissolved. However, it is known that gases injected during the extrusion process affect the properties of the melt. For example, the melt viscosity and surface tension tend to decrease (Goel and Beckman 1994a; Elkovitch and Tomasko 2000; Lee 2000; Tomasko et al. 2003; Sauceau et al. 2011). These changes in material properties could potentially affect the dissolution process of the API in the polymer, because they are translated into changes in the capillary number of the melt and in the viscosity ratio between materials been blended; these critical parameters during melt compounding with polymers (Tomasko et al. 2003; Tadmor and Gogos 2006). For example, Elkovitch and Tomasko (Elkovitch and Tomasko 2000) observed significant changes in the morphology of a blend of two immiscible polymers by injecting $CO_2$ during melt compounding. Verreck et al. (Verreck et al. 2007) observed for some conditions incomplete dissolution of Itraconazole in Ethyl Cellulose during foam extrusion while complete dissolution was observed by conventional HME. Another factor that may affect API dissolution is associated with the necessary changes which have to be made in the process variables to have successful foam extrusion. Compared to the conventional HME process, during foam extrusion the melt temperatures needs to be lower in order to provide the necessary melt strength needed to prevent rupture of the expanding cells during foaming or consequent collapse of the cellular structure. This reduction in temperature may also be beneficial and sought when working with thermally sensitive APIs. On the other hand it

may be detrimental to the dissolution rates and solubility of the API in the excipient. Additionally, as mentioned before in Chapter 2 in section 2.4, $CO_2$ it is known to act as anti-solvent for some APIs and also to promote polymorphic transformation of some APIs. Specific to INM, in section 4.3, it was shown that $CO_2$ facilitates INM's recrystallization from the amorphous state. Therefore, it is important to establish if the presence of $CO_2$ during HME process, where foamed S30INM extrudates were produced, affected the dissolution of INM in the excipient. The state of INM in the S30INM binary blends was analyzed through FT-IR, and the spectra obtained are shown in Figure 4.17.

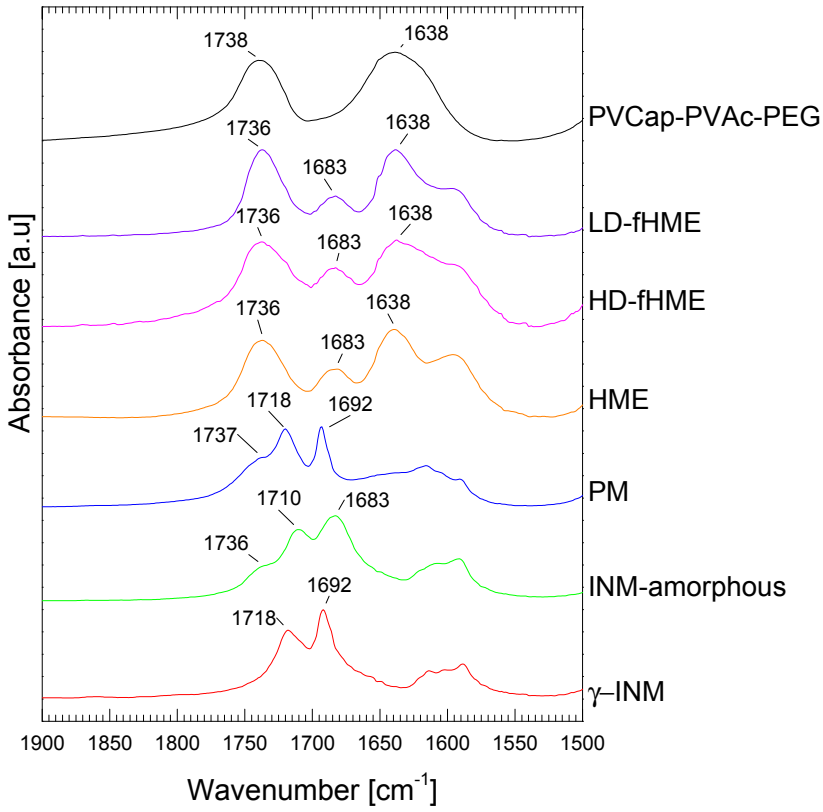


**Figure 4.17** Comparison of the FT-IR spectra of the un-foamed and the foamed S30INM systems produced by HME and foam extrusion. Spectra of pure PVCap-PVAc-PEG, INM (in its γ-form and amorphous state), and physical mixture (PM) are shown as reference.

As discussed in detail before in section 4.1, FT-IR allows to accurately differentiate between amorphous INM, γ-INM and α-INM. In the case of the S30INM systems, the shifts in the peak associated with the stretching vibration of the C=O bond in the benzoyl group has shown to be the best indicator to identify the state of INM in the blends. This peak is not overlapped or affected by peaks associated with the excipient and it has a strong intensity.

By comparing the location of the benzoyl peak in the extrudates with its location in the PM and γ-INM, it is evident that in all the extrudates (foamed and non-foamed) the drug was in amorphous state. This peak is located at 1683 $cm^{-1}$ in all the extrudates, while in the samples were INM is crystalline is seen at 1692 $cm^{-1}$. The first peak corresponds to amorphous INM while the latter to the crystalline γ-INM (see Table 4.2 and Figure 4.17).

### 4.4.3 Effect of Foam Cellular Structure on Milling

As described in Chapter 3, milling of the extrudates was carried out in batches of 25 g for 20 s in a laboratory coffee grinder. Figure 4.18 shows the particle size distribution (PSD) obtained by milling the un-foamed and foamed extrudates. From these results it is evident that milling of the foamed extrudates lead to narrower PSDs. The PSD of the ground un-foamed extrudates presented in Figure 4.18 (a) clearly shows a tail of very big particles, lager than 1.8 mm, which is above the maximum detection limit of the instrument. A summary of the characteristics of the milled extrudates is shown in Table 4.9. In addition, the morphology of the particles produced can be seen in the SEM images presented in Figure 4.19.

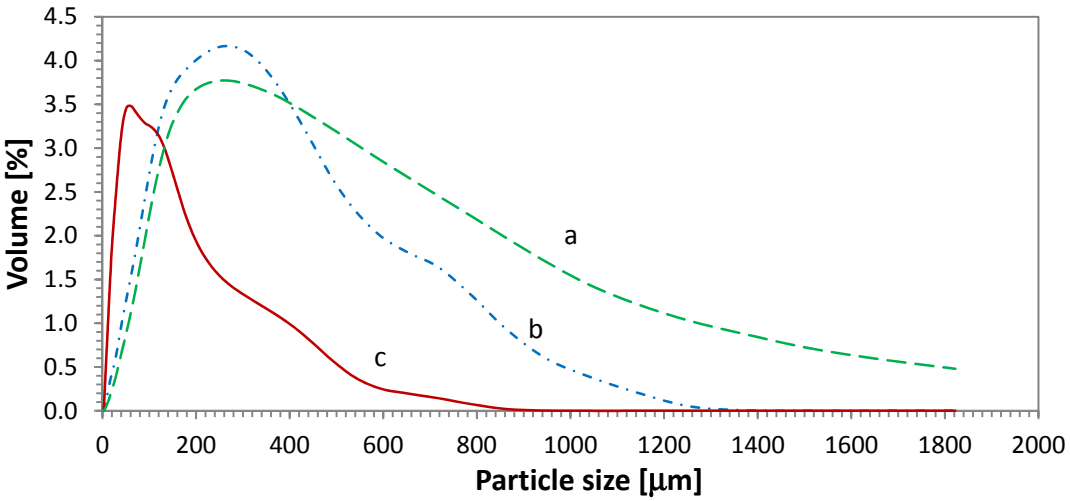


**Figure 4.18** Particle size distribution (PSD) of the three milled extrudates: (a) ground HME sample, (b) ground HD-fHME sample, and (c) ground LD-fHME sample.

Combining the results presented in Figure 4.18 and Table 4.9 it is clear that the smallest particles with the tightest PSD were produced by milling the LD-fHME extrudate, followed by the HD-fHME extrudate and finally the HME extrudate. As expected the bulk density of the milled samples follows the same trend as the particle size, that is, lower bulk density as the particles become smaller with narrower PSD.

**Table 4.9** Summary of the Properties of the Milled Extrudates

| Property | Sample | | |
|---|---|---|---|
| | HME | HD-fHME | LD-fHME |
| $CO_2$ concentration [w/w%] | 0 | 12 | 4 |
| Bulk density [g/cm$^3$] | 0.69 ± 0.01 | 0.55 ± 0.01 | 0.21 ± 0.01 |
| d10 [µm] | 72 ± 1 | 50 ± 6 | 16.4 ± 0.2 |
| d50 [µm] | 296 ± 7 | 206 ± 10 | 67 ± 1 |
| d90 [µm] | 864 ± 4 | 574 ± 56 | 256 ± 13 |

It is interesting to note that the size of the particles produced by milling the LD-fHME extrudate tends to be bigger that the cell wall thicknesses measured from the SEM images of the cross-section of the extrudates. The median particle size was determined to be 16.4 ± 0.2 μm, while the cell wall thicknesses are in the range 0.4 – 7.7 μm (see Tables 4.9 and 4.5, respectively). This result suggests that even after milling some of the cellular structure was retained in the particles. Evidence of this can be seen in Figures 4.19 (e) and (f) where some of the cellular structure is still present although now, after milling, with open cells; this was also observed by Nagy et al. (Nagy et al. 2012). The incomplete destruction of the cellular structure could bring additional benefits to the drug product. On one hand, the presence of cells can potentially aid tableting operations of the product by facilitating particle deformation during compression of otherwise tough and brittle particles, and on the other hand, the remaining cellular structure results in particles with higher surface area thus dissolution rate enhancement is possible. The higher surface area of the particles produced by milling foamed extrudates compared to un-foamed ones has also been observed in other HME products (Verreck et al. 2005; Verreck et al. 2006b; Verreck et al. 2007).

Results shown in Figure 4.18 and Table 4.9 indicate that even though the milled HD-fHME sample has a "tighter" PSD, at least up to the mean particle size, its distribution (although with a slight shift to smaller particles) is comparable to the one obtained for the un-foamed extrudate characterized by a larger particulate size tail, as seen in Figures 4.18 (a) and (b). In addition, by comparing the SEM images of the particles obtained from these two samples in Figures 4.19 (b) and (d) it can be seen that the particles have similar shapes.

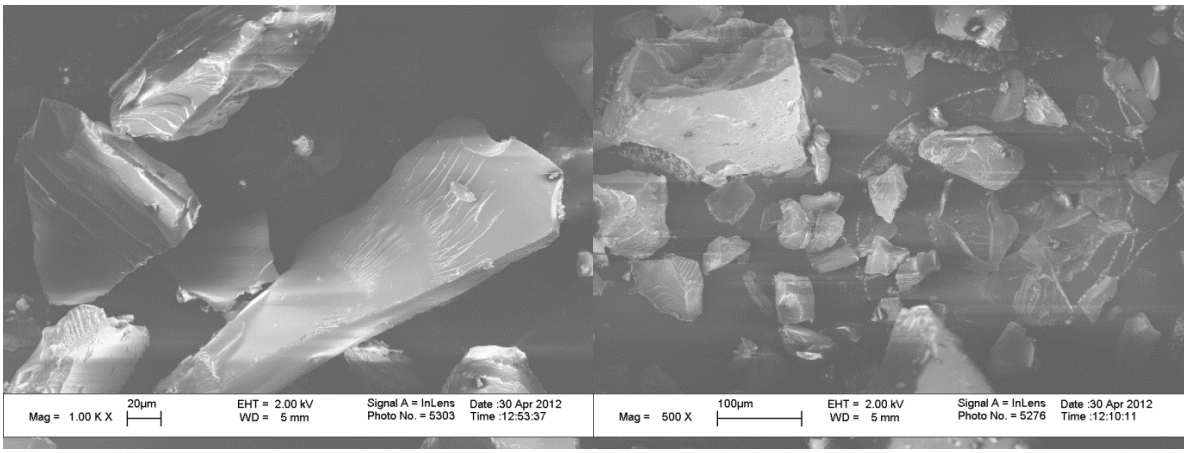


(a) (b)

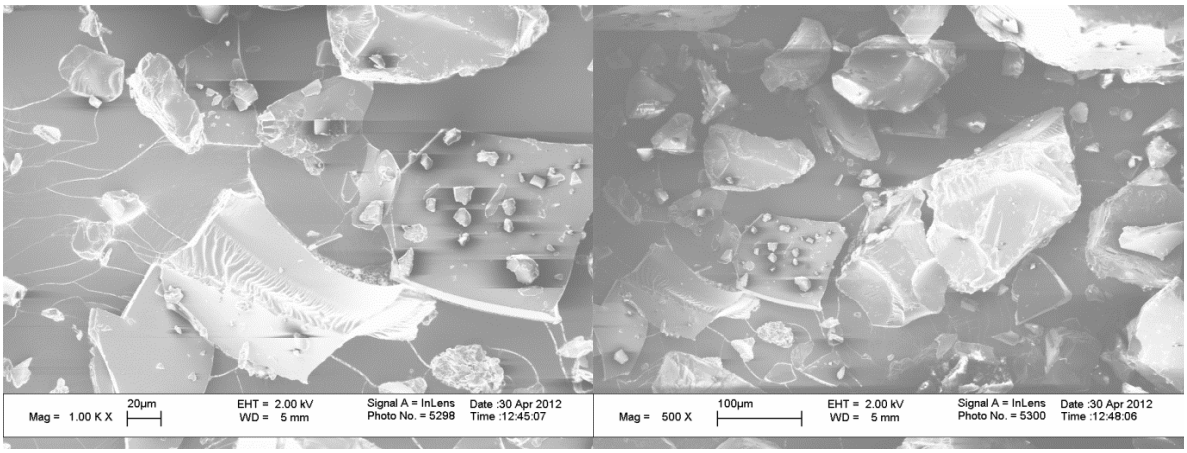


(c) (d)

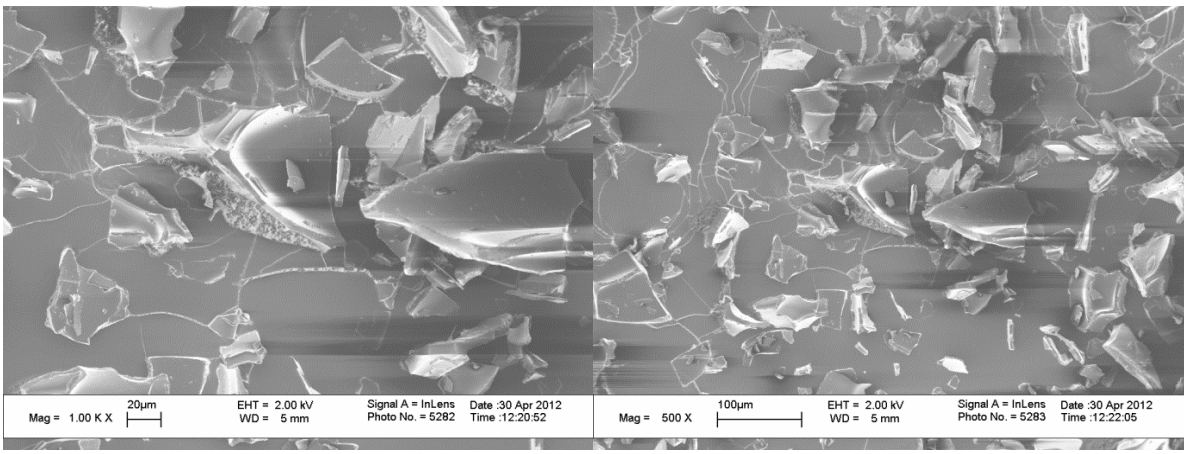


(e) (f)

**Figure 4.19** SEM images of milled S30INM extrudates. Ground HME sample: (a) 1.00kX and (b) 500X; ground HD-fHME: (c) 1.00kX and (d) 500X; and ground LD-fHME: (e) 1.00kX and (f) 500X.

The improvement in milling efficiency observed for the S30INM system by utilizing the foam extrusion technology has also been observed for pure excipients and solid solutions (Verreck et al. 2005; Verreck et al. 2006b; Verreck et al. 2007).

Milling of an extrudate becomes easier upon foaming due to the void fraction in the foam, which affects the stress levels acting on the material during milling. In a foamed extrudate the effective area on which an applied force is acting is very small compared to the same force acting in an un-foamed extrudate. Thus, the effective stress acting on the extrudate is higher in a foamed sample than in a un-foamed one. In addition, if the cells are small enough to act as stress concentrators, then the milling efficiency can be further increased. The same reasoning can be used to understand the change in milling efficiency between the two foamed samples. On one hand, the LD-fHME samples have thinner walls than the HD-fHME samples (two orders of magnitude difference in the thickest walls, see Table 4.5). On the other hand, the density of the LD-fHME extrudate is one order of magnitude lower than in the HD-fHME sample, thus the former has a significantly higher void fraction. Therefore, the LD-fHME extrudate will be subjected to much higher stress levels during milling than the HD-fHME extrudates.

Another approach that can be used to understand the effect of foaming and cellular morphology on the change in milling efficiency is through understanding the changes in their mechanical properties due to cell morphology. The type of cells (i.e. open vs. closed cells), cell size, and foam density are known to affect the mechanical properties of a foam (Shutov 1991; Sun et al. 2002; Wolff et al. 2011). In general, as the density of the foam decreases, the elastic modulus and the strength of the foam tend to decrease, thus a foam with lower density is easier to fracture.

In summary, it is found that the milling efficiency of HME extrudates is increased through cellular structures. Foamed extrudates compared to un-foamed extrudates allowed, under the same milling conditions, to produce smaller particles with a narrower particle size distribution and lower bulk density. However, by simply introducing some degree of porosity in the extrudate without actually producing a foamed structure with closely packed cells and thin walls, the particles produced by milling the extrudate are very similar to the ones produced by milling an un-foamed extrudate.

### 4.4.4 Release of INM from Milled Extrudates

The release profiles of INM from HPMC capsules containing an average of 25 mg of drug are presented in Figure 4.20. While the API in the capsules containing pure INM is in its crystalline γ-form, in the ones containing the milled extrudates INM is amorphous having formed a solid solution with the excipient during extrusion, as was shown in section 4.4.2. The *in vitro* dissolution tests are conducted in a phosphate buffer solution with pH 7.4. The release profiles in Figure 4.20 clearly indicate that INM is released faster from the milled extrudates in capsules, than from capsules containing pure crystalline INM. In 30 min the amount of INM released from capsules containing pure γ-INM is 50 ± 5 %, while from the milled extrudates it is 95 ± 3 % for ground HME sample, 97 ± 1 % for ground HD-fHME and 96 ± 2 % for ground LD-fHME. Since INM is amorphous in the milled extrudates its release is faster compared to the crystalline samples. As mentioned before in section 4.2.1, dissolution of a material in the amorphous state, compared to its crystalline counterpart, is facilitated by the lack of lattice structure and higher free energy (Leuner and Dressman 2000; Bhugra and Pikal 2008).

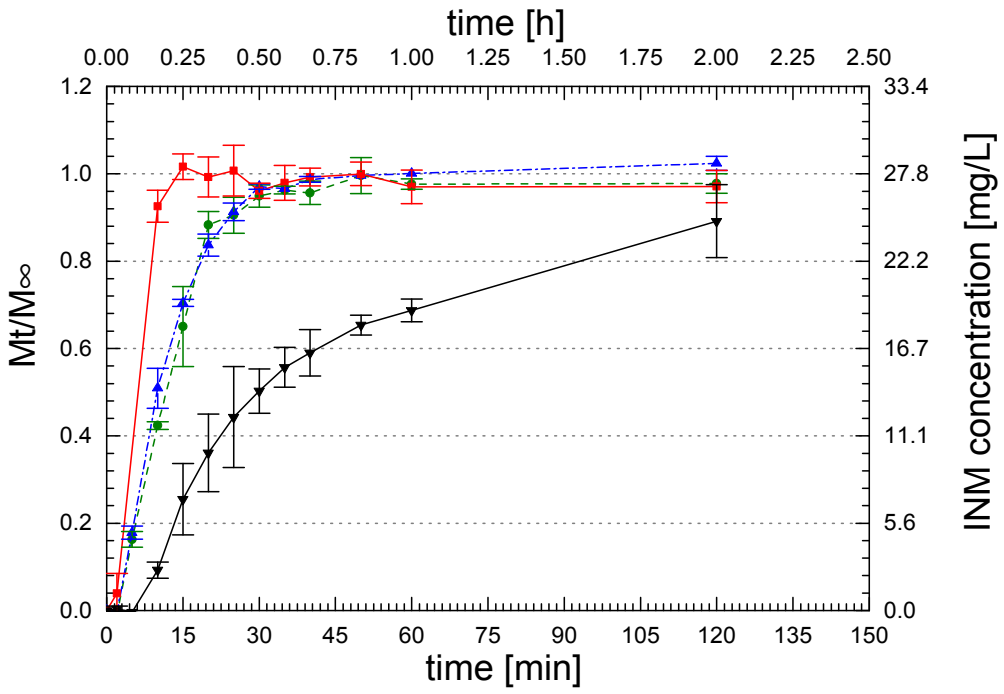


**Figure 4.20** Release profiles from HPMC capsules of pure INM (▼), ground HME sample (●), ground HD-fHME sample (▲), and ground LD-fHME sample (■) in phosphate buffer solution with pH 7.4. Dissolution tests obtained using a USP apparatus 2. Tests were performed in triplicate.

From a general perspective, it can be seen that the release profile of pure INM is characterized by a delay in API's release of approximately 5 min. During this time no API was detected by the UV analysis. In section 4.2.1 this was attributed to the dissolution of the HPMC capsule. However, in this case all the samples were analyzed by placing the powder in the capsules, since the milled extrudates also showed a delay in the API release, although shorter of ~2min, then, it can be concluded that for the pure INM this delay is not only due to the dissolution of the capsule, but also results from slower wetting of the crystalline API compared to the amorphous solid solution particles. In the latter case, the amorphous API was embedded in a polymer which is highly hydrophilic and soluble in the buffer solution, thus wetting was favored in the solid solutions compared to γ-INM.

Up to this point, the release profiles of milled extrudates have been compared to the release profile for pure crystalline INM, and as expected the release rate of the API was accelerated through the formation of an amorphous solid solution during extrusion processing. .

By comparing the release profiles of milled extrudates shown in Figure 4.20 it is clear that ground LD-fHME leads to the fastest INM release, while the release profiles of ground HME and HD-fHME samples are very similar and their release profiles overlap. The amount of INM released in 10 min from ground LD-fHME sample is 93 ± 4 %, from ground HD-fHME sample is 51 ± 5 % and from ground HME sample 42 ± 2 %. These results suggest that there is a direct correlation between release rate and particle size. Other reports can be found in the literature, where it has been shown that solid solution particles produced from milling foam extrudates lead to faster dissolution/release rate than particles produced by milling un-foam extrudates (Lyons et al. 2007; Verreck et al. 2007; Nagy et al. 2012), the same results have also been reported for placebo formulations (Verreck et al. 2006b).

In the literature, numerous mathematical models have been proposed to describe API release/dissolution (Higuchi et al. 1965; Nogami et al. 1970; Ritger and Peppas 1987a; b; Peppas and Sahlin 1989; Narasimhan 2000; Costa and Sousa Lobo 2001). All these models, regardless of the API release mechanism, show a correlation between dissolution/release rate and either a characteristic dimension or the surface area of the particles. In general, a reduction in particle size or an increase in surface area is expected to result in faster release/dissolution rates. As shown in section 4.4.3, the smallest particles were produced by milling the LD-fHME extrudate (see Figure 4.18 and

Table 4.9) and thus this sample showed the fastest API release. On the other hand, the ground HME and HD-fHME samples have very similar particle size distributions, and thus their release profiles are also very similar. However, the release from ground HD-fHME is slightly faster than from the milled un-foam extrudates, because the former has slightly smaller particles and higher surface area. Similar results were obtained by Nagy et al (Nagy et al. 2012) for the solid solution of Carvedilol with EPO, with 20 wt% of drug loading. Andrews et al. (Andrews et al. 2010), on the other hand, did not observe any difference between the release profiles from milled foamed and un-foamed samples; the systems evaluated being also solid solutions comprising Celecoxib and Polyvinyl pyrrolidone with 30wt% of drug loading.

## 4.5 Impact of Foamed Structure and Morphology on API Release Rates from Binary Systems with Different API Release Mechanisms

The impact of foamed structures on the release rate of several API has been reported in the literature, where publications have shown two main trends: in the majority of cases it has been reported that the API release rate is increased upon foaming (Fukuda et al. 2006; Lyons et al. 2007; Verreck et al. 2007; Andrews et al. 2010); on the other hand, few reports indicate that the cellular structures have very little influence or do not affect the API release rate (Fukuda et al. 2006; Lyons et al. 2007; McKelvey et al. 2010). Therefore, it is natural to question if there is some degree of system specificity regarding the impact of a cellular morphology on API release. Therefore the main objective of this section is to study the impact of foaming on the API release profile from different binary systems, and more specifically, examine if a correlation exists between API release mechanisms and the impact of foaming on its release rate.

In order to do this three binary systems are evaluated: PVCap-PVAc-PEG loaded with 30 wt% of INM (S30INM), PVCap-PVAc-PEG loaded with 15 wt% of CBZ (S15CBZ), and EPO loaded with 30 wt% of INM (EPO30INM).

### 4.5.1 Characterization of the Binary Systems: S30INM, S15CBZ and EPO30INM

The state of the API in the three binary systems is characterized combining thermal analysis, FT-IR and XRD. A summary of the glass transitions of S30INM, S15CBZ and EPO30INM obtained by DSC and MTDSC is shown in Table 4.10.

Thermal analyses indicate that in all cases the API is in the amorphous state; no endothermic peaks are observed due to melting and/or API dissolution in the polymeric excipient during the first heating of the HME-prepared samples (see Figure 4.4 in section 4.1, and Figures 4.21 and 4.22 below).

**Table 4.10** Summary of the Glass Transition Temperatures ($T_g$) of the HME-Prepared Binary Systems: S30INM, S15CBZ and EPO30INM

| System | $T_g$ [°C] |
|---|---|
| S30INM* | 62 ± 1 |
| S15CBZ* | 72 ± 1 and 63 ± 1 |
| EPO30INM** | 47.8 ± 0.5 |

Thermal analyses performed by *DSC and **MTDSC

The S30INM and EPO30INM systems showed a single glass transition temperature ($T_g$). This indicates that an amorphous solid solution is produced through the HME process. In other words, the API was fully dissolved in the excipient during compounding and both materials are in amorphous state forming a single phase. Additionally, in both cases a $T_g$ shift with respect to the polymer's glass transition temperature is observed. As mentioned before in section 4.1, in the case of S30INM the

resulting $T_g$ is ~11°C lower that PVCap-PVAc-PEG due to the plasticizing effect of INM on the excipient. Conversely, the $T_g$ of the EPO30INM systems is ~ 3°C higher than EPO's, which has also been reported by other authors and results from very strong interactions between INM and EPO (Chokshi et al. 2005; Liu 2010).

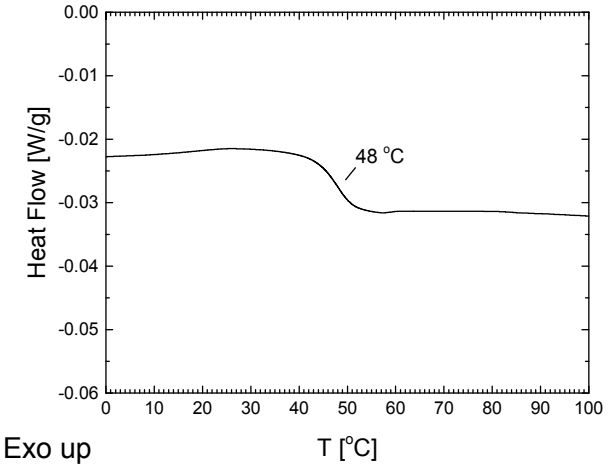


**Figure 4.21** Characteristic 1st heating MTDSC thermogram of HME-prepared EPO30INM binary system.

On the other hand, S15INM showed two glass transition temperatures one at 63 ± 1 °C and the other at 72 ± 1 °C; thus a two phase amorphous system is produced through HME process (i.e. an amorphous solid dispersion). The latter is within the range of PVCap-PVAc-PEG (i.e. 73 ± 2 °C) and the former is between the $T_g$s of the excipient and CBZ. The $T_g$ of CBZ has been reported by other authors to be in the range between 53° and 56 °C (Li et al. 2000; Patterson et al. 2005). These results suggest that CBZ dissolved in the polymer during the HME process, but it is not homogeneously distributed along the matrix. However, this is not indicative of incomplete mixing; content uniformity analysis indicated good content uniformity (14.3 ± 0.5 wt% in the extrudates), which attests to good distributive mixing. Therefore the two $T_g$s most likely

reflect that CBZ is being dissolved within preferential sites within the terpolymer. Since PVCap-PVAc-PEG is a graft terpolymer, then CBZ may be driven to dissolve preferentially in one of the blocks giving rise to two $T_g$s.

While the S30INM system was already analyzed in detail in sections 4.1 and 4.2 and the system EPO30INM was studied in detail by Liu (Liu 2010), the S15CBZ systems has not been studied before. Therefore this discussion is mostly concerned with the properties of this last blend.

Characteristic 1$^{st}$ heating thermograms of CBZ, HME-prepared S15CBZ, and PVCap-PVAc-PEG are shown in Figure 4.22. The two glass transition temperatures for the HME-prepared S15CBZ are clearly shown in the low temperature region of the thermograms in Figure 4.22 (a). In the high temperature region of the thermograms – see Figure 4.22 (b) – it is evident that the HME sample does not have any thermal transitions in this region. On the contrary, pure CBZ shows two endotherms and one exotherm during its 1$^{st}$ heating. The first endoderm corresponds to the melting of p-Monoclinic CBZ, with onset and peak temperatures of 174.5 ± 0.3° and 175.6 ± 0.2 °C, respectively. Following this endotherm, CBZ immediately crystallizes as Triclinic CBZ (peak crystallization temperature of 176.5 ± 0.4 °C). The melting peak for this form is seen as a second endotherm with onset and peak temperatures of 190.4 ± 0.2° and 191.5 ± 0.2 °C, respectively. Similar behavior has been reported extensively in the literature for commercially available CBZ (Otsuka et al. 1999; Rustichelli et al. 2000; Sethia and Squillante 2004; Ugaonkar et al. 2007).

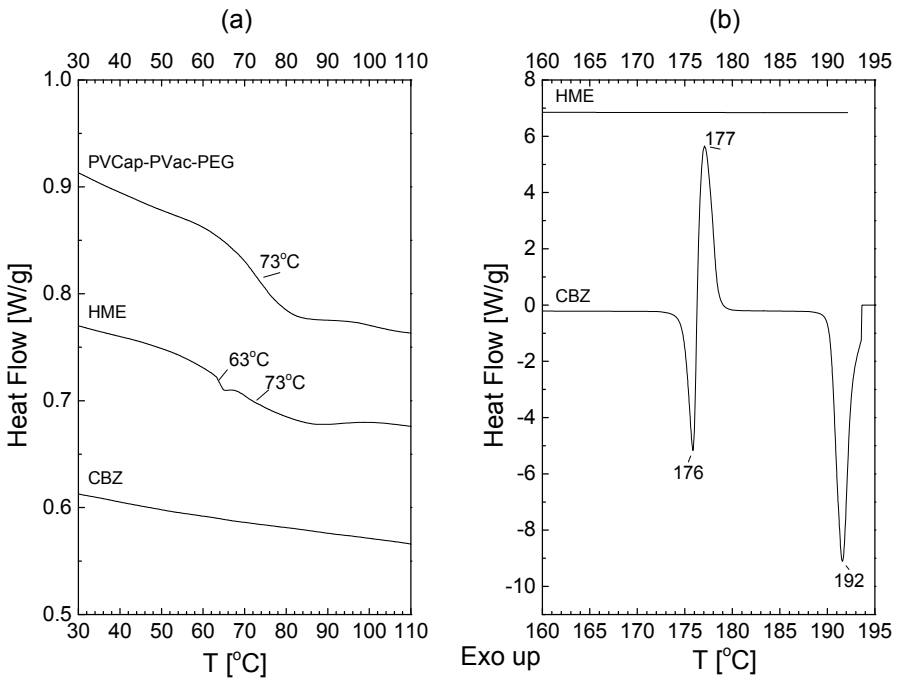


**Figure 4.22** Characteristic 1st heating DSC thermograms of PVCap-PVAc-PEG, HME-prepared S15CBZ, and CBZ. (a) Low temperature region, and (b) high temperature region

Another commonly used characterization technique to assess the state of the APIs in the samples is FT-IR. In the case of INM, FT-IR has been shown to be a very accurate characterization technique to differentiate between its three forms. Figure 4.23 shows the characteristic spectra for both systems containing INM (i.e. S30INM and EPO30INM). As can be seen in Figures 4.23 (a) and (b) in both S30INM and EPO30INM, respectively, the API is in its amorphous state in the extrudates and it remains amorphous after foaming (spectra f-S30INM and f-EPO30INM). As mentioned above, the peak for the stretching vibration of the benzoyl group is seen at 1683 $cm^{-1}$ which corresponds to amorphous INM (see Table 4.2 in section 4.1 and Figure 4.23 below). On the other hand, in the physical mixtures and γ-INM this peak can be seen at 1692 $cm^{-1}$, since the API is crystalline and in its γ-form in both samples.

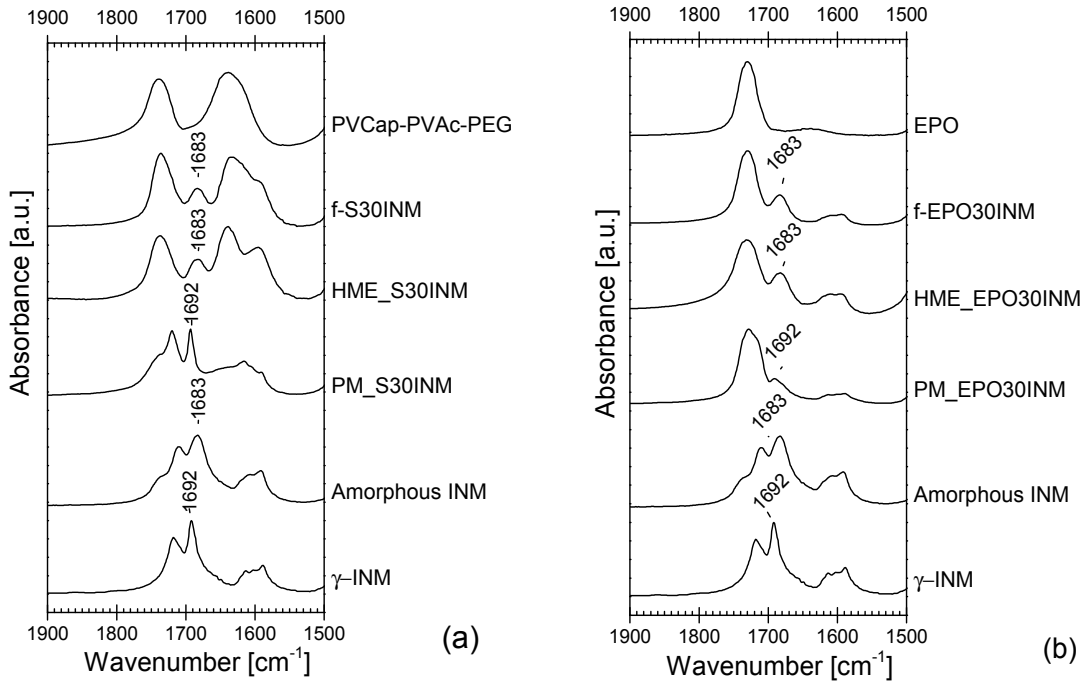


**Figure 4.23** FT-IR spectra of the binary systems: (a) S30INM and (b) EPO30IM. The prefices PM, HME and f are used to indicate the physical mixture, the HME-prepared and foamed samples, respectively. Spectra of the pure excipients PVCap-PVAc-PEG and EPO as well as INM (in its γ-form and amorphous state) are shown as reference.

FT-IR has also been widely used to identify the different polymorphic forms of CBZ (Matsuda et al. 1994; Otsuka et al. 1999; Rustichelli et al. 2000; Kipouros et al. 2006). The region between 3400 – 3600 $cm^{-1}$ shows the most characteristics differences between the different forms of CBZ (Kipouros et al. 2006). In this region the peaks associate with the stretching vibration of N-H bond in the primary amide group in CBZ can be found (Rustichelli et al. 2000; Sethia and Squillante 2004; Kipouros et al. 2006). In the case of p-Monoclinic this peak appears between 3464 - 3466 $cm^{-1}$ (Rustichelli et al. 2000; Kipouros et al. 2006).

As can be seen in Figure 4.24 (a), crystalline CBZ and the physical mixture (PM_S15CBZ), show a strong and sharp peak at 3466 $cm^{-1}$. Since in both these samples CBZ is in the crystalline state, it can be concluded that the crystalline form of the API is

p-Monoclinic. This finding is in agreement with the DSC results presented above. It is interesting to note that the peak at 3466 $cm^{-1}$ is no longer present in the spectra of the un-foamed and foamed S15CBZ samples (HME_S15CBZ and f-S15CBZ, respectively). The absence of this peak indicates that CBZ's amide group is no longer forming hydrogen bonds with itself but with PVCap-PVAc-PEG. The same has been reported for dihydrate CBZ where the CBZ-CBZ hydrogen bonds are replaced with CBZ-$H_2O$ hydrogen bonds (Otsuka et al. 1999), as well as when solid solutions of CBZ and Polyvinyl pyrrolidone (PVP) have been produced (Nair et al. 2001; Sethia and Squillante 2004).

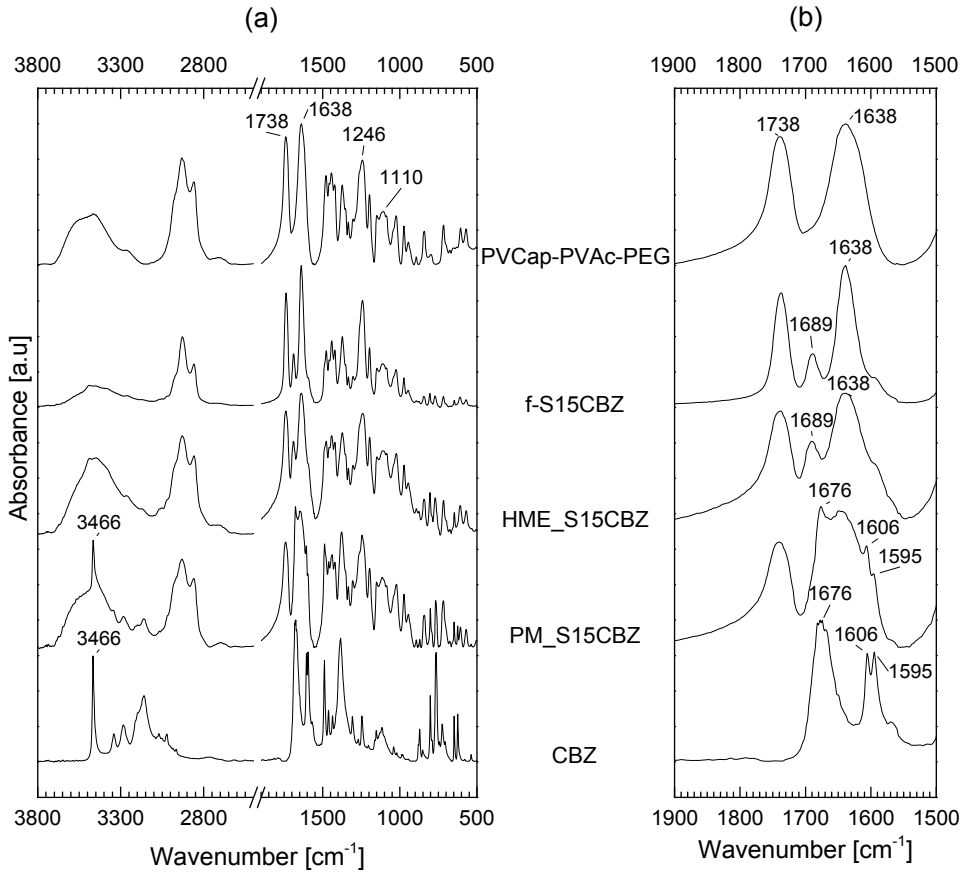


**Figure 4.24** FT-IR spectra of the binary system S15CBZ, (b) shows a detail of (a). The prefices PM, HME and f are used to indicate physical mixture, HME-prepared and foamed samples, respectively. Spectra of the pure PVCap-PVAc-PEG as well as crystalline CBZ are shown as reference.

As described in section 4.1 for the pair INM / PVCap-PVAc-PEG CBZ and PVCap-PVAc-PEG are also capable of forming hydrogen bonds. The amide group in the API has two proton donors ($–NH_2$) capable of participating in hydrogen bonding. However, hydrogen bonds formed between CBZ and PVCap-PVAc-PEG are expected to be weaker than those formed between this excipient and INM. The dipole moment of the O-H bond in INM is 1.53 D while the N-H bond in CBZ has a dipole moment of 1.31 D (Wade 1993).

As described also in section 4.1, the most favorable site for CBZ to be hydrogen-bonded with the excipient are the oxygen atoms double bonded with carbon (C=O) along the branches of PVCap and PVAc, followed by the oxygen atoms in the PVAc branches, and along the PEG backbone. The characteristic FT-IR peaks for these functional groups are indicated in the spectrum of PVCap-PVAc-PEG in Figure 4.24. The peaks seen at 1738 $cm^{-1}$ and 1246 $cm^{-1}$ are characteristic to PVAc, the former corresponds to the C=O stretching vibration and the second one is due to the asymmetric stretching of the acetate (C-O-C) group. The band seen at 1638 $cm^{-1}$ is characteristic of the C=O stretching vibration in the PVCap. Finally, the band at 1110 $cm^{-1}$ results from the asymmetric stretching vibration of the C-O-C in PEG (Socrates 2000). Shifts in these peaks are expected, as hydrogen bonds between CBZ and the polymer are formed. However, in Figure 4.24 (a) it is only in the region between 1710 and 1500 $cm^{-1}$ that appreciable differences can be seen between the spectra of the PM and solid dispersions. These changes in the spectra can be seen more clearly in Figure 4.24 (b) where detail of the spectra between 1900 and 1500 $cm^{-1}$ are shown.

The peaks observed in the spectrum of CBZ in Figure 4.24 (b) at 1676 $cm^{-1}$ correspond to the stretching vibration of hydrogen bonded C=O (Otsuka et al. 1999; Rustichelli et al. 2000). This peak is still detectable in the spectrum of the PM_S15CBZ. After compounding this peak shifted to higher waive number; in the HME_S15CBZ and f-S15CBZ samples this peak can be seen at 1689 $cm^{-1}$. Since CBZ is now dissolved in the polymer, its carbonyl group is no longer participating in hydrogen bonding and the position of this characteristic peak is changed. Prior to compounding CBZ is forming hydrogen bonds with itself through the primary amide group, where its oxygen atom (i.e. oxygen in the carbonyl group C=O) is the proton acceptor and the hydrogen atoms (-$NH_2$). As mentioned before, after compounding the hydrogen bonds are formed between CBZ's proton donors and PVCap-PVAc-PEG's proton acceptors, as a result CBZ's proton donor (C=O) is not involved in the newly hydrogen bonding between CBZ and the polymer excipient.

Another evident change with respect to the spectra of CBZ and the physical mixture is the disappearance of the double peak at 1606 and 1595 $cm^{-1}$. These two peaks are also associated with vibrations of the C=O and N-H bonds. Since the former does not participate in hydrogen bonding after compounding and the latter now forms hydrogen bond with the polymer, then these peaks are no longer clearly visible in the HME and f-S15CBZ samples. Finally, with respect to the characteristic peak of PVCap at 1638 $cm^{-1}$, although a peak shift is not observed after the HME and foaming processes, this peak appears narrower, probably due to interaction between the excipient and CBZ.

In addition to thermal and FT-IR analyses, XRD was also performed for the system S15CBZ. XRD was only performed for this system since it has not been studied

before. Figure 4.25 shows the XRD diffraction patterns for crystalline CBZ, the PM_S15CBZ, HME-prepared S15CBZ, and PVCap-PVAc-PEG. These results clearly show sharp peaks associated with the presence of a crystalline phase only in the PM and crystalline CBZ. However, in the former the peaks are less intense and the baseline is not as flat as for pure CBZ due to the presence of 85 wt% of PVCap-PVAc-PEG which is an amorphous material. In agreement with DSC and FT-IR results, the XRD pattern of the HME-prepared S15CBZ sample indicates that this system is totally amorphous.

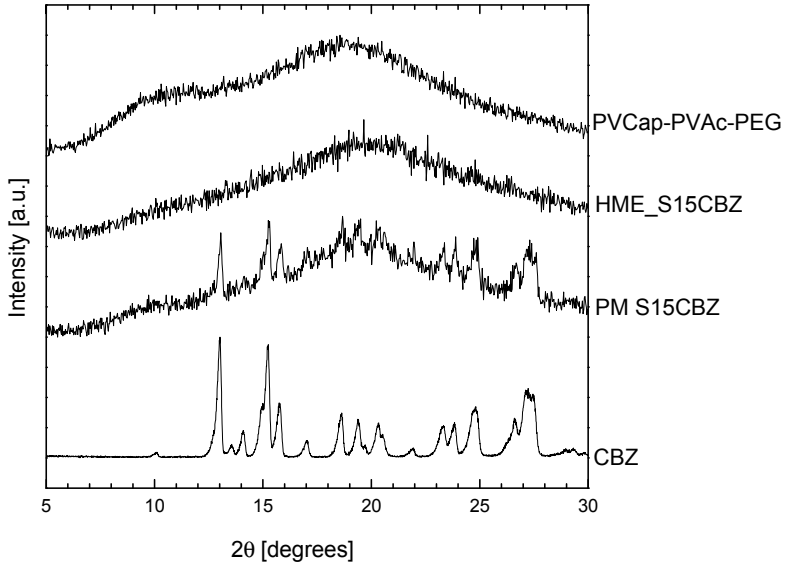


**Figure 4.25** XRD patterns of crystalline CBZ, S15CBZ samples – physical mixture (PM_S15CBZ), and HME-prepared sample (HME_S15CBZ) – and PVCap-PVAc-PEG.

In summary, combining thermal and spectroscopic characterization techniques it is shown that the S30INM and EPO30INM systems are amorphous solid solutions. On the other hand, characterization of the S15CBZ system by DSC, FT-IR and XRD indicates that it is an amorphous solid dispersion.

### 4.5.2 Cellular Morphology in the Foamed Binary Systems: S30INM, S15CBZ and EPO30INM

As described in section 3.2.3 in Chapter 3 following HME process, the extrudates are ground and compression molded into disks of 19 ∅ x 0.3 mm. Since molding is carried out above the glass transition temperature of the systems and under pressure, flow and consolidation are possible and thus the resulting samples are continuous and lacking porosity, as can be seen in Figure 4.26 (a) for the S30INM's sample. Then, through batch foaming process using $ScCO_2$ as PBA, cellular structures were produced as shown the one in Figure 4.26 (b). Foamed samples showed density reductions between 94.3 and 96.5 % (see Table 4.11) with respect to their original compression molded density (i.e. un-foamed disks) due to the high degree of foaming expansion induced by the dissolved $ScCO_2$ coming out of solution with the sudden decompression.

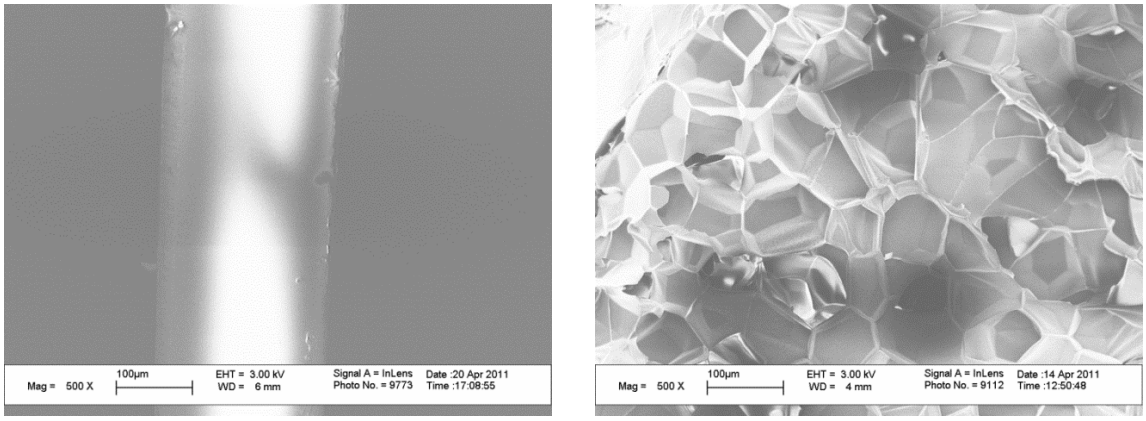


(a) (b)

**Figure 4.26** SEM images of cross-sectional surfaces of the S30INM samples: (a) un-foamed disk of 19 ∅ x 0.3 mm, and (b) foamed disk.

All foamed samples have predominantly closed cell morphology, as can be seen in all SEM images of the cross-sectional area of foamed samples (see Figures 4.27, 4.28 and 4.29). In other words, the cells (or bubbles) are not interconnected and the cross-

sections of the foamed samples have honeycomb-like morphology. The foamed S30INM and S15CBZ samples (f-S30INM and f-S15CBZ, respectively) have very similar cellular morphologies. As can be seen in Table 4.11 their densities, cell size and wall thickness are very similar.

**Table 4.11** Summary of the Characteristics of the Foamed Binary System: S30INM, S15CBZ, and EPO30INM

| Property | Binary System | | |
|---|---|---|---|
| | S30INM | S15CBZ | EPO30INM |
| Density of the un-foamed disk [g/cm$^3$] | 1.01 ± 0.05 | 1.09 ± 0.03 | 1.11 ± 0.02 |
| Density of the foamed disks [g/cm$^3$] | 0.038 ± 0.001 | 0.038 ±0.005 | 0.06 ± 0.02 |
| Density reduction after foaming [%] | 96.2 | 96.5 | 94.3 |
| Cell size range [μm] | 16-130 | 14-128 | 7-215 |
| Wall thickness range [μm] | 0.4-1.7 | 0.8-2.1 | 0.5-10.6 |

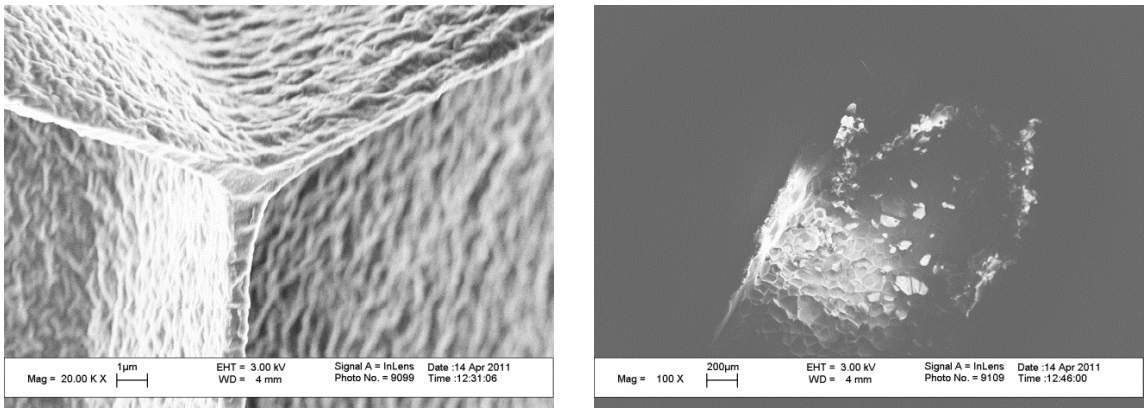


(a) (b)

**Figure 4.27** SEM images of cross-sectional surfaces of a f-S30INM disk: (a) 20.00kX and (b) 100X.

The foamed EPO30INM samples (f-EPO30INM) have slightly different morphology than the systems containing PVCap-PVAc-PEG as the matrix. In the

summary presented in Table 4.11 it is evident that the f-EPO30INM samples have a broader cell size and wall thickness distributions, with overall bigger cells and thicker walls, which lead to a smaller reduction in density upon foaming than the other two systems. In addition, in the high magnification SEM images of the cross-section of the samples it is evident that the surfaces of the cells of the f-EPO30INM samples are smooth, [see Figure 4.29 (a)], while the surfaces of the cells of the f-S30INM and f-S15CBZ samples have regularly rough (ribbed) patterns [see Figures 4.27 (a) and 4.28 (a), respectively].

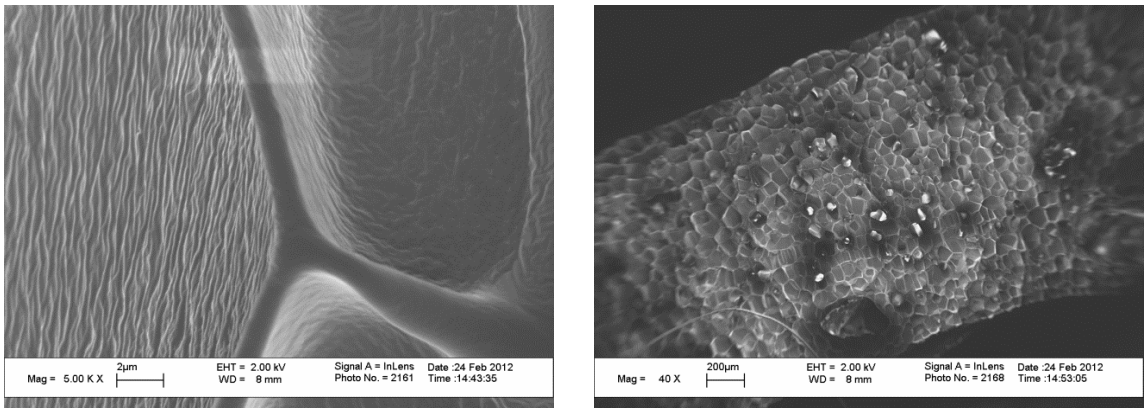


(a) (b)

**Figure 4.28** SEM images of cross-sectional surfaces of a f-S15CBZ disk: (a) 5.00kX and (b) 40X

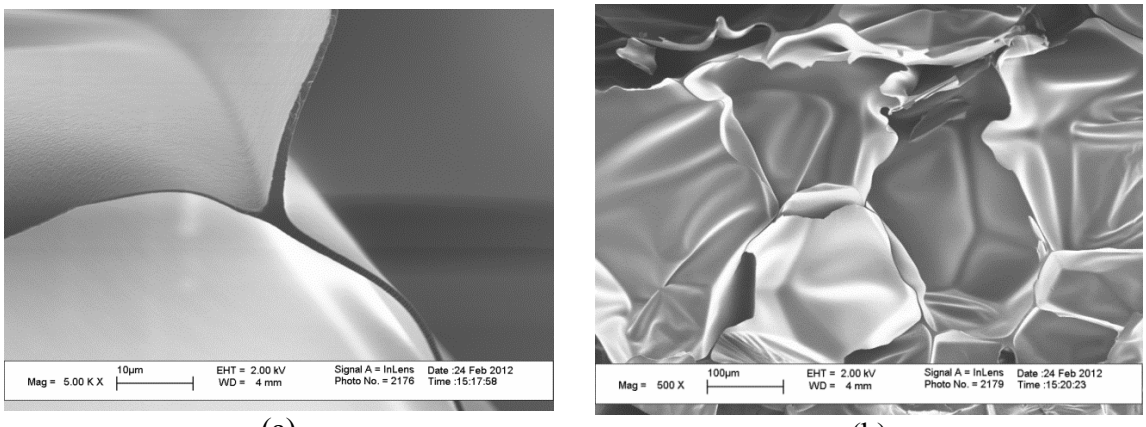


(a) (b)

**Figure 4.29** SEM images of cross-sectional surfaces of a f-EPO30INM: (a) 5.00kX and (b) 500X.

In all three cases batch foaming is performed above the $T_g$ of the systems (38 °C in the case of S30INM and 47 °C in the other two cases). At these foaming temperatures the materials are in a rubbery state, which is quite elastic and thus not capable of purely viscous flow. During cellular growth the material is subjected to bi-axial tension and deformation. Therefore the rough patterns observed in the f-S30INM and f-S15CBZ samples can be attributed to the rheological properties of the excipient at the foaming conditions. Since PVCap-PVAc-PEG has significantly higher viscosity than EPO – e.g. at 170°C the zero shear rate viscosities are 3.5 x $10^3$ Pa·s (see Appendix D) and 5 x $10^2$ Pa·s (Liu 2010), respectively; then elongational flow is easier for EPO30INM than for S30INM and S15CBZ, and thus smother surfaces without elastic instabilities are generated during batch foaming.

As mentioned above, the f-EPO30INM samples have predominantly closed cells; close inspection of the surface of the samples however showed the presence of open cells or porosities along the face of the samples that is contact with the heated surface of the mold during the batch foaming process, that is, the "bottom" face in Figure 4.30 (a). The other surface – the "top" or free surface during the batch foaming process – has only closed cells, with no open cells visible in Figure 4.30 (b). This fraction of open cells on the bottom surface in the EPO30INM system is expected to have an impact in INM release from the foamed samples, since it constitutes further increase in surface area.

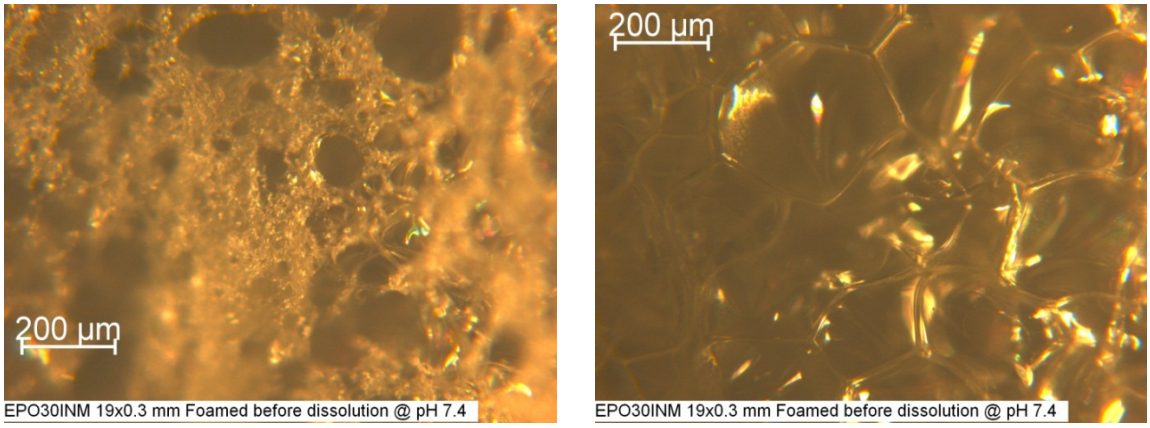


(a) (b)

**Figure 4.30** Optical microscope images of: (a) bottom face and (b) top face of a f-EPO30INM disk.

### 4.5.3 Mathematical Models Describing API Release from Continuous Non-porous Planar Polymer Sheet

From a general physical perspective, the release mechanism of an API from an amorphous solid solution or dispersion into a "solvent" involves the following processes: (1) surface wetting, (2) solvent penetration into the system, (3) polymer swelling, (4) API diffusion, and (5) polymer dissolution (if polymer dissolution is possible) (Narasimhan and Peppas 1997; Narasimhan 2001; Siepmann and Peppas 2001). The three mass transfer processes involved (i.e. solvent penetration, API diffusion and dissolution) are schematically presented in Figure 4.31.

All three mass transfer processes take place during the API release from any delivery system where the API in imbibed in a polymeric matrix. However, one will be the rate limiting step and thus the controlling mechanism. There are three main mechanisms that control API release, these are: (1) diffusion controlled, also known as Fickian or Case I release; (2) relaxation-controlled, also known as Case II, swelling controlled, zero order release or mass erosion; and (3) anomalous transport. Well established mathematical models have been used to describe API release from the first to

controlling models and are discussed in more detail below. Additionally, empirical and semi-empirical mathematical models can be used to identify the controlling release mechanism for an API in a given formulation; one of which is discussed in detail in section 4.5.4.

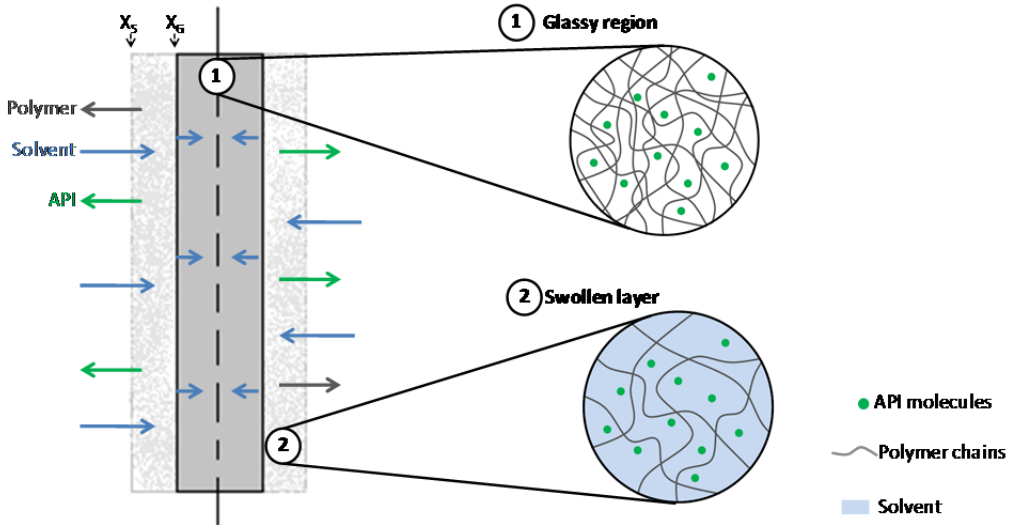


**Figure 4.31** Schematic representation of the API release mechanism from solid solution. On the left, the three mass transfer processes are indicated (i.e. solvent penetration, API diffusion, and polymer dissolution). On the right, the difference between (1) the glassy core region (dry region) and (2) the swollen surface layers are illustrated. The green dots represent the API molecules dissolved in the polymer; the polymer chains are shown as gray lines, and the solvent in blue.

**4.5.3.1 Mathematical Model Describing API Release from a Thin Polymer Film Through Fickian Diffusion.** Equation 4.8 represents Fick's second law in the case of a thin film or slab, where one-dimensional diffusion in the x direction and constant diffusion coefficient are assumed.

$$\frac{\partial C}{\partial t} = D\frac{\partial^2 C}{\partial x^2} \tag{4.8}$$

Where C represents the API concentration, t represents time, and x the diffusional direction.

Then, equation 4.8 can be solved considering the appropriate boundary conditions for API release from a thin polymer sheet or slab of thickness 2L (with a symmetry line at x=0). In the present case, initially the concentration of API in the slab is considered to be uniform and constant and defined as $C_1$, and the concentration of API at the surface is maintained constant as $C_s$. These boundary conditions are summarized in expression 4.9, and the corresponding exact solution of Fick's second law is shown in equation 4.10.

$$\begin{array}{lll} t = 0 & -L < x < L & C=C_1 \\ t > 0 & x= \pm L & C=C_s \end{array} \tag{4.9}$$

$$\frac{M_t}{M_\infty} = 1 - \frac{8}{\pi^2}\sum_{n=0}^{\infty}\frac{1}{(2n+1)^2}exp\left\{\frac{-D(2n+1)^2\pi^2 t}{L^2}\right\} \tag{4.10}$$

Where $M_t$ denotes the amount of API released at time *"t"* and $M_\infty$ the corresponding amount at infinite time.

It is well know that expression 4.10 can be a simplified for short times (i.e. for $M_t/M_\infty \leq 0.6$) as shown in equation 4.11 (Crank 1975).

$$\frac{M_t}{M_\infty} = 4\left(\frac{Dt}{\pi L^2}\right)^{1/2} \tag{4.11}$$

**4.5.3.2 Mathematical Model Describing Relaxation Controlled API Release from a Thin Polymer Film.** In the case of API release from a thin film described by Case II transport (i.e. relaxation controlled system) the mathematical model was developed by

Enscore et al. (Enscore et al. 1977) by combining a kinetic expression which describes the rate at which the penetrant is absorbed by the systems and a mass balance expression. The two principal assumption with a case II transport are: (1) the concentration profile of the penetrant is step-like, and (2) both the dissolving front and the swollen-glassy interphase (boundaries shown as $X_S$ and $X_G$, respectively in Figure 4.31) move at a constant velocity (Comyn 1985; Narasimhan and Peppas 1997). It should point out that this model was developed to describe sorption of solvents into a glassy polymer. However, this model is used to describe the release profile of drug delivery systems where API release is said to be relaxation controlled, since the swelling and dissolution kinetics of the polymer film control the release of the API.

Having the aforementioned assumptions in mind, then a mass balance for one-dimensional transport can be defined by expression 4.12, and the kinetic expression is given by equation 4.13.

$$M_t = (L - x)YZ\ C_o \tag{4.12}$$

$$\frac{dM_t}{dt} = k_o YZ \tag{4.13}$$

Where the product $(L - x)YZ$ represents the volume of the swollen layer, in more detail $(L - x)$ is the thickness of the swollen layer, $L$ the characteristic length of the film (i.e. half it thickness) and $0 \leq x \leq L$. The constants $C_o$ and $k_o$ represent the equilibrium penetrant concentration and the relaxation constant respectively.

Then, equation 4.14 is obtained by substituting the mass balance expression into the kinetic expression (equations 4.12 and 4.13, respectively). This expression is used to obtain a relationship between *x* and time.

$$\frac{d[(L-x)C_o N(a) YZ]}{dt} = k_o YZ\ N(L) \tag{4.14}$$

Through differentiation and simplification expression 4.14 becomes:

$$\frac{dx}{dt} = -\frac{k_o}{C_o} \tag{4.15}$$

Then, the algebraic relationship for x as a function of time is given by equation 4.16, only for $0 \leq t \leq L \cdot C_o/k_o$; in other words, from the beginning of dissolution until the "glassy" or dry region is completed depleted.

$$x = L - \frac{k_o}{C_o} t \tag{4.16}$$

By substituting equation 4.16 in 4.12 and by further simplification results in expression 4.17, this expression described the release of an API from a relaxation controlled systems until the "glassy" region is completely depleted.

$$\frac{M_t}{M_\infty} = \frac{k_o}{C_o L} t \tag{4.17}$$

### 4.5.4 Determination of API Release Mechanisms from Several API / Polymer Excipient Binary Systems

In the present study the experimental data for the three binary systems: S30INM, S15CBZ and EPO30INM are fitted using a semi-empirical mathematical model known as the Power Law model shown in equation 4.18.

$$\frac{M_t}{M_\infty} = k \cdot t^n \tag{4.18}$$

Where $M_t$ and $M_\infty$ are the masses of released API at time "$t$" and at infinite time, respectively, $k$ is a constant which accounts for structural and geometric characteristics of the sample, $t$ is the release time, and $n$ is the release exponent which depends on sample geometry and release mechanism.

In the literature this model is widely known as the Power Law, the Korsmeyer-Peppas model or simply the Peppas model (Costa and Sousa Lobo 2001; Siepmann and Peppas 2001), and can be used to identify the mechanism (i.e. Fickian diffusion, relaxation-controlled or anomalous transport) controlling API release from a polymer based system according to the values of the release exponent ($n$) in equation 4.18 as summarized in Table 4.12. However, it should be mentioned that this approach was first used by Enscore et al. (Enscore et al. 1977) to identify the mechanism of fluid sorption and desorption (i.e. Fickian vs. Case II – relaxation controlled – transport) in polymer microspheres. Latter this model was introduced by Ritger and Peppas. (Ritger and Peppas 1987a; b; Peppas and Sahlin 1989) to describe drug release from polymeric devices. Since then many researchers have used this model or variations of it to identify the release mechanism from diverse drug delivery systems (Korsmeyer et al. 1983; Bruce

et al. 2005; Huang et al. 2006; Andrews et al. 2008; Yang et al. 2010; Ha and Xanthos 2011).

In order to accurately use the Power Law model it is essential to understand the assumptions associated with it as well as its limitations. First of all, equation 4.18 was adapted from the short time solutions for Fickian and non-Fickian transport through a thin film or slab (Ritger and Peppas 1987a). Therefore, when applying this model two key conditions must be fulfilled: (1) one-dimensional transport must be assured, and (2) the model is only valid up to 60% of drug released (Ritger and Peppas 1987a). While the latter can be easily meet, it is harder to comply with the former as in reality three-dimensional transport takes place. Nonetheless, certain geometrical consideration may be used in order to approximate three-dimensional transport process to a one-dimensional process. By considering a disk with diameter $2a$ and thickness $l$ and defining the aspect ratio of the samples as $2a/l$, then three limiting conditions can be defined where the one-dimensional transport can be assumed. These are: a thin film when $2a >> l$, a sphere when $2a \cong l$, and cylinder when $2a << l$. In these cases transport in the longest path (largest dimension) can be neglected with respect to the shortest path, thus the one-dimensional approximation becomes valid.

Since the release exponent "$n$" in equation 4.18 depends not only on the API release mechanism but it is also a function of the sample's geometry (see Table 4.12), it is also important to know the aspect ratio of the sample in order to do a correct interpretation of the fitting results. This geometry dependence can be seen clearly in Figure 4.32, which shows the correlation between the release exponent "$n$", for a diffusion controlled system, and the aspect ratio of the sample.

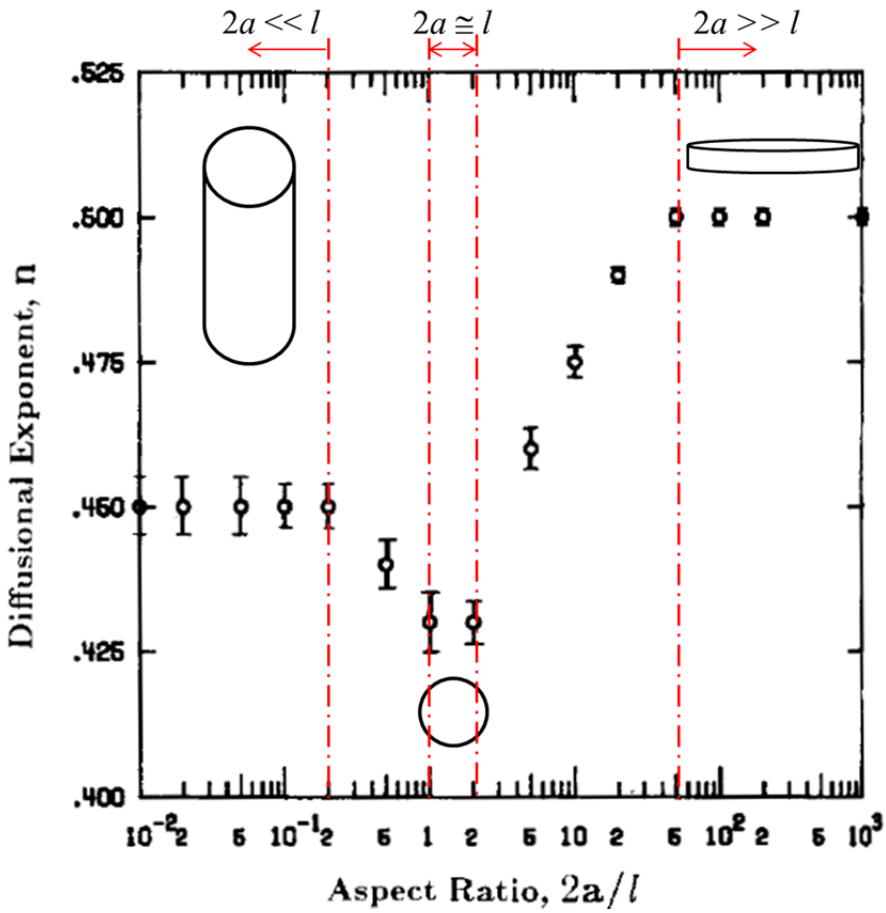


**Figure 4.32** Release exponent (*n*) in the Power law model for API release controlled by Fickian diffusion as a function of the aspect ratio of the sample. Figure adapted from: (Ritger and Peppas 1987a).

In the present study, the release mechanism of INM and CBZ from the amorphous solid solutions and dispersion S30INM, EPO30INM and S15CBZ are determined using compression molded samples of 19∅ x 0.3 mm which resulted in an aspect ratio of 63, thus it can be considered a thin film geometry or slab.

**Table 4.12** Values of the Power Law Release Exponent "*n*" for Each API Release Mechanism and Sample Geometry

| Mechanism Controlling the API Release | Release Exponent (*n*) Values | | |
|---|---|---|---|
| | Cylindrical Sample* $2a/l \leq 0.2$ | Spherical Sample* $1 \leq 2a/l \leq 2$ | Thin Film* $2a/l \geq 50$ |
| Fickian diffusion | 0.45 | 0.43 | 0.50 |
| Relaxation controlled | 0.89 | 0.85 | 1 |
| Anomalous transport | 0.45<n<0.89 | 0.43<n<0.85 | 0.50<n<1 |

*Limiting values for the aspect rations, $2a/l$, were determined from Figure 4.32
Source: (Ritger and Peppas 1987a)

*In vitro* dissolution tests of the S30INM system are performed in a phosphate buffer solution with pH 7.4 and containing an average of 35 mg of drug loading. The S15CBZ system containing an average of 16 mg of drug loading is tested in deionized water, which is the dissolution medium established for CBZ in its USP monograph. Finally the EPO30INM system is tested in two solutions: a hydrochloric acid buffer solution with pH 1.2 and a phosphate buffer solution with pH 7.4. In both cases the samples' drug loading is an average of 30 mg. These two buffer solutions were selected because they provide two extreme scenarios. At pH 1.2 INM solubility is extremely low (i.e. 1 mg/L (Yazdanian et al. 2004)) but the excipient is soluble. On the other hand, at pH 7.4 the drug solubility is much higher (i.e. 1300 mg/L (Yazdanian et al. 2004)) but the excipient is insoluble, it only swells as the solvent is absorbed.

Figure 4.33 shows the experimentally determined APIs release profiles under the four *in vitro* dissolution conditions evaluated together with the Power law fittings. It should be pointed out that in the case of S30INM, S15CBZ and EPO30INM in pH 1.2 only partial release profiles are shown – up to 60 % - since this is the range where the

model can be applied. As can be seen in Figure 4.33 the fittings, obtained using OriginPro® software, are in very good agreement with the experimental data. A summary of the values of the release exponent ($n$) and the Power law constant ($k$) determined for each system are shown in Table 4.13.

**Table 4.13** Determined Values of the Release Exponent ($n$) and the Power Law Constant ($k$) for the Binary Systems Using Samples of 19 ∅ x 0.3 mm (Thin Film Geometry).

| Parameter | S30INM | S15CBZ | EPO30INM | |
|---|---|---|---|---|
| | | | pH 1.2 | pH 7.4 |
| $n$ | 1.02 ± 0.05 | 0.71 ± 0.01 | 1.0 ± 0.1 | 0.499 ± 0.008 |
| $k$ [$min^{-n}$] | 0.040 ± 0.004 | 0.027 ± 0.001 | 0.06 ± 0.02 | 0.0030 ± 0.0001 |
| $R^2$ | 0.998 | 0.998 | 0.974 | 0.998 |
| Release mechanism | Relaxation controlled | Anomalous controlled | Relaxation controlled | Diffusion controlled |

As can be seen in Table 4.13 and Figures 4.33 (a) and (c), the API release rate of two of the systems is independent of time, often referred to as zero order release (Narasimhan 2000; Costa and Sousa Lobo 2001). The two systems that show this behavior are S30INM and EPO30INM in pH 1.2; in both cases the release exponent obtained is 1 (specifically 1.02 ± 0.05 and 1.0 ± 0.1, respectively), which corresponds to relaxation-controlled API release in a thin film or slab. From a physical point of view the release rate of INM from these systems is controlled by the swelling of the solid solution, as the solvent is absorbed by the thin film, and its consequent dissolution.

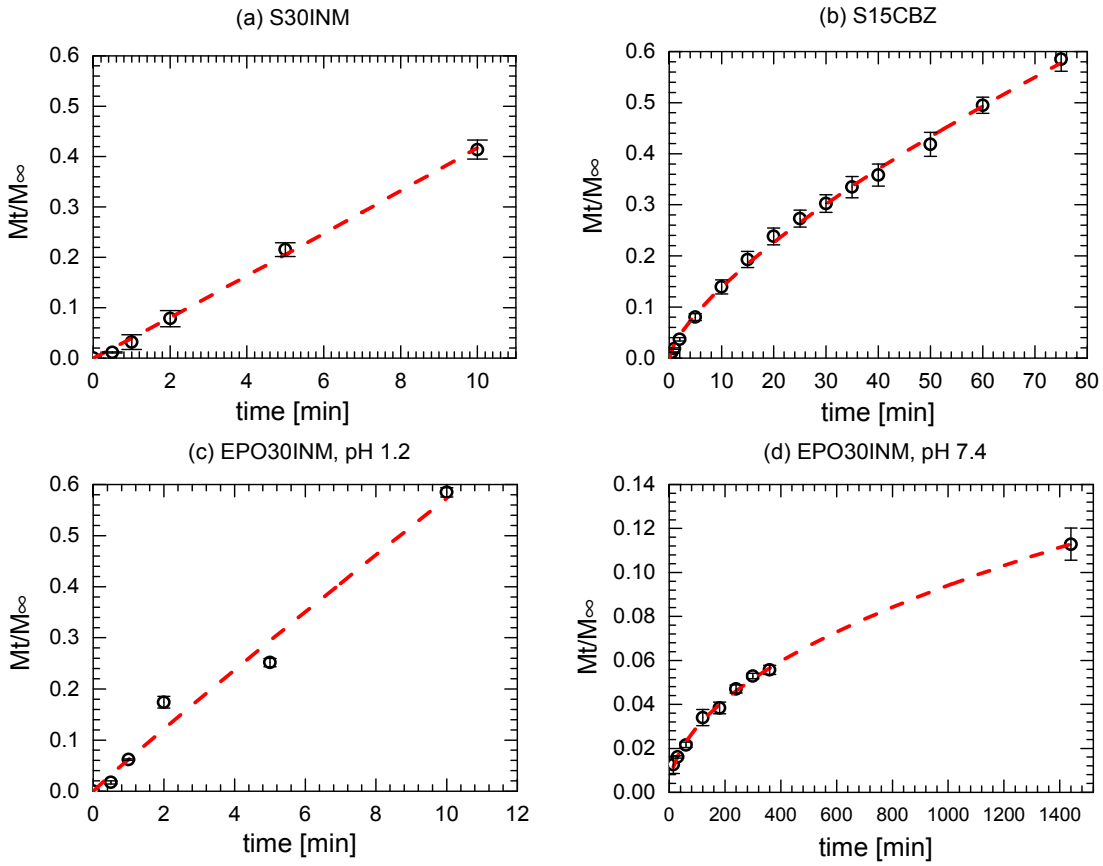


**Figure 4.33** Comparison between experimentally determined API release from disks of 19 ∅ x 0.3 mm (O), and the power law fitting (dashed lines) for the binary systems: (a) S30INM in pH 7.4, (b) S15CBZ in deionized water, (c) EPO30INM in pH 1.2, and (d) EPO30INM in pH 7.4. All dissolution tests performed using a USP apparatus 2 and in triplicate.

In this liming case, a thin film geometry where the Power law release exponent takes the value $n = 1$ the empirical constant ($k$) has physical meaning, and it is defined by equation 4.19, as follows:

$$k = \frac{2\,k_o}{C_o L} \tag{4.19}$$

Where $k_o$ is the relaxation constant [mg/cm$^2$min], $C_o$ is the equilibrium penetrant concentration, and $L$ is the sample's characteristic length (in the case of a thin film it corresponds to the half-thickness of the sample, ½ $l$).

It should be noted that there are two more considerations associated with a case II transport: (1) the concentration profile of the penetrant (buffer solution in the present case) is step-type, and (2) both the dissolving front and the swollen-glassy interphase (boundaries shown as $X_S$ and $X_G$, respectively in Figure 4.31) move at a constant velocity (Comyn 1985; Narasimhan and Peppas 1997).

The results in Table 4.13 show that the S30INM system has a lower $k$ value than the EPO30INM system in pH 1.2, these are 0.040 ± 0.004 min$^{-1}$ and 0.06 ± 0.02 min$^{-1}$, respectively. Then it can be inferred that the ratio between relaxation constant and equilibrium penetrant concentration (i.e. $k_o/C_o$) for the system EPO30INM in pH 1.2 is slightly higher than in the system S30INM. This ratio represents the rate at which the relaxation front moves toward the core of the sample (Enscore et al. 1977); thus, the advance rate of the dissolving face and of the glassy-swollen interface is faster in the case of EPO30INM in pH 1.2 than in the case of S30INM. As the name of this mechanism indicates, the release rate is controlled by the relaxation rate of the solid solution triggered by solvent absorption and subsequent swelling. Therefore, overall system mobility and more specifically the mobility of the polymeric phase will greatly affect the release rate, and hence polymer swelling can be can be seen as a viscous response of the material (Comyn 1985). Since EPO has lower viscosity than PVCap-PVAc-PEG as well as lower molecular weight (47 x 10$^3$ g/mol and 118 x 10$^3$ g/mol, respectively), then relaxation and dissolution of EPO is easier compared to that of PVCap-PVAc-PEG.

Thus, the relaxation front can move faster in the EPO30INM system than in the S30INM system resulting in higher *k* value and faster release.

As expected the INM release from the EPO30INM systems in pH 7.4 is diffusion controlled and the release exponent is 0.499 ± 0.008 (see Tables 4.12 and 4.13). Since EPO is insoluble at pH 7.4 while INM is soluble, then it is logical that its release is described by Fickian diffusion though the swollen polymer. As discussed above for the limiting case for a thin film with $n = 1$, when $n = 0.5$ then the constant "$k$" in equation 4.18 also has physical meaning and is defined by equation 4.20.

$$k = 4\sqrt{\frac{D}{\pi L^2}} \tag{4.20}$$

Where $D$ is the diffusion coefficient [$cm^2/s$], and $L$ is the sample's characteristic length (i.e. half thickness of the sample, ½ $l$). In this case the Power law model becomes the short time approximated solution for the diffusion equations through a thin film (Crank 1975; Comyn 1985). Then the diffusion coefficient of INM through EPO in a buffer solution with pH 7.4 is $6.6 \times 10^{-12}$ $cm^2/s$, which is in the same order of magnitude compared to the values reported in the literature for other APIs and small molecules diffusing through polymers (Enscore et al. 1977; Huang et al. 2006).

From a physical perspective, INM release in this case is driven by the solvent concentration gradient across the sample (Peppas and Sahlin 1989; Amidon et al. 2000). In addition, INM diffusion through the swollen layer with respect to the glassy region is possible due to higher mobility and weaker API-polymer interactions. As mentioned in

section 4.2.1, INM ionization is highly favored at pH 7.4 and thus its release under these conditions is further favored.

Finally, CBZ's release mechanism from the S15CBZ system is controlled by anomalous transport. As can be seen in Table 4.13 the release exponent was determined to be 0.71 ± 0.01. Anomalous transport results from the combined influence of both diffusion and relaxation phenomena during drug release (Vrentas et al. 1975; Frisch 1980; Ritger and Peppas 1987a). Specifically for the S15CBZ system coupling of relaxation and diffusion may result from the two phases present in the system. It was shown above that this system is an amorphous solid dispersion.

### 4.5.5 Effect of Cellular Structure on the API Release Rate

Figures 4.34 through 4.37 show comparisons between the API release profiles from foamed and un-foamed disks of S30INM, S15CBZ and EPO30INM in pHs 1.2 and 7.4. It is important to point out the in all cases the samples were placed in the USP apparatus 2 as disks without modifying the geometry of the samples. In other words, the cellular structures were not disrupted or destroyed. Therefore, the changes in release/dissolution profiles of the foamed samples with respect to their un-foamed counterpart can be attributed solely to geometrical changes introduced by the cellular structure.

The results shown in Figures 4.34 through 4.37 indicate that API release was accelerated upon foaming in all cases. However, the degree in which the foamed structure enhances API release rate differs among the systems been evaluated.

In the case of the S30INM system (see Figure 4.34) complete release is achieved for both foamed and un-foamed samples. However, the time for completing release for

the f-S30INM sample is 20 min, while the un-foamed sample required 35 min for completing INM release; this represents a reduction in release time of 43 %.

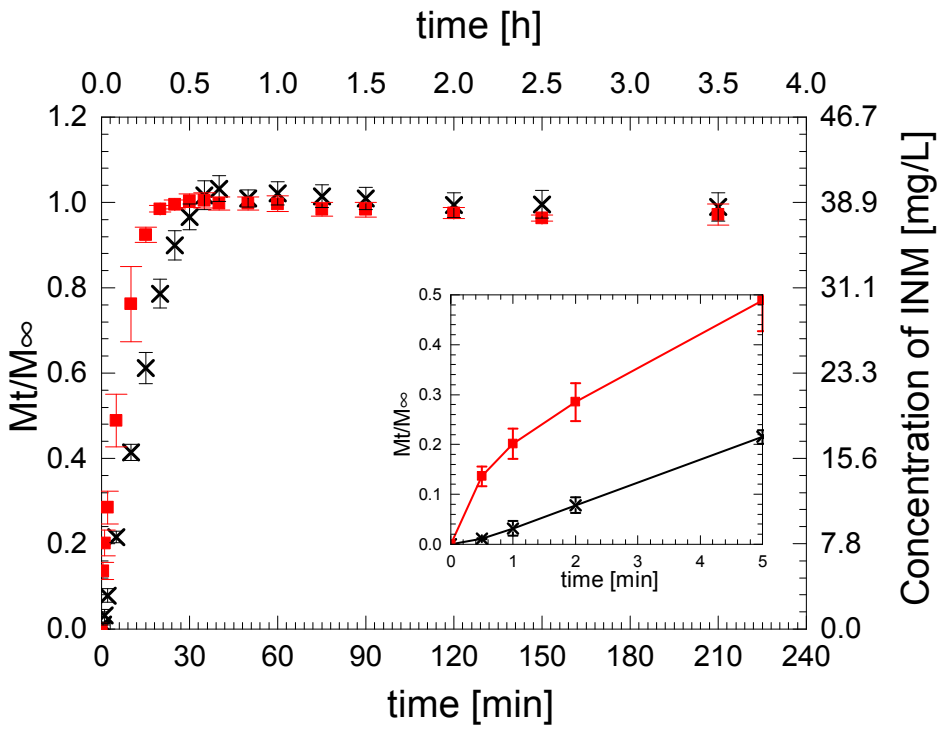


**Figure 4.34** INM's release profiles from the S30INM solid solutions: (×) un-foamed disks (19∅ x 0.3 mm), and the corresponding (■) foamed disks in phosphate buffer solution with pH 7.4. Inset plot shows a detail of the initial 5 min of the release profiles. Dissolution profiles obtained using a USP apparatus 2. Tests were performed in triplicate.

Since INM's monograph states – for all its immediate release dosage forms – that no less than 80 % of the drug must be released in 20 min then it is relevant to compare the amount of INM released in 20 min and the time required to release 80 % of the API. Within 20 min, 78 ± 3 % of INM is released from the un-foamed samples, but 99 ± 1 % from the f-S30INM disks; this represents a 27 % increase in the amount of API been released upon foaming. On the other hand, from the release profile it can be established that 80 % of INM is released within 10 to 15 min from f-S30INM, but 20 to 25 min are

required for the un-foamed samples. Therefore, by using cellular structures it is possible to assure that the immediate release requirement is fulfilled.

The inset plot in Figure 4.34 shows a detail of the first 5 min of the release profiles of the S30INM samples. In this detail of the release profiles a "burst" in release can be seen for the f-S30INM sample; 13-fold more API is released from the foamed sample compared to the un-foamed one. In 30 s the amount of INM released from f-S30INM is 14 ± 2 % while only 1.1 ± 0.1 % from its un-foamed counterpart. This behavior results from faster solvent absorption in the foamed samples compared to the un-foamed ones due to higher surface area and shorter characteristic lengths along the cell walls in the latter case. The characteristic length for the un-foamed disk is 150 μm (half-thickness of the disk) while in the foamed samples it is 0.4 - 1.7 μm (i.e. the cell wall thicknesses, reported in Table 4.11).

In the previous section it was shown that INM release from the S30INM system is relaxation-controlled, in other words the swelling and dissolution kinetics of the solid solution drive the release of the API. Therefore, the change in sample geometry introduced by the cellular structure affects the swelling kinetics of the solid solution not only by changing the characteristic lengths but by introducing very complex velocity profiles of the penetrant advancing front throughout the foamed structure. Since there is a distribution of characteristic lengths there is also a distribution of swelling or "relaxation" rates. This further contributes to accelerate the release rate in foamed samples and it will be discussed in more detail in section 4.7.2.

The other system that has relaxation-controlled API release is EPO30INM in pH 1.2. The release profiles of INM from foamed and un-foamed samples from this system

are shown in Figure 4.35. As with S30INM, the most significant difference in release rate due to the cellular structure is observed in the initial region of the release profile. In 30 s the amount of API released from the foamed samples is one-order of magnitude higher compared to the amount released from the un-foamed samples; 10.8 ± 0.3 % from f-EPO30INM and only 1.3 ± 0.3 % from the un-foamed disks. This results from faster solvent absorption and faster swelling of the foamed samples sample due to an increase in surface area and reduction in characteristic lengths from 150 μm to 0.5 - 10.6 μm (see Table 4.11). However, after 2 min the profiles become parallel to each other.

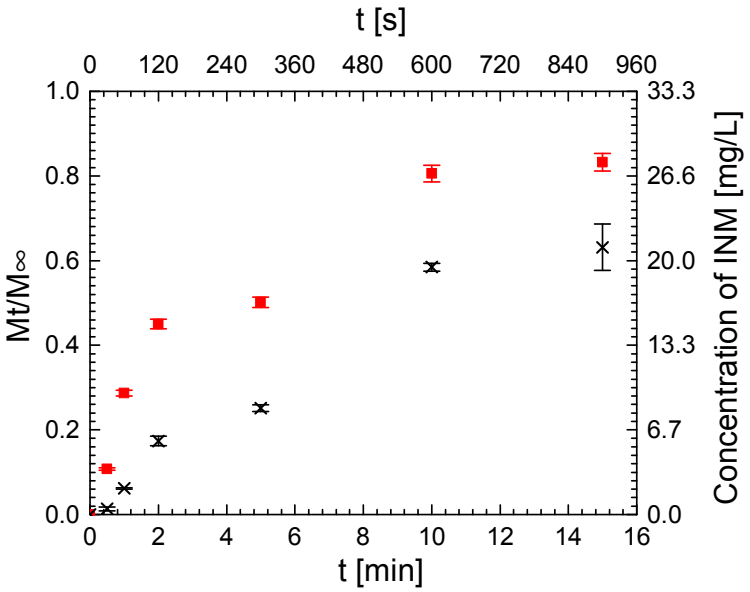


**Figure 4.35** INM release profiles from the EPO30INM solid solutions: (×) un-foamed disks (19∅ x 0.3 mm), and the corresponding (■) foamed disks in hydrochloric acid buffer solution with pH 1.2. Dissolution profiles obtained using a USP apparatus 2. Tests were performed in triplicate.

On the other hand, in both, foamed and un-foamed samples the apparent solubility of INM in pH 1.2 is increased. A very high degree of oversaturation of INM in the solution is evident in Figure 4.35; by UV analysis the concentration of drug was determined to be as high as 28 mg/L while the solubility limit of INM in pH 1.2

hydrochloric buffer solution is only 1 mg/L (Yazdanian et al. 2004). These results show that a higher degree of oversaturation is obtained with the f-EPO30INM samples than with the un-foamed ones. Due to this oversaturated state, INM tents to recrystallize and precipitates, and as a result 100 % of release was not reached even if the solid solution dissolved or disintegrated completely. Liu et al. (Liu et al. 2010) observed for this system that the level of oversaturation as well as the duration of the oversaturated state are related to the processing conditions used to produce the solid solution. Consequently, it can be inferred that because the batch foaming process changes the thermal history of the solid solution, then the increase in apparent solubility observed for the foamed samples could result not only from the increase in release rate but also be due to the conformation changes (i.e. changes in the spatial arrangement of the molecules) introduced during the batch foaming process.

Figure 4.36 shows the release profiles of CBZ from foamed and un-foamed amorphous solid dispersions. These results clearly show a significant enhancement on the API release rate upon foaming. As an example in 60 min 90 ± 2 % of CBZ is released from the f-S15CBZ disks while 49 ± 2 % from the un-foamed ones. In other words, 83 % more CBZ is released from the foamed disks than from the un-foamed disks. The monograph for CBZ establishes that in 60 min at least 75 % of the API should be released, which is achieved after foaming the solid dispersion.

Also in Figure 4.36 it is evident that the final concentration of drug released, from both foamed and un-foamed S15CBZ disks corresponds to 90 to 95 % of the nominal drug loading. Since the *in vitro* dissolution tests is performed under sink conditions, and no evidence of API precipitation is observed after completing the tests, then it can be

assumed that a portion of the released CBZ is trapped within the PVCap-PVAc-PEG micelles. As mentioned before, in section 4.2.1, the drug concentration been determined through the UV analysis correspond to free drug. When studying the dissolution behavior of PVCap-PVAc-PEG, no UV signal of the polymer was observed when the PVDF filters with pores size of 0.45µm were used, even though the polymer is a chromophore. The dissolution profiles of pure PVCap-PVAc-PEG presented in section 4.6.2 were obtained through UV analysis without filtration. This observation suggests that the PVCap-PVAc-PEG micelles cannot pass through the filter and therefore micellar CBZ can not be detected.

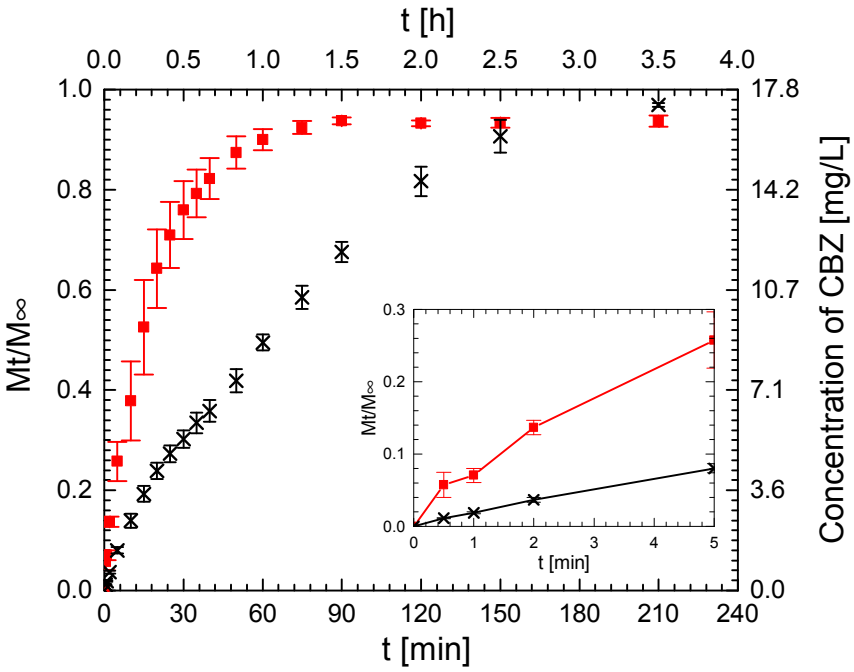


**Figure 4.36** CBZ's release profiles from the S15CBZ solid dispersion: (×) un-foamed disks (19∅ x 0.3 mm), and the corresponding (■) foamed disks in deionized water. Inset plot shows a detail of the initial 5min of the release profiles. Dissolution profiles obtained using a USP apparatus 2. Tests were performed in triplicate.

The inset in Figure 4.36 shows a detail of the first 5 min of the release profiles of CBZ from the S15CBZ system. As observed for the complete release profiles, faster API release is also observed from f-S15CBZ than from the un-foamed disk at the beginning of the dissolution test. In 30 s, 5.5-fold more CBZ is released from the foamed sample than from the un-foamed ones (6 ± 2 % and 1.1 ± 0.1 %, respectively). However, this increment in the API release rate within 30 s is not as significant as it was observed for S30INM and EPO30INM at pH1.2. These two systems have relaxation-controlled API release, while the S15BZ system has anomalous controlled API release. Because the swelling kinetics of the amorphous solid is not the limiting process for the release of CBZ from the S15CBZ, then faster swelling contributes to enhanced release rate, but its influence is less dominant than in the relaxation-controlled systems.

Finally, the effect of foaming on the release profile of INM from the solid solution EPO30INM in pH 7.4 is shown in Figure 4.37. As in all other cases, faster API release rate is achieved upon foaming. In 24 h the amount of INM released from the f-EPO30INM samples is 36 % more than from the un-foamed samples (15 ± 1 % and 11 ± 1%, respectively).

It is surprising that the release rate was enhanced even though INM's release in controlled by Fickian diffusion through swollen EPO that does not dissolve under the test conditions. Slower API rerelease upon foaming was expected for a system such as EPO30INM in pH 7.4. Tortuosity generated by a honeycomb-like structure in a non-dissolving cellular structure should extend the effective diffusional path of the API and thus slow its release. However, as mentioned before some degree of open cells were observed in the surface of the EPO30INM samples, therefore lessening the effect of

tortuosity along the closed cells. In addition, as can be seen in Figure 4.38, dimensional integrity of the foamed sample is disrupted during the *in vitro* dissolution test. In these photographs it is evident that the porosity and number of open cells is increased considerably after the 24 h dissolution test. This change in morphology also contributed in the enhancement in release rate.

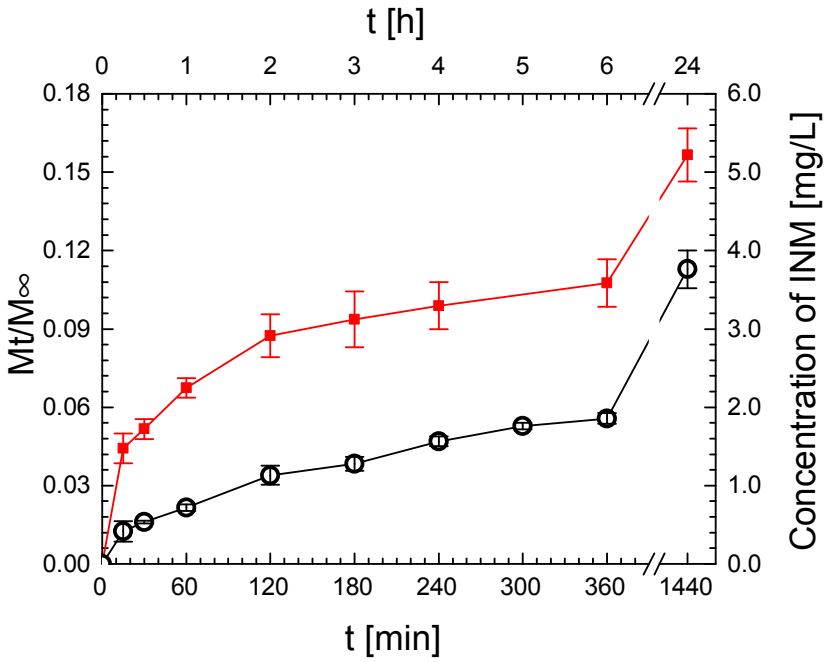


**Figure 4.37** INM's release profiles from the EPO30INM solid solutions: (O) un-foamed disks (19∅ x 0.3 mm), and the corresponding (■) foamed disks in phosphate buffer solution with pH7.4. Dissolution profiles obtained using a USP apparatus 2. Tests were performed in triplicate.

For this system the amount of solvent absorbed by the samples during the dissolution test is determined by weight difference of the samples immediately after extracting them from the dissolution apparatus and after drying under vacuum for 12 h. The amount of solvent absorbed by the f-EPO30INM samples is 51 ± 4 wt % while 26 ± 4 wt% is absorbed by the un-foamed samples. This increase in the amount of absorbed solvent upon foaming results from an increase in surface area and reduction in diffusional

length. Additionally, as the cellular structure collapses new available surfaces are created further enhancing solvent absorption and API release. Furthermore, an increment in absorbed water results in higher degree of swelling which then favors API diffusion by providing increased mobility to the EPO chains, more available space for the diffusion of the INM molecules and weaker INM-EPO interactions.

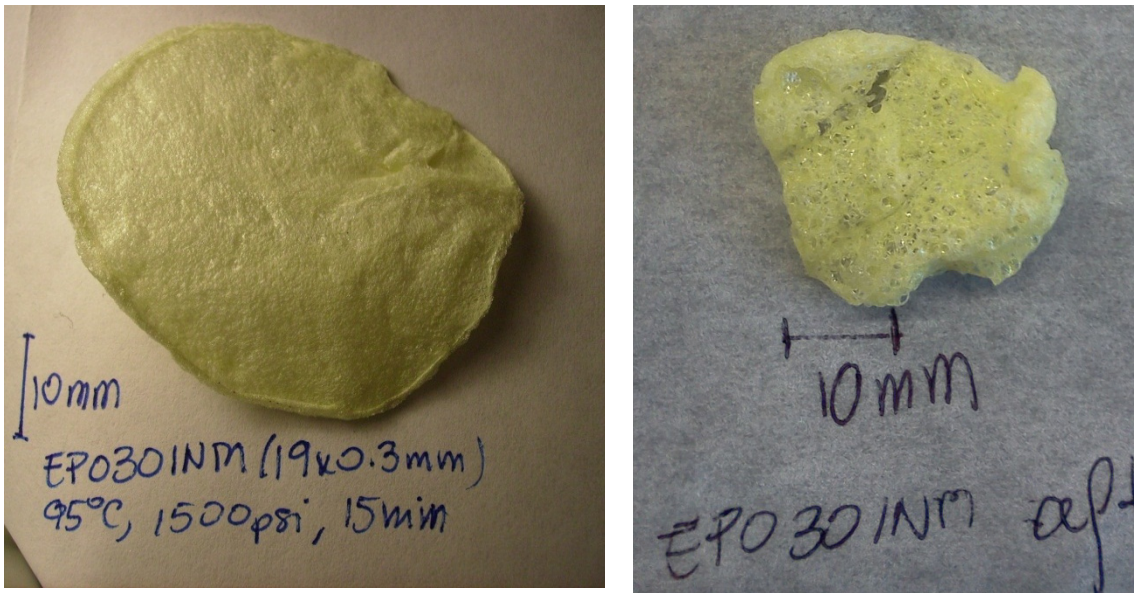


(a) (b)

**Figure 4.38** Photographs of foamed EPO30INM samples: (a) initial state of a foamed sample, and (b) final state of a foamed sample after 24 h dissolution test in a phosphate buffer solution with pH 7.4.

In summary, cellular structures allow to increase the release rate of an API regardless of the mechanism controlling its release. However, in cases where the API release is controlled by the swelling and dissolution kinetics of the amorphous solid solution, foamed structures have a very strong impact in the very early stages of the release of the API.

**4.5.5.1 Quantitative Comparison Between the Release Profiles from Foamed and Un-Foamed Disks.** In order to establish a quantitative comparison between two release profiles, the USA Food and Drug Administration (FDA) in its Guidance for Industry (FDA 1997) recommends the use of two mathematical indices, the difference factor ($f_1$) and similarity factor ($f_2$). These indices were proposed by Moor and Flanner and are defined according to the following expressions (FDA 1997; Shah et al. 1998):

$$f_1 = \frac{\sum_{t=1}^{m} |R_t - T_t|}{\sum_{t=1}^{n} R_t} \, 100 \tag{4.21}$$

$$f_2 = 50 \, log \left\{ \left[ 1 + \frac{1}{m} \sum_{t=1}^{m} (R_t - T_t)^2 \right]^{-0.5} \, 100 \right\} \tag{4.22}$$

Where $m$ is the number of time points, $R_t$ percentage of API released from the reference sample (in the present case the un-foamed sample) at time $t$ and $T_t$ is the percentage of API released from the post change sample (in the present cases the foamed sample) at time $t$.

The cumulative difference between two curves at each time point is given by $f_1$. In other words, $f_1$ is a measure of the error between two curves and the closer its value is to 0 the more alike the two release profiles are. Conversely, $f_2$ is a measure of the similarity between two curves. The value of $f_2$ ranges between 0 and 100; a higher value indicates that the two curves are more similar to each other. According to FDA's guidance, to consider two API release profiles to be similar $f_1$ should be less than 15 and $f_2$ should be greater than 50. (FDA 1997; Shah et al. 1998)

The difference and similarity factors are calculated for each un-foamed / foamed pair using the software Wolfram Mathematica®. The results as well as the time ranges used for the calculations are summarized in Table 4.14. The time ranges were selected according to FDA's guidance.

**Table 4.14** Calculated Difference Factor ($f_1$) and Similarity Factor ($f_2$) for Foamed vs. Un-foamed Release Profiles of S30INM, S15CBZ and EPO30INM

| System | $f_1$ | $f_2$ | Time Range Used for the Calculations [min] |
|---|---|---|---|
| S30INM | 105.3 | 29.9 | 0.5-15 |
| S15CBZ | 139.3 | 25.3 | 0.5-75 |
| EPO30INM_pH1.2 | 73.5 | 33.0 | 0.5-15 |
| EPO30INM_pH7.4 | 109.4 | 66.0 | 15-1440 |

The results obtained for the EPO30INM in pH 7.4 are inconclusive. Using FDA criteria the difference factor suggest that the profiles are different ($f_1 >> 15$), but the difference factor indicates that the profiles are similar ($f_2>50$).

On the other hand, since $f_1 >> 15$ and $f_2 < 50$ for the following systems: S30INM, S15CBZ and EPO30INM in pH 1.2, then it can be stated that the API release profile from foamed samples is statistically different that the API release profile from the un-foamed sample. Using these factors the impact foaming on API release can be ranked from higher to lower impact as follows: S15CBZ > S30INM > EPO30INM in pH 1.2.

## 4.6 Impact of Foaming on the Dissolution Profile of PVCap-PVAc-PEG

### 4.6.1 Morphology of Foamed PVCap-PVAc-PEG

Disks of 16∅ x 1 mm of PVCap-PVAc-PEG are foamed through the batch foaming process described in Chapter 3 using $ScCO_2$ as PBA at 90 °C and 10.34 MPa. During bubble growth, free expansion of the sample takes place; the resulting foamed disks have a closed cell structure as shown in Figure 4.39. The obtained cell size varied from 100 to 500 μm with cell wall thickness in the range 1-100 μm. The average density of the foamed disks is 0.25 ± 0.05 g/cm$^3$, approximately 4 times lower than the polymer's density 1.090 ± 0.005 g/cm$^3$.

Figure 4.39 shows the SEM images of the cross-sectional surface of a foamed disk. In the low magnification SEM in Figure 4.39 (a), is evident that the cells tend to be much smaller toward the edges or skin of the sample than toward the center line of the disk. This distribution in cell sizes results from a non-uniform $CO_2$ concentration across the sample at the moment of expansion. It is reasonable to state that it is higher toward the surface compared to the central region of the samples. This results in a greater amount of nucleation sites toward the surfaces than in the mid-section and therefore formation of smaller cells toward the edges of the sample. The effect of exposure time of the sample to the $ScCO_2$ prior to foaming on cell morphology is discussed in more detail in section 4.7.1.1.

The high magnification SEM image in Figure 4.39 (b) shows a similar rough pattern as the one observed in the S30INM and S15CBZ samples. As mentioned before, this surface pattern results from viscoelastic instabilities of the polymer undergoing

biaxial deformation during cellular growth. Additionally, this pattern is expected to favor the dissolution rate of the foamed samples.

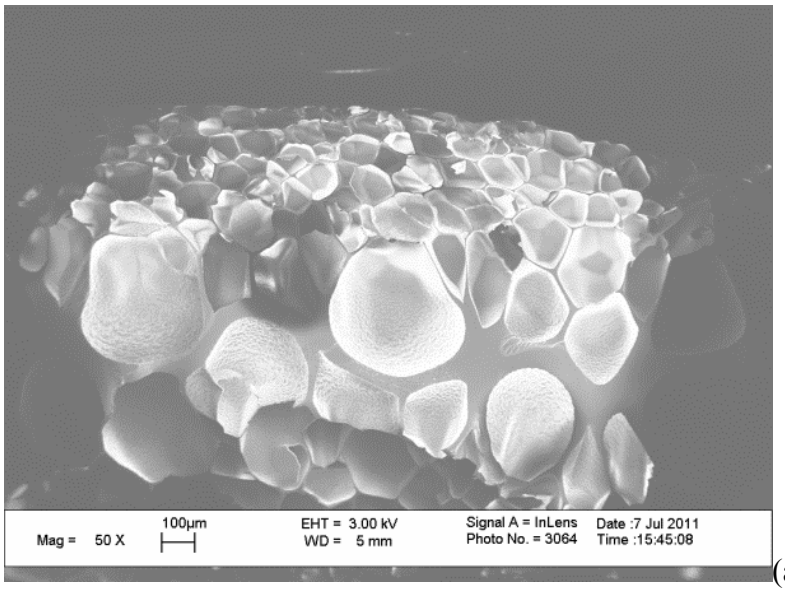


(a)

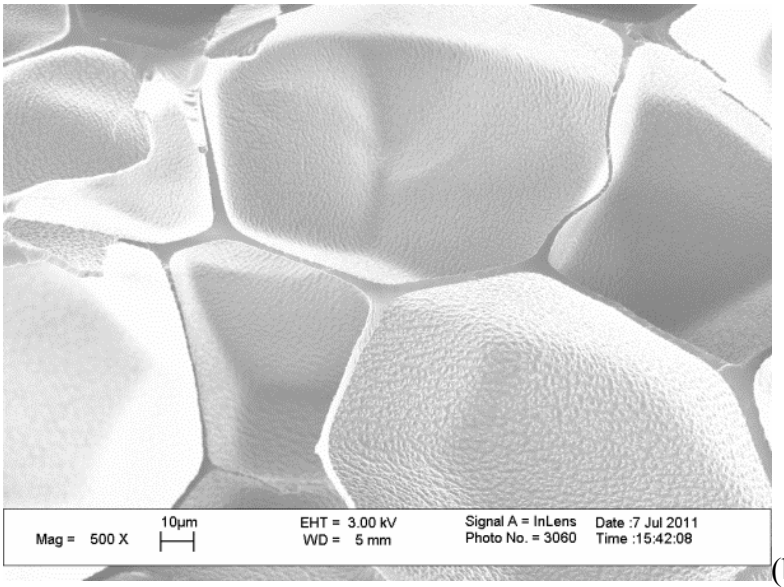


(b)

**Figure 4.39** SEM images of the cross-sectional area of a foamed PVCap-PVAc-PEG disk: (a) 50X and (b) 500X

### 4.6.2 Comparison Between Dissolution Profiles of Foamed and Un-Foamed PVCap-PVAc-PEG

A comparison between the dissolution behavior of pure PVCap-PVAc-PEG in their un-foamed and foamed states is presented in Figure 4.40. The *in vitro* dissolution tests are carried out in deionized water in a USP apparatus 2. The un-foamed and foamed disks of approximately 240 mg are tested without breaking them or disturbing their morphology.

Complete dissolution was attained for both foamed and un-foamed samples. However, Figure 4.40 clearly shows that the time required to complete dissolution is significantly reduced upon foaming. The un-foamed disks require between 8.5 h and 9 h to be completely dissolved, while foamed disks are completely dissolved within 5 h. This represents a reduction in dissolution time of 70 to 80 % upon foaming.

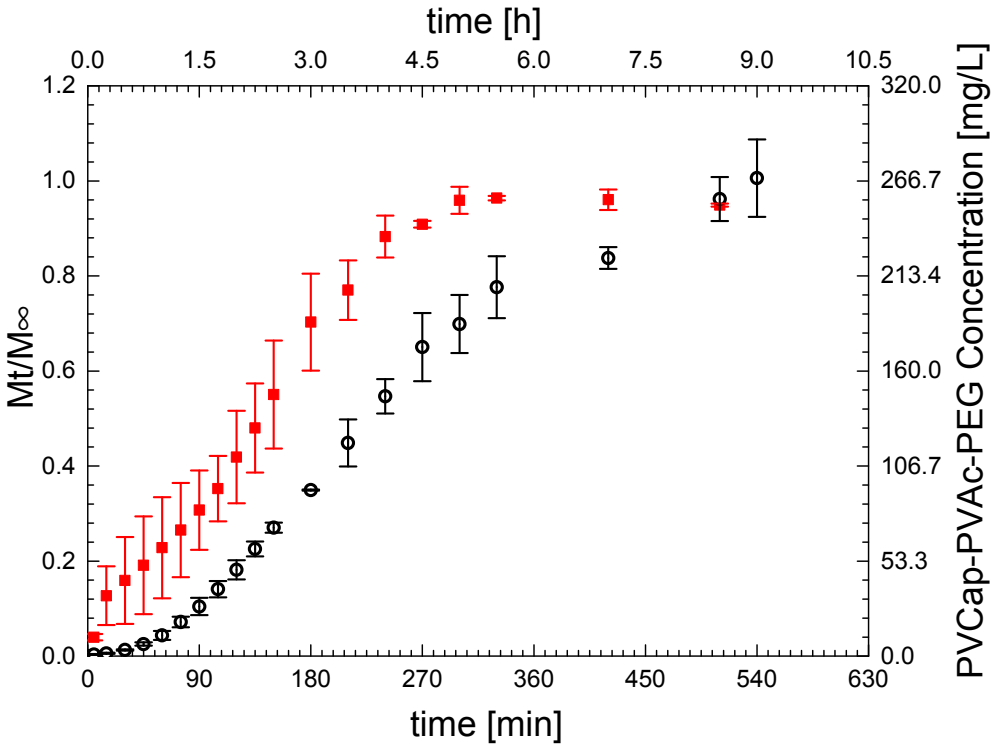


**Figure 4.40** PVCap-PVAc PEG's dissolution profiles: (O) un-foamed disks (16∅ x 1 mm), and the corresponding foamed disks (■) in deionized water. Dissolution profiles obtained using a USP apparatus 2. Tests were performed in triplicate.

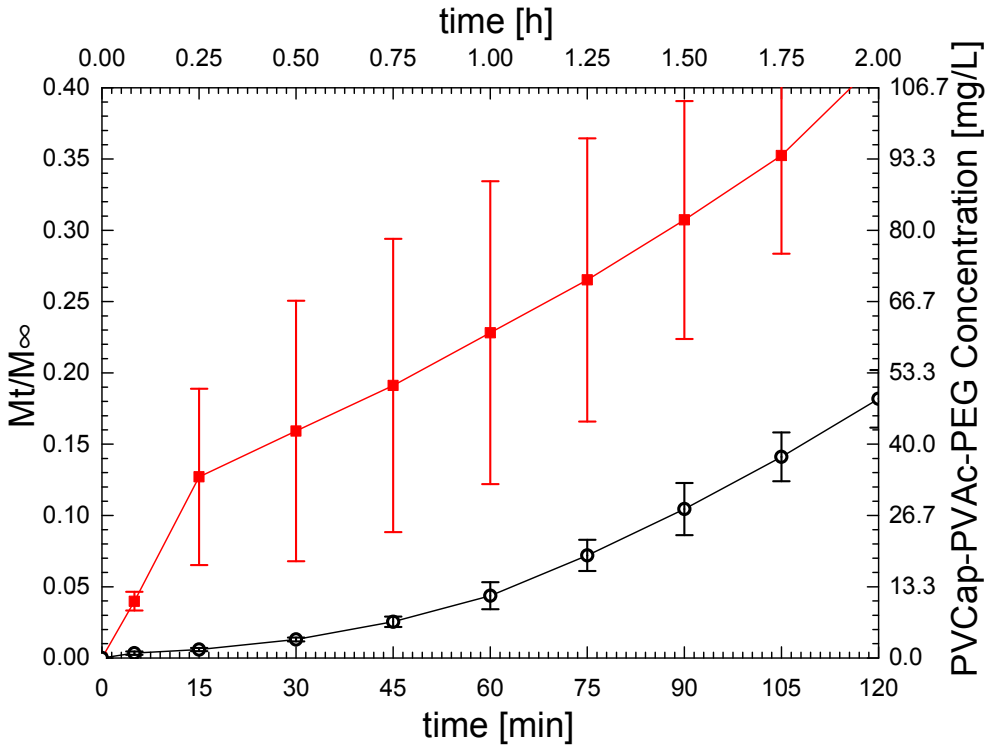


**Figure 4.41** Detail of the first 2 h of PVCap-PVAc PEG's dissolution profiles: (O) un-foamed disks (16∅ x 1 mm), and the corresponding foamed disks (■).in deionized water. Dissolution profiles obtained using a USP apparatus 2. Tests were performed in triplicate.

The dissolution profile of the un-foamed PVCap-PVAc-PEG clearly has an "S" shape; Nogami et al. (Nogami et al. 1970) observed a similar shape for the dissolution profile of PVP in 4:1 acetone:water solution. In Figure 4.41 it can be clearly seen that the dissolution profile of the un-foamed samples has a very slow initial dissolution rate; the amount of material been dissolved increases very slowly during the initial 60 min of the *in vitro* dissolution test. During that time surface wetting, followed by water absorption and polymer swelling take place. It is only after this swollen layer is formed and established that true polymer dissolution can occur. Absorbed water plasticizes the polymer providing enough molecular mobility for chain reptation to occur, which, as depicted in Figure 4.42, is the molecular mechanism that controls disentanglement and

mobility of the polymer chains as they go into solution (Narasimhan and Peppas 1997). The time lag prior to true polymer dissolution is considered as the induction time for dissolution (Narasimhan 2001; Miller-Chou and Koenig 2003).

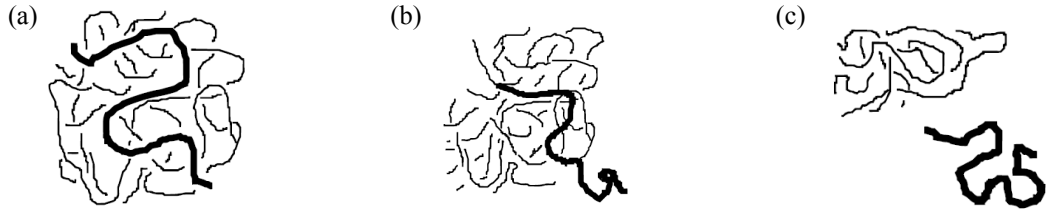


**Figure 4.42** Chain reptation and disentanglement process along the swollen layer: (a) swollen and highly entangled system, (b) macromolecular disentanglement through chain reptation, and (c) disentangled/dissolved chain (in bold). Source: (Narasimhan and Peppas 1997).

By comparing the shape of the two curves in Figure 4.41 it is clear that, the induction time for the un-foamed PVCap-PVAc-PEG disks is approximately 60 min, but becomes extremely short for the foamed disks, less than 5 min. Therefore, it can be concluded that wetting, water absorption and swelling rates are significantly enhanced upon foaming.

Additionally, close comparison of the dissolution profiles suggests that the most significant change in dissolution rates occurs during the initial stages of the test. For example, in 15 min the amount of polymer dissolved from the foamed samples is 21-fold higher than that dissolved from the un-foamed sample (13 ± 6 % of polymer dissolves from the foamed sample, while only 0.6 ± 0.1 % dissolves from the un-foamed disk). However, after the first 60 min the two curves seem to be parallel to each other (see Figures 4.40 and 4.41), suggesting that once the foamed structure has formed the swollen layer, dissolution proceeds as it would occur in an un-foamed sample.

In addition to the difference in shape of the dissolution profiles, differences in the swelling behavior were also observed. In the case of the un-foamed disk, first a swollen layer is formed which progressively moves toward the interior core of the sample and at the same time the size of the disks is reduced due to dissolution. In the case of the foamed disks, the whole sample becomes very flexible (from being rigid and brittle) as soon it is immersed in deionized water, an indication that the polymer is plasticized by the absorbed water. Subsequently the cellular structure seems to collapse, and holes throughout the samples can be seen as it dissolves. This collapse is similar to the one shown for the EPO30INM system at pH 7.4 in Figure 4.38.

The enhancement in dissolution rate observed for PVCap-PVAc-PEG is a consequence of faster solvent absorption, which is reflected as a large reduction in induction time. Reduction in characteristic length for mass transfer and higher surface area in the foamed disks promotes faster solvent absorption. In addition, the collapse of the cellular structure as the polymer dissolves, further contributes to enhance its dissolution rate.

## 4.7 Impact of Foam Morphology on the Release / Dissolution Behavior of the S30INM Binary System

In section 4.6 it was shown that cellular structures can accelerate the API release rates independently of their release mechanism. Then, in section 4.7 it was also shown that the dissolution rate of pure PVCap-PVAc-PEG can be accelerated as well, through the formation of closed cell foamed structures. The objective of this section is to gain fundamental understanding of the influence of the cellular morphology of foamed

samples on the API release rate and disintegration behavior of an amorphous solid solution.

### 4.7.1 Characterization of the S30INM Foams Produced by Batch Foaming with $ScCO_2$

The batch foaming process using $ScCO_2$ as PBA is used to produce foamed samples with different cellular morphologies. The detailed morphological characterization of the cellular structures produced is presented next. Additionally, the impact of the foaming process and the morphology of the foams produced on the state of INM are evaluated immediately after foaming and after a 6-month physical stability test.

**4.7.1.1 Morphology of the Cellular Structures of the Foamed S30INM Binary System.** Solid foams were produced through the batch foaming process described in Chapter 3 employing $ScCO_2$ as PBA. Disks of 16 ∅ x 1 mm were exposed to the PBA at a 100°C (a temperature above the $T_g$ of the S30INM system which is 62 ± 1°C as reported in section 4.1) for 15, 30, and 60 min. The corresponding foamed samples are referred to in the text as F15, F30 and F60, respectively.

The differences between un-foamed and foamed disks can be clearly seen macroscopically in Figure 4.43 and in more detail in the SEM images of their cross-sectional surfaces in Figure 4.44. The photographs of the samples (Figure 4.43) show great levels of expansion of the disks as a result of the batch foaming process. This is a consequence of the creation of closed-cells in the foamed samples. These can be clearly seen in the SEM images of the cross-sectional areas of the samples in Figure 4.44, where all foamed samples have honeycomb-like cross-sections. As expected, un-foamed disks have a continuous non-porous cross-section, see Figures 4.44 (a) and (b).

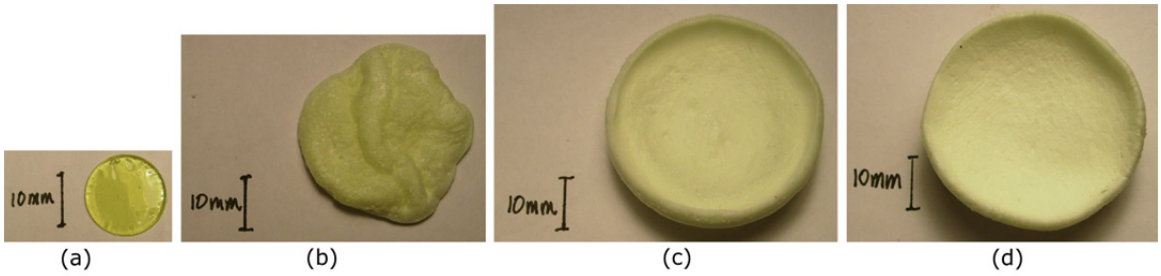


**Figure 4.43** Photographs of (a) un-foamed disk and foamed disks: (b) F15, (c) F30, and (d) F60.

The batch foaming process used in this study has four process variables which can affect the foam characteristics and cellular morphology. These variables are: chamber temperature, gas pressure, $CO_2$ exposure time, and depressurization rate. A detailed study of the effect of these process variables on the foam structure (i.e. cell sizes and density) is out of the scope of the present discussion. However it can be found elsewhere (Goel and Beckman 1994a; b; Arora et al. 1998; Sun et al. 2004), and in Appendix E where photographs of foamed PVCap-PVAc-PEG samples produced at different temperatures and pressures are shown.

The $ScCO_2$ exposure time is varied between 15 and 60 min in order to produce different foam morphologies and study their influence on API release. By varying $ScCO_2$ exposure time the concentration of gas dissolved varies, affecting the cellular structure. Furthermore under non-equilibrium conditions a gas concentration gradient across the sample can be expected (Goel and Beckman 1994a; b). This is shown schematically in Figure 4.45 and its consequences on the morphology of the foam morphology are analyzed latter in this section. The different morphologies produced can be observed in Figure 4.44, and a summary of their characteristics is presented in Table 4.15.

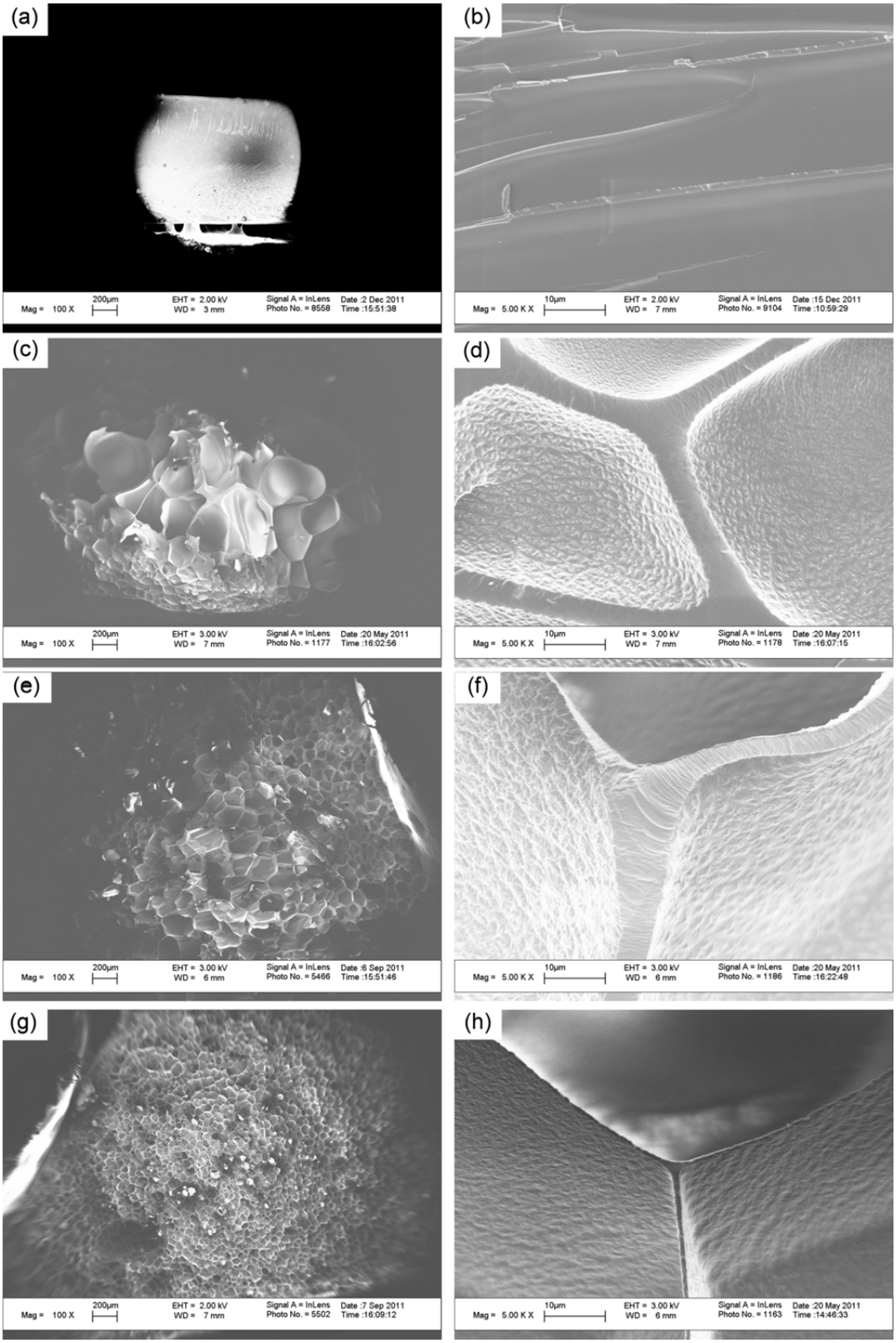


**Figure 4.44** SEM images of a cross-sectional surfaces of the S30INM samples (250X in the left column and 5.00kX in the right). Un-foamed disk: (a) and (b), F15: (c) and (d), F30: (e) and (f), and F60 (g) and (h).

From the low magnification SEM images of the foamed samples [Figures 4.44 (c), (e), and (g)] it becomes evident that as the $ScCO_2$ exposure time increases, the cellular structure becomes more uniform with overall smaller cells. The values reported in Table 4.15 show that the size of the largest cells is reduced from 600 to 200 μm by increasing the gas exposure time. In addition, also in Table 4.15, it is evident that the distribution of wall thickness becomes narrower with increasing $ScCO_2$ exposure time. The upper limit of the wall thickness is reduced significantly from 40.7 to 1.2 μm by increasing the $ScCO_2$ exposure time from 15 to 60 min.

**Table 4.15** Summary of the Characteristics of the Foams Produced by the Batch Foaming Process with $ScCO_2$ at 10.34 MPa and 100 °C of S30INM Disks of 16∅ x 1 mm. Density of the Un-foamed Samples is Presented as Reference.

| Sample | $ScCO_2$ Exposure Time [min] | Sample's Density [$g/cm^3$] | Cell Size Range [μm] | Wall Thickness [μm] |
|---|---|---|---|---|
| HME (un-foamed) | 0 | 1.01±0.05 | - | - |
| F15 | 15 | 0.095±0.006 | 18-600 | 0.2-40.7 |
| F30 | 30 | 0.036±0.002 | 18-400 | 0.2-9.7 |
| F60 | 60 | 0.033±0.002 | 60-200 | 0.5-1.2 |

In addition to the cell sizes, close inspection of the cross sectional surfaces of the foamed disks showed that the F15 and F30 samples have two cell size populations, see Figures 4.44 (c) and (e), respectively. Even though the difference in cell sizes is significantly more pronounced for the F15 samples than for the F30 ones, in both cases a skin / core-like morphology is obtained. Larger cells are obtained toward the core of the disks and smaller ones formed toward and at the edges. On the other hand, foamed disks produced by exposing the samples to $ScCO_2$ for 60min (F60) have very uniform cell size throughout the sample [Figure 4.44 (g)].

The lack of uniformity observed in the F15 and F30 samples can be attributed to a non-uniform $CO_2$ concentration across the sample prior to foaming. During the pressurized step of the batch foaming process, the PBA diffuses and dissolves in the sample. However, this is not an instantaneous process; sufficient time is needed to reach equilibrium and uniform $CO_2$ concentration throughout the disk (Goel and Beckman 1994a; Arora et al. 1998). In the cases of F15 and F30, the gas concentration at the moment the pressure is release has not reached equilibrium resulting in a $CO_2$ concentration gradient, being higher toward the edges (that is the "skin" region) than toward the core of the sample, as it is schematically represented in Figure 4.45. Based on the homogenous nucleation theory (Colton and Suh 1987; Kumar and Suh 1990; Goel and Beckman 1994a), nucleation rates tend to be faster in high $CO_2$ concentration regions (i.e. disk's "skin"). It is generally accepted that faster nucleation rates result in more nuclei, leading to smaller cells toward the edges compared to the core.

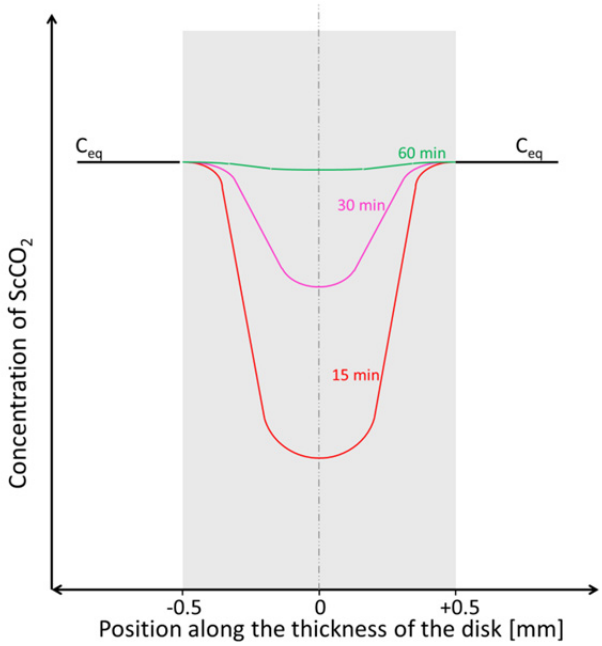


**Figure 4.45** Schematic representation of the $CO_2$ concentration along the thickness of a S30INM disk of 16∅ x 1 mm as a function of exposure time (15, 30, and 60 min) to $ScCO_2$; $C_{eq}$ represent equilibrium $CO_2$ concentration.

On the other hand, as mentioned before, the low magnification SEM image of the cross-sectional area of a F60 sample, Figure 4.44 (g), clearly shows that the cell size distribution across the thickness of the disk is very uniform. These results suggest that after 60 min of exposure to $ScCO_2$, the gas concentration in the S30INM disk is uniform, as shown schematically in Figure 4.45, and probably very close to the equilibrium gas concentration. Therefore, it can be conclude that a uniform cell size distribution was produced for the F60 samples due to uniform gas concentration.

The presence of the closed cells in the foamed samples resulted in a reduction in density with respect to compression molded disks (i.e. un-foamed samples). From the data presented in Table 4.15 it can be seen that all foamed samples have a significant reduction in density with respect to the un-foamed HME sample (which is $1.01 \pm 0.05$ g/cm$^3$). The F15 samples showed a ~10-fold reduction in density, while F30 and F60 have very similar densities, namely ~28 and ~30-fold density reduction with respect to the un-foamed disks. These results indicate that the F30 and F60 samples have similar porosities or void fractions, but, the cellular morphology or spatial arrangement of the bubbles are different. This can be easily visualized through Figure 4.46. These schemas represent an idealization of two foamed structures with same void fractions, and therefore same densities, but with completely different cell sizes; one represents a foam with large cells and the other a foam with small cells. Theoretically, the same free area, and therefore the same density, can be obtained by replacing one big cell with several small ones.

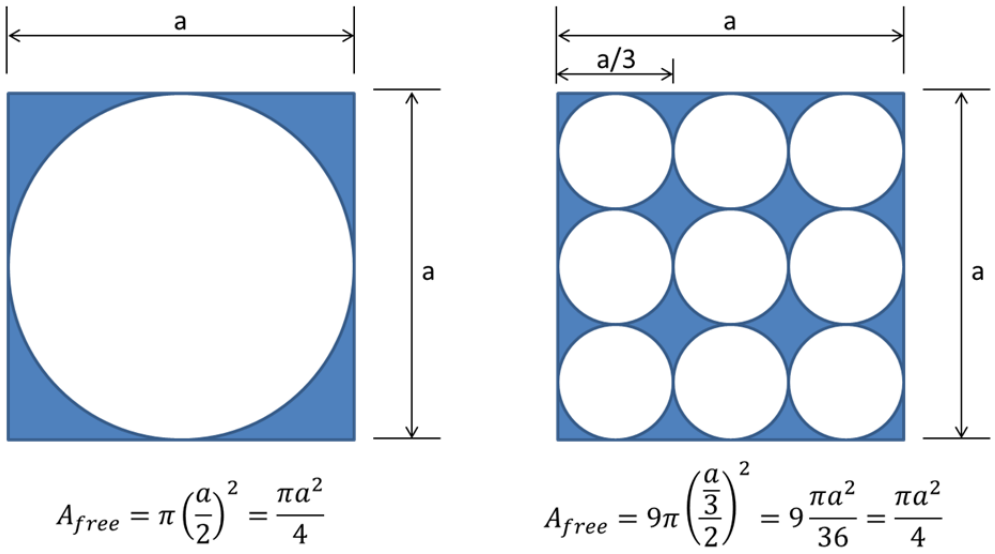


$$A_{free} = \pi\left(\frac{a}{2}\right)^2 = \frac{\pi a^2}{4} \qquad A_{free} = 9\pi\left(\frac{\frac{a}{3}}{2}\right)^2 = 9\frac{\pi a^2}{36} = \frac{\pi a^2}{4}$$

**Figure 4.46** Schematic representation of two closed-cell geometries with same free space but with different configurations. These schematic representations are idealizations of two foamed structures with same densities (i.e. same void fractions), but one has very big cells and the other has small cells.

As observed for the F30 and F60 disks, where samples with similar densities have different cell sizes is not uncommon and it has been reported in the literature by other authors (Goel and Beckman 1994b; Arora et al. 1998). As mentioned before, the differences in cell sizes in these two samples results from differences in the amount of gas dissolved in the sample at the moment of depressurization. The amount of dissolved gas not only affects the nucleation rate and number of nuclei, but it also affects the kinetics of bubble growth and therefore the final packing of the cells. The effect of gas concentration in cellular growth is rather complex because many of the material properties are affected by the amount of $CO_2$ dissolved. Furthermore, the concentration of dissolved $CO_2$ is continuously changing during cellular growth, as dissolved gas diffuses from bulk into the growing cells and is also lost along the sample outer surfaces during expansion. From a general perspective, as the concentration of dissolved $CO_2$ increases the system has lower viscosity and lower surface energy of the gas bubble /

polymer interface. As a result the gas diffusion rate from the bulk into the bubbles is increased. Additionally, the bi-axial stretching deformation of the material as the gas bubbles grow is affected due to changes in the viscoelastic properties of the material (Colton and Suh 1987; Goel and Beckman 1994a; b).

Finally, the high magnification SEM images of the cross-sectional areas of all the foamed samples showed regular rough patterns similar to the ones observed for the foamed samples f-S30INM and f-S15CBZ and PVCap-PVAc-PEG, which we discussed earlier.

**4.7.1.2 State of INM in the Foamed S30INM Samples.** Comprehensive characterization of all samples is performed combining SEM, DSC, XRD and FT-IR. Since each technique has a different level of detection sensitivity of crystalline content, several characterization techniques were employed and combined in order to have a higher level of confidence regarding the morphological state of INM in the different samples.

It should be mentioned that the characterization of the samples is conducted before and after the batch foaming process using $ScCO_2$ as the PBA in order to establish if this process induces morphological changes in the S30INM binary system after compounding. Several factors may induce morphological changes in the API during batch foaming operations with $ScCO_2$. First, since amorphous states are metastable, by increasing the system's mobility through heating or in the presence of $ScCO_2$, API recrystallization may be induced. As mentioned above batch foaming of the S30INM system is carried out above its $T_g$ and the samples are subjected to this process temperature for extended periods of time. Additionally, $ScCO_2$ is known to act as

plasticizer for many polymers, further contributing to increase macromolecular mobility during batch foaming operations. Another factor that may contribute to introduce morphological changes to the S30INM system during batch foaming is the fact that $ScCO_2$ accelerates the crystallization of INM from its amorphous state, as was discussed in detail in section 4.3.

Through SEM inspection of the samples, there is no evidence of crystalline particles within the bulk of the samples, nor along the walls of the cells of foamed disks (see Figure 4.44). This can be seen as a strong indicator that INM exists in the amorphous state in the un-foamed samples and it remains amorphous after the post-processing batch foaming process. SEM analysis of fracture surfaces of melt mixed samples has been used effectively by other authors to determine the presence of crystalline API within the sample (Yang et al. 2010; Ha and Xanthos 2011).

A summary of the thermal properties of foamed and un-foamed samples is presented in Table 4.16 and characteristic thermograms of the samples can be seen on Figure 4.4. The results in Table 4.16 show that the $T_g$ of un-foamed and foamed samples are lower than that for the pure polymer (73 ± 2 °C), due to the plasticizing effect of dissolved INM in PVCap-PVAc-PEG, but higher than that of amorphous INM (46.33 ± 0.07 °C).

**Table 4.16** Summary of the Thermal Transitions Determined from DSC First Heating (Unless Otherwise Specified) of Foamed and Un-foamed S30INM Samples. Properties of PVCap-PVAc-PEG and INM are Shown as Reference (DSC Thermal Analyses Were Performed in Triplicate)

| Sample | $T_g$ [°C] | $T_m$ [°C] |
|---|---|---|
| PVCap-PVAc-PEG | 73 ± 2 | - |
| INM | 46.33 ± 0.07* | 161.0±0.3 |
| Un-foamed disk | 62 ± 1 | - |
| F15 | 62 ± 3 | - |
| F30 | 63 ± 1 | - |
| F60 | 65 ± 1 | - |

* Value determined through DSC second heating

All the foamed and un-foamed samples showed a single glass transition temperature and no endothermic peaks can be seen in the high temperature region on the DSC thermograms of these samples (see Figure 4.4). These results suggest that in both the un-foamed and foamed samples INM and the excipient exist as a single phase amorphous system (i.e. an amorphous solid solution). As mentioned before, the un-foamed sample has a $T_g$ 11 °C lower than that of the pure polymer, additionally, all foamed samples show a similar shift in $T_g$ with respect to PVCap-PVAc-PEG as the un-foamed sample. Although the F30 and F60 samples show slightly higher $T_g$ values, the small difference with respect to the un-foamed sample can be considered negligible and within the experimental error (given by standard deviation). Also, it is important to keep in mind that, although DSC is one of the most commonly used techniques to determine residual crystallinity, it may not be capable of detecting small amounts of residual crystallinity. Its minimum detection limit has been estimated to be ~2 wt% by Leuner and Dressman (Leuner and Dressman 2000).

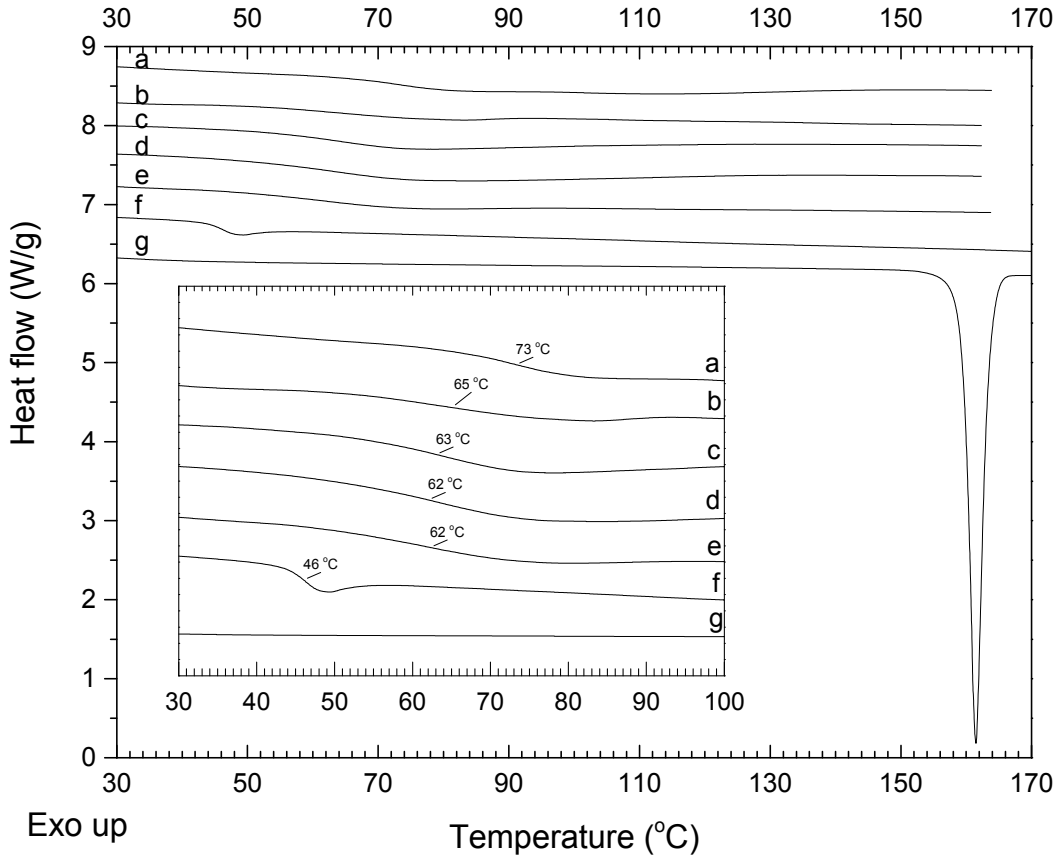


**Figure 4.47** Characteristic 1st heating thermograms (unless otherwise indicated) of: (a) PVCap-PVAc-PEG, (b) F60, (c) F30, (d) F15, (e) un-foamed, (f) INM (2nd heating), and (g) INM.

In agreement with SEM and DSC results, XRD patters show no evidence of the presence of crystalline INM in both the un-foamed and foamed samples (see Figure 4.48). Only pure INM (γ-INM) and the physical mixture show sharp peaks which indicate the presence of a crystalline material. More specifically, diffraction patters of these two samples show the characteristic γ-INM peaks, which are seen at 11.7°, 19.7°, 21.9° and 26.7° (2θ), as reported by Otsuka et al. (Otsuka et al. 2001). However, it should be pointed out that in the physical mixture sample the intensity and definition of these peak decreases compared to that of crystalline INM due to the presence of 70 wt% of PVCap-PVAc-PEG, which is an amorphous material. On the other hand, PVCap-

PVAc-PEG, and all the foamed and un-foamed S30INM samples only show the broad diffraction pattern characteristic of amorphous materials.

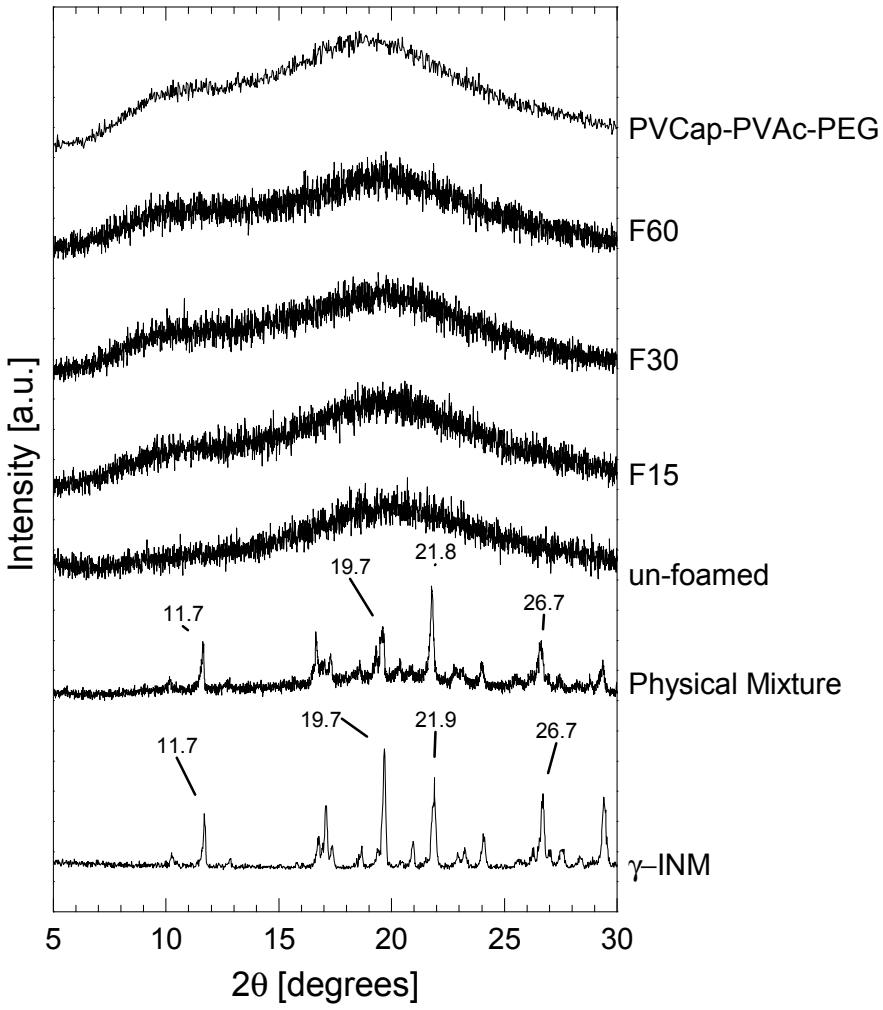


**Figure 4.48** XRD patterns of crystalline INM, S30INM samples – physical mixture, un-foamed sample, and foamed samples (F15, F30, and F60) – and PVCap-PVAc-PEG.

Finally, FT-IR analysis of all the samples also shows strong evidence that INM exists in the amorphous state in both the un-foamed and foamed samples (see Figure 4.49). The characteristic peak for the stretching vibration of the C=O bond of INM's benzoyl group in un-foamed and all foamed samples appears at 1683 $cm^{-1}$, which corresponds to amorphous INM.

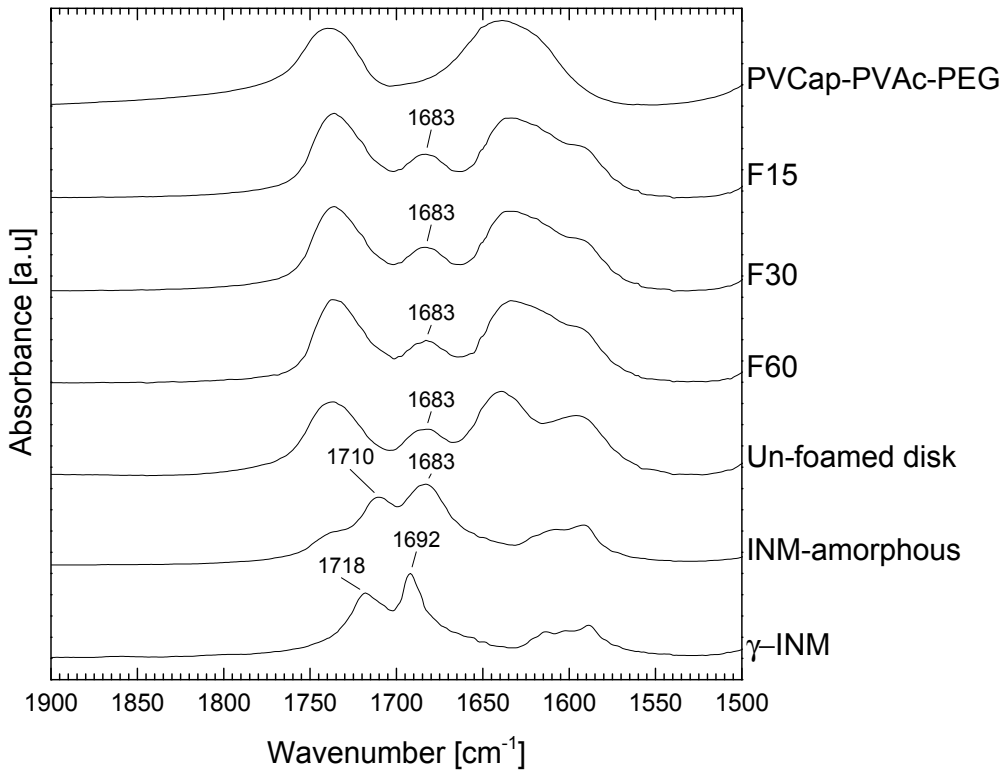


**Figure 4.49** Comparison of the FT-IR spectra of the un-foamed and foamed (F15, F30, and F60) S30INM samples. Spectra of pure PVCap-PVAc-PEG and INM (in its γ-form and amorphous state) are shown as reference.

In summary, the comprehensive characterization of the foamed and un-foamed S30INM samples carried out in this work through SEM, DSC, XRD, and FT-IR, strongly suggests that INM is in amorphous state and forming a single phase with PVCap-PVAc-PEG. Furthermore, the system remains as an amorphous solid solution after the batch foaming process with $ScCO_2$.

**4.7.1.3 Long Term Physical Stability of the Foamed S30INM samples.** Amorphous solid solutions as any other amorphous material are frozen in a high-energy metastable state (Hancock and Zografi 1997; Zhang et al. 2004). This high energy state is one of the reasons amorphous systems exhibit higher API dissolution / release rates and higher apparent solubility compared to their crystalline counterparts, and these may potentially

lead to increased bioavailability. However, the high energy state in which an amorphous material is frozen renders it thermodynamically driven toward a lower energy and a more stable state, by recrystallization of the API (Hancock and Zografi 1997). This transition is particularly critical in amorphous drug delivery systems because a change in state in the active ingredient during the shelf-life of dosage forms results in a change in its performance, and specifically in its bioavailability.

In addition to the higher free energy state in amorphous solid solution another factor that may contribute to a phase transition of the API is water absorption by the excipients. The majority of the polymeric excipients used during HME process are either highly hydrophilic or water soluble, and, thus, prone to absorbing water from the environment. Absorbed water acts as a plasticizer for the system and, as a result, the $T_g$ of the amorphous system is decreased and its mobility increased. As an example, the $T_g$ of PVP has been reported to decrease by 10 °C when stored at 25 °C and 80 % RH (Ahlneck and Zografi 1990). Thus, as a result of increased mobility the recrystallization of the API may be facilitated. API recrystallization, under high humidity conditions, in HME-prepared amorphous solid solutions has been reported in the literature for several API / polymer excipient pairs (Prodduturi et al. 2004; Patterson et al. 2007).

In the case of the foamed dosage forms, another factor that may further affect the shelf life of a drug product is the considerable increase in surface area of the samples upon foaming, as is evident in the SEM images shown in Figure 4.44. Therefore, water uptake and exposure to environmental conditions is enhanced and thus potentially detrimental to the stability of the amorphous solid solution. Specifically for the S30INM system, the rough patterns along the wall of the cells, observed in the high magnification

SEMs in Figure 4.44, signify an increase the surface area beyond the already higher surface area that results from the cellular structure.

The shelf-life or long term physical stability of the S30INM system is evaluated by placing the foamed and un-foamed samples in open container for 6 months in an environmental chamber at constant 75 % RH. The temperature in the chamber was continuously monitored but not controlled, with the recorded temperatures showing fluctuations between 15° and 32 °C with average temperature of 25 ± 3 °C in the 6-month period.

The state of INM in all the foamed and un-foamed samples after been stored for 6-month at 25 ± 3 °C and 75 % RH is examined through FT-IR spectroscopy. Figure 4.50 shows the spectra of the foamed and un-foamed samples before and after the long term stability test. These results clearly show no change in the state of INM in any of the samples. There are no detectible changes in the spectra, as it can be seen in Figure 4.50 (a) in the range between 2000 and 500 $cm^{-1}$. In more detail, in Figure 4.50 (b) is evident that the peak associated with stretching vibration of the C=O bond in the benzoyl group in INM appears at 1683 $cm^{-1}$, corresponding to amorphous INM. These results clearly indicate that INM did not recrystallize in either foamed or un-foamed samples after the 6-month stability test.

Another important factor associated with the shelf life stability of a dosage form is its dimensional stability. Figure 4.51 shows a comparison of the physical dimensions of the samples before [Figure 4.51 (i)] and after the stability test [Figure 4.51 (ii)]. These photographs clearly show that while the un-foamed samples have very high dimensional stability, the foamed ones tent to shrink during the 6-month stability test. During the

batch foaming process, the solid solution is subjected to plastic deformation at a temperature where the material is softened but not in molten state. Therefore, residual stresses are introduced to the material as well as high levels of orientation are introduced to the sample. Once humidity is absorbed by the foamed samples, water is dissolved in the amorphous solid solution plasticizing it. Due to the increased mobility and reduction in mechanical strength of the solid solution (caused by plasticization), oriented polymer chains can relax and as a result the foamed samples shrink.

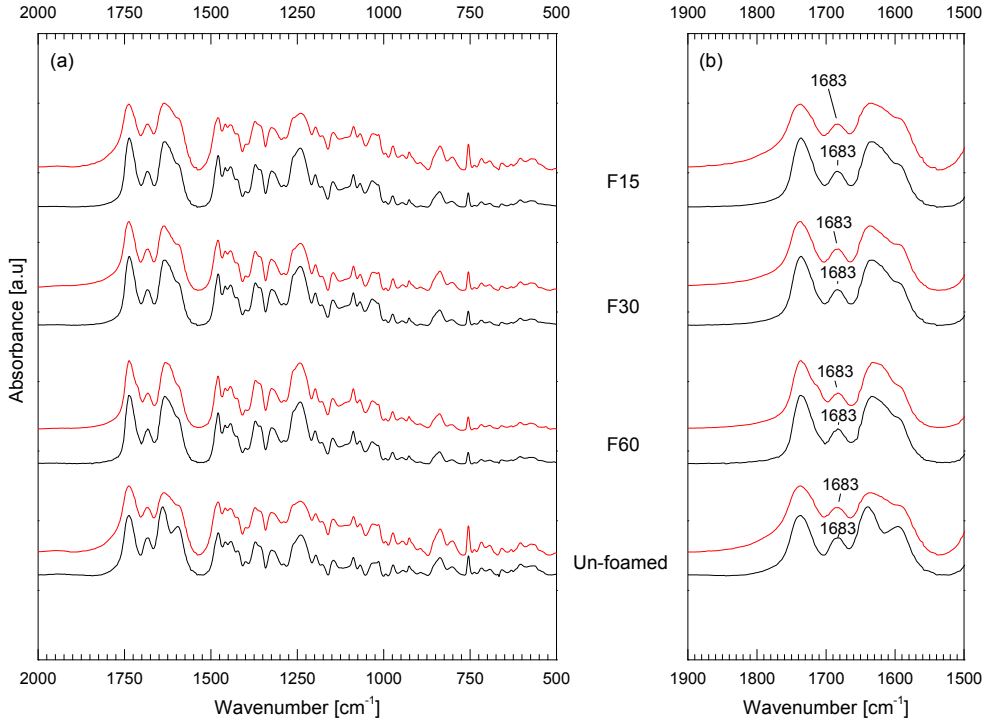


**Figure 4.50** Comparison of the FT-IR spectra of the S30INM un-foamed and foamed (F15, F30, and F60) samples: (black spectra) before and (red spectra) after 6-month storage in open containers at 25 ± 3 °C and 75 % RH.

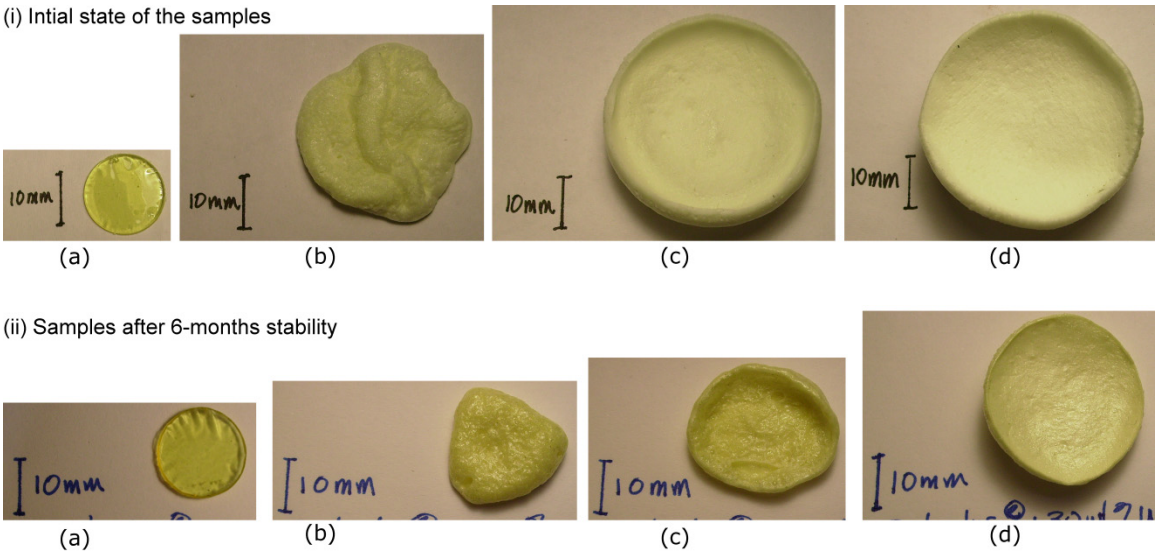


**Figure 4.51** Photographs comparing the S30INM samples (a) un-foamed, (b) F15, (c) F30, and (d) F60 disks: (i) before stability test, and (ii) after 6-month in the environmental chamber at 25 ± 3 °C and 75 % RH.

### 4.7.2 Effect of the Cellular Morphology on INM's Release Rate

The release profiles of INM from un-foamed and foamed S30INM disks are presented in Figure 4.52. However, when analyzing these results, it is important to have the following key information in mind regarding the samples used in this study. First, all samples were analyzed *without grinding* or in any way breaking the cellular structure. In other words, the samples were placed in the dissolution bath as the disks shown in Figure 4.43. Since the weight of the samples was kept constant (~240 mg of total weight and hence ~72 mg of INM), the differences observed in the release profiles can be solely attributed to the morphological dissimilarities of the three cellular structures. Second, it should be mentioned that, although the dimensions of the samples are "not patient compliant", they were chosen in order to gain fundamental understanding of the influence of the morphology of the cellular structure on the release rate and disintegration behavior of the dosage forms.

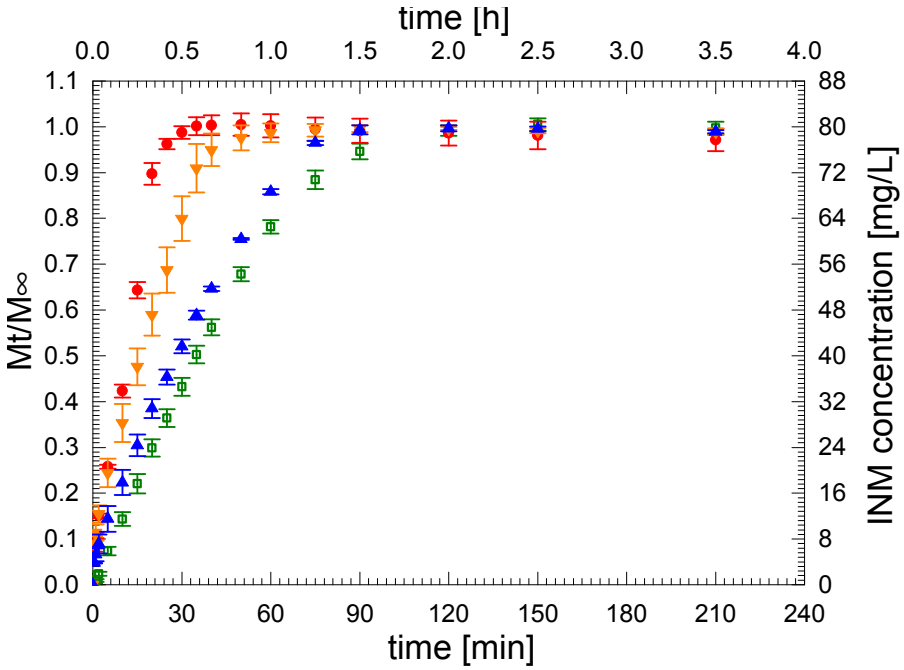


**Figure 4.52** INM's release profiles from the S30INM solid solutions: (□) un-foamed disks (16∅ x 1 mm), and the corresponding foamed disks F15 (●), F30 (▼), and F60 (▲) in phosphate buffer solution with pH 7.4. Dissolution profiles obtained using a USP apparatus 2. Tests were performed in triplicate.

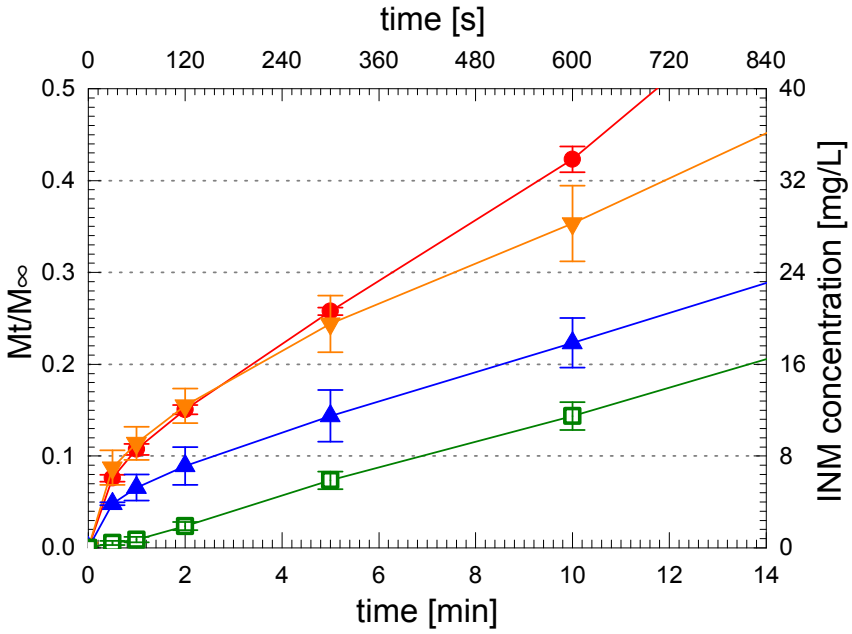


**Figure 4.53** Detail of the initial 14 min of INM's release profiles from the S30INM solid solutions: (□) un-foamed disks (16∅ x 1 mm), and the corresponding foamed disks F15 (●), F30 (▼), and F60 (▲) in phosphate buffer solution with pH 7.4. Dissolution profiles obtained using a USP apparatus 2. Tests were performed in triplicate.

From the complete dissolution profiles presented in Figure 4.52, it is evident that all samples reached 100 % of release, although at different rates. Experimentally, it was found that the release rate of the samples decreases in the following order: F15 > F30 > F60 > un-foamed disks. The time required to reach 100% release is 120 min (2 h) for the un-foamed disks, while for the foamed disks F15, F30, and F60 the times required for completing INM's release are 30, 60 and 90 min, respectively. In other words, the time to complete the release of INM from the foamed samples is 25 to 75% shorter than that of the un-foamed disks.

In Figures 4.52 and 4.53, it is evident that the shape of the INM's release profiles is affected by the cellular morphology of the sample. The differences among the release profiles reflect differences in the disintegration/dissolution behavior of the samples, as will be discussed below in more detail.

In section 4.5 was shown that INM release from the S30INM amorphous solid solution is relaxation controlled, in order words it is controlled by the swelling and dissolution kinetics of the whole solid solution. Figure 4.54 schematically shows the physical aspects of "one-dimensional" swelling and dissolution of in polymer based systems. Initially, a sample of thickness 2L is in a glassy state (as in the case of the un-foamed disks evaluated in this study).

The first steps toward dissolution are wetting of the amorphous solid solution surface and solvent absorption. As the solvent (or body fluid) penetrates into the sample, it acts as a plasticizer *locally* lowering the glass transition temperature of the system and greatly increasing molecular mobility. Once the concentration of the solvent in the boundary layer reaches a critical value the local glass transition temperature reaches the

temperature of the solvent and a swollen layer is formed (see Figure 4.54 (b)) (Peppas et al. 1994; Narasimhan and Peppas 1997). Due to the higher polymer mobility along the swollen layer, the material in this region is in a rubbery state while in the dry region it remains in a glassy state. As mentioned before, the length of time required to form the swollen layer is the induction time of the dissolution process. Since the mobilities of the polymer and API through this swollen layer are very high, it is only after the induction time that API diffusion and true polymer dissolution can begin, see Figure 4.54 (c) (Peppas et al. 1994; Narasimhan and Peppas 1997; Narasimhan 2001).

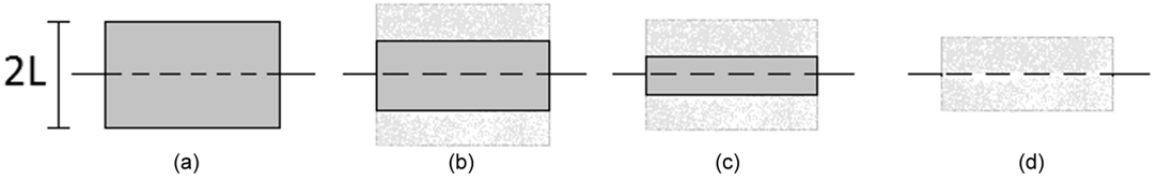


**Figure 4.54** Schematic representation of one-dimensional polymeric swelling and dissolution processes. (a) initial glassy solid solution of thickness 2L, (b) initial swelling step where two boundaries are seen: rubbery-solvent inter-phase and glassy-rubbery inter-phase, (c) true dissolution process starts when both inter-phases move inward, and (d) final dissolution step where the entire solid solution is in the rubbery state.

In relaxation controlled systems, reports in the literature indicate that, once the swollen layer is formed, the rates of solvent absorption and polymer dissolution are synchronized, i.e., become equal (Peppas et al. 1994; Narasimhan and Peppas 1997; Miller-Chou and Koenig 2003). In other word, the thickness of the swollen layer remains constant and the two boundaries (i.e. the swollen-solvent and the swollen-glassy inter-phases) move at the same rate. This is represented in the relaxation model by a constant advance rate of the swelling front (i.e. $k_o/C_o$ in equation 4.19 in section 4.5.4). Then, as polymer and API molecules are released to the solution, both glassy-rubbery and rubbery-solvent inter-phases continue to move toward the core of the sample until the

glassy region is completely depleted, followed by complete dissolution (Peppas et al. 1994; Narasimhan and Peppas 1997; Colombo et al. 2000; Narasimhan 2001; Siepmann and Peppas 2001).

In the case of un-foamed disks, the release/dissolution behavior is in agreement with the API release mechanism described above. Un-foamed disks show an induction time of about one minute; in Figure 4.53 this is seen as a smooth and slow increase in the release rate during the initial stages of the dissolution test. Afterwards, disintegration of the sample occurs from the outside toward the inside. In other words, the sample's size is reduced slowly and gradually.

In the case of INM's release from foamed samples, although all the mass transfer processes described above take place, there are some differences in the disintegration behavior. These differences lead to *faster release* and are described below.

First, it is interesting to note that in Figure 4.53 the induction time for the un-foamed disk can be clearly identified, but this is not the case for the foamed disks. In other words, the release profiles of the foamed samples do not show a gradual and slow increase in the amount of INM been released during the initial stages of the dissolution test. On the contrary, all foamed samples show an initial "burst" on API release. For example in the first one minute, the amount of INM released from the F15 disks is ~12-fold more than that from the un-foamed disks (10.7 ± 0.6 % and 0.9 ± 0.2 % from the F15 and un-foamed disks, respectively). This suggests that in the foamed structures the induction time is reduced from ~1 min to less than 30 s – time at which the first sample is draw from the dissolution apparatus. Therefore, it can be concluded that solvent absorption rate is significantly accelerated upon foaming.

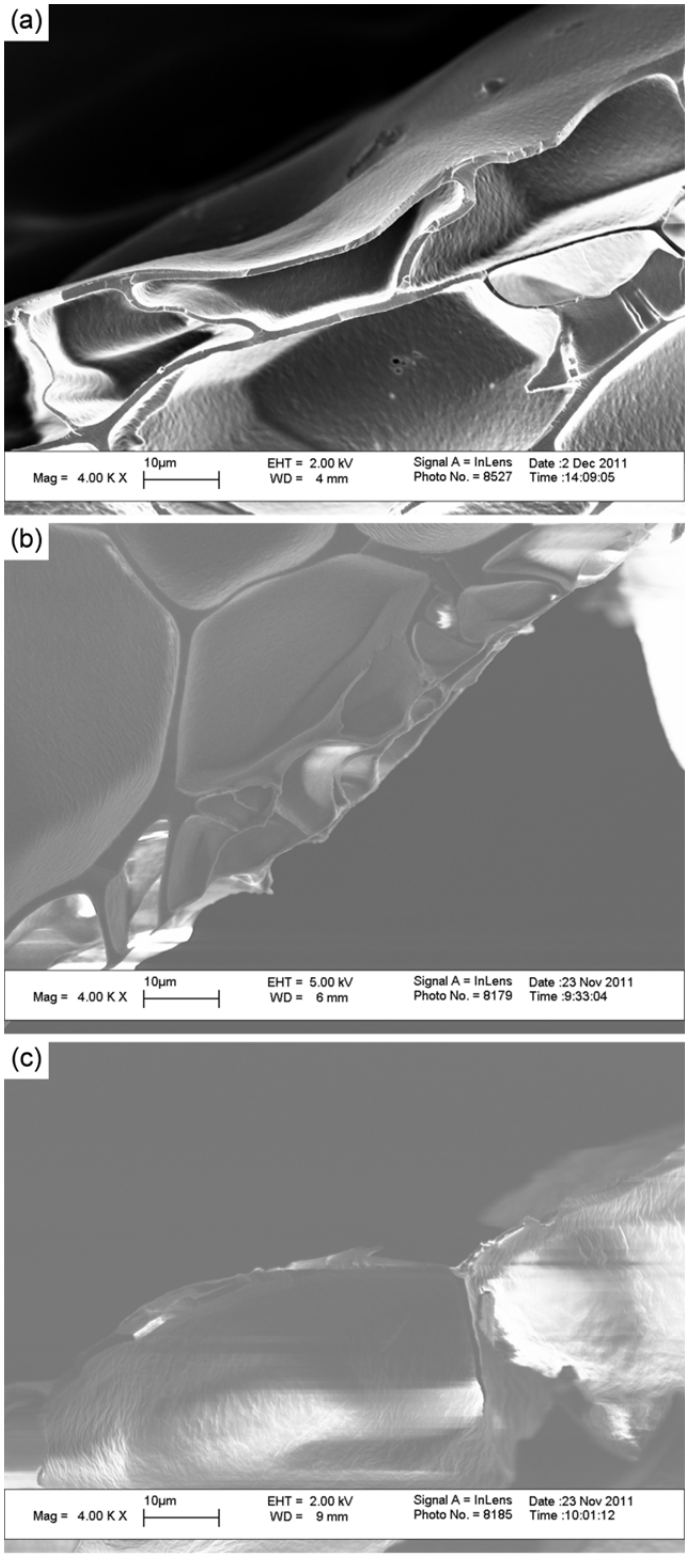


**Figure 4.55** SEM images of edge section of the fracture surface of foamed S30INM disks: (a) F15, (b) F30, and (c) F60.

In systems where the API release is relaxation controlled, as is the case for the S30INM system, the API release rate and solvent absorption rates are inversely proportional to the sample's characteristic length (Enscore et al. 1977). For example, the induction time for the S30INM disks is reduced from ~ 1 min for a sample of 16∅ x 1 mm to ~30 s for a sample of 19∅ x 0.3 mm (see Figure 4.34). Therefore, the reduction in induction time in the foamed samples with respect to the un-foamed disk results from shorter characteristic length and higher surface area through the walls of the cells. The characteristic length for un-foamed disk is 0.5 mm (half its thickness); while for foamed samples characteristic lengths are between 40.7 and 0.2 μm (i.e. wall thickness reported in Table 4.15).

Among the foamed samples there are also differences during the initial stages of the dissolution profiles. Within 30 s the amount of INM released from the F60 samples is 4.8 ± 0.2 %, while from the F15 and F30 samples it is 7.6 ± 0.4 % and 9 ± 2 %, respectively (see Figure 4.53). At the beginning of the test, the F15 and F30 samples have even faster release rates than F60 because they have higher cell density and smaller cells along the disk surface, see Figure 4.55. As dissolution starts, these smaller cells open due to dissolution and as a result the surface area for F15 and F30 is higher compared to F60, thus the release rate of INM is further enhanced for F15 and F30.

It should also be noted that during the first 5 min of the dissolution test, the release profiles of INM from the F15 and F30 samples are almost identical, see Figure 4.53. This is most likely associated with the similarities observed through the SEM images of the cross section of these foamed disks. In Figures 4.55 (a) and (b) is clear that F15 and F30, respectively, have an outer layer of cells of approximately 18 μm.

However, it seems that once the outer layers are depleted, the dissolution of these two samples continues at different rates (see Figure 4.53).

Even though all foamed samples showed a reduction in induction time, two distinct disintegration behaviors are observed. These are schematically presented in Figures 4.56 (a) and (b) and compared to the dissolution mechanism of the un-foamed disks, Figure 4.56 (c).

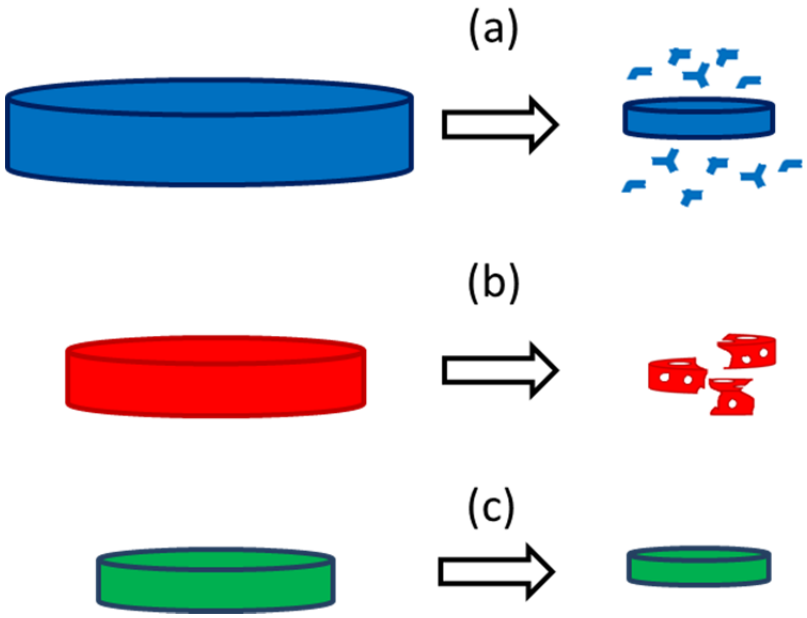


**Figure 4.56** Schematic representation of the dissolution/disintegration mechanism observed for different samples: (a) F60 foamed disks, (b) F15 and F30 foamed disks and (c) un-foamed disks.

Similar to the un-foamed disks, during the dissolution test of the F60 disks, the samples progressively becomes smaller as disintegration/dissolution takes place. However, the size reduction results from breakage of small pieces of the outer layers of the foamed structure as shown schematically in Figure 4.56 (a). These small pieces dissolve completely afterwards in the aqueous solution. Given that the disintegration process occurs from the outside toward the inside, the shape of the release profiles of the

un-foamed samples and the F60 samples are parallel to each other, see Figure 4.52. Therefore, *the release rate enhancement observed for the F60 disks* with respect to the un-foamed disks is *primarily due to reduction of the induction time* (i.e. faster swelling).

On the other hand, during dissolution of the F15 and F30 samples, random and extensive breakage of the foamed structure is observed, this is shown schematically in Figure 4.56 (b). In more detail, after swelling, the cellular structure started to collapse by forming holes throughout the disk followed by random breakage/cleavage of the disks into smaller pieces. This random and extensive breakage of the cellular structure resulted in a significant increase in INM's release rate with respect to un-foamed disk.

Based on the different disintegration mechanisms observed, it can be concluded that the random and extensive breakdown of the disks is favored primarily by a non-uniform wall thickness distribution. Unlike F60, F15 and F30 have very broad distribution of wall thicknesses (see Table 4.15). Sections of the foamed sample, with thinner wall thickness, tend to swell faster than the ones with thicker walls, introducing stresses that induce disintegration by random breakage/cleavage of the foamed sample. As it can be seen in Table 4.15, the wall thicknesses observed in the F15 samples have a 2 order of magnitude span (0.2 - 40.7 μm); while the wall thicknesses of the F30 samples are in the range 0.2 – 9.7 μm. Therefore, F15 disks have a more pronounced non-uniformity of the cellular structure than F30 and thus it shows faster release rate. The F60 samples only have a very small difference between maximum and minimum wall thicknesses (0.5 -1.2 μm) and thus these samples do not experience extensive breakage during dissolution.

Besides the differences in swelling rates through the foamed samples caused by differences in wall thickness, also residual stresses and chain orientation introduced during batch foaming process affect the swelling and dissolution kinetics of polymer based systems. In terms of orientation, it has been reported that when the solvent absorption front moves parallel to the preferential orientation of the polymer chains then $M_t/M_\infty \propto t$; in contrast when absorption is perpendicular to its preferential orientation $M_t/M_\infty \propto t^{1/2}$ (Frisch 1980). In the case of un-foamed disks, due to the nature of the compression molding process, polymer chains are radially oriented, thus, mass transfer during swelling and dissolution is dominantly parallel to the polymer chains' preferential orientation. On the other hand, in the foamed samples polymer chains are bi-axially oriented along the walls of the cells. These may also contribute toward a distribution of swelling and dissolution rates through the samples, because in some regions the advancing swelling front may be moving at a constant rate while in other regions at a variable rate. As a result, internal stresses are buildup throughout the foamed structure, and, thus, fracture is promoted during dissolution.

In terms of residual stresses, which exist in the foamed samples and became evident during the 6-month stability stat, these may also favor fracture of the foamed samples during dissolution. Although these residual stresses tent to be relaxed as a result of solvent absorption, they may also promote environmental stress cracking during dissolution.

**4.7.2.1 Quantitative Comparison Between the Release Profiles from Foamed and Un-Foamed Disks.** The difference and similarity factors ($f_1$ and $f_2$, respectively) are calculated using equations 4.21 and 4.22 presented in section 4.5.5.1 and the software

Wolfram Mathematica®. INM's release profiles from each foamed sample are compared to that of the un-foamed samples. In addition INM's release profiles from foamed samples are also compered. The results from these analyses are summarized in Table 4.14, together with the time ranges used for the calculations, and the sample's release profile is used as reference in the calculation.

**Table 4.17** Calculated Difference Factor ($f_1$) and Similarity Factor ($f_2$) for Several Pairs of INM's Release Profiles from S30INM solid solutions (UF is used to indicate the Un-foamed sample)

| Sample pair | $f_1$ | $f_2$ | Time Range Used for the Calculations [min] | Reference Sample |
|---|---|---|---|---|
| UF-F15 | 229.5 | 25.3 | 0.5 - 20 | UF |
| UF-F30 | 123.1 | 31.4 | 0.5 - 30 | UF |
| UF-F60 | 24.1 | 55.5 | 0.5 - 60 | UF |
| F15-F30 | 22.7 | 43.3 | 0.5 - 20 | F15 |
| F15-F60 | 50.7 | 30.1 | 0.5 - 20 | F15 |
| F30-F60 | 36.3 | 39.4 | 0.5 - 30 | F30 |

The results obtained for the pair UF-F60 (un-foamed vs. F60) are inconclusive. Using FDA criteria (FDA 1997) the difference factor suggest that the profiles are different ($f_1 > 15$), but the difference factor indicates that the profiles are similar ($f_2>50$). It is interesting to note, that this behavior was also observed when comparing INM's release profiles from f-EPO30INM with un-foamed EPO30INM in pH 7.4, where the release profiles also appear to be parallel to each other.

On the other hand, since $f_1 >> 15$ and $f_2 < 50$ for the F15 and F30 samples, when compared to the un-foamed sample, then it can be stated that INM's release profile from these two foamed samples is statistically different than that of the un-foamed samples.

Using these factors, the impact of the foam morphology on INM release can be ranked from higher to lower impact as follows: F15 > F30 >F60.

Using the same approach the release profiles among foamed samples are also compared. From the results presented in Table 4.17 it can be concluded that the release profiles of INM from all three foamed morphologies are statistically different. Additionally, the biggest statistical difference is observed between the pair F15 - F60, followed by F30 - F60, and, finally, the least different are the pair F15 - F30.

The results from the statistical analyses are in agreement with the observed disintegration/dissolution behavior of the samples. In the case of F15 and F30, which both showed extensive breakage of the sample during disintegration, are the ones that showed the highest statistical difference with respect to the release profile of the un-foamed sample, but among the foamed samples the pair F15 - F30 showed to be must similar. On the other hand, F60 which has similar disintegration behavior as the un-foamed samples is the most statistically similar to the un-foamed disks and statistically different to the profiles from F15 and F30.

**4.7.2.2 Summary.** The initial stages of API release from a solid solution is a "surface" phenomenon, in other words is controlled by the surface characteristics of the samples and, in the case of foamed samples, by the outer layer of cells. Therefore independently of the overall cellular morphology, by reducing the characteristic length along the sample's surface (and as a consequence increasing its surface area of the sample), the API release rate can be increased. And this enhancement in API release rate results solely from a reduction in induction time (i.e. wetting, solvent absorption and swelling are accelerated).

On the other hand, in order to significantly reduce the dissolution/release rate, it is essential to promote extensive and random breakage of the sample. In other words, promote fast disintegration of the dosage form. The key feature of the cellular morphology in achieving this is to produce a non-uniform cellular structure with very broad distribution of wall thicknesses, which introduces internal stresses to the foamed structure by differences in the swelling rates throughout the sample.

It should be noted that in the present case, the non-uniformities in the cellular structure are achieved by a batch process under non-equilibrium conditions. Therefore it may not be possible to directly apply these findings to a commercial manufacturing setting. However, the fundamental knowledge gained indicates that differences in swelling rates introduce internal stresses that promote disintegration by extensive fracture of the foamed dosage form. Thus, it may be possible to mimic this phenomenon by incorporating additional excipients, such as super-disintegrants (examples of which include croscarmellose sodium and crospovidone) into the formulation been extruded. Such disintegrant particulates, whose action mechanism is rapid swelling, will introduce strong localized internal stresses and promote fracture and disintegration of the cellular structure accelerating API release. Furthermore by doing so it may be possible to manufacture fast dissolving dosages by continuous or semi-continuous processes such as foam extrusion and foam injection molding.

# CHAPTER 5

# CONCLUDING REMARKS AND SUGGESTED FUTURE WORK

## 5.1 Summary

The batch HMM and continuous HME processes are used to produce several amorphous API / Polymer systems. Foamed samples are produced by batch foaming using $ScCO_2$ as the PBA, and by foamed extrusion via $CO_2$ continuous injection between two melt seals in the extruder. Comprehensive characterization of the binary systems is carried out combining DSC, FT-IR, XRD, and SEM analyses. These analyses show that the S30INM and EPO30INM systems produced are amorphous solid solutions, while the S15CBZ system is an amorphous solid dispersion. Furthermore, while subjecting pure amorphous INM to the batch foaming process caused it to accelerate its recrystallization, neither INM nor CBZ experienced any morphology changes during batch foaming of both the amorphous solid solutions and the amorphous solid dispersion.

The most important contributions of this dissertation can be grouped into three areas: (a) an understanding of the mechanism by which foamed dosages can lead to faster API release as well as the key morphological aspects of the cellular structure needed to achieve this, (b) an understanding of the correlation between the mechanism controlling the release of an API from an amorphous dosage and the enhancement in its release rate upon foaming, and (c) an understanding of the impact of the morphology of the cellular structure on the milling efficiency of HME products and the dissolution performance of the particles produced.

Foamed S30INM samples with three different morphologies are produced via batch foaming. The API release rate and disintegration/dissolution behavior for the

foamed samples are compared to that of the un-foamed sample. The time to complete the release of INM from the foamed S30INM solid solutions is 25 to 75 % shorter than that of the un-foamed samples. Furthermore, a strong correlation between foam morphology and release rate enhancement is observed. On one hand, the induction time for dissolution (i.e. the time necessary for surface wetting, solvent absorption and swelling) is significantly shorter for the foamed sample, as a result of higher surface area and shorter characteristic lengths for mass transfer along the walls of the cells. However, the *key* aspect for significantly enhancing the API release rate is shown to be the extensive and random breakage / cleavage of the foamed dosage forms, leading to their *disintegration*. This is facilitated in foamed structures with very *broad distribution of wall thicknesses*, which leads to internal stresses due to different *local* swelling rates in the sample. In this sense, such foam morphologies act as *disintegrant-less disintegrants*, speeding up API release.

The impact of foaming on the API release profile from binary systems with different release mechanisms is also investigated. Fitting the *in vitro* dissolution data to the Power law model allowed the identification of the mechanism controlling the release of the API from several systems. In the cases of the EPO30INM in pH 1.2 as well as the S30INM systems, the INM's release is relaxation controlled. On the contrary, INM's release from the EPO30INM system in pH 7.4 is controlled by Fickian diffusion. And in the case of CBZ from the S15CBZ amorphous solid dispersion anomalous transport controls its release. In all four cases the release rate of the APIs is increased upon foaming. However, in the systems where the API release is controlled by the swelling and dissolution kinetics of the amorphous system, the foamed structure has a stronger impact in the very early stages of API release. Conversely, in the late stages of the

dissolution process the API release rate is mainly affected by the disintegration behavior (or dimensional integrity) of the foamed sample, which creates fresh and large surface areas for release/dissolution. In addition, statistical indices are used to quantify the impact of foaming on the release profile for all the systems; these statistical analyses show that the strongest impact is observed for S15CBZ, followed by S30INM and then EPO30INM in pH 1.2.

The foam extrusion process is used to produce the cellular S30INM amorphous solid solutions. By varying the foam extrusion conditions two distinct cellular structures are produced: (1) a high density foam of $0.24 \pm 0.05$ g/cm$^3$, which showed a highly non-uniform morphology with loosely packed cells of 0.8- 2.2 mm, and (2) a low density foam of $0.071 \pm 0.004$ g/cm$^3$, with small and closely packed cells of 27 - 320 μm, these results in a cellular structure with thinner walls. The milling efficiency of these two foamed extrudates is compared to that of the un-foamed extrudates prepared by conventional HME process. It is shown that the milling efficiency of the HME extrudates is increased because of the presence of cellular structures. Foamed extrudates compared to un-foamed ones, milled under the same conditions resulted in smaller particles with a narrower particle size distribution and lower bulk density. Nonetheless, by simply introducing some degree of porosity in the extrudate (as in the case of the high density foam) without actually producing a foamed structure with closely packed cells and thin walls still results in a tighter particle size distribution compared to un-foamed extrudates; however, the particles produced by milling the high density foams have comparable morphology and average size as the ones produced by milling the un-foamed extrudates. Furthermore, the similarities between the particles produced by milling the high-density foam and un-foamed extrudates are also reflected in their dissolution

performance, these two samples show to have almost identical API release profiles. Conversely, milled low-density extrudates have considerably smaller particles with higher surface area, and, thus, their dissolution rate is significantly enhanced with respect to that of crystalline INM and the other two milled solid solutions.

The substantial improvement in milling efficiency achieved through the foamed extrudates has a direct impact in the currently used commercial manufacture practices, because it signifies that in one milling pass it is possible to produce particles with narrow particle size distributions and the desired mean size for the production of the final dosage forms. Therefore, manufacturing time and costs can be reduced.

## 5.2 Suggested Future Work

### 5.2.1 Fast Disintegration of Foamed Samples

As mentioned earlier, in order to achieve a significant enhancement in API release rate through foamed structures, it is necessary to have non-uniform cellular structures. In this study these non-uniformities are obtained by a batch process under non-equilibrium $CO_2$ concentration conditions. Therefore it may not be possible to directly apply these findings in a commercial manufacturing setting. However, the fundamental knowledge gained indicates that differences in swelling rates introduced internal stresses that promote disintegration of the foamed dosage form. Thus, it may be possible to mimic this phenomenon by incorporating additional excipients, such as super-disintegrants (examples of which include croscarmellose sodium and crospovidone) into the formulation been extruded. Such disintegrant particulates, whose action mechanism is rapid swelling, will introduce strong localized internal stresses and promote fracture and

extensive disintegration of the cellular structure accelerating API release. Furthermore by doing so it may be possible to manufacture fast dissolving dosages by continuous or semi-continuous processes such as foam extrusion and foam injection molding.

### 5.2.2 Dimensional Stability of Cellular Structures

Since the foamed samples produced by batch foaming with $ScCO_2$ showed poor dimensional stability in a high humidity environment, it would be of interest to evaluate the use of enteric coatings to act as a barrier against humidity during the shelf life of the product. However, to achieve this a solvent-free coating method must also be investigated.

### 5.2.3 Milling Efficiency of Foamed Structures

Since a strong and positive correlation between foam structure and milling efficiency is observed, it will be technologically important to perform a more detailed study of the broad area of foam morphology-mechanical properties-milling efficiency, involving parametric studies with the extrusion and milling processes, and characterization of the fracture and compaction properties of the foamed structures and milled particulates.

Finally, studying the tableting performance of the particles produced by milling of foamed and un-foamed extrudates is of great importance. Compaction of the ground foamed extrudates during the tableting operation is expected to be facilitated, when compared to the compaction of particles produced by milling un-foamed extrudates. The particles produced by milling the foamed extrudates retained some of their cellular structure, a feature which should enable particle deformation during compression of otherwise tough and brittle particles.

### 5.2.4 Foam Extrusion of Pharmaceutical Systems

During the HME process of a miscible binary system comprised of an API and polymer excipient, it is well known that the API gradually dissolves in the molten polymer. However, during the foam extrusion process (or gas - assisted HME process) the system being processed becomes a ternary one composed by an API, the blowing agent gas and the polymer excipient. Therefore, it is of great importance to understand how the presence of the gas affects the dissolution of the API in the polymer melt from a thermodynamic as well as a kinetic perspective. Comprehensive rheology studies of binary and ternary blends with different compositions should be performed in order to gain rigorous understanding of the behavior of such ternary systems.

## APPENDIX A

## SCREW NOMENCLATURE

Figures A.1 and A.2 schematically shown the nomenclature used for the screw elements

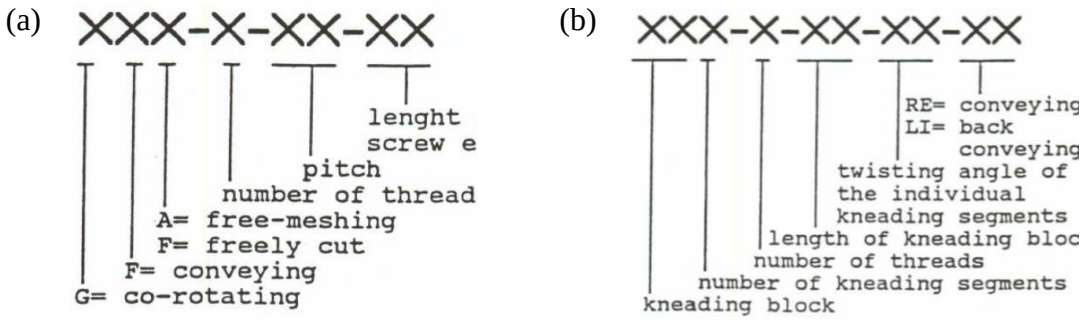


**Figure A.1** Detailed description of the nomenclature used for: conveying screw elements and (b) kneading blocks. Source: (Leistritz 2012)

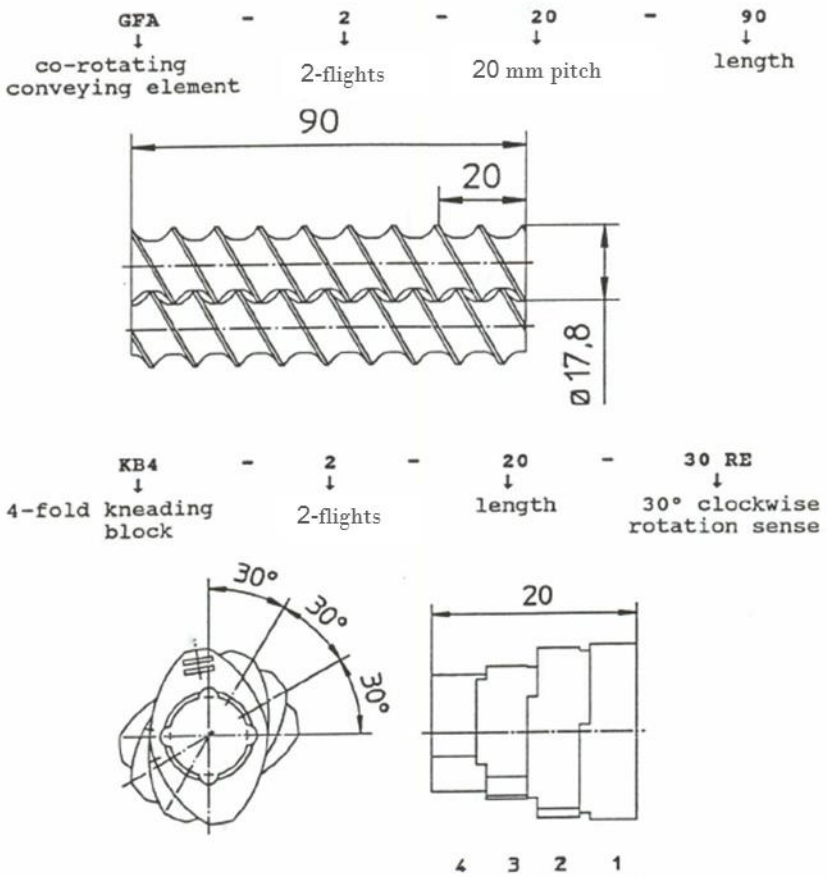


**Figure A.2** Schematic representation of a conveying screw element and a kneading block. Source: (Leistritz 2012)

# APPENDIX B

# THERMAL STABILITY THROUGH TGA

## B.1 TGA Ramp Analyses

Figures B.1 through B.3 show the weight loss curves for PVCap-PVAC-PEG, INM and CBZ obtained through TGA ramp analyses performed at heating rate of 10 °C/min in dry air atmosphere.

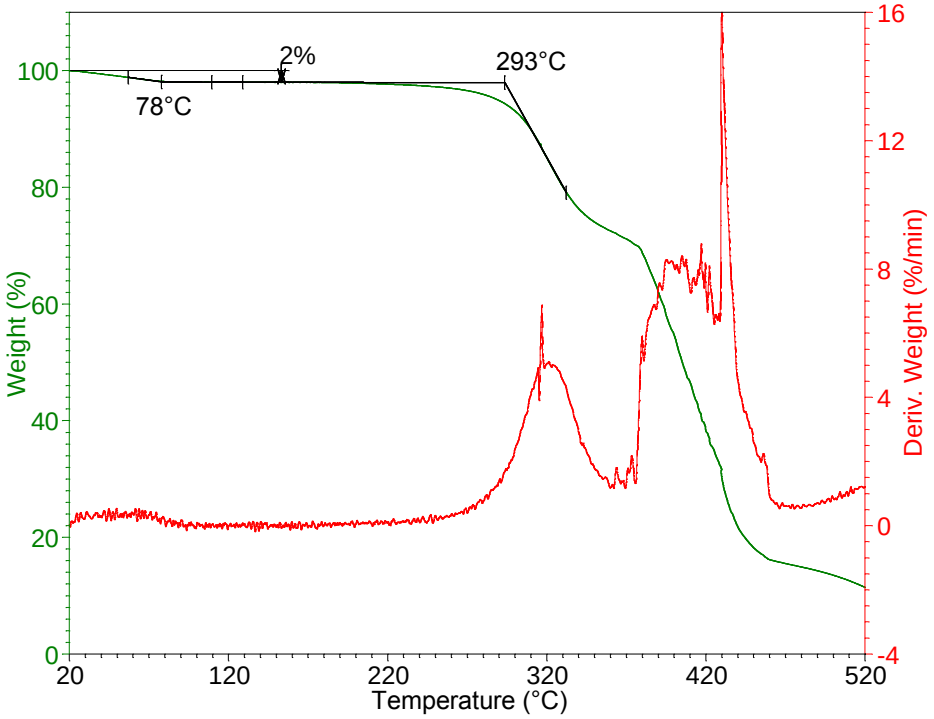


**Figure B.1** TGA weight loss for PVCap-PVAc-PEG in dried air at a heating rate of 10 °C/min.

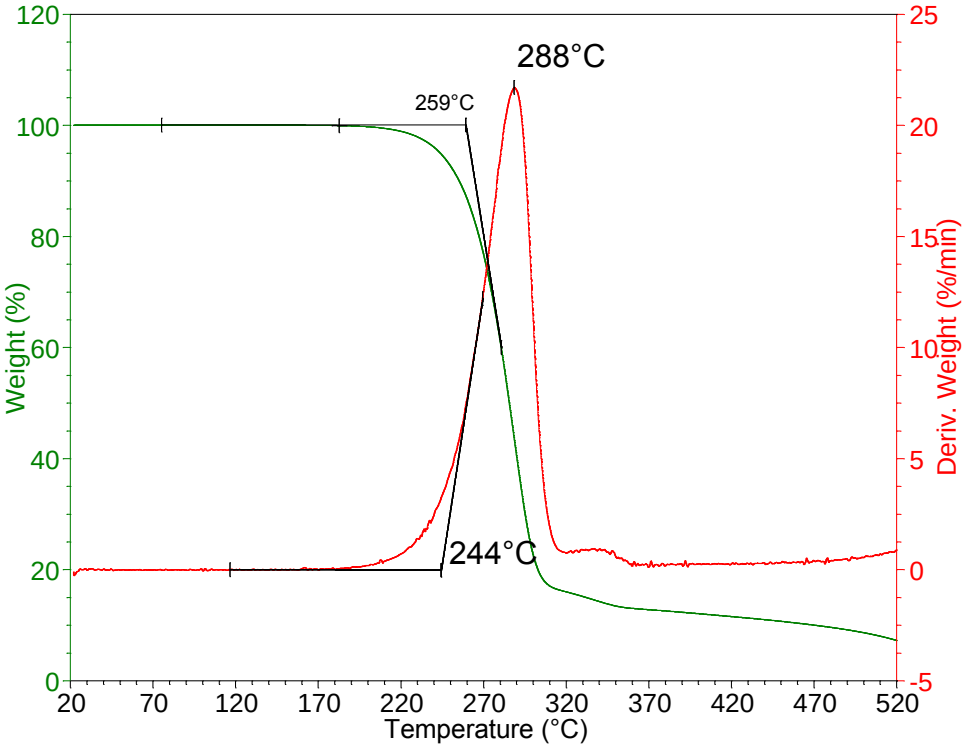


**Figure B.2** TGA weight loss for INM in dried air at a heating rate of 10 °C/min.

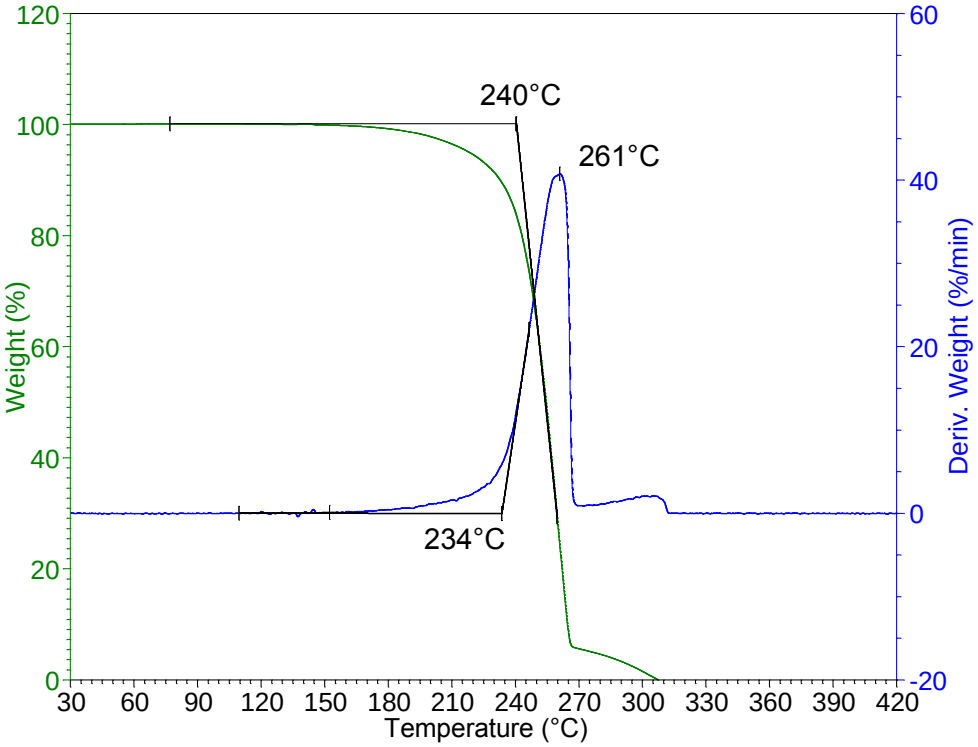


**Figure B.3** TGA weight loss for CBZ in dried air at a heating rate of 10 °C/min.

## B.2 TGA Isothermal Analyses

Figures B.4 through B.5 show the TGA results for isothermal analyses for PVCap-PVAC-PEG, INM and CBZ in dry air atmosphere.

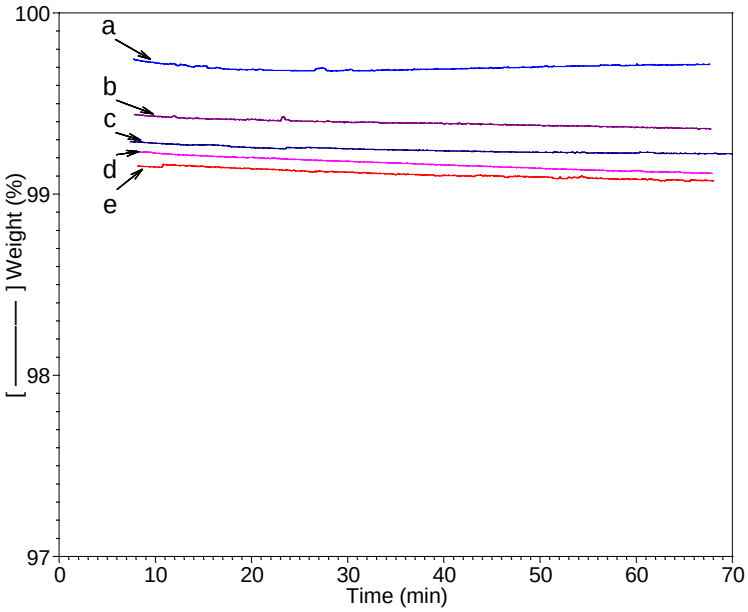


**Figure B.4** TGA results for PVCap-PVAc-PEG isothermal analyses in dry air at: (a) 110 °C, (b) 120 °C, (c) 130 °C, (d) 140 °C, and (e) 150 °C. Samples were heated to the prescribed temperature at 40 °C and held isothermally for 60 min.

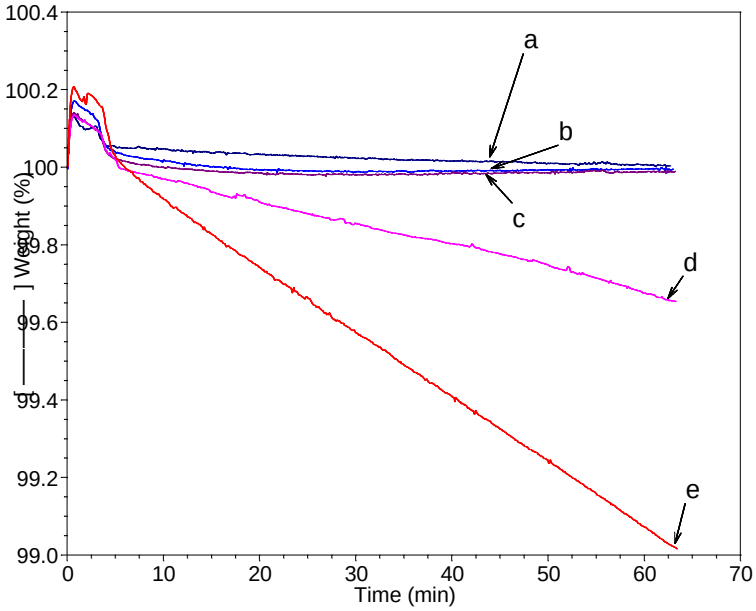


**Figure B.5** TGA results for PVCap-PVAc-PEG isothermal analyses in dry air at: (a) 130 °C, (b) 140 °C, (c) 150 °C, (d) 155 °C, and (e) 160 °C. Samples were heated to the prescribed temperature at 40 °C and held isothermally for 60 min.

# APPENDIX C

# CALCULATION OF THE THEORETICAL DENSITY OF FOAMED EXTRUDATES

## C.1 Theoretical Density Calculations for the LD-fHME Samples (4 w/w% $CO_2$)

Flow rate of solids (S30INM) base of feeding rate of 1.5kg/h and measured density of un-foamed extrudates:

$$1.5\frac{kg}{h}\left(\frac{1000g}{1kg}\right)\left(\frac{1mL}{1.01g}\right) = 1485\,{}^{mL}/_{h}\;S30INM \tag{C.1}$$

Flow rate of $CO_2$ exiting the die, based on experimentally set feeding rate of 1 g/min and $CO_2$ density at 0.101MPa (NIST 2011):

$$1\frac{g}{min}\left(\frac{60min}{1h}\right)\left(\frac{mL}{0.001g}\right) = 60000\,{}^{mL}/_{h}\,CO_2 \tag{C.2}$$

Then the volume fraction occupied by the gas can be calculated as follows:

$$\frac{60000\,{}^{mL}/_{h}}{(1485 + 60000)} = 0.976 \tag{C.3}$$

Theoretical foam density can be calculated used the expression for void fraction as follows:

$$v = 1 - \frac{\rho_f}{\rho_{uf}} \;=>\; \rho_f = (1 - v)\rho_{uf} \tag{C.4}$$

Where *v* is the void fraction, $\rho_f$ density of the foamed material and $\rho_{uf}$ the density of the un-foamed material (Kaewmesri et al. 2006).

$$\rho_f = (1 - 0.976)1.01\,{}^{g}/_{mL} = 0.025\,{}^{g}/_{mL}$$

## C.2 Density Values of $CO_2$ at the Foam Extrusion Processing Conditions

The density values of $CO_2$ used for the volume calculations in Chapter 4, section 4.4.1 are summarized in Table C.1.

**Table C.1** Density Values of $CO_2$ at Various Pressures and Temperatures

| Temperature [°C] | Pressure [MPa] | Density [g/cm$^3$] |
|---|---|---|
| 102 | 3.7 | 0.057 |
| 102 | 1.8 | 0.026 |
| 102 | 0.101 | 0.001 |
| 97 | 3.4 | 0.053 |
| 97 | 1.7 | 0.025 |
| 97 | 0.101 | 0.001 |

Source: (NIST 2011)

## APPENDIX D

## RHEOLOGICAL PROPERTIES OF PVCAP-PVAC-PEG

Rheological properties of PVCap-PVAc-PEG were determined combining capillary rheometry and Rheometrics Mechanical Spectrometer (RMS) at different temperatures.

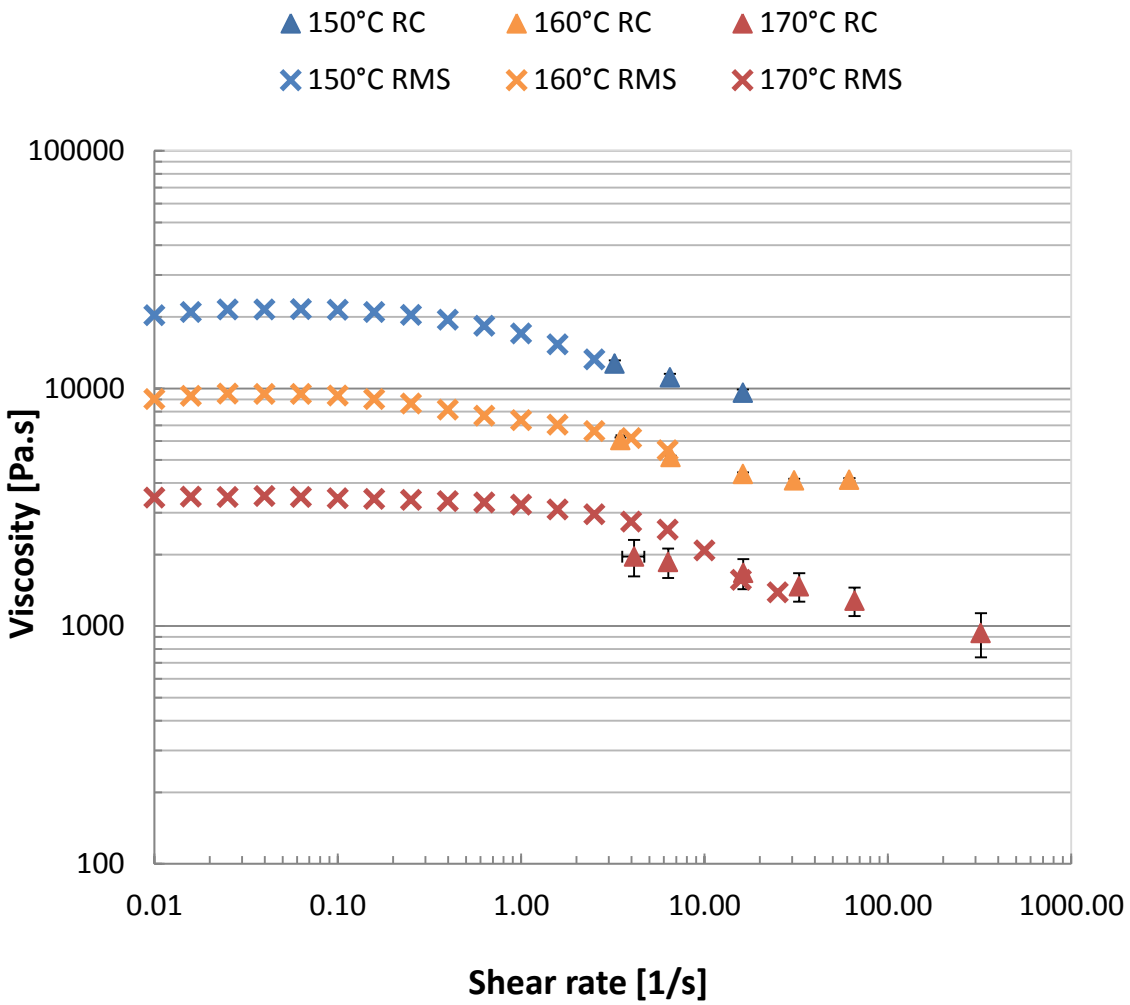


**Figure D.1** Superposition of shear viscosity with shear rate at several temperatures (150°, 160° and 170°C). RC refers to Capillary Rheometry and RMS to Rheometrics Mechanical Spectrometer.

## APPENDIX E

## BATCH FOAMING PROCESSING WINDOW

Figure E.1 shows the effect of the batch foaming temperature and pressure on the morphology of the foamed PVCap-PVAc-PEG samples


**Figure E.1** Photographs of PVCap-PVAc-PEG (a) Un-foamed sample, and foamed samples with $CO_2$ for 30 min at (b) 74 °C and 6.89 MPa, (c) 80 °C and 6.89 MPa, (d) 85 °C and 6.89 MPa, (e) 74 °C and 4.83 MPa, and (f) 90 °C and 4.83 MPa.

## REFERENCES


Ahlneck, C. and G. Zografi (1990). "The Molecular Basis of Moisture Effects on the Physical and Chemical Stability of Drugs in the Solid State." International Journal of Pharmaceutics **62**(2-3): 87-95.

Ahuja, N., O. P. Katare and B. Singh (2007). "Studies on Dissolution Enhancement and Mathematical Modeling of Drug Release of a Poorly Water-Soluble Drug Using Water-Soluble Carriers." European Journal of Pharmaceutics and Biopharmaceutics **65**(1): 26-38.

Amidon, G. L., P. I. Lee and E. M. Topp (2000). Transport Processes in Pharmaceutical Systems. Marcel Dekker, Inc, New York, NY. USA.

Amidon, G. L., H. Lennernäs, V. P. Shah and J. R. Crison (1995). "A Theoretical Basis for a Biopharmaceutic Drug Classification: The Correlation of in Vitro Drug Product Dissolution and in Vivo Bioavailability." Pharmaceutical Research **12**(3): 413-420.

Andrews, G. P., O. Abu-Diak, F. Kusmanto, P. Hornsby, Z. Hui and D. S. Jones (2010). "Physicochemical Characterization and Drug-Release Properties of Celecoxib Hot-Melt Extruded Glass Solutions." Journal of Pharmacy and Pharmacology **62**(11): 1580-1590.

Andrews, G. P., D. S. Jones, O. A. Diak, C. P. McCoy, A. B. Watts and J. W. McGinity (2008). "The Manufacture and Characterisation of Hot-Melt Extruded Enteric Tablets." European Journal of Pharmaceutics and Biopharmaceutics **69**(1): 264-273.

Andronis, V. and G. Zografi (2000). "Crystal Nucleation and Growth of Indomethacin Polymorphs from the Amorphous State." Journal of Non-Crystalline Solids **271**(3): 236-248.

Arkenau-Maric, E. and J. Bartholomaus (2008). "Process for the Production of an Abuse-Proofed Solid Dosage Form". United States Patent 2008/0312264.

Arora, K. A., A. J. Lesser and T. J. McCarthy (1998). "Preparation and Characterization of Microcellular Polystyrene Foams Processed in Supercritical Carbon Dioxide." Macromolecules **31**(14): 4614-4620

Badgujar, B. and A. Mundada (2011). "The technologies used for developing orally disintegrating tablets: A review." Acta Pharmaceutica **61**(2): 117-139.

Banbury, S. and K. MacGregor (2011). "Fast-Dispersing Dosage Forms for Pedriatic Market." Drug Development and Delivery **11**(2): 32-35.

BASF (2010). "Soluplus. Technical Information", Limburgerhof, Germany.

Benet, L. Z., C.-Y. Wu and J. M. Custodio (2006). "Predicting drug absorption and the effects of food on oral bioavailability." Bulletin Technique Gattefassé **99**: 9-16.

Bhugra, C. and M. J. Pikal (2008). "Role of Thermodynamic, Molecular, and Kinetic Factors in Crystallization from the Amorphous State." Journal of Pharmaceutical Sciences **97**(4): 1329-1349.

Breitenbach, J. (2002). "Melt extrusion: from process to drug delivery technology." European Journal of Pharmaceutics and Biopharmaceutics **54**(2): 107-117.

Breitenbach, J. and H. Baumgartl (2000). "Solid Foamed Active Substance Preparations". Unated States Patent 6,158,424.

Brittain, H. G. (2009). Polymorphism in Pharmaceutical Solids. Informa Healthcare USA, Inc, New York, NY. USA.

Brown, C. D., N. Faridi, C. A. McKelvey, H. Suwardie, L. Zhu, M.-W. Young, P. Wang and C. G. Gogos (2011). "Evaluation of Foaming of Pharmaceutical Polymers by $CO_2$ and $N_2$ to Enable Drug Products". ANTEC 2011. Society of Plastic Engineers, Boston, MA. USA**:** 1224-1228.

Bruce, L. D., N. H. Shah, A. Waseem Malick, M. H. Infeld and J. W. McGinity (2005). "Properties of Hot-Melt Extruded Tablet Formulations for the Colonic Delivery of 5-Aminosalicylic Acid." European Journal of Pharmaceutics and Biopharmaceutics **59**(1): 85-97.

Burnett, E. S. (1923). "Experimental Study of the Joule-Thomson Effect in Carbon Dioxide." Physical Review **22**(6): 590-616.

Campbell, D., R. A. Pethrick and J. R. White (2000). Polymer Characterization. Physical Techniques. Stanley Thornes Ltd., Cheltenham. UK.

Cho, K. Y. and S. S. H. Rizvi (2010). "New Generation of Healthy Snack Fodd by Supercritical Fluid Extrusion " Journal of Food Processing and Preservation **34**(2): 192-218.

Chokshi, R. J., H. K. Sandhu, R. M. Iyer, N. H. Shah, A. W. Malick and H. Zia (2005). "Characterization of Physico-Mechanical Properties of Indomethacin and Polymers to Assess their Suitability for Hot-Melt Extrusion Processs as a Means to Manufacture Solid Sispersion/Solution." Journal of Pharmaceutical Sciences **94**(11): 2463-2474.

Chokshi, R. J., N. H. Shah, H. K. Sandhu, A. W. Malick and H. Zia (2008). "Stabilization of Low Glass Transition Temperature Indomethacin Formulations: Impact of Polymer-Type and its Concentration." Journal of Pharmaceutical Sciences **97**(6): 2286-2298.

Choudhary, M., Y. Delaviz, R. Loh, M. Polasky, C. Wan, D. B. Todd, K. S. Hyun, S. Dey and F. Wu (2005). "Measurement of Shear Viscosity and Solubility of Polystyrene Melts Containing Various Blowing Agents." Journal of Cellular Plastics **41**(6): 589-599.

Clarke, A. J. (2005). "Novel Pharmaceutical Dosage Forms and Method for Producing Same". United States Patent Application 2005/0202090 A1.

Colombo, P., R. Bettini, P. Santi and N. A. Peppas (2000). "Swellable Matrices for Controlled Drug Delivery: Gel-layer Behaviour, Mechanisms and Optimal Performance." Pharmaceutical Science & Technology Today **3**(6): 198-204.

Colton, J. S. and N. P. Suh (1987). "The Nucleation of Microcellular Thermoplastic Foam With Additives: Part I: Theoretical Considerations." Polymer Engineering & Science **27**(7): 485-492.

Comyn, J., Ed. (1985). Polymer Permeability. New York, NY. USA, Elsevier Applied Science.

Costa, P. and J. M. Sousa Lobo (2001). "Modeling and Comparison of Dissolution Profiles." European Journal of Pharmaceutical Sciences **13**(2): 123-133.

Crank, J. (1975). The Mathematics of diffusion. Oxford Science Publications, New York, NY. USA.

Crowley, M. M., F. Zhang, M. A. Repka, S. Thumma, S. B. Upadhye, S. Kumar Battu, J. W. McGinity and C. Martin (2007). "Pharmaceutical Applications of Hot-Melt Extrusion: Part I." Drug Development and Industrial Pharmacy **33**(9): 909-926.

Dahan, A. and J. Miller (2012). "The Solubility–Permeability Interplay and Its Implications in Formulation Design and Development for Poorly Soluble Drugs." The AAPS Journal **14**(2): 244-251.

Davies, O. R., A. L. Lewis, M. J. Whitaker, H. Tai, K. M. Shakesheff and S. M. Howdle (2008). "Applications of Supercritical $CO_2$ in the Fabrication of Polymer Systems for Drug Delivery and Tissue Engineering." Advanced Drug Delivery Reviews **60**(3): 373-387.

DiNunzio, J. (2011). "Amorphous Formulation Desing for Melt Exrusion". Leistritz Pharmaceutical Extrusion Seminar, Somerville, NJ.

Doelker, E. (1993). "Cellulose Derivatives". Biopolymers I. R. Langer and N. Peppas. Springer Berlin Heidelberg, New York, NY. USA. **107:** 199-265.

Doherty, C. and P. York (1989). "Microenvironmental pH Control of Drug Dissolution." International Journal of Pharmaceutics **50**(3): 223-232.

Doseva, V., S. Shenkov and V. Y. Baranovsky (1997). "Complex Formation Between Polymethacrylic Acid and Copolymers of Adipic Acid with Poly(ethylene glycol) in Aqueous Solution." Polymer **38**(6): 1339-1344.

Edwards, A. D., B. Y. Shekunov, A. Kordikowski, R. T. Forbes and P. York (2001). "Crystallization of Pure Anhydrous Polymorphs of Carbamazepine by Solution Enhanced Dispersion with Supercritical Fluids (SEDS™)." Journal of Pharmaceutical Sciences **90**(8): 1115-1124.

Elkovitch, M. D. and D. L. Tomasko (2000). "Effect of Supercritical Carbon Dioxide on Morphology Development During Polymer Blending." Polymer Engineering & Science **40**(8): 1850-1861.

Enscore, D. J., H. B. Hopfenberg and V. T. Stannett (1977). "Effect of Particle Size on the Mechanism Controlling n-Hexane Sorption in Glassy Polystyrene Microspheres." Polymer **18**(8): 793-800.

Faridi, N. and D. B. Todd (2007). "Solubility Measurements of Blowing Agents in Polyethylene Terephthalate." Journal of Cellular Plastics **43**(4-5): 345-356.

FDA (1997). "FDA Guidance for Industry: Dissolution Testing of Immediate Release Solid Oral Dosage Forms". FDA, Rockville, MD. USA.

FDA (2004). "Guidance for Industry. PAT - A Framework for Innovative Pharmaceutical Development, Manufacturing and Quality Assurance". FDA, Rockville, MD. USA.

FDA (2008). "FDA Guidance for Industry: Orally Disintegrating Tablets". FDA, Rockville, MD. USA.

Follonier, N., E. Doelker and E. T. Cole (1995). "Various ways of modulating the release of diltiazem hydrochloride from hot-melt extruded sustained release pellets prepared using polymeric materials." Journal of Controlled Release **36**(3): 243-250.

Forster, A., J. Hempenstall, I. Tucker and T. Rades (2001). "Selection of Excipients for Melt Extrusion with Two Poorly Water-Soluble Drugs by Solubility Parameter Calculation and Thermal Analysis." International Journal of Pharmaceutics **226**(1-2): 147-161.

Frisch, H. L. (1980). "Sorption and Transport in Glassy Polymers–A Review." Polymer Engineering & Science **20**(1): 2-13.

Fukuda, M., N. A. Peppas and J. W. McGinity (2006). "Floating Hot-Melt Extruded Tablets for Gastroretentive Controlled Drug Release System." Journal of Controlled Release **115**(2): 121-129.

Ghebre-Sellassie, I. and C. Martin (2007). Pharmaceutical Extrusion Technology. Informa Healthcare USA, Inc, New York, NY. USA.

Goel, S. K. and E. J. Beckman (1994a). "Generation of Microcellular Polymeric Foams Using Supercritical Carbon Dioxide. I: Effect of Pressure and Temperature on Nucleation." Polymer Engineering & Science **34**(14): 1137-1147.

Goel, S. K. and E. J. Beckman (1994b). "Generation of Microcellular Polymeric Foams Using Supercritical Carbon Dioxide. II: Cell Growth and Skin Formation." Polymer Engineering & Science **34**(14): 1148-1156.

Gogos, C. G. (2012). "Fundamentals of Dispersive and Distributive Mixing with Dissolution and Applications to Hot Melt Extrusion". Leistritz Pharmaceutical Extrusion Seminar, Somerville, NJ.

Govindarajan, R., A. Zinchuk, B. Hancock, E. Shalaev and R. Suryanarayanan (2006). "Ionization States in the Microenvironment of Solid Dosage Forms: Effect of Formulation Variables and Processing." Pharmaceutical Research **23**(10): 2454-2468.

Greenhalgh, D. J., A. C. Williams, P. Timmins and P. York (1999). "Solubility Parameters as Predictors of Miscibility in Solid Dispersions." Journal of Pharmaceutical Sciences **88**(11): 1182-1190.

Guo, Q., P. T. Knight, J. Wu and P. T. Mather (2010). "Blends of Paclitaxel with POSS-Based Biodegradable Polyurethanes: Morphology, Miscibility, and Specific Interactions." Macromolecules **43**(11): 4991-4999.

Ha, J. U. (2011). "Study of controlled release of active pharmaceutical ingredients from functionalized nanoclays and polymer matrices". Ph.D Dissertation, New Jersey Institute of Technology, Newak, NJ. USA.

Ha, J. U. and M. Xanthos (2011). "Drug Release Characteristics from Nanoclay Hybrids and Their Dispersions in Organic Polymers." International Journal of Pharmaceutics **414**(1-2): 321-331.

Han, C. D., Y. W. Kim and K. D. Malhotra (1976). "A Study of Foam Extrusion Using a Chemical Blowing Agent." Journal of Applied Polymer Science **20**(6): 1583-1595.

Han, X., K. W. Koelling, D. L. Tomasko and L. J. Lee (2002). "Continuous Microcellular Polystyrene Foam Extrusion with Supercritical $CO_2$." Polymer Engineering & Science **42**(11): 2094-2106.

Han, X., K. W. Koelling, D. L. Tomasko and L. J. Lee (2003). "Effect of Die Temperature on the Morphology of Microcellular Foams." Polymer Engineering & Science **43**(6): 1206-1220.

Hancock, B. C. and G. Zografi (1997). "Characteristics and Significance of the Amorphous State in Pharmaceutical Systems." Journal of Pharmaceutical Sciences **86**(1): 1-12.

Hardung, H., D. Djuric and S. Ali (2010). "Combining HME & Solubilization: Soluplus The Solid Solution." Drug Delivery Technology **10**(3): 20-27.

Hemker, D. J. and C. W. Frank (1990). "Dynamic Light-Scattering Studies of the Fractal Aggregation of Poly(methacrylic acid) and Poly(ethylene glycol)." Macromolecules **23**(20): 4404-4410.

Higuchi, W. I., N. A. Mir and S. J. Desai (1965). "Dissolution Rates of Polyphase Mixtures." Journal of Pharmaceutical Sciences **54**(10): 1405-1410.

Holl, M. R., V. Kumar, J. L. Garbini and W. R. Murray (1999). "Cell Nucleation in Solid-State Polymeric Foams: Evidence of a Triaxial Tensile Failure Mechanism." Journal of Materials Science **34**(3): 637-644.

Hsu, Y.-Y., J. D. Gresser, D. J. Trantolo, C. M. Lyons, P. R. J. Gangadharam and D. L. Wise (1996). "Low-Density Poly(-lactide-co-glycolide) Foams for Prolonged Release of Isoniazid." Journal of Controlled Release **40**(3): 293-302.

Hsu, Y. Y., J. D. Gresser, D. J. Trantolo, C. M. Lyons, P. R. J. Gangadharam and D. L. Wise (1997). "Effect of Polymer Foam morphology and Density on Kinetics of *in vitro* Controlled Release of Isoniazid from Compressed Foam Matrices." Journal of Biomedical Materials Research **35**(1): 107-116.

Huang, J., R. J. Wigent, C. M. Bentzley and J. B. Schwartz (2006). "Nifedipine Solid Dispersion in Microparticles of Ammonio Methacrylate Copolymer and Ethylcellulose Binary Blend for Controlled Drug Delivery: Effect of Drug Loading on Release Kinetics." International Journal of Pharmaceutics **319**(1-2): 44-54.

Kaewmesri, W., P. C. Lee, C. B. Park and J. Pumchusak (2006). "Effects of $CO_2$ and Talc Contents on Foaming Behavior of Recyclable High-melt-strength PP." Journal of Cellular Plastics **42**(5): 405-428.

Kipouros, K., K. Kachrimanis, I. Nikolakakis, V. Tserki and S. Malamataris (2006). "Simultaneous Quantification of Carbamazepine Crystal Forms in Ternary Mixtures (I, III, and IV) by Diffuse Reflectance FTIR Spectroscopy (DRIFTS) and Multivariate Calibration." Journal of Pharmaceutical Sciences **95**(11): 2419-2431.

Kolter, K., M. Karl, S. Nalawade and N. Rottmann (2010). Hot-Melt Extrusion with BASF Pharma Polymers. Extrusion Compendium. BASF The Chemical Company, Ludwigshafen, Germany.

Korsmeyer, R. W., R. Gurny, E. Doelker, P. Buri and N. A. Peppas (1983). "Mechanisms of Solute Release from Porous Hydrophilic Polymers." International Journal of Pharmaceutics **15**(1): 25-35.

Kumar, V. and N. P. Suh (1990). "A Process for Making Microcellular Thermoplastic Parts." Polymer Engineering & Science **30**(20): 1323-1329.

Lee, M., C. B. Park and C. Tzoganakis (1999). "Measurements and Modeling of PS/Supercritical $CO_2$ solution viscosities." Polymer Engineering & Science **39**(1): 99-109.

Lee, S. T. (2000). Foam Extrusion. Principles and Practice. Technomic Publishing Company, Inc., Lancaster, PA. USA.

Lee, S. T. and D. Scholz (2009). Polymeric Foams. Technology and Developments in Regulation, Process, and Products. CRC Press, Boca Raton, FL.

Leistritz (2012). "Extruder Manual". Leistritz, Somerville, NJ. USA.

Leitner, W. (2000). "Green chemistry: Designed to dissolve." Nature **405**(6783): 129-130.

Lele, B. S. and A. S. Hoffman (2000). "Mucoadhesive Drug Carriers Based on Complexes of Poly(acrylic acid) and PEGylated Drugs Having Hydrolysable PEG-Anhydride-Drug Linkages." Journal of Controlled Release **69**(2): 237-248.

Leuner, C. and J. Dressman (2000). "Improving Drug Solubility for Oral Delivery Using Solid Dispersions." European Journal of Pharmaceutics and Biopharmaceutics **50**(1): 47-60.

Li, Y., J. Han, G. G. Z. Zhang, D. J. W. Grant and R. Suryanarayanan (2000). "In Situ Dehydration of Carbamazepine Dihydrate: A Novel Technique to Prepare Amorphous Anhydrous Carbamazepine." Pharmaceutical Development and Technology **5**(2): 257-266.

Liu, H. (2010). "Hot Melt Mixing/Extrusion and Dissolution of Drug (Indomethacin) in Acrylic Copolymer Matrices". Ph.D. Disseratation, New Jersey Intitute of Technology, Newark, NJ. USA.

Liu, H., P. Wang, X. Zhang, F. Shen and C. G. Gogos (2010). "Effects of Extrusion Process Parameters on the Dissolution Behavior of Indomethacin in Eudragit® E PO Solid Dispersions." International Journal of Pharmaceutics **383**(1-2): 161-169.

Lowes, M. M. J., M. R. Caira, A. P. Lotter and J. G. D. Van Watt (1987). "Physicochemical properties and X-ray structural studies of the trigonal polymorph of carbamazepine." Journal of Pharmaceutical Sciences **76**(9): 744-752.

Loxley, A. (2010). "Hot Melt Extrusion in the Production of Drug Elution Medical Devices". APV Experts' Workshop on Hot Melt Extrusion and its Use in the Manufacturing of Pharmaceutical Dosages Forms. A. International Association for Pharmaceutical Technology, Tarrytown, NY. USA.

Lyons, J. G., M. Hallinan, J. E. Kennedy, D. M. Devine, L. M. Geever, P. Blackie and C. L. Higginbotham (2007). "Preparation of Monolithic Matrices for Oral Drug Delivery Using a Supercritical Fluid Assisted Hot Melt Extrusion Process." International Journal of Pharmaceutics **329**(1-2): 62-71.

Malaj, L., R. Censi, M. Mozzicafreddo, L. Pellegrino, M. Angeletti, R. Gobetto and P. Di Martino (2010). "Influence of Relative Humidity on the Interaction Between Different Aryl Propionic Acid Derivatives and Poly(vinylpyrrolydone) K30: Evaluation of the Effect on drug Bioavailability." International Journal of Pharmaceutics **398**(1-2): 61-72.

Matsuda, Y., R. Akazawa, R. Teraoka and M. Otsuka (1994). "Pharmaceutical Evaluation of Carbamazepine Modifications: Comparative Study for Photostability of Carbamazepine Polymorphs by using Fourier-transform Reflection-absorption Infrared Spectroscopy and Colorimetric Measurement." Journal of Pharmacy and Pharmacology **46**(3): 162-167.

McKelvey, C. A., C. D. Brown, L. Schenck, M. Lowinger and J. Moser (2010). "Engineering Solid Solutions Physical Properties to Enable Pharmaceutical Products". ANTEC 2010. Society of Plastics Engineers, Orlando, FL. USA**:** 1184-1188.

McLaughlin, R., S. Banbury and K. Crowley (2009). "Orally Disintegration Tablets. The effect of Recent FDA Guidance on ODT Technologies and Applications." Pharmaceutical Technology.

Meeussen, F., E. Nies, H. Berghmans, S. Verbrugghe, E. Goethals and F. Du Prez (2000). "Phase behaviour of poly(N-vinyl caprolactam) in water." Polymer **41**(24): 8597-8602.

Miller-Chou, B. A. and J. L. Koenig (2003). "A Review of Polymer Dissolution." Progress in Polymer Science **28**(8): 1223-1270.

Mills, N. (2007). Polymer Foams Handbook. Engineering and Biomechanics Applications and Design Guide. Elsevier, Burlington, MA. USA.

Moneghini, M., I. Kikic, D. Voinovich, B. Perissutti and J. Filipović-Grčić (2001). "Processing of carbamazepine–PEG 4000 solid dispersions with supercritical carbon dioxide: preparation, characterisation, and in vitro dissolution." International Journal of Pharmaceutics **222**(1): 129-138.

Moraru, C. I. and J. L. Kokini (2003). "Nucleation and Expansion During Extrusion and Microwave Heating of Cereal Foods." Comprehensive Reviews in Food Science and Food Safety **2**(4): 147-165.

Moribe, K., Y. Tozuka and K. Yamamoto (2008). "Supercritical Carbon Dioxide Processing of Active Pharmaceutical Ingredients for Polymorphic Control and for Complex Formation." Advanced Drug Delivery Reviews **60**(3): 328-338.

Nagy, Z. K., M. Sauceau, K. Nyúl, E. Rodier, B. Vajna, G. Marosi and J. Fages (2012). "Use of Supercritical $CO_2$-Aided and Conventional Melt Extrusion for Enhancing the Dissolution Rate of an Active Pharmaceutical Ingredient." Polymers for Advanced Technologies **23**(5): 909-918.

Nair, R., N. Nyamweya, S. Gönen, L. J. Martínez-Miranda and S. W. Hoag (2001). "Influence of Various Drugs on the Glass Transition Temperature of Poly(vinylpyrrolidone): A Thermodynamic and Spectroscopic Investigation." International Journal of Pharmaceutics **225**(1–2): 83-96.

Nakamichi, K., H. Yasuura, H. Fukui, M. Oka and S. Izumi (2001). "Evaluation of a Floating Dosage Form of Nicardipine Hydrochloride and Hydroxypropylmethylcellulose Acetate Succinate Prepared Using a Twin-Screw Extruder." International Journal of Pharmaceutics **218**(1-2): 103-112.

Narasimhan, B. (2000). "Accurate Models in Controlled Drug Delivery Systems". Handbook of Pharmaceutical Controlled Release Technology. D. L. Wise. Marcel Dekker, New York, NY. USA**:** 155-181.

Narasimhan, B. (2001). "Mathematical Models Describing Polymer dissolution: Consequences for Drug Delivery." Advanced Drug Delivery Reviews **48**(2-3): 195-210.

Narasimhan, B. and N. A. Peppas (1997). "Molecular Analysis of Drug Delivery Systems Controlled by Dissolution of the Polymer Carrier." Journal of Pharmaceutical Sciences **86**(3): 297-304.

Nikitine, C., E. Rodier, M. Sauceau, J.-J. Letourneau and J. Fages (2010). "Controlling the Structure of a Porous Polymer by Coupling Supercritical $CO_2$ and Single Screw Extrusion Process." Journal of Applied Polymer Science **115**(2): 981-990.

NIST. (2011). "NIST Chemistry WebBook." Retrieved January 2013, from http://webbook.nist.gov/chemistry/.

Nogami, H., T. Nagai and A. Kondo (1970). "Dissolution Kinetics of Polyvinylpyrrolidone." Chemical and Pharmaceutical Bulletin **18**(6): 1185-1190.

Oshlack, B., C. Wright and D. J. Haddox (2001). "Tamper-Resistant Oral Opioid Agonist Formulations". United States Patent 6,696,088 B2.

Otsuka, M., F. Kato and Y. Matsuda (2001). "Determination of Indomethacin Polymorphic Contents by Chemometric Near-Infrared Spectroscopy and Conventional Powder X-Ray Diffractometry." Analyst **126**(9): 1578-1582.

Otsuka, M., T. Ofusa and Y. Matsuda (1999). "Effect of Environmental Humidity on the Transformation Pathway of Carbamazepine Polymorphic Modifications During Grinding." Colloids and Surfaces B: Biointerfaces **13**(5): 263-273.

Ozeki, T., H. Yuasa and Y. Kanaya (1998). "Mechanism of Medicine Release from Solid Dispersion Composed of Poly(ethylene oxide)-Carboxyvinylpolymer Interpolymer Complex and pH Effect on Medicine Release." International Journal of Pharmaceutics **171**(1): 123-132.

Patterson, J. E., M. B. James, A. H. Forster, R. W. Lancaster, J. M. Butler and T. Rades (2005). "The Influence of Thermal and Mechanical Preparative Techniques on the Amorphous State of Four Poorly Soluble Compounds." Journal of Pharmaceutical Sciences **94**(9): 1998-2012.

Patterson, J. E., M. B. James, A. H. Forster, R. W. Lancaster, J. M. Butler and T. Rades (2007). "Preparation of Glass Solutions of Three Poorly Water Soluble Drugs by Spray Drying, Melt extrusion and Ball milling." International Journal of Pharmaceutics **336**(1): 22-34.

Peppas, N. A. and J. J. Sahlin (1989). "A simple Equation for the Description of Solute Release III. Coupling of Diffusion and Relaxation." International Journal of Pharmaceutics **57**(2): 169-172.

Peppas, N. A., J. C. Wu and E. D. von Meerwall (1994). "Mathematical Modeling and Experimental Characterization of Polymer Dissolution." Macromolecules **27**(20): 5626-5638.

Prodduturi, S., R. V. Manek, W. M. Kolling, S. P. Stodghill and M. A. Repka (2004). "Water Vapor Sorption of Hot-Melt Extruded Hydroxypropyl Cellulose Films: Effect on Physico-Mechanical Properties, Release Characteristics, and Stability." Journal of Pharmaceutical Sciences **93**(12): 3047-3056.

Qi, S., A. Gryczke, P. Belton and D. Q. M. Craig (2008). "Characterisation of Solid Dispersions of Paracetamol and EUDRAGIT® E Prepared by Hot-Melt Extrusion Using Thermal, Microthermal and Spectroscopic Analysis." International Journal of Pharmaceutics **354**(1-2): 158-167.

Ramesh, N. S. (2004). "Fundamentals of Bubble Nucleation and Growth in Polymers". Polimeric Foames. Mechanisms and Materials. S. T. Lee and N. S. Ramesh. CRC Press, New York, NY. USA**:** 73-110.

Ramesh, N. S., D. H. Rasmussen and G. A. Campbell (1991). "Numerical and Experimental Studies of Bubble Growth During the Microcellular Foaming Process." Polymer Engineering & Science **31**(23): 1657-1664.

Repka, M. A., S. K. Battu, S. B. Upadhye, S. Thumma, M. M. Crowley, F. Zhang, C. Martin and J. W. McGinity (2007). "Pharmaceutical Applications of Hot-Melt Extrusion: Part II." Drug Development and Industrial Pharmacy **33**(10): 1043-1057.

Ritger, P. L. and N. A. Peppas (1987a). "A Simple Equation for Description of Solute Release I. Fickian and Non-fickian Release from Non-swellable Devices in the Form of Slabs, Spheres, Cylinders or Discs." Journal of Controlled Release **5**(1): 23-36.

Ritger, P. L. and N. A. Peppas (1987b). "A simple Equation for Description of Solute Release II. Fickian and Anomalous Release from Swellable Devices." Journal of Controlled Release **5**(1): 37-42.

Rowe, R. C., P. J. Sheskey and M. E. Quinn (2009). Handbook of Pharmaceutical Excipients. Pharmaceutical Press, Washington D.C.. USA.

Rustichelli, C., G. Gamberini, V. Ferioli, M. C. Gamberini, R. Ficarra and S. Tommasini (2000). "Solid-State Study of Polymorphic Drugs: Carbamazepine." Journal of Pharmaceutical and Biomedical Analysis **23**(1): 41-54.

Sato, Y., T. Takikawa, S. Takishima and H. Masuoka (2001). "Solubilities and Diffusion Coefficients of Carbon Dioxide in Poly(vinyl acetate) and Polystyrene." Journal of Supercritical Fluids **19**(2): 187-198.

Sauceau, M., J. Fages, A. Common, C. Nikitine and E. Rodier (2011). "New Challenges in Polymer Foaming: A Review of Extrusion Processes Assisted by Supercritical Carbon Dioxide." Progress in Polymer Science **36**(6): 749-766.

Saunders, J. H. (1991). "Fundamentals of Foam Formation". Handbook of Polymeric Foams and Foam Technology. D. Klempner and K. C. Frisch. Hanser, New York, NY. USA**:** 5-15.

Schneider, H. A., J. Rieger and E. Penzel (1997). "The Glass Transition Temperature of Random Copolymers: 2. Extension of the Gordon-Taylor Equation for Asymmetric Tg vs Composition Curves." Polymer **38**(6): 1323-1337.

Sears, J. K. and N. W. Touchette (1985). "Plasticizers". Encyclopedia of Polymer Science and Engineering. H. F. Mark, N. M. Bikales, C. G. Oveberger and G. Menges. John Wiley & Sons, New York, NY. **Supplement:** 568-648.

Sethia, S. and E. Squillante (2004). "Solid Dispersion of Carbamazepine in PVP K30 by Conventional Solvent Evaporation and Supercritical Methods." International Journal of Pharmaceutics **272**(1–2): 1-10.

Shah, V. P., Y. Tsong, P. Sathe and J.-P. Liu (1998). "In Vitro Dissolution Profile Comparison—Statistics and Analysis of the Similarity Factor, f2." Pharmaceutical Research **15**(6): 889-896.

Shutov, F. A. (1991). "Cellular Strucuture and Properties of Foamed Polymers". Handbook of Polymeric Foams and Foam Technology. D. Klempner and K. C. Frisch. Hanser, New York, NY. USA**:** 16-46.

Siepmann, J. and N. A. Peppas (2001). "Modeling of Drug Release from Delivery Systems Based on Hydroxypropyl Methylcellulose (HPMC)." Advanced Drug Delivery Reviews **48**(2-3): 139-157.

Smith, K. L., A. E. Winslow and D. E. Petersen (1959). "Association Reactions for Poly(alkylene Oxides) and Polymeric Poly(carboxylic Acids)." Industrial & Engineering Chemistry **51**(11): 1361-1364.

Socrates, G. (2000). Infrared and Raman Charcateristic Group Frequencies. Tables and Charts. John Wiley & Sons, LTD, New Yrok, NY. USA.

Sriwongjanya, M. and R. Bodmeier (1998). "Effect of ion exchange resins on the drug release from matrix tablets." European Journal of Pharmaceutics and Biopharmaceutics **46**(3): 321-327.

Streubel, A., J. Siepmann and R. Bodmeier (2003). "Floating Matrix Tablets Based on Low Density Foam Powder: Effects of Formulation and Processing Parameters on Drug Release." European Journal of Pharmaceutical Sciences **18**(1): 37-45.

Sun, H., G. S. Sur and J. E. Mark (2002). "Microcellular Foams from Polyethersulfone and Polyphenylsulfone: Preparation and Mechanical Properties." European Polymer Journal **38**(12): 2373-2381.

Sun, X., H. Liu, G. Li, X. Liao and J. He (2004). "Investigation on the Cell Nucleation and Cell growth in Microcellular Foaming by Means of Temperature Quenching." Journal of Applied Polymer Science **93**(1): 163-171.

Tadmor, Z. and C. G. Gogos (2006). Principles of Polymer Processing. Wiley-Interscience, Hoboken, NJ. USA.

Taylor, L. S. and G. Zografi (1997). "Spectroscopic Characterization of Interactions Between PVP and Indomethacin in Amorphous Molecular Dispersions." Pharmaceutical Research **14**(12): 1691-1698.

Throne, J. L. (2004). Thermoplastic Foam Extrusion. An Introduction. Hanser, Munich. Germany.

Todd, D. B. (1998). "Introduction to Compounding". Polymer Processing Institute Books from Hanser Publishers. D. B. Todd. Hanser/ Gardner Publications, Inc., Cincinnati, OH**:** 1-12.

Todd, D. B., C. G. Gogos and D. Champarampopoulos (1998). "Helical Barrel Rheometer". United States Patent 5,708,197.

Tomasko, D. L., H. Li, D. Liu, X. Han, M. J. Wingert, L. J. Lee and K. W. Koelling (2003). "A Review of $CO_2$ Applications in the Processing of Polymers." Industrial & Engineering Chemistry Research **42**(25): 6431-6456.

Ugaonkar, S., A. C. Nunes and T. E. Needham (2007). "Effect of n-sc$CO_2$ on crystalline to amorphous conversion of carbamazepine." International Journal of Pharmaceutics **333**(1–2): 152-161.

Verreck, G., A. Decorte, K. Heymans, J. Adriaensen, D. Cleeren, A. Jacobs, D. Liu, D. Tomasko, A. Arien, J. Peeters, P. Rombaut, G. Van den Mooter and M. E. Brewster (2005). "The Effect of Pressurized Carbon dioxide as a Temporary Plasticizer and Foaming Agent on the Hot Stage Extrusion Process and Extrudate Properties of Solid Dispersions of Itraconazole with PVP-VA 64." European Journal of Pharmaceutical Sciences **26**(3-4): 349-358.

Verreck, G., A. Decorte, K. Heymans, J. Adriaensen, D. Liu, D. Tomasko, A. Arien, J. Peeters, G. Van den Mooter and M. E. Brewster (2006a). "Hot Stage Extrusion of p-Amino Salicylic Acid with EC Using $CO_2$ as a Temporary Plasticizer." International Journal of Pharmaceutics **327**(1-2): 45-50.

Verreck, G., A. Decorte, K. Heymans, J. Adriaensen, D. Liu, D. L. Tomasko, A. Arien, J. Peeters, P. Rombaut, G. Van den Mooter and M. E. Brewster (2007). "The Effect of Supercritical $CO_2$ as a Reversible Plasticizer and Foaming Agent on the Hot Stage Extrusion of Itraconazole with EC 20 cps." Journal of Supercritical Fluids **40**(1): 153-162.

Verreck, G., A. Decorte, H. Li, D. Tomasko, A. Arien, J. Peeters, P. Rombaut, G. Van den Mooter and M. E. Brewster (2006b). "The Effect of Pressurized Carbon Dioxide as a Plasticizer and Foaming Agent on the Hot Melt Extrusion Process and Extrudate Properties of Pharmaceutical Polymers." Journal of Supercritical Fluids **38**(3): 383-391.

Vrentas, J. S., C. M. Jarzebski and J. L. Duda (1975). "A Deborah Number for Diffusion in Polymer-Solvent Systems." AIChE Journal **21**(5): 894-901.

Wade, L. G., Jr. (1993). Quimica Organica (In Spanish). Pearson Educacion, Mexico D.C.. Mexico.

Wishart, D., C. Knox and V. Law. (2012). "DrugBank. Open Data Drug & Drug Target Database." Retrieved September, 2012, from http://www.drugbank.ca/.

Wolff, F. F., L. Zirkel, S. Betzold, M. Jakob, V. Maier, F. Nachtrab, B. C. Nicolat, T. Fey and H. Münstedt (2011). "Using Supercritical Carbon Dioxide for Physical Foaming of Advanced Polymer Materials." International Polymer Processing **26**(4): 437-443.

Yang, M., P. Wang, C.-Y. Huang, M. S. Ku, H. Liu and C. G. Gogos (2010). "Solid Dispersion of Acetaminophen and Poly(ethylene oxide) Prepared by Hot-Melt Mixing." International Journal of Pharmaceutics **395**(1-2): 53-61.

Yang, M., P. Wang, H. Suwardie and C. G. Gogos (2011). "Determination of Acetaminophen's Solubility in Poly(ethylene oxide) by Rheological, Thermal and Microscopic Methods." International Journal of Pharmaceutics **403**(1-2): 83-89.

Yazdanian, M., K. Briggs, C. Jankovsky and A. Hawi (2004). "The “High Solubility” Definition of the Current FDA Guidance on Biopharmaceutical Classification System May be too Strict for Acidic Drugs." Pharmaceutical Research **21**(2): 293-299.

Zhang, F. and J. DiNunzio (2010). "Application of Hot-Melt Extrusion for Bioavailability Enhancement of Poorly Soluble Drugs". ANTEC 2010. Society of Plastic Engineers, Orlando, FL. USA**:** -.

Zhang, G. G. Z., D. Law, E. A. Schmitt and Y. Qiu (2004). "Phase Transformation Considerations During Process Development and Manufacture of Solid oral Dosage Forms." Advanced Drug Delivery Reviews **56**(3): 371-390.

Zhang, Q. and M. Xanthos (2004). "Material Properties Affecting Extrusion Foaming". Polymeric Foams. Mechanisms and Materials. S. T. Lee and N. S. Ramesh. CRC Press, Washington, D.C.. USA.

Zhang, X., I. Burgar, M. D. Do and E. Lourbakos (2005). "Intermolecular Interactions and Phase Structures of Plasticized Wheat Proteins Materials." Biomacromolecules **6**(3): 1661-1671.